Multi-wavelength follow-up of ANTARES neutrino alerts

A. Mathieu

CPPM-T-2015-005

Aix-Marseille Université
Faculté des Sciences de Luminy
163 avenue de Luminy
13288 Marseille Cedex 09

Thèse de doctorat

Spécialité : *Physique et Sciences de la Matière*

Mention : *Physique des Particules et Astroparticules*

présentée par

Aurore MATHIEU

en vue d'obtenir le grade de docteur de l'Université d'Aix-Marseille

Multi-wavelength follow-up of ANTARES neutrino alerts

soutenue le 01/10/2015 devant le jury composé de

Dr.	J.-L. Atteia	Rapporteur
Dr.	S. Basa	Directeur de thèse
Dr.	V. Bertin	Co-directeur de thèse
Prof.	M. Dennefeld	Rapporteur
Dr.	D. Dornic	Co-encadrant de thèse
Dr.	E. Kajfasz	Président du jury
Dr.	C. Lachaud	Examinateur
Prof.	M. Spurio	Examinateur

Remerciements

Etape incontournable d'une thèse : les remerciements, car sans la contribution plus ou moins importante des personnes que je vais lister ci-dessous, mon travail n'aurait pas été le même.

Tout d'abord, je tiens à remercier Eric Kajfasz, le directeur du CPPM, ainsi que tout le personnel du laboratoire pour m'avoir accueillie pendant ces trois années, et pour faire du CPPM un lieu de travail si agréable.

Je tiens ensuite à remercier tous les membres de mon jury pour non seulement avoir accepté d'en faire partie, mais aussi pour m'avoir permis d'améliorer mon manuscrit, et en particulier mes deux rapporteurs Jean-Luc Atteia et Michel Dennefeld pour avoir consciencieusement fait leur travail.

Un grand merci également à mon équipe d'encadrement, Vincent, Stéphane et Damien. Merci à vous trois pour tout ce que vous m'avez apporté et pour m'avoir permis de faire une thèse dans de très bonnes conditions. Merci à Stéphane pour son expertise en analyse d'images et ses conseils judicieux et un très grand merci à Damien pour le temps qu'il m'a consacré et tout ce qu'il m'a appris.

Je tiens ensuite à remercier toute l'équipe TAToO : Fabian, Bertrand, Michel, Jurgen, Auguste, Alain et Damien T., avec qui il a été très agréable de travailler et d'échanger au cours de ces trois dernières années. Je n'oublie pas non plus l'équipe ANTARES/KM3NeT du CPPM et souhaite bonne réussite aux deux nouveaux doctorants qui ont rejoint l'équipe cette année, Ilenia et Liam.

Je remercie aussi toutes les personnes que j'ai pu côtoyer au cours de ces trois dernières années, en particulier et pour n'en citer que quelques-uns : Fanny, Raymond, Thomas, Jérôme, Walaa, Mathieu, Marta, Margaux, Pierre...

Pour finir, je remercie ma famille qui a non seulement fait le déplacement de loin le jour J, mais qui s'est également toujours intéressée à mon travail. Enfin, merci à Renaud, mon mari, pour m'avoir toujours soutenue, et surtout supportée pendant les derniers mois de rédaction parfois éprouvants. Merci !

Résumé

Découverts en 1912 par Victor Hess, les rayons cosmiques font partie des sujets les plus étudiés en astrophysique de nos jours. Ce flux, principalement composé de particules chargées et de noyaux, bombarde notre atmosphère en permanence et s'étend sur plus de 10 ordres de grandeur en énergie (1 GeV-10^{11} GeV). Depuis plusieurs années, de nombreuses expériences ont été développées pour comprendre les sources et mécanismes à l'origine de leur accélération. Parmi les sources candidates à la production de rayons cosmiques de haute énergie, les sursauts gamma, les noyaux actifs de galaxie ou encore les supernovae à effondrement de coeur font figure de favoris. Ces sources font partie des phénomènes les plus violents de l'Univers et sont également des sources prodigieuses de photons à différentes énergies. Cependant, la détection de photons n'est pas suffisante pour sonder les processus mis en jeu au coeur de ces sources, et l'utilisation de nouveaux messagers devient indispensable.

Les neutrinos présentent plusieurs avantages pour tenir ce rôle de messagers cosmiques. Contrairement aux particules chargées, ils ne sont pas déviés par les nombreux champs magnétiques qu'il peut y avoir dans l'Univers et pointent donc directement vers leurs sources. De plus, comme ils n'interagissent que très faiblement et ne sont pas absorbés à l'inverse des photons, ils peuvent s'échapper des régions d'accélération et des environnements astrophysiques les plus denses.

Des neutrinos à différentes énergies sont créés par diverses sources dans l'Univers, comme illustré en Figure 1. Les réactions nucléaires au coeur du Soleil ou encore les captures électroniques qui ont lieu lors de l'effondrement de supernovae sont à l'origine d'une production de neutrinos au MeV. La détection de neutrinos solaires en 1968 avec l'expérience Homestake a d'ailleurs marqué le début de l'astronomie neutrino, renforcée en 1987 par la première détection de neutrinos d'origine extra-solaire lors de l'explosion de la supernova SN1987A. A plus haute énergie ($>$ GeV), des neutrinos atmosphériques sont produits lors de l'interaction de rayons cosmiques avec les couches supérieures de notre atmosphère, et constituent un grand bruit de fond pour l'astronomie neutrino. Aux énergies du GeV à plusieurs dizaines de EeV, des neutrinos pourraient être produits par des processus hadroniques lors de l'interaction de rayons cosmiques avec la matière ou le rayonnement environnant les sources astrophysiques. Les neutrinos étant les

produits de désintégration des pions et kaons créés lors de ces interactions (Equation 1). La détection d'une source astrophysique de neutrinos de haute énergie serait donc une preuve irréfutable de la présence de mécanismes hadroniques au coeur de ces sources, et serait également la première observation d'une source de rayons cosmiques.

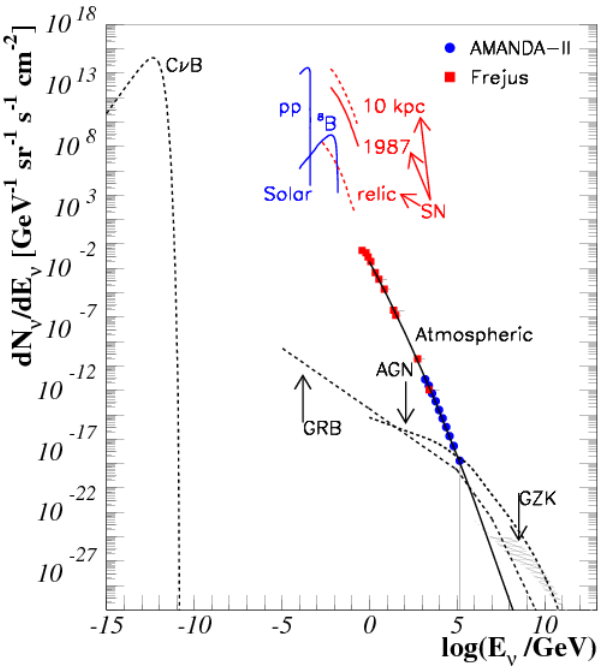

Figure 1: Spectres neutrino attendus pour différentes sources. Le Soleil et SN1987A (trait plein) sont les seules sources confirmées à ce jour.

$$p + p \longrightarrow \begin{cases} p + p + \pi^0 \\ p + n + \pi^+ \end{cases} \qquad p + \gamma \xrightarrow{\Delta^+} \begin{cases} p + \pi^0 \\ n + \pi^+ \end{cases} \qquad \begin{array}{l} \pi^0 \longrightarrow \gamma + \gamma \\ \pi^+ \longrightarrow \mu^+ + \nu_\mu \\ \mu^+ \longrightarrow e^+ + \nu_e + \overline{\nu}_\mu \\ n \longrightarrow p^+ + e^- + \overline{\nu}_e \end{array} \tag{1}$$

La faible interaction des neutrinos est un avantage pour l'astronomie mais rend aussi la détection très difficile. A cause de leur petite section efficace d'interaction et des faibles flux de neutrinos de haute énergie attendus, de larges volumes de détection sont nécessaires. L'idée d'installer des détecteurs au fond d'un lac ou de la mer a été proposée par Markov dès les années 60.

Les télescopes à neutrinos sont basés sur la détection des particules secondaires issues de l'interaction des neutrinos avec la matière. En effet, un neutrino de haute énergie émis par une source astrophysique va pouvoir traverser la Terre et interagir dans la croûte terrestre ou à proximité du détecteur. Suite à cette interaction, un lepton correspondant au neutrino (électron, muon ou tau) va être produit et créer, en arrivant dans un milieu tel que l'eau ou la glace, une cône de

lumière Tcherenkov (Figure 2). Cette lumière va ensuite être détectée grâce à un réseau de photomultiplicateurs.

Les télescopes à neutrinos sont soumis à plusieurs bruits de fond. En effet, les gerbes créées lors de l'interaction de rayons cosmiques avec notre atmosphère produisent des muons et neutrinos atmosphériques. Les muons atmosphériques peuvent traverser plusieurs kilomètres d'eau ou de glace avant de se désintégrer. Pour réduire ce bruit de fond, les télescopes à neutrinos sont installés à de grandes profondeurs. La matière au-dessus du détecteur agit alors comme bouclier contre ces muons. Cependant, le flux de muons descendants est toujours très élevé comparé au flux de muons issus de neutrinos cosmiques. La recherche de signal astrophysique se concentre donc sur les événements montants, qui correspondent à des neutrinos qui ont traversé la Terre et interagi à proximité du détecteur. La décroissance des pions et des kaons produits dans les gerbes atmosphériques donne aussi lieu à un flux important de neutrinos atmosphériques. Ceux-ci peuvent être détectés comme événements montants et représentent donc un bruit de fond irréductible.

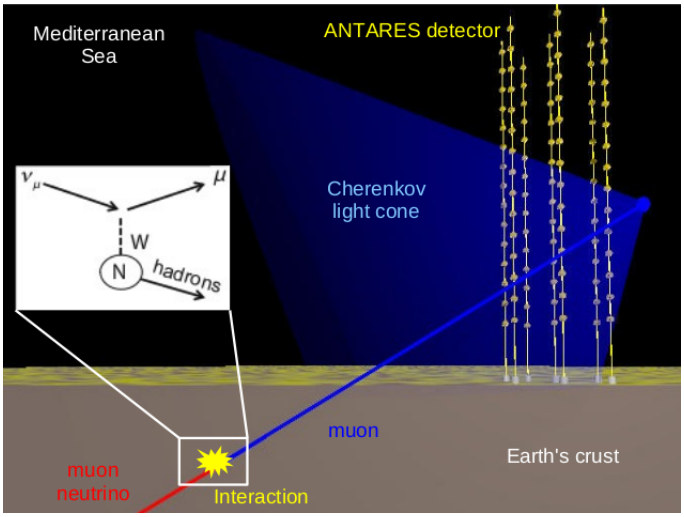

Figure 2: Principe de détection de neutrinos de haute énergie. Le lepton issu de l'interaction d'un neutrino avec la croûte terrestre va produire un cône de lumière Tcherenkov détectable par un réseau de photomultiplicateurs.

Le télescope ANTARES, situé au fond de la Méditerranée ($\sim$ 2500 m) à 40 km au large de Toulon en France, a été conçu pour détecter des neutrinos de haute énergie d'origine cosmique. Il est constitué de 12 lignes verticales d'environ 480 m en opération depuis 2008. Chaque ligne comporte 25 étages équipés de trois modules optiques contenant un photomultiplicateur. Au total, un réseau tridimensionnel de 885 photomultiplicateurs permet à partir des différents temps et positions d'arrivée de la lumière Tcherenkov sur les modules optiques de reconstruire la direction du neutrino incident. Bien que les trois saveurs de neutrinos soient détectables par ANTARES, les longues traces générées par le passage des muons vont permettre une reconstruction plus précise de la direction du neutrino incident, contrairement aux électrons ou taus qui vont générer des cascades électromagnétiques et hadroniques. Aux énergies auxquelles ANTARES est sensible

(> 100 GeV), une résolution angulaire d'environ 0.3° peut être atteinte sur la reconstruction. Depuis 2008, plus de 10 000 candidats neutrinos ont été détectés pas ANTARES et toute la difficulté de l'astronomie neutrino est de distinguer des neutrinos cosmiques parmi le flux de neutrinos atmosphériques.

Actuellement, aucune source de neutrinos de haute énergie n'a encore été identifiée, bien que le premier signal de neutrinos d'origine cosmique ait été observé par IceCube en 2012. Ce télescope à neutrinos de 86 lignes au Pôle Sud a détecté un total 37 événements avec une énergie supérieure à 30 TeV et un niveau de confiance de 5.7 σ. Cet excès par rapport aux bruits de fond atmosphériques est représenté en Figure 3. Bien qu'ANTARES soit de petite taille par rapport à IceCube, quelques événements cosmiques sont attendus dans les données d'ANTARES. Cependant, le manque de statistique et le bruit de fond important n'ont jusqu'à présent pas permis de détecter un excès significatif.

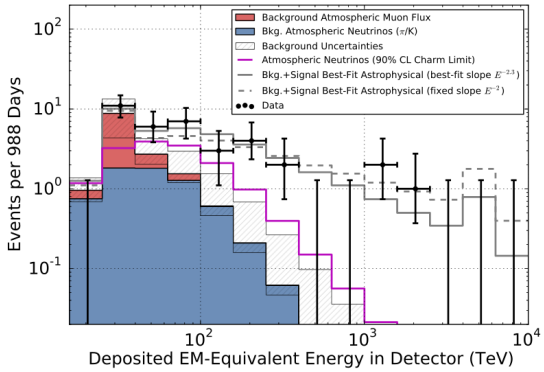

Figure 3: Distribution des événements cosmiques et du bruit de fond atmosphérique détectés par IceCube en fonction de l'énergie déposée dans le détecteur.

Une façon d'augmenter la sensibilité de détection est de combiner les informations provenant de plusieurs messagers, tels que les photons et les neutrinos, dans une fenêtre limitée en temps et en espace. L'avantage de la recherche de sources transitoires permet de prendre en compte l'information temporelle. En effet, en recherchant une émission de neutrinos coïncidente avec un événement transitoire, les bruits de fond peuvent être significativement réduits. Il existe deux méthodes pour y parvenir. La première repose sur une information extérieure fournie par des satellites gamma ou X. Suite à la détection d'une source, telle qu'un sursaut gamma, des satellites comme *Fermi* ou *Swift* envoient une alerte à la communauté via une notice GCN (Gamma-ray Coordinates Network). Une analyse des données neutrinos enregistrées pendant cet événement est ensuite effectuée pour extraire un excès possiblement corrélé à la source observée en photons.

La deuxième méthode, inverse, consiste à utiliser la détection de neutrinos comme déclencheur d'autres observatoires. L'avantage de cette méthode est que les télescopes à neutrinos ont instantanément un champ de vue d'au moins un hémisphère avec une grande efficacité. La détection d'un neutrino spécial, c'est-à-dire avec des caractéristiques qui pourraient correspondre à celles d'un neutrino d'origine cosmique, permet d'envoyer une alerte à un réseau de télescopes qui vont pointer dans la direction du neutrino pour tenter d'observer une contrepartie électromagnétique.

C'est sur ce principe qu'est basé TAToO (Telescopes-ANTARES Target Of Opportunity), le programme de suivi multi-longueur d'onde de la collaboration

ANTARES, illustré en Figure 4. Lorsqu'un neutrino est détecté par ANTARES,

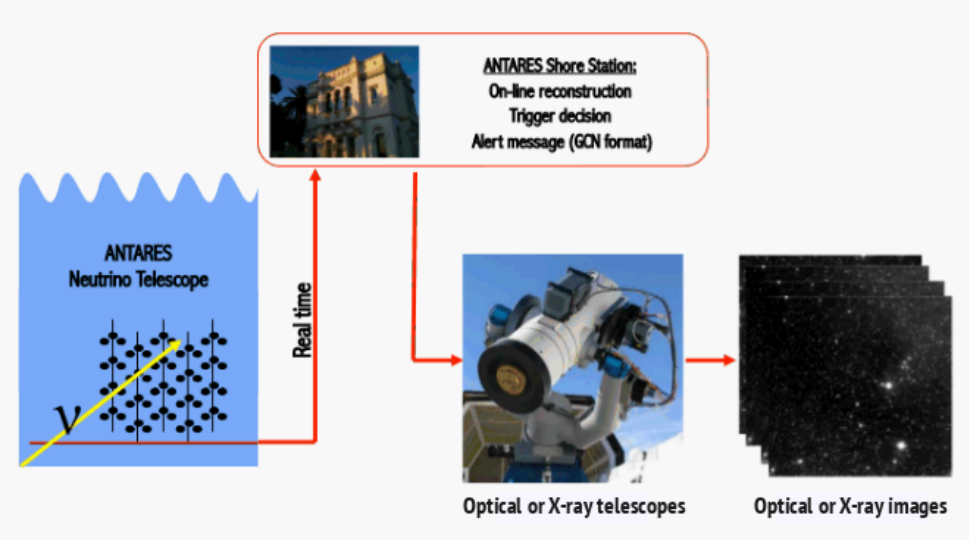

Figure 4: Système d'alerte TAToO. La détection d'un neutrino "spécial" par ANTARES permet de déclencher un réseau de télescopes pour identifier une possible contrepartie électromagnétique à cette émission neutrino.

les données sont envoyées à terre à La Seyne-Sur-Mer, puis reconstruites par différents algorithmes. Des coupures sont ensuite appliquées pour décider de l'envoi d'une alerte. Il y a actuellement 3 critères qui permettent de déclencher le réseau de télescopes mis en place dans TAToO :

- Directionnel : détection d'un neutrino dans la direction ($< 0.4°$) d'une galaxie locale (< 20 Mpc).
- Haute énergie : détection d'un neutrino de haute énergie ($<E> = 7$ TeV).
- Multiplet : détection d'au moins deux neutrinos dans un cône de 3° et dans un intervalle de temps de 15 minutes.

Si l'un de ces trois critères est rempli, une alerte est envoyée à un réseau de télescopes optiques et à l'instrument XRT (X-ray telescope) du satellite *Swift*. Actuellement, neuf télescopes optiques font partie du réseau TAToO :

- TAROT Calern et TAROT Chili, deux télescope de 25 cm avec un champ de vue de $1.9°\times1.9°$.
- Six télescopes de 2×40 cm du réseau MASTER (4 en Russie, 1 en Afrique du Sud et 1 aux Canaries) avec un champ de vue de $2\times(2°\times2°)$.
- Le télescope de 1 m Zadko en Australie, avec un champ de vue de $23.6'\times23.6'$.

Jusqu'à fin 2014, les 4 télescopes ROTSE (Australie, Etats-Unis, Namibie, Turquie) faisaient également partie du réseau mais ont été déconnectés au fur et à mesure de leur mise hors service. Les critères de sélection des neutrinos ci-dessus dépendent

en partie du nombre d'alertes qu'il est possible d'envoyer aux différents télescopes. Un envoi moyen de 12 alertes haute énergie et 12 alertes directionelles par an a été accepté par les différentes collaborations[1]. En revanche, pour le suivi en X, 6 alertes par an peuvent être envoyées au satellite *Swift*. Une sélection plus stricte des événements haute énergie est donc effectuée, correspondant à des neutrinos avec une énergie moyenne de 20 à 30 TeV.

Pour qu'un tel système d'alerte soit efficace et que l'observation coïncidente d'un neutrino et d'une contrepartie optique ou X soit possible, deux conditions principales sont requises. Il faut que le temps de réponse du système soit comparable, voire plus rapide, que la durée de l'événement transitoire et que le champ de vue des télescopes soit adapté à la résolution angulaire du télescope à neutrinos. Avec TAToO, les alertes peuvent être envoyées avec un délai de 3 à 5 secondes après la détection du neutrino, et le grand champ de vue des télescopes (au moins $1.9°\times1.9°$) permet de couvrir la boîte d'erreur sur la reconstruction de la direction du neutrino détecté qui a en moyenne un rayon de 0.3°. En revanche, pour Zadko et *Swift*-XRT qui ont un plus petit champ de vue ($\sim$ 24 arcmin$\times$24 arcmin), la combinaison de plusieurs observations autour de la direction du neutrino est nécessaire.

Bien que cette approche ait l'avantage de ne faire aucune hypothèse sur la source ayant pu émettre le neutrino, cette recherche est principalement motivée par les modèles d'émission de neutrinos des sursauts gamma et des supernovae à effondrement de coeur (Figure 5). En effet, pour les sursauts gamma, des neutrinos de 10 TeV à 10 PeV pourraient être produits par des processus hadroniques en même temps que l'émission électromagnétique. Des électrons et protons seraient accélérés lors de chocs internes à l'intérieur du jet. Les protons interagiraient ensuite avec les photons produits par le rayonnement synchrotron des électrons accélérés. Des pions et kaons seraient alors produits lors de ces interactions via la résonance Δ. La décroissance des pions et kaons chargés donnerait donc lieu à une émission de neutrinos, tandis que les pions et kaons neutres se désintègreraient en rayons gamma. Le jet de matière serait ensuite ralenti par des chocs externes avec le milieu interstellaire, créant une émission rémanente en X, optique, infrarouge et radio. L'échelle de variabilité caractéristique de ces sources est de l'ordre de quelques secondes pour l'émission prompte à plusieurs heures pour l'émission rémanente.

En ce qui concerne les supernovae à effondrement de coeur, les connexions déjà observées avec les sursauts gamma suggèrent la présence de jets moyennement relativistes qui pourraient être produits lors de l'effondrement de l'étoile. Ces jets seraient confinés à l'intérieur de l'enveloppe stellaire, absorbant l'émission électromagnétique mais produisant efficacement des neutrinos de 100 GeV à 10 TeV via des interactions proton-proton. Ces neutrinos seraient alors la seule signature prompte de ces sources cachées, jusqu'à la dissipation de l'enveloppe stellaire qui laisserait apparaître la supernova en optique quelques heures plus tard et qui durerait jusqu'à plusieurs semaines après l'explosion.

Pour détecter ces sources, deux stratégies d'observation ont été mises en place

[1]Jusqu'à présent, aucune alerte n'a été envoyée suite à la détection d'un multiplet de neutrinos.

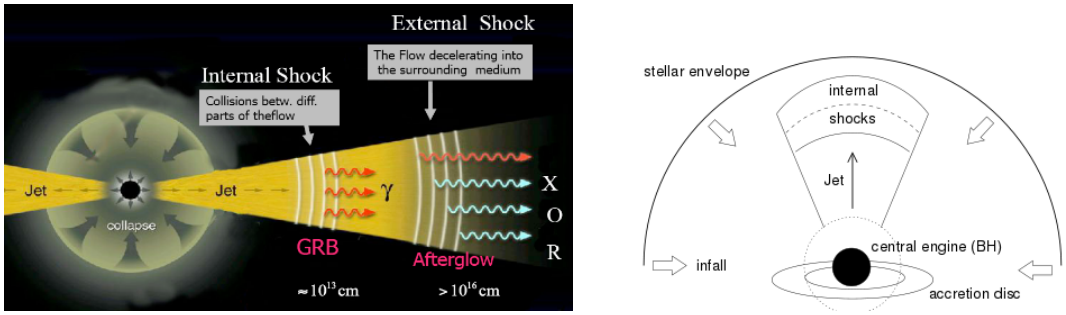

Figure 5: Modèles d'émission des jets de sursauts gamma (gauche) et supernovae (droite).

dans TAToO pour le suivi optique. Une stratégie prompte avec des images prises dès que possible après réception de l'alerte et dans un délai maximum de 24 heures, et une stratégie de suivi avec des observations programmées jusqu'à 60 jours après l'alerte neutrino[2]. Concernant le suivi en X, *Swift* réalise pour chaque alerte 4 observations autour de la direction du neutrino de 2 ks chacune et avec un délai de quelques heures après la réception de l'alerte. Les données sont directement analysées et des observations de suivi sont programmées uniquement si un candidat transitoire est détecté.

Depuis la mise en place de TAToO en 2009, plus de 160 alertes ont été envoyées aux télescopes optiques, dont 10 ont également été envoyées à *Swift* depuis son entrée dans le réseau mi-2013. Les premières observations en optique et X ont été faites 17 secondes et 1.1 heures après la détection du neutrino, respectivement. Une carte de ces événements en coordonnées galactiques est représentée en Figure 6.

L'analyse des images prises par les différents télescopes pour chaque alerte a été réalisée au cours de cette thèse. Pour cela, un programme d'analyse d'images optiques basé sur une méthode de soustraction a été développé. Cette méthode, illustrée en Figure 7, consiste à soustraire une image de référence, c'est-à-dire une image de très bonne qualité où le signal transitoire recherché ne serait pas ou plus visible, à une image prise lors du suivi d'une alerte neutrino et dans laquelle une contrepartie transitoire est recherchée. Le choix de la référence est donc très important pour qu'une source transitoire nouvelle puisse apparaître sur la soustraction. Pour des sources transitoires rapides, telles que les sursauts gamma, une image de référence est choisie parmi les images prises plusieurs jours après l'alerte neutrino, alors que pour des sources transitoires lentes, telles que les supernovae qui vont avoir leur pic de luminosité environ 20 jours après leur explosion, une image de référence est choisie parmi les premières nuits d'observation ou deux mois après l'alerte lorsque le signal attendu est supposé plus faible que dans l'image à analyser.

La soustraction d'images est une technique couramment utilisée en astronomie pour étudier le ciel variable ou transitoire et de nombreux programmes d'analyse basés sur cette méthode existent déjà (programmes SNLS, ROTSE...). Cepen-

[2]Pour le suivi avec MASTER, des observations de suivi sont uniquement programmées à 7 et 20 jours après l'alerte neutrino.

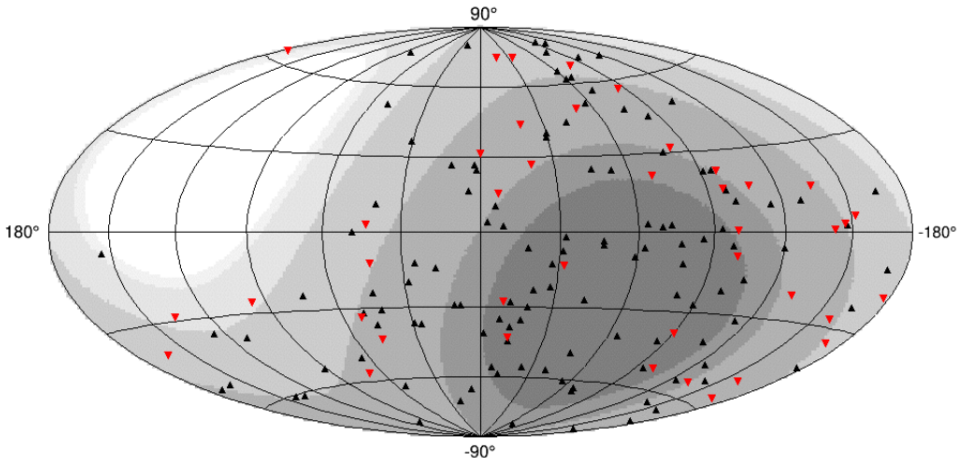

Figure 6: Carte en coordonnées galactiques des 165 alertes neutrinos envoyées depuis 2009. Les événements directionnels et haute énergie sont représentés en rouge et noir respectivement. Le dégradé de gris montre la visibilité d'ANTARES, avec une zone blanche non observable.

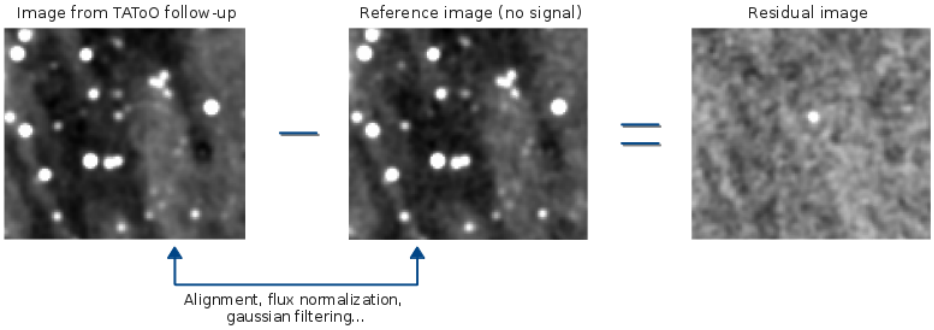

Figure 7: Méthode de soustraction d'images pour détecter des sources transitoires.

dant, avec un système d'alertes comme TAToO, la qualité des images prises par les différents télescopes est très variable, comme illustré en Figure 8. Cela est principalement dû au fait que les conditions d'observation ne peuvent être choisies et sont donc rarement optimales. En effet, lorsqu'une alerte est reçu par les télescopes, ceux-ci vont prendre des images s'ils sont aptes à observer et que le champ est visible. Des programmes tels que SNLS, développé pour analyser des images prises par le CFHT d'Hawaii, ne sont donc pas adaptés au traitement d'images avec des qualités bien plus basses et très variables selon les observations. De plus, les programmes existants ont généralement été développés pour traiter les images prises par un même télescope. Dans le réseau TAToO, des observations sont faites par les télescopes TAROT, ROTSE et Zadko, aux caractéristiques différentes[3]. Au cours de cette thèse, un programme d'analyse d'images robuste et efficace a été développé à partir d'outils publics. Un travail a notamment été fait sur l'optimisation des paramètres de ces outils pour pouvoir traiter une large variété

[3]La collaboration MASTER a développé son propre programme d'analyse d'images.

d'images et obtenir des résultats consistants.

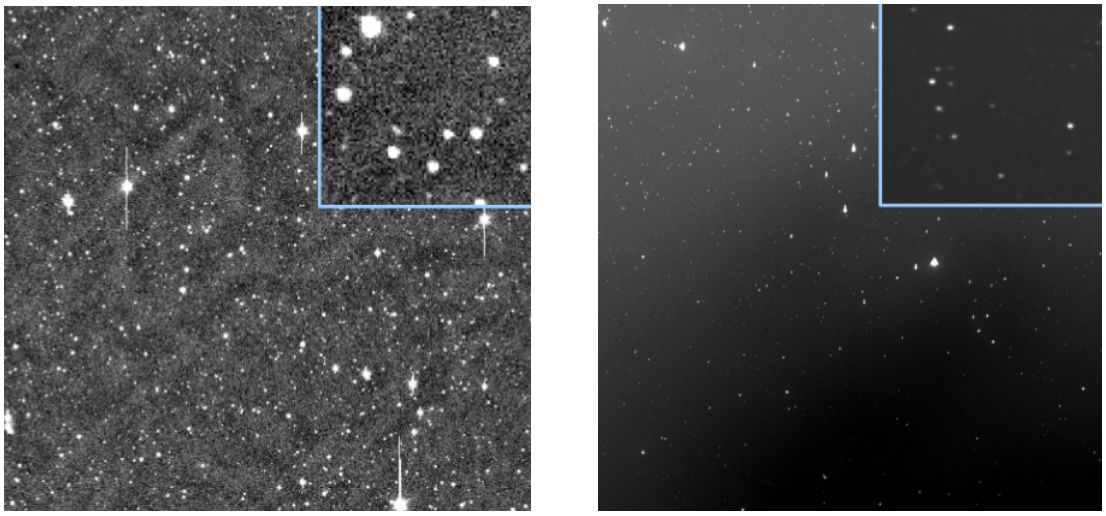

Figure 8: Images prises par TAROT Chili (gauche) et ROTSE 3c-Namibie (droite). Un zoom de chaque image est encadré en bleu.

Le programme repose essentiellement sur quatre grandes étapes :

- Calibration astrométrique et photométrique : cette étape permet d'aligner toutes les images d'une alerte sur une même grille de pixels et de convertir le flux mesuré pour chaque source en magnitude calibrée par rapport à un système de référence.

- Co-addition : la co-addition d'images permet d'augmenter le rapport signal sur bruit d'une série d'images et donc la limite de détection, mais dégrade également l'information temporelle, et est donc utilisée ou non selon le type de recherche effectuée.

- Choix de la référence et soustraction : l'image de référence est choisie comme expliqué précédemment et est ensuite soustraite pixel par pixel à une image de suivi d'une alerte.

- Détection et inspection visuelle des candidats : le programme sélectionne automatiquement les sources variables ou transitoires d'une image si elles remplissent un des deux critères suivants :
  - Nouvelle source : une source est présente dans l'image mais pas dans la référence.
  - Variabilité : une source est au moins 0.5 magnitude plus brillante dans l'image que dans la référence.
  Les candidats sélectionnés sont ensuite inspectés à l'oeil, les courbes de lumières sont construites, et une comparaison avec des catalogues est effectuée pour tenter d'identifier les candidats.

Grâce à ce programme, deux analyses ont été réalisées au cours de cette thèse pour rechercher une contrepartie transitoire à une émission neutrino. La première

a été dédiée à la recherche de sources transitoires rapides, telles que les sursauts gamma. Pour cela, un total de 42 alertes envoyées entre octobre 2009 et janvier 2015 avec des images optiques promptes, c'est-à-dire prises dans un délai de 24 heures après la détection du neutrino, ont été traitées avec le programme. A ces images s'ajoutent les données prises par l'instrument XRT du satellite *Swift* lors du suivi de 10 alertes envoyées entre juillet 2013 et septembre 2015. Ces données ont été automatiquement analysées par des algorithmes dédiés de *Swift*. Pour ces deux longueurs d'onde, aucune source transitoire rapide n'a pu être identifiée comme contrepartie optique ou X à l'émission neutrino, bien que quelques candidats intéressants aient été détectés. Dans les deux cas, des limites supérieures sur la magnitude ou le flux des sources transitoires possiblement associées à une émission neutrino ont été placées. L'implication de ces limites a ensuite été discutée dans la cas des sursauts gamma. L'hypothèse que les neutrinos détectés aient été produits par des sursauts gamma a pu être rejetée à un haut niveau de confiance pour les alertes les plus rapidement suivies.

Concernant la deuxième analyse, dédiée à la recherche de sources transitoires variant à l'échelle de la journée ou de la semaine, 71 alertes envoyées entre octobre 2009 et janvier 2015 aux télescopes optiques ont été analysées. Pour ces alertes, des observations de suivi ont été faites jusqu'à 60 jours après la détection du neutrino, avec en moyenne 8 nuits d'observation pour chaque alerte. Les images ont été co-additionnées nuit par nuit lorsque la qualité le permettait. Au terme de cette analyse, aucune contrepartie transitoire n'a été identifiée en corrélation avec une émission neutrino. Des contraintes ont donc pu être placées sur les paramètres Γ et $E_{\rm jet}$ du modèle Ando & Beacom, qui prédit la production de neutrinos dans des jets moyennement relativistes de supernovae à effondrement de coeur, mais également sur le taux de supernovae ρ produisant de tels jets.

CONTENTS

Introduction

The transient and variable Universe is increasingly studied with the development of facilities for sky monitoring across, and beyond, the electromagnetic spectrum. Transient phenomena, such as gamma-ray bursts (GRBs), active galactic nuclei (AGN) or core-collapse supernovae (CCSNe) are often associated with the most violent explosions in the Universe and are prodigious sources of photons at various energies. Furthermore, those sources are thought to be the acceleration sites of high energy cosmic rays. Although they have been discovered a century ago, their origin and acceleration mechanisms are still unknown. To solve this puzzle, the combination of different messengers is required, since the detection of photons alone is not sufficient to provide a complete picture of those sources.

Multi-messenger astrophysics is a young and promising research field derived from the extension of traditional astronomy beyond the electromagnetic spectrum. It relies on a quest to use the messenger particles of the four fundamental forces: photons, neutrinos, cosmic rays and gravitational waves. Of particular interest to this thesis is the information coming from neutrinos and photons. Unlike charged particles, they are not deflected by magnetic fields and can thus point back to their source. In addition, neutrinos easily escape from the acceleration regions and propagate through space without interaction, as they do not suffer from absorption and interact weakly.

High energy neutrinos are thought to be produced in hadronic processes during the interaction of charged cosmic rays with matter or radiation fields within or surrounding astrophysical sources. The identification of those sources would thus reveal the acceleration sites of cosmic rays, and would provide key information for a better understanding of processes at work within them.

The ANTARES telescope, completed in 2008 in the Mediterranean Sea, aims at detecting the sources of high energy neutrinos with a 3-dimensional array of 885 photomultiplier tubes. The detection of Cherenkov light induced by the propagation of up-going muons in water is used as a signature of muon neutrino interaction close or within the instrumented volume. However, the greatest challenge in neutrino astronomy is to discern neutrinos of astrophysical origin from those of atmospheric origin, which represent an irreducible background. To identify steady neutrino sources, the standard method is to search for a significant

neutrino excess over background in the direction of known gamma-ray sources. The advantage to search for transient sources is that the temporal information is added. By searching for neutrinos in a limited space/time window around the transient event, the background is significantly reduced. Furthermore, as a neutrino detector has an instant coverage of at least a hemisphere with a high duty cycle, a neutrino detection can be used to trigger electromagnetic observations at various wavelengths. A coincident detection would allow the identification of a neutrino progenitor from a single detected event.

It is in this context that a multi-wavelength follow-up program, denoted as TAToO, has operated within the ANTARES Collaboration since 2009. It is based on optical and X-ray follow-up of selected high energy neutrino events very shortly after their detection. These follow-up observations have the potential to reveal the electromagnetic counterpart of transient neutrino sources. Although this approach has the advantage that it does not require an *a priori* hypothesis on the nature of the underlying neutrino source, this online search is mostly motivated by models of neutrinos from GRBs and CCSNe.

In the first chapter of this manuscript, an overview of time domain and multi-messenger astroparticle physics, as well as neutrino astronomy is presented. The physics and neutrino production is then detailed for two candidate sources of particular interest to this thesis: GRBs and CCSNe. In the second chapter, the neutrino detection techniques, the current and future neutrino telescopes, as well as the ANTARES detector are described. In the third chapter, the TAToO alert system is presented. The neutrino event reconstruction, the alert trigger criteria, as well as the alert sending and the telescope network are detailed. The fourth chapter describes the optical image analysis pipeline developed during this thesis, as well as the X-ray data analysis automatically performed at the UK Swift Science Data Center. The fifth and sixth chapters are devoted to the analyses performed in this thesis. The search for fast transient sources, such as GRB afterglows, in early follow-up images is presented in Chapter 5, while the search for slowly varying transient sources, such as CCSNe, is presented in Chapter 6.

CHAPTER 1

High energy transient sky

Transient phenomena are often associated with the most extreme conditions in the Universe, where violent explosions and outbursts can occur. Of galactic or extragalactic origin, powerful sources classified as transient include gamma-ray bursts (GRBs), active galactic nuclei (AGN), supernovae (SNe), and many others which emit over the entire electromagnetic spectrum with typical timescales ranging from seconds to days or weeks. Those sources emit large amount of energy, but the processes driving the high energy emission are still not well understood, and several questions remain.

The era of time domain astronomy has begun over the past decades with a variety of instruments devoted to the study of time variation of powerful astrophysical objects.The *Fermi* [1] and *Swift* [2] satellites are exploring the transient sky in γ-ray and X-ray wavelengths with unprecedented sensitivity and coverage, playing a crucial role in understanding transient phenomena.

Our current view of the γ-ray sky at GeV energies has been largely provided by the *Fermi* satellite (Figure 1.1). Launched in 2008, the Large Area Telescope (LAT) and the Gamma-ray Burst Monitor (GBM) on board the *Fermi* satellite are revealing the high energy spectra of numerous transient sources, with particularly important discoveries in the GRB field. The *Swift* satellite, launched in 2004, has already completed ten years of discoveries in time domain astronomy. Originally envisioned to chase GRBs, *Swift* has become a discovery machine for new types of behavior, such as SN shock break-out, tidal disruption event, high energy emission from flaring stars.

At higher energies ($>$ TeV), the γ-ray flux is too low to be efficiently measured by satellite detectors. Nevertheless, when γ-rays collide with the matter in the upper layers of the atmosphere, they produce showers of particles emitting Cherenkov radiation which can be detected with Imaging Atmospheric Cherenkov Telescopes (IACTs) on ground. The current generation of IACTs includes H.E.S.S., MAGIC and VERITAS, which all carry out transient search programs.

Key information about high energy transient sources can also come from their activity at other wavelengths. The use of optical and radio facilities is of high

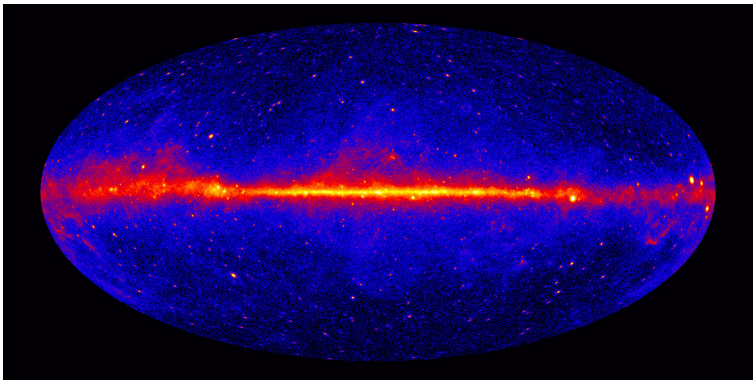

Figure 1.1: The γ-ray sky as seen by *Fermi*. Picture taken from http://fermi.sonoma.edu/multimedia/gallery/3YearSkyMap.jpg.

interest to monitor the transient sky, and to trigger, for example, γ-ray observations. For instance, the MWA and the future SKA experiments will greatly enhance our understanding of the transient radio sky. In the same way, optical facilities are necessary to lead to potential insights into the high energy emission of transient sources.

To catch the most extreme and unusual phenomena in the Universe, many instruments are becoming increasingly coordinated, complementing each other across the energy spectrum from radio emission up to gamma-rays. Indeed, a dynamic synergy between space- and ground-based observatories has been developed over the last years, as time domain astronomy, and particularly the study of high energy transient sources, requires rapid response capabilities. This allows for wide-ranging interactions between different observatories tailored to meet the demands imposed by different transients.

1.1 Multi-messenger approach

While high energy photons have revealed important insights for many astrophysical transient phenomena, the Universe is not completely transparent to photons which are easily absorbed. For instance, above TeV energies, the photon mean free path is considerably reduced due to the interaction with the cosmic microwave background (CMB) and the extragalactic background light [3]. Therefore, the Universe becomes opaque for the most energetic sources at high distances. In addition, PeV energy photons produced at the edge of our own Galaxy cannot be detected because they convert into an electron pair during their travel to the Earth. To probe the physics of the most energetic transients, the detection of photons is not sufficient and other messengers have to be used.

The production of the GeV-TeV γ-ray emission in those sources is mainly explained by two models, depicted in Figure 1.2:

The leptonic model The basic interpretation for the production of high energy photons in the astrophysical leptonic model is the so-called Synchrotron Self-Compton mechanism. Synchrotron radiation from electrons moving

in a magnetic field generates photons. These photons have an energy spectrum peaked from infrared to X-ray wavelengths and constitute a target for their own parent electrons. The inverse Compton scattering allows low energy photons to gain energy by collisions with high energy electrons. With this model, high energy photons can be produced up to TeV energies.

The hadronic model The second competitive scenario to produce high energy photons is the hadronic model, in which accelerated protons interact with matter (pp collisions) or radiation ($p\gamma$ interactions) within or around astrophysical sources. High energy photons are produced along with high energy neutrinos through the subsequent decay of neutral and charged pions, respectively (see Section 1.2.3).

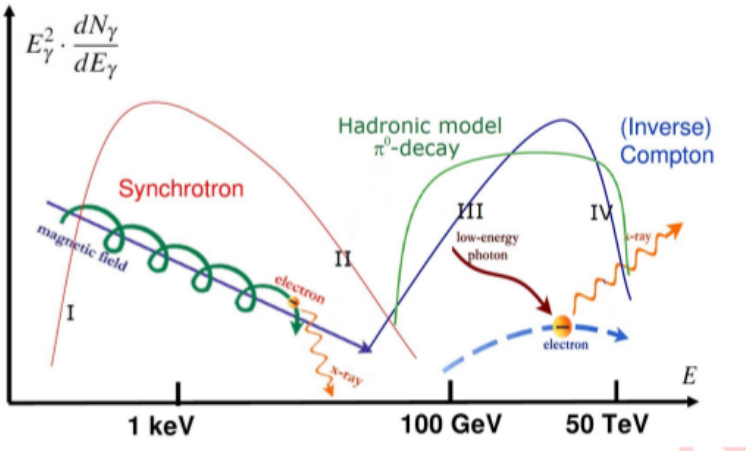

Figure 1.2: Spectral energy distribution of photons produced in leptonic/hadronic models. Synchrotron radiation is caused by relativistic electrons accelerated in a magnetic field. Photons from synchrotron emission represent also the target for inverse Compton scattering of the parent electrons. When hadrons interact with matter or ambient photons, a distribution of γ-rays from π^0 decays as indicated by the green curve could be obtained. Superimposition of γ-rays from both leptonic and hadronic mechanisms is assumed in case of mixed models. Image taken from [4].

Considering hadronic mechanisms, high energy neutrinos produced along with γ-rays can serve as probes for the highest energy environments. So far, none of these two models has been universally favored. While detailed modeling of γ-ray morphology and spectra has in some cases produced a preference for the hadronic model, it is generally possible to fit the γ-ray data with either leptonic or hadronic models. The detection of high energy neutrinos from an astrophysical source would provide an unambiguous "smoking gun" evidence that hadronic processes occurred in such a source. Conversely, the non-detection of neutrinos from particular sources would be sufficient to rule them out as hadronic accelerators. The existence of high energy astrophysical neutrinos has been motivated by the observations of high energy hadronic cosmic rays. Their origin is still unknown but is likely to be associated with the most energetic processes in the Universe. At their acceleration sites, but also during propagation through space,

cosmic rays would produce neutrinos in collision with ambient matter and radiation fields. The detection of high energy neutrinos would thus reveal the presence of cosmic ray accelerators, and would provide important clues on the origin and acceleration mechanisms of high energy cosmic rays.

Multi-messenger astronomy relies on a quest to use the messenger particles of the four fundamental forces: photons, neutrinos, cosmic rays and gravitational waves. The connection between these messengers has been made possible by the synergy of various detectors such as the ANTARES and IceCube neutrino telescopes, the Pierre Auger cosmic ray observatory and the Advanced LIGO and Virgo gravitational-wave detectors. On ground and in space, they are complemented by high energy radiation observatories including the *Swift* and *Fermi* satellite, the H.E.S.S., MAGIC, VERITAS and HAWC TeV gamma-ray observatories. This connection is of fundamental importance for a better understanding of the processes driving the most energetic phenomena, since none of these messengers alone is able to give a complete picture. In this way, considerable efforts have been made since a few years to link current and future multi-messenger and follow-up observatories. The Astrophysical Multi-messenger Observatory Network (AMON) [5] provides a good example of these efforts. This network aims to enable near real-time coincidence searches for multi-messenger astrophysical transients and their electromagnetic counterparts, by sending alerts within the network and to interested external observers.

On smaller scales, multi-messenger searches are carried out within different collaborations, such as in the ANTARES experiment. The combination of neutrinos with other messengers, mainly photons at various wavelengths, offers a unique opportunity to study the high energy transient sky. Furthermore, by including the time information, the observation of only one neutrino in correlation with an electromagnetic signal would be a significant event and would provide unprecedented information about the processes at work inside the most violent phenomena of the Universe.

It is in this context that the multi-wavelength follow-up program of the ANTARES experiment, TAToO[1], has been drawn up. This program focuses on the search for optical and X-ray transient counterparts associated with a neutrino event. The sky in these two wavelengths is rich in transient and variable sources, with decay timescales ranging from a few seconds to a few months, as illustrated in Figures 1.3 and 1.4. The combination of optical and X-ray observations provides a large picture of the sky, and is thus well-suited to search for the unknown high energy neutrino sources.

1.2 Neutrinos as cosmic messengers

During the last decades, considerable efforts have been made to establish high energy neutrinos as cosmic messengers. The motivation derives from the special properties of neutrinos. They are neutral and stable, interact weakly and travel directly from their source without absorption. Hence, neutrinos easily escape

[1] Telescopes-ANTARES Target Of Opportunity

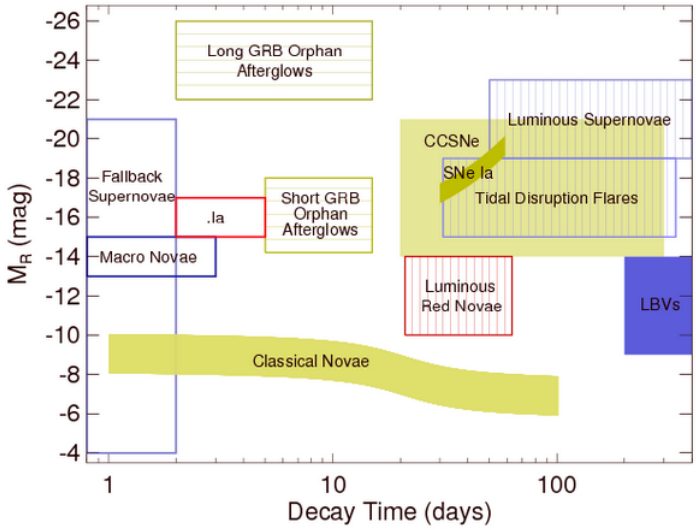

Figure 1.3: Overview of the most luminous optical transients and variables as a function of characteristic decay timescale (typically the time to fade from peak by 2 magnitudes). Image taken from [6]

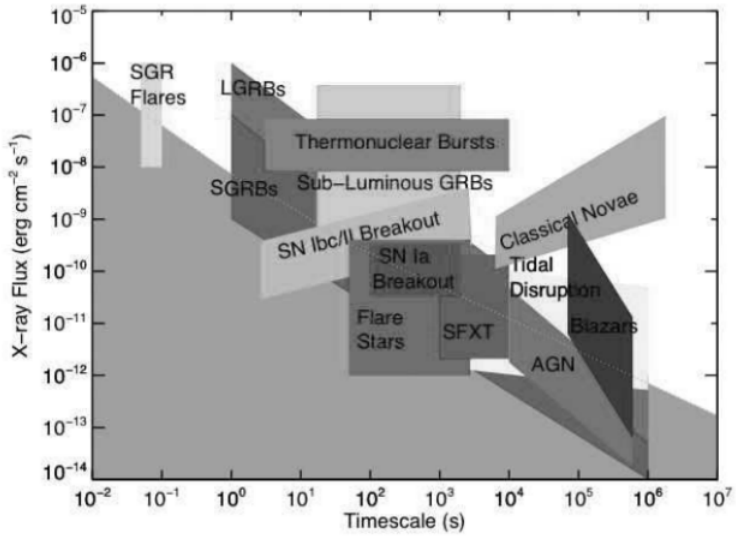

Figure 1.4: Overview of the X-ray transient sky. Image taken from [7].

energetic and dense astrophysical environments otherwise opaque to electromagnetic radiation and propagate through space without interaction, unlike charged particles which are deflected by magnetic fields and no longer point back to their source. It is for these reasons that neutrinos promise to provide unique insights into a number of extreme astrophysical phenomena.

1.2.1 Neutrino astronomy

Neutrino astronomy is a relatively young field. It began in 1968 with the detection of solar neutrinos by R. Davis at the Homestake experiment [8] and gained in

importance in 1987 with the first detection of neutrinos from outside our solar system. SN1987A, produced by the explosion of the blue giant Sanduleak-69202 in the Large Magellanic Cloud, was the first supernova visible with the naked eye since 1604. Three different detectors Kamiokande-II [9], the Irvine Michigan Brookhaven (IMB) experiment [10] and Baksan [11] observed 12, 8 and 5 neutrino interaction events, respectively, approximately 3 hours before the light from the supernova reached the Earth. While solar and supernova neutrinos reach energies of several tens of MeV, high energy neutrinos from TeV to PeV energies are expected to be produced in violent astrophysical phenomena. Figure 1.5 shows predicted neutrino spectra from various sources.

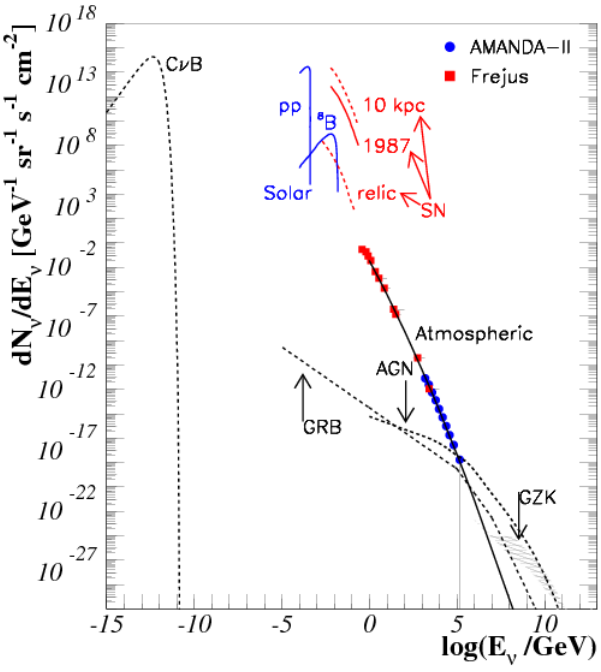

Figure 1.5: Predicted neutrino spectra from a wide range of sources. Confirmed sources (solid lines) are the Sun, SN1987A and atmospheric neutrinos, which are produced in the interaction of high energy cosmic rays with the upper layers of our atmosphere. Image taken from [12]

A watershed moment in neutrino astronomy was reached in 2013 when the IceCube Collaboration reported the observation of high energy neutrino events of extraterrestrial origin (see Section 1.2.4). These events, inconsistent with what is expected from atmospheric muon and neutrino background, constitute the first high energy neutrino flux ever observed and have thus opened new perspectives for high energy neutrino astronomy.

1.2.2 Cosmic rays

First discovered during balloon ascents in 1912 by V. Hess, cosmic rays still remain the subject of several questions.

Almost 90 % of cosmic rays entering the Earth's atmosphere are protons, nearly 10 % are helium nuclei, and slightly under 1 % are composed of heavier elements. The cosmic ray spectrum (Figure 1.6) covers an energy range of more than 12 orders of magnitude, and can be described by a sequence of power laws. A first break, called the *knee*, appears between 10^{15} and 10^{16} eV. It is believed that cosmic rays up to these energies are of galactic origin, probably accelerated in supernova remnants (SNRs) [13]. A second break between 10^{18} and 10^{19} eV, called the *ankle*, might indicate the transition between a galactic and an extra-galactic component [14]. Above these energies, protons cannot be confined in the Galaxy because of a Larmor radius larger than the size of the Galaxy. At energies above 4×10^{19} eV, a suppression of the flux with respect to a power law extrapolation is found [15, 16] (the Greissen-Zatsepin-Kuzmin (GZK) cutoff). It could be explained by the dominant photo-pion production of protons with the CMB, but could also be related to the maximum energy that can be reached at the sources [17].

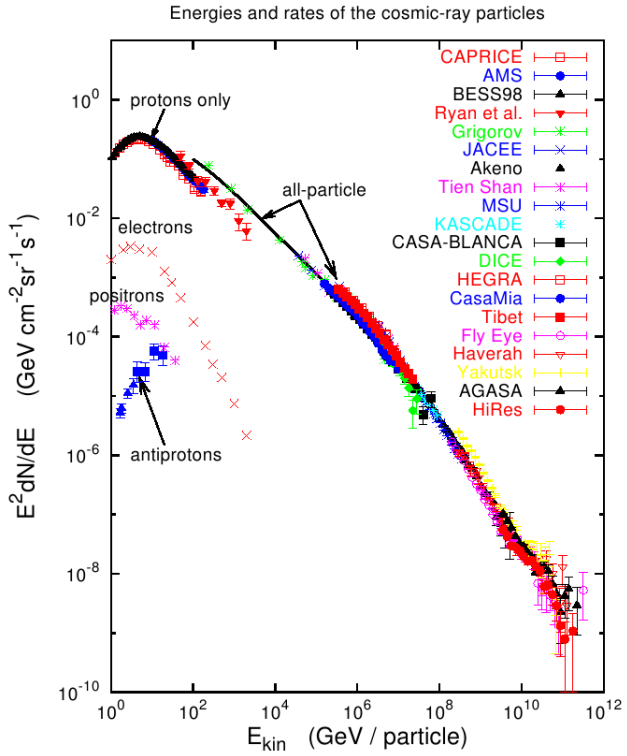

Figure 1.6: Cosmic ray spectrum from different experiment measurements. Image taken from [18].

Despite extensive measurement campaigns, the sources and mechanisms responsible for the acceleration of the highest energy cosmic rays are still unknown. Acceleration of protons to very high energies is expected to take place in astrophysical shocks where charged cosmic rays interact with ambient photons or baryons and produce high energy neutrinos (see [19, 20, 12, 21] for reviews).

In 1949, Fermi proposed a mechanism for the acceleration of cosmic rays relying on a stochastic process where each cosmic ray particle acquires its high

energy in many collisions with moving plasma clouds (Figure 1.7 (left)). The clouds carry turbulent magnetic fields and act as magnetic mirrors transferring on average a positive amount of energy to the scattering particles with $\langle \Delta E \rangle / E \propto \beta^2$, where β indicates the cloud velocity. This process, named second order Fermi acceleration, was updated in 1978 by introducing shock waves. This more efficient process, the first order Fermi acceleration, considers a plane shock front where the particles do not come into a moving gas magnetic cloud but go back and forth across the shock wave front (Figure 1.7 (right)). The particles are thus accelerated with an average gain of $\langle \Delta E \rangle / E \propto \beta$.

This mechanism can operate every time a shock wave in an astrophysical fluid is present. Hence, such an acceleration may occur for example in jets of GRBs or in spherical blast waves of SN ejecta.

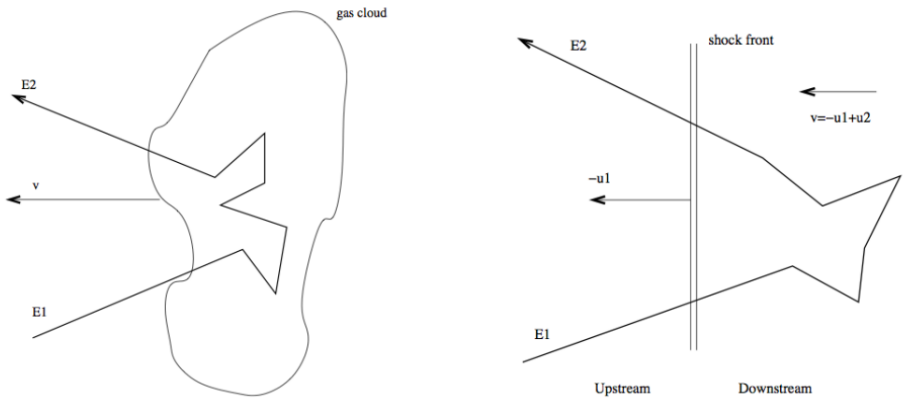

Figure 1.7: Left: second order Fermi acceleration, where a particle with energy E1 is accelerated by collisions in a plasma cloud up to an energy E2. Right: first order Fermi acceleration, where a particle with energy E1 goes back and forth across a shock wave front and exits with an energy E2.

1.2.3 Astrophysical neutrino production

The production of high energy neutrinos (> GeV) in the Universe is closely related to the acceleration of cosmic rays and the production of gamma-rays. High energy neutrinos are thought to be created in the interaction of cosmic rays with matter or radiation surrounding astrophysical sources. The density of matter near the sources must be sufficient to cause many of the cosmic rays to interact instead of escaping. The dominant channel for proton-proton (pp) interactions is:

$$p + p \longrightarrow \begin{cases} p + p + \pi^0 \\ p + n + \pi^+ \end{cases} \tag{1.1}$$

For proton-photon (pγ) interactions, the relevant channel is:

$$p + \gamma \xrightarrow{\Delta^+} \begin{cases} p + \pi^0 \\ n + \pi^+ \end{cases} \tag{1.2}$$

The subsequent decays of neutral pions (branching ratio of 2/3) produce gamma-rays, while the charged pions (branching ratio of 1/3) decay to neutrinos, following:

$$\begin{aligned} \pi^0 &\longrightarrow \gamma + \gamma \\ \pi^+ &\longrightarrow \mu^+ + \nu_\mu \\ \mu^+ &\longrightarrow e^+ + \nu_e + \overline{\nu}_\mu \\ n &\longrightarrow p + e^- + \overline{\nu}_e \end{aligned} \tag{1.3}$$

Kaons may also be produced in the same interactions and decay similarly. Counting neutrino (and antineutrino) flavors produced at the source, the ratio for the 3 flavors is $(\nu_e : \nu_\mu : \nu_\tau) = (1 : 2 : 0)$. After oscillation mechanisms, the neutrino flavor ratio at Earth [22] is $(\nu_e : \nu_\mu : \nu_\tau) = (1 : 1 : 1)$.

The above equations show the important connection between high energy cosmic rays and neutrino astronomy. Detection of neutrinos would be an unambiguous signature for hadronic cosmic rays, since there is no equivalent leptonic process.

1.2.4 First evidence for high energy astrophysical neutrinos

The recent IceCube evidence for extraterrestrial high energy neutrinos [23] opened new windows in the field of astroparticle physics. Using 2 years of data, they reported the observation of 28 high energy cosmic neutrino events, including two events with energies above 1 PeV. To disentangle this excess from the atmospheric neutrino component, which represents an irreducible background for neutrino telescopes (Section 2.1.4), they focused on events starting in the detector (see Section 2.2 for a description of the IceCube detector). An atmospheric neutrino would inevitably be produced in coincidence with atmospheric muons from the same air shower. Hence, by requiring a neutrino interaction within the detector (the outer layers provide a veto), a downward going neutrino that can be identified without a coincident through-going (atmospheric) muon track would be rather strong evidence for being of extraterrestrial origin. With this self-vetoing technique [24], the IceCube Collaboration has shown that the majority of the 28 High Energy Starting Events (HESE) identified are consistent with an extraterrestrial origin. This analysis was extended from 2 to 3 years of data, resulting in 37 HESE in total (Figure 1.8) and allowing the atmospheric-only hypothesis to be rejected with 5.7 σ [25]. The HESE flux observed by IceCube is compatible with flavor ratios $\nu_e : \nu_\mu : \nu_\tau = 1 : 1 : 1$, as expected from charged meson decays in cosmic ray accelerators and neutrino oscillation during propagation to Earth. The energy spectrum of these events is shown in Figure 1.9 (left).

The observation of this high energy cosmic neutrino flux has fixed the scale of neutrino fluxes in the Universe and has inspired a large number of hypotheses on their origin. Because the observed neutrino energies are reaching only up to a few PeV, a connection to the extragalactic cosmic rays observed with 3 or 4 orders of magnitude higher energies is not obvious. However, a North/South

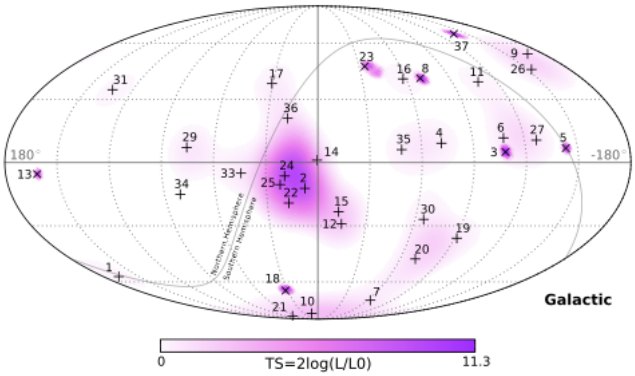

Figure 1.8: Arrival directions of the 37 events detected by IceCube in galactic coordinates. Shower-like events are marked with +, while those containing muon tracks are marked with ×. The gray line indicates the equatorial plane. Colors show the test statistic (TS) for the point source clustering test at each location. No significant clustering was observed.

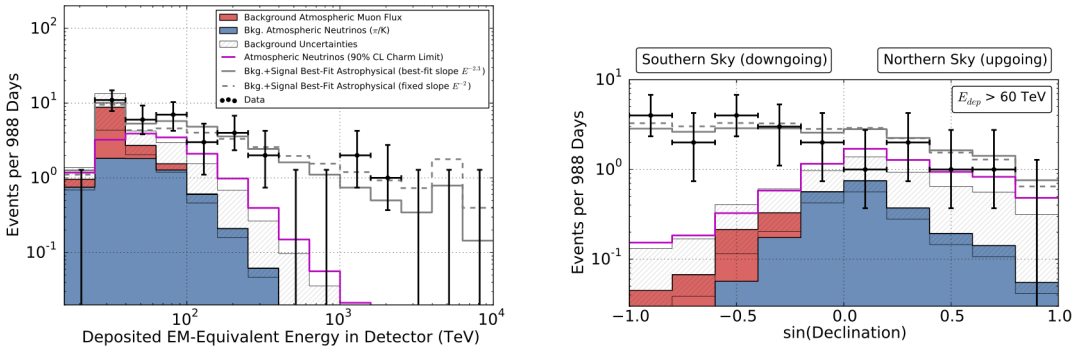

Figure 1.9: Distribution of the deposited energies (left) and declination angles (right) of the observed events compared to model predictions. Energies plotted are reconstructed in-detector visible energies, which are lower limits on the neutrino energy. Note that the deposited energy spectra are always harder than the incident neutrinos spectrum due to the neutrino cross-section increasing with energy. The expected rates of atmospheric neutrinos and muons are shown in blue and red, respectively. Combined statistical and systematic uncertainties on the sum of backgrounds are indicated with a hatched area. The gray line shows the best-fit E^{-2} astrophysical spectrum with a per-flavor normalization (1:1:1) of $E^{-2}\Phi_\nu(E) = 1.5 \times 10^{-8}(E/100\ \text{TeV})^{-0.3}$ GeV cm^{-2} s^{-1} sr^{-1}. The choice to use 100 TeV as the pivot point in the parameterization minimizes the correlation between the spectra index and the normalization. Images taken from [25].

asymmetry in the data set, as shown in Figure 1.9 (right), suggests the presence of a possible galactic component [26]. The majority of HESE are down-going and as the IceCube detector is at the South Pole, this corresponds to a larger flux from the Southern sky, where most of the galactic plane is present. The Northern sky, inducing up-going events in IceCube, contains only a small fraction of the Galaxy, therefore, the 3.6 estimated HESE from cosmic neutrinos arising from

the Northern sky are assumed to be of extragalactic origin. Considering a E^{-2} spectrum, a symmetric contribution from the North/South extragalatic sources and taking into account the different effective areas of the IceCube detector for events coming from the North and South hemispheres, 6.2 events are expected from the Southern sky. However, 13.7 signal events have been found in the data. This excess of 7.5 events coming from the South represents $\sim$ 40 % of the total signal.

The ANTARES neutrino telescope [27], located in the Mediterranean Sea, can observe a signal originating from the Southern sky through the ν_μ charged current interaction with a much higher angular precision ($\sim 0.4^\circ$ compared to $\sim 1^\circ$ for ν_μ and $\sim 10^\circ - 15^\circ$ for ν_e and ν_τ in IceCube) and with an effective area[2] comparable to that of the IceCube HESE sample. Despite the fact that the ANTARES instrumented volume is much smaller than 1 km^3, Figure 1.10 shows that the ANTARES ν_μ effective area is larger than the IceCube ν_e, ν_μ and ν_τ effective areas below $\sim$ 60 TeV. At higher energies ($\sim$ 1 PeV), the ANTARES ν_μ effective area is a factor of 0.45 that the IceCube ν_μ effective area, while the total IceCube effective area, considering the 3 flavors, is a factor of 7.3 larger than that of the ANTARES ν_μ flavor. However, the ANTARES and IceCube effective areas depend on the selection efficiency used for the particular analyses. The IceCube selection criteria necessary for a 4π sr selection of cosmic neutrinos (up-going and down-going) reduce the effective area due to the requested ν interaction inside a restricted instrumented volume. Furthermore, a large deposited energy in this volume is required. These criteria are able to largely suppress the background produced by atmospheric muons and atmospheric neutrinos but they induce a suppression of ν_μ candidates, inhibiting the detection of neutrino-induced muons with vertices outside the instrumented volume. The criteria used in the ANTARES analysis limit the selection to up-going ν_μ and no volume restriction for the neutrino interaction is imposed. Atmospheric neutrinos and a small fraction of wrongly reconstructed atmospheric muons ($\leq$ 10 % of atmospheric neutrinos) constitute the background to the cosmic signal.

The ANTARES detector has an equivalent capability than IceCube to extract a signal if the cosmic source is located in the Southern sky, and its sensitivity is sufficient to test different models that could explain a fraction of the HESE sample in terms of a galactic component. However, the search for high energy astrophysical neutrinos from point-like sources [28], diffuse flux [29] or Fermi bubbles [30] within the ANTARES Collaboration have so far yielded null result, but limits on the neutrino production have been placed.

The search for transient sources is a promising way for detecting high energy astrophysical neutrinos. By searching for coincident detection of neutrinos and electromagnetic counterparts during the transient event, the sensitivity is enhanced since the neutrino background is significantly reduced. In addition, through combining neutrino information with multi-wavelength observations, it would be possible to identify the source of high energy neutrinos.

[2]The neutrino effective area at a given energy is defined as the ratio between the neutrino event rate in the detector (s^{-1}) and the neutrino flux (cm^{-2} s^{-1}) at that energy.

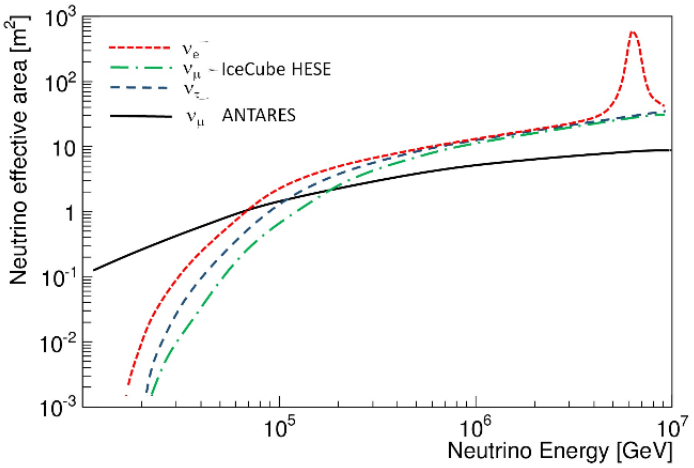

Figure 1.10: Black solid line: ANTARES ν_μ effective area obtained in the search for point-like sources [28]. Colored dashed lines: IceCube ν_e, ν_μ and ν_τ effective areas from the analysis providing the first evidence for a high energy neutrino flux of extraterrestrial origin [23]. Below ∼60 TeV, the ANTARES ν_μ effective area is larger than the IceCube ν_e, ν_μ and ν_τ effective areas.

1.3 Transient neutrino sources

The production of high energy neutrinos has been proposed to occur in several kinds of astrophysical sources, such as GRBs, CCSNe, AGN or microquasars, in which the acceleration of hadrons may occur. Many of these astrophysical accelerators, thought to be able to produce high energy cosmic rays, show transient behavior. Of particular interest to this thesis are GRBs and CCSNe. In the following sections, the physics of GRBs and CCSNe is outlined and the neutrino flux expected from these sources is presented.

1.3.1 Gamma-ray bursts

Bursts of high energy neutrinos are assumed to be produced in the most powerful processes known in the Universe. Promising candidate sources are GRBs, which are the most luminous known astrophysical objects. As their name suggests, GRBs are detected as brief, intense and totally unpredictable flash of high energy γ-rays, releasing an energy in the electromagnetic domain of typically 3×10^{51} erg in a few seconds. The high energy prompt emission is usually followed by a rapidly fading afterglow radiation in lower energy bands, which can sometimes be observed up to several weeks later.

Observations

GRBs were first detected in the 1960s by military satellites launched by the United States to monitor the compliance with the nuclear test ban treaty. These satellites were capable of observing the brief but intense γ-ray signal from a

nuclear detonation. On July 1967, the U.S. Vela satellites indeed detected a γ-ray signal but it was not compatible with a nuclear weapon explosion. This became public information only several years later, with the publication of the results from the Vela satellites [31], quickly confirmed by data from the Soviet Kosmos satellites [32].

In 1991, the Burst and Transient Source Experiment (BATSE) on board the *Compton Gamma Ray Observatory* (CGRO) was launched, with the main objective to detect and further study GRBs. During its 9 years of operation, more than 2700 GRBs were identified, as shown in Figure 1.11. The main result of BATSE was that it showed that GRBs were essentially isotropically distributed in the sky, suggesting a cosmological distribution [33]. Thanks to the BATSE data, it has also been possible to measure the typical fluence of GRBs, leading to the classification of GRBs into two distinct types: short GRBs and long GRBs. The emission spectra of the GRBs show a peculiar non-thermal behavior, peaking at around a few hundred keV and extending up to several GeV. The spectrum is usually well described by a smoothly joining broken power law, the so-called *Band function* [34, 35].

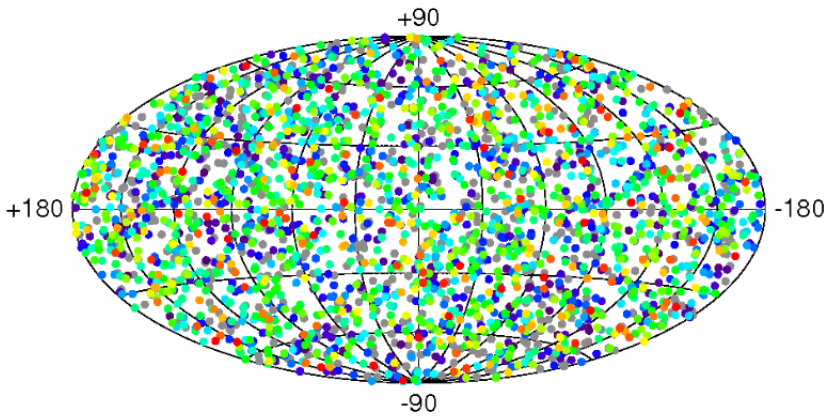

Figure 1.11: Distribution of the 2704 GRBs recorded by BATSE during the nine-year CGRO mission. The uniformity of the distribution strongly points toward an extragalactic origin of the bursts [33]. (Figure from http://www.batse.msfc.nasa.gov/batse/grb/skymap).

A decisive watershed was reached in 1997, when the Italian-Dutch satellite *BeppoSAX* succeeded to localize GRBs quickly with uncertainties of only few arcminutes. This allowed a newly discovered feature of GRBs to be detected: the X-ray afterglow. The arcminute accuracy positions made possible the optical detection and the follow-up of GRB afterglows at longer wavelengths [36, 37]. This paved the way for the measurement of redshift distances, the identification of host galaxies and the confirmation of the cosmological origin [38].

In the meantime, the Gamma-ray Coordinate Network (GCN) system has been developed [39]. It allows the distribution of information about the location of a GRB to other facilities. Hence, follow-up observations can be made by ground-based and space-based optical, radio and X-ray observatories. With this system,

the observation of GRB afterglows in different wavelengths became possible and allowed a better characterization of GRBs.

The multi-wavelength *Swift* satellite, launched in 2004, succeeded *BeppoSAX* and improved the measurement capabilities for GRBs, especially the short ones. With three instruments, the Burst Alert Detector (BAT), the X-ray telescope (XRT) and the UV-optical telescope (UVOT), *Swift* provides excellent coverage of the transition between the prompt γ-ray phase to the lower-frequency afterglow emission phase. It enabled a record-breaking number of GRBs to be well localized, including many short GRBs.

The latest milestone was the launch of the *Fermi* satellite in 2008, which allows the investigation of the very high energy regime thanks to the GBM and the LAT instruments. Several bursts have been detected by the *Fermi*-LAT at energies above 1 GeV, improving considerably our knowledge of the high energy γ-ray emission.

Classification

Observations from BATSE led to the classification of GRBs into two families according to the distribution of their duration (Figure 1.12). The duration of a GRB is usually given as the time T_{90} in which 90 % of the photon flux is detected. In this sense, $T_{90} \lesssim 2$ s for short GRBs and $T_{90} \gtrsim 2$ s for long GRBs.

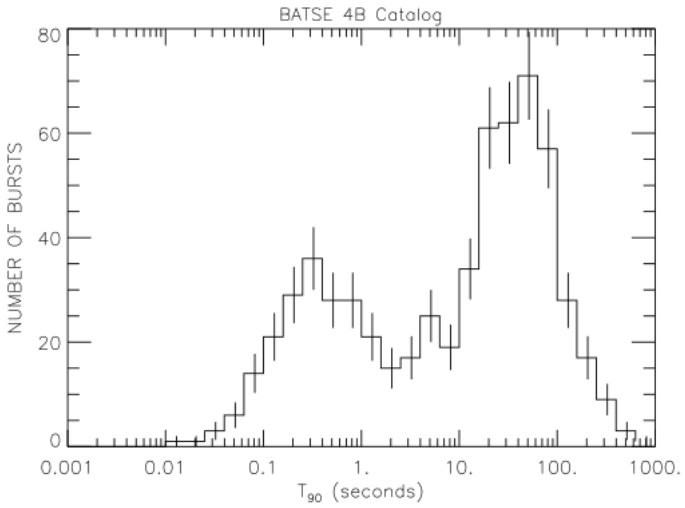

Figure 1.12: Duration distribution of BATSE bursts. Long GRBs last more than 2 seconds while short GRBs last less than 2 seconds [40].

Each family of GRBs is likely associated with a different progenitor. Long GRBs are the most observed and, therefore, the best understood. Observations show that long GRB host galaxies are active star forming galaxies [41] and in several cases it has been proved that long GRBs occurred in correlation with CCSNe (see Section 1.3.2). This category of GRBs is thus thought to be produced with the explosive death of massive star. In the *collapsar model* [42], a very massive star ($M_\star \gtrsim 25 - 30\ M_\odot$) in the latest stages of its life has burnt all

its central light elements and is therefore not longer able to generate energy by nuclear fusion. Under the pressure of the gravitational force, the star subsequently collapses in a supernova (SN) and forms a black hole. If the core is fast-rotating (i.e., with high angular momentum in the range $(3 - 20) \times 10^{16}$ cm^2 s^{-1}), an accretion disk is created by the matter swirling around the central engine. The black hole and disk accretion can serve as an energy source for powering a long GRB. The accretion of material into the center of the black hole produces two relativistic jets along the rotational axis and is believed to lead to the GRB event.

For short GRBs, the current hypothesis attributes their origin to the merging of two compact objects, such as neutron star binaries or neutron star-black hole binaries. Observations, mainly by *Swift*, show that short GRBs are distributed uniformly among all types of galaxies including those that contain a considerable quantity of old stars. As no evidence of significant star formation has been found in those galaxies, such an old population is compatible with the presence of neutron star binary systems. Furthermore, the model of a merger, where no explosion is required, is supported by the lack of connection with a SN observation. In such binary systems, energy is lost due to gravitational radiation, as predicted by the General Relativity, and the two objects will fall into a spiral until tidal forces will disintegrate the neutron star, releasing an enormous quantity of energy before merging into a single black hole. This process is thought to be extremely fast and to last no more than a few seconds, in agreement with the observations of short GRBs.

The relativistic fireball shock model

The *fireball model* [43, 44] is the most widely used theoretical framework to describe the physics of the GRBs. This model does not provide any constraint on the central engine, as the acceleration mechanism that gives rise to the γ-rays themselves is most likely independent of the progenitor of the event, but yields a phenomenological description of the actual burst observations.

In this model, a fireball consisting of baryons (primarily protons and neutrons), electron and positron pairs, and photons is produced in cataclysmic events such as mergers of binary neutron stars [45] (short GRBs) or collapses of massive stars [46] (long GRBs). The inner engine resulting from the explosion (a black hole or a fast spinning magnetar) powers highly relativistic outflows of energy and material collimated in two opposite jets along the rotational axis. Due to collisions and instabilities within the ejecta, internal shocks between faster and slower shells emerge and accelerate charged particles up to ultra-relativistic speeds via Fermi mechanisms. The internal shocks, occurring at a radius $R \sim 10^{11} - 10^{12}$ m, are proposed to be responsible for the prompt γ-ray emission.

The ejected particles are slowed down by the external shocks with the circumburst matter of the interstellar medium, occurring at $R \sim 10^{12} - 10^{14}$ m. A forward shock is responsible for the long-lasting afterglow emission in the X-ray, optical and radio wavelengths, while a short-lived reverse shock propagates into the ejecta and produces optical and UV emission.

The fireball scenario of internal and external shocks is illustrated in Figure 1.13.

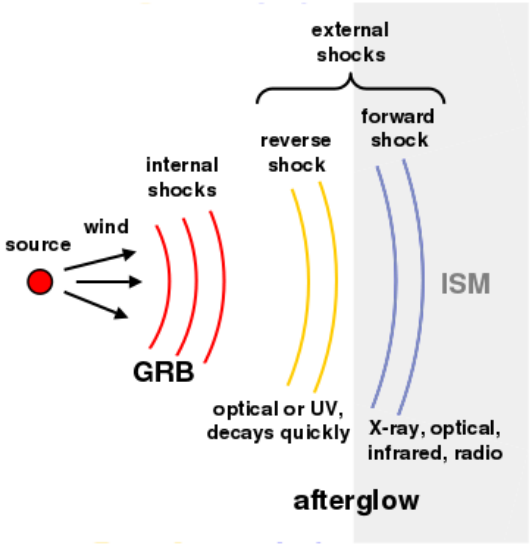

Figure 1.13: The relativistic fireball shock model: internal shocks between faster and slower shells produce the prompt γ-ray emission, while external shocks with the surrounding matter are responsible for the long duration afterglow emission in many wavelengths and a short lived reverse shock creates optical and UV emission. Image taken from [47].

Neutrino flux from GRBs

In the standard framework of the fireball internal shock model, the neutrino flux is thought to be produced in coincidence with the electromagnetic GRB by hadronic processes [48, 49]. Electrons and protons are shock accelerated in internal shocks within the jets of a GRB and photons are produced by synchrotron radiation of the accelerated electrons. Fermi-accelerated protons in the relativistic ejecta of the burst interact with these photons and produce neutral and charged pions via the Δ-resonance. The subsequent decay of the charged pions and muons gives rise to high energy neutrinos peaking at the TeV regime and accompanying the electromagnetic emission (Equations 1.2 and 1.3).

Assuming that the photo-meson production is dominated by the contribution of the Δ-resonance, the prompt neutrino spectrum can be derived from the observed photon spectrum (see [35], appendix A):

$$F_\nu(E_\nu) = \frac{dN(E_\nu)}{dE_\nu} = f_\nu \times \begin{cases} \left(\frac{\epsilon_1}{\mathrm{GeV}}\right)^{\alpha_\nu} \left(\frac{E_\nu}{\mathrm{GeV}}\right)^{-\alpha_\nu} & \text{for } E_\nu < \epsilon_1 \\ \left(\frac{\epsilon_1}{\mathrm{GeV}}\right)^{\beta_\nu} \left(\frac{E_\nu}{\mathrm{GeV}}\right)^{-\beta_\nu} & \text{for } \epsilon_1 \leq E_\nu < \epsilon_2 \\ \left(\frac{\epsilon_1}{\mathrm{GeV}}\right)^{\beta_\nu} \left(\frac{\epsilon_2}{\mathrm{GeV}}\right)^{\gamma_\nu - \beta_\nu} \left(\frac{E_\nu}{\mathrm{GeV}}\right)^{-\gamma_\nu} & \text{for } E_\nu \geq \epsilon_2 \end{cases} \tag{1.4}$$

with photon indices

$$\alpha_\nu = 3 - \beta_\gamma, \;\; \beta_\nu = 3 - \alpha_\gamma, \;\; \gamma_\nu = \beta_\nu + 2 \tag{1.5}$$

and break energies

$$\epsilon_1 = 5 \times 10^5 \text{ GeV} \frac{1}{(1+z)^2} \left(\frac{\Gamma}{10^{2.5}} \right)^2 \left(\frac{\text{MeV}}{\epsilon_\gamma} \right) \tag{1.6}$$

$$\epsilon_2 = 10^7 \text{ GeV} \frac{1}{1+z} \sqrt{\frac{\epsilon_e}{\epsilon_B}} \left(\frac{\Gamma}{10^{2.5}} \right)^4 \left(\frac{t_{\text{var}}}{0.01\text{s}} \right) \sqrt{\frac{10^{52} \text{ erg s}^{-1}}{L_\gamma^{\text{iso}}}} \tag{1.7}$$

where z is the redshift of the GRB, L_γ^{iso} is its isotropic luminosity, t_{var} is the variability of the γ-ray light curve and, ϵ_e and ϵ_B are the fractions of jet energy in electrons and magnetic field, respectively. The two last parameters have never been measured for any GRB, therefore default values are considered: $\epsilon_e = 0.1$ and $\epsilon_B = 0.1$. A default value is also assumed for the variability: $t_{\text{var}} = 0.01$ s, although it has already been measured for some GRBs (e.g., [50]). As the photon spectrum, described by the Band function, has a characteristic break at ϵ_γ, the neutrino spectrum shows a first break at ϵ_1 connected to the photon spectrum break, which is thus due to the effective synchrotron cooling of the electrons in the magnetic field. The second break at ϵ_2 is due to the same mechanism which leads to energy losses of the secondary muons.

The normalization of the neutrino spectrum, contained in f_ν, depends on the photon fluence $\mathcal{F}_\gamma$, as well as on the total fraction of the energy transferred from protons to pions. Considering that on average, $\langle x_{p\to\pi} \rangle = 20$ % of the proton energy is transferred to the pion in each interaction [48, 49], a total energy of $1 - (1 - \langle x_{p\to\pi} \rangle)^{\Delta R/\lambda_{p\gamma}}$ is converted, where ΔR is the size of the shock region and $\lambda_{p\gamma}$ is the mean free path of a proton for $p\gamma$ interactions. Their ratio is given by:

$$\frac{\Delta R}{\lambda_{p\gamma}} = \left(\frac{L_\gamma^{\text{iso}}}{10^{52} \text{ erg s}^{-1}} \right) \left(\frac{0.01\text{s}}{t_{\text{var}}} \right) \left(\frac{10^{2.5}}{\Gamma} \right)^4 \left(\frac{\text{MeV}}{\epsilon_\gamma} \right) \tag{1.8}$$

yielding to a neutrino spectrum normalization of:

$$\int_0^\infty dE_\nu E_\nu F_\nu(E_\nu) = \frac{1}{8} \frac{1}{f_e} \left(1 - (1 - \langle x_{p\to\pi} \rangle)^{\Delta R/\lambda_{p\gamma}} \right) \times \mathcal{F}_\gamma \tag{1.9}$$

where f_e is the ratio between energy in electrons and protons.

A typical GRB neutrino spectrum is illustrated in Figure 1.14 with values taken from [48]: $\epsilon_1 \sim 10^5$ GeV, $\epsilon_2 \sim 10^7$ GeV, $\mathcal{F}_\gamma = 10^{-5}$ erg cm^{-2}, and $f_\nu \sim 7 \times 10^{-4}$ GeV cm^{-2}.

1.3.2 Core-collapse supernovae

SNe are some of the most luminous events in the Universe for the few weeks that they are at peak brightness. Among them, CCSNe, which are believed to have a similar origin as long GRBs, are other transient neutrino source candidates.

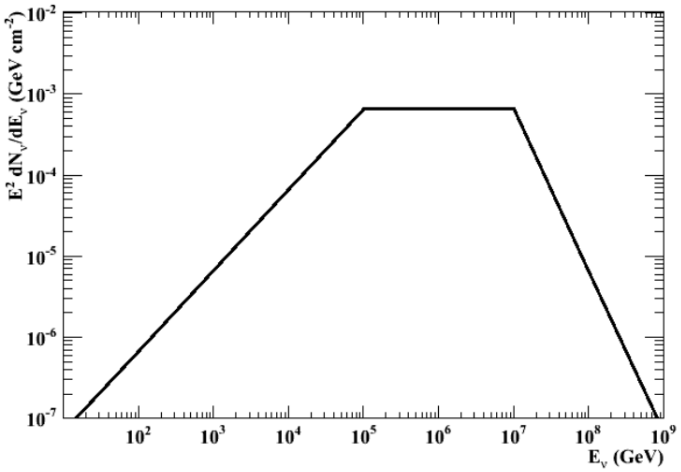

Figure 1.14: Neutrino spectrum shape for an individual typical GRB with values from [48].

Classification and mechanisms

SNe are classified in two main categories depending on the composition of their spectra. SNe of type I do not show a hydrogen line in their spectra while for type II, the hydrogen line is present (Figure 1.15). However, the most important physical characteristic that distinguishes SNe of type Ia from SNe of type Ib, Ic and II is the mechanism that generates the SN. Type Ia SNe are generated by thermonuclear explosions exclusively in binary systems (white dwarf-companion star), while SNe of type Ib, Ic and II are produced by the collapse of the core of massive stars ($M_\star \gtrsim 8\ M_\odot$). In this thesis, we will focus on these CCSNe, as they are thought to be linked to GRBs and are expected to produce high energy neutrinos.

CCSNe are the explosive death of massive stars occurring when the iron core collapses into a neutron star or a black hole [52]. All stars, regardless of mass, progress through the first stages of their lives in a similar way, by converting hydrogen to helium. Once the fuel of hydrogen is consumed, fusion reactions slow down. Hence, the gravitational pressure exceeds the radiation pressure and the core starts to contract. This raises the temperature of the core, generally to the point where the fusion of helium to carbon can take place. For massive stars ($M_\star \gtrsim 8 - 10 M_\odot$), fusion processes do not stop here but go on until iron is produced in the core, as shown in Figure 1.16. The formation of iron effectively concludes fusion processes and, with no energy to support it against gravity, the star begins to collapse. Beyond the density of electron degeneracy, electrons and

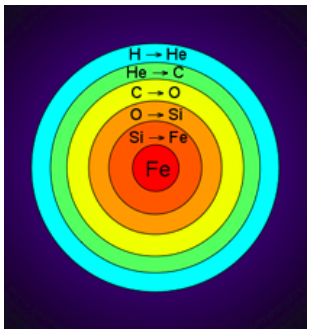

Figure 1.16: Fusion processes inside a massive star. Heavier elements are produced in the core-region of the star while lighter elements are produced in shells around the core.

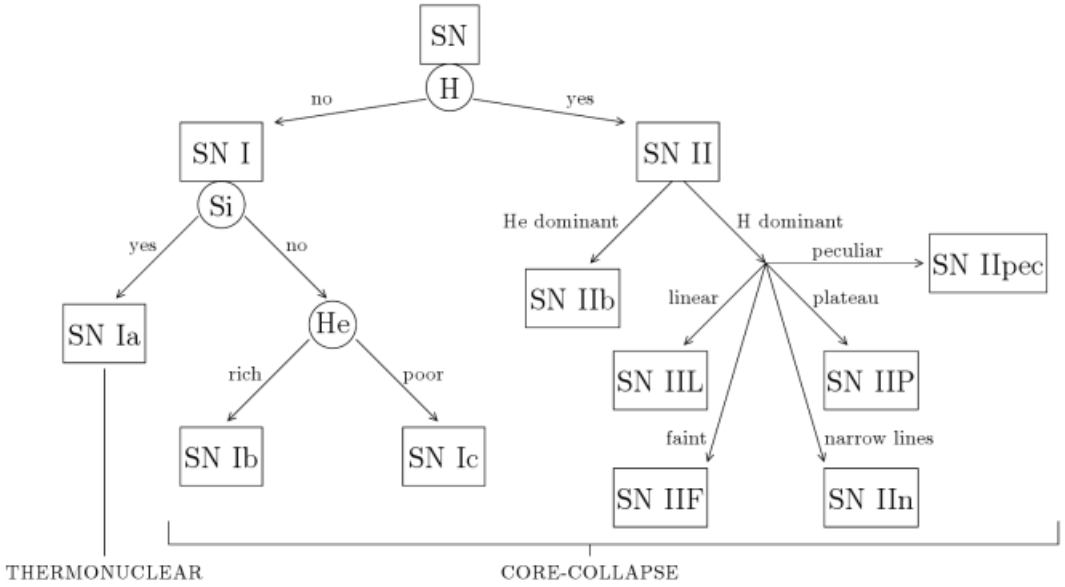

Figure 1.15: Classification scheme of SNe [51].

protons are forced to combine to form neutrons, releasing vast quantities of neutrinos ($\sim 10^{58}$) carrying substantial amounts of energy ($\lesssim 10^{52}$ erg) [53]. The contraction is finally halted once the density of the core reaches the point of nuclear density ($\rho \approx 10^{12}$ g/cm^3), where the strong nuclear force becomes repulsive. Therefore, the in-falling material bounces while the outer layers continue to fall inwards. This gives rise to a shock wave which, in combination with the high neutrino luminosity, triggers the SN explosion a few hours later, when it reaches the surface of the star and expels stellar material in the interstellar medium. Electromagnetic radiation is initially emitted at this shock breakout, as short X-ray or UV flash, which happens long before the SN light curve reaches its maximum. Hence, they have only been detected for a few SNe (for example in the case of SN2006aj [54]). Then, as the SN expands, the surface area of the photosphere increases and the density lowers, so the radiation can diffuse out more freely resulting in a rise of the light curve in optical wavelengths [55]. Finally, depending on whether the progenitor star had a mass below or above $\sim 25 - 30$ M$_\odot$, the nascent remnant will evolve into a neutron star or collapse to a black hole.

In addition to the neutrinos produced in the stellar envelope with energies of 10-30 MeV, as those detected for SN1987A, CCSNe are thought to generate jets with high energy neutrinos of a hundred of GeV to TeV, which are aimed to be detected in this work.

Connection between SNe and GRBs

In the late 1990s, observations confirmed that CCSNe and long duration GRBs could have a similar origin, the death of massive stars. For decades, it was thought that these two phenomena had no relation to one another [56, 43], but the discovery of a GRB on April 25, 1998 (GRB980425) coincident both

in time and place with a SN (SN1998bw) [57] brought the SN-GRB connection to the forefront. Since then, several SNe have been associated with long duration GRBs as, for example, GRB021211/SN2002lt [58], GRB030329/SN2003dh [59] and GRB031203/SN2003lw [60].

So far, in each case of association, it has been found that the SNe were of type Ib/c, which represent ~ 25 % of the local CCSN rate [61]. However, while all long duration GRBs may be accompanied by CCSNe, not all CCSNe make GRBs. Even correcting for the effects of jet opening angle (i.e., GRBs can only be observed if their jet is pointing at the Earth), observations hint that the frequency of highly relativistic jets in CCSNe is at ~ 1 in 1000, which is roughly the ratio of GRB to SN rates [62, 63]. This suggests that GRBs require special conditions to be generated. Rotation is emerging as the distinguishing ingredient. Indeed, GRBs may only come from the most rapidly rotating and most massive stars, while for ordinary CCSNe the rotation could play a smaller role or no role at all.

On the other hand, the fact that most long GRBs do not have a detected associated SN could be explained by observational biases such as high burst redshifts, obscuration by dust, contamination of the SN light by the host galaxy or poor localization of the bursts from their afterglows which hampers the follow-up with large aperture telescopes to discover emerging SNe [41].

The SN-GRB connection gives rise to the idea that the jet signature may be common to CCSNe, which are much more frequent than GRBs. Compared to highly relativistic jets in GRBs, a significantly larger fraction of CCSNe ($\lesssim 1 - 10$ % of type Ib/c rate [53]) is expected to have mildly relativistic jets associated with them. Although GRBs and CCSNe were found to release a comparable amount of kinetic energy, the jets are expected to be more baryon-rich in CCSNe (a "dirty fireball"), and hence more mildly relativistic. In this scenario, the soft relativistic jets would be choked inside the envelope of the collapsing star, as shown in Figure 1.17. This would lead to the absorption of the electromagnetic radiation emitted by the jets and an efficient production of high energy neutrinos, which would be the only prompt signature of these hidden sources. The detection of high energy neutrinos correlated with an optical SN would strongly and directly show the existence of such mildly relativistic jets, as well as potentially being the first detection of a source of high energy neutrinos.

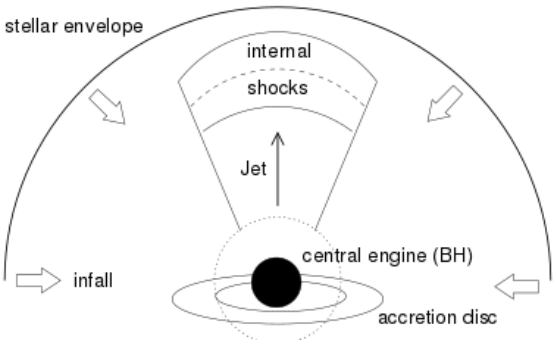

Figure 1.17: Illustration of a mildly relativistic jet buried inside the envelope of a collapsing star [53].

Neutrino flux from CCSNe

Motivated by the GRB-SN connection, Razzaque, Mészáros and Waxman (RMW) developed a model to calculate the high energy (TeV) neutrino emission coming from CCSNe [53]. Because of the low Lorentz factor and high baryon density expected in CCSNe, collisions among protons (pp) accelerated by Fermi mechanisms occur efficiently, producing pions and kaons (Equation 1.1). The subsequent decays of pions and kaons produce neutrinos following Equation 1.3 and:

$$K^+ \longrightarrow \begin{cases} \nu_\mu + \mu^+ \\ \pi^+ + \pi^0 \end{cases} \tag{1.10}$$

However, the initial formulation of the RMW model only took into account the neutrino production through pion decays. Thus, this model has been extended by Ando & Beacom (AB05) [64] by considering the kaon contribution. Compared to pions, kaons have larger mass and shorter lifetime, undergoing less energy loss before decaying into neutrinos. Therefore, the neutrino spectrum from kaons is harder and more easily detectable than that from pions.

In the AB05 model, the neutrino spectrum is calculated with a typical jet kinetic energy $E_{\rm jet,0} = 3 \times 10^{51}$ erg, a mildly relativistic value for the bulk Lorentz factor $\Gamma_0 = 3$ and an assumed opening angle of $\theta_0 \sim \Gamma_0^{-1} = 0.3$. Here, in order to test a broader parameter space, the neutrino flux is calculated as a function of the Lorentz factor Γ, and the jet energy $E_{\rm jet}$. In the following, the neutrino spectrum is derived for one CCSN at distance $d = 10$ Mpc with a jet pointing at the Earth. Since high energy photons are absorbed in the SN jet, the neutrino spectrum cannot be derived from the photon spectrum as in the case of GRBs. Instead, the neutrino spectrum is calculated from the expected proton spectrum.

In the AB05 model, pions and kaons are assumed to carry 20 % of the parent proton energy, so that they follow the original spectrum of accelerated protons $\propto E^{-2}$. However, they lose energy by synchrotron radiation and inverse Compton scattering (radiative cooling) and by πp and Kp processes (hadronic cooling). Above a first break energy, the cooling is dominated by hadronic processes which steepen the spectrum by a factor E^{-1}. A total suppression factor of E^{-2} appears above a second break energy when the radiative cooling dominates. The daughter neutrinos produced through pion and kaon decays with branching ratios 100 % and 63 % respectively, carry on average 25 % of the pion energy and 50 % of the kaon energy, and their energy in the observer frame is related to the parent meson energy in the jet rest frame[3] as follows:

$$E_{\nu,\pi(K)} = \Gamma E'_{\pi(K)}/4(2) \tag{1.11}$$

The hadronic cooling break strongly depends on the jet Lorentz factor Γ and the jet energy $E_{\rm jet}$, and is assumed by the AB05 model at 30 GeV for pions and 200 GeV for kaons:

$$E^{(1)}_{\nu,\pi(K)} = \left(\frac{E_{\rm jet}}{E_{\rm jet,0}}\right)^{-1} \left(\frac{\Gamma}{\Gamma_0}\right)^{5} 30(200)\ \text{GeV} \tag{1.12}$$

[3]Variables in the comoving frame, i.e., the jet frame, are denoted with a prime.

The radiative cooling break (100 GeV for pions and 20 000 GeV for kaons assumed by AB05) depends only on Γ:

$$E^{(2)}_{\nu,\pi(K)} = \frac{\Gamma}{\Gamma_0} 100(20\,000)\ \text{GeV} \tag{1.13}$$

Finally, the proton energy reaches its maximum at the photo-pion production threshold of $E'_{\text{p,max}} = 7 \times 10^4$ GeV, where protons interact with the high photon density. Therefore the cutoff in the proton spectrum results in a cutoff in the neutrino spectrum at

$$E^{\text{cutoff}}_{\nu,\pi(K)} = \frac{\Gamma}{\Gamma_0} 10\,500(21\,000)\ \text{GeV} \tag{1.14}$$

The normalization of the neutrino spectrum scales with the jet energy as follows:

$$\begin{aligned} F_{\nu,\pi(K),0} &= \frac{\langle n \rangle B_\nu}{8} \frac{E_{\text{jet}}}{2\pi\theta^2 d^2 \ln(E'_{\text{p,max}}/E'_{\text{p,min}})} \text{GeV}^{-1}\text{cm}^{-2} \\ &= \frac{E_{\text{jet}}}{E_{\text{jet},0}} \left(\frac{\Gamma}{\Gamma_0}\right)^2 45(2)\ \text{GeV}^{-1}\text{cm}^{-2} \end{aligned}$$

where d is the source distance, $\langle n \rangle$ is the meson multiplicity (1 for pions and 0.1 for kaons), B_ν is the branching ratio of the decay into neutrino mode (1 for pions and 0.6 for kaons) and the factor $\ln(E'_{\text{p,max}}/E'_{\text{p,min}})$ normalizes the proton spectrum to the jet energy.

The resulting neutrino spectrum follows a power law with two breaks:

$$E_\nu^2 \frac{dN_{E_\nu}}{dE_\nu} = \sum_{i=\pi,K} F_{\nu,i} \times \begin{cases} 1 & \text{for } E_\nu < E^{(1)}_{\nu,i} \\ E^{(1)}_{\nu,i}/E_\nu & \text{for } E^{(1)}_{\nu,i} < E_\nu < E^{(2)}_{\nu,i} \\ E^{(1)}_{\nu,i} E^{(2)}_{\nu,i}/E_\nu^2 & \text{for } E_\nu > E^{(2)}_{\nu,i} \end{cases} \tag{1.15}$$

Figure 1.18 shows the behavior of the neutrino spectrum from pions, kaons and both pions and kaons, for different Lorentz boost factors and jet energies. In the energy range which ANTARES is sensitive (> 100 GeV), the kaon contribution makes the spectrum harder, increasing the detectability of such neutrinos. In addition, more neutrinos are expected to be detected from jets with high Lorentz boost factor.

If such mildly relativistic jets accompanied SN1987A and were directed towards Earth, many events would have been detected by the Kamiokande-II and IMB detectors. Their small sizes being compensated by the close distance of the SN (51.4 kpc). This suggests that such jets did not exist in SN1987A.

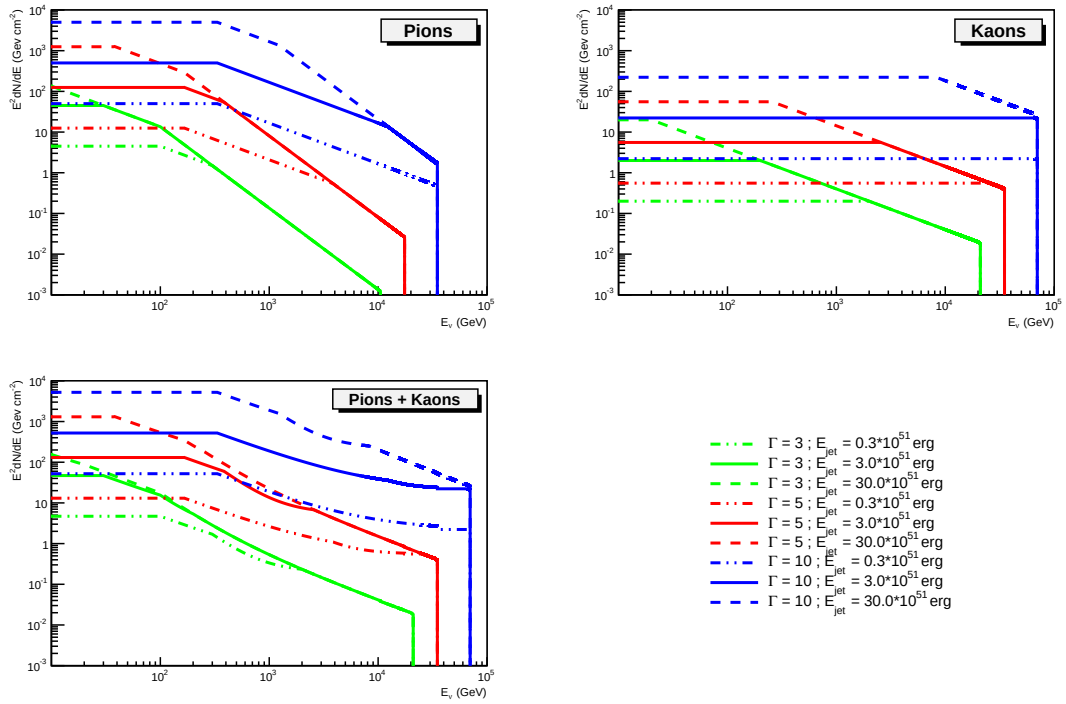

Figure 1.18: SN neutrino spectrum according to the Ando & Beacom model for a nearby source at 10 Mpc for different Lorentz boost factors Γ and jet energies $E_{\rm jet}$, considering pion, kaon and the sum of pion and kaon contributions.

CHAPTER 2

Neutrino telescopes and ANTARES

The weak interaction of neutrinos with matter represents an asset for astronomy but also makes the detection challenging. Due to the very low flux of high energy neutrinos from astrophysical sources and to the very small neutrino interaction cross-section, large instrumented volumes are required. The idea to install detectors deep in a lake or in the sea was first proposed by Markov in the 1960s [65]. Neutrino telescopes are based on the detection of the secondary particles produced in neutrino interactions with matter. A tridimensional array of photomultiplier tubes (PMTs) determines the direction of the charged leptons (mainly muons, but also electron- or tau-induced showers) with the help of the Cherenkov radiation.

In this chapter, the neutrino detection principle as well as an overview of the existing and future neutrino telescopes are presented. A general description of the ANTARES experiment is given in Section 2.3.

2.1 Neutrino detection

2.1.1 Neutrino interaction

In the energy range of interest for neutrino astronomy, the neutrino interaction is dominated by the deep inelastic scattering on a target nucleon. Two main channels can be distinguished depending on the weak gauge boson exchanged:

$$\nu_l + N \rightarrow l + X \qquad \text{charged current (CC)} \tag{2.1}$$

$$\nu_l + N \rightarrow \nu_l + X \qquad \text{neutral current (NC)} \tag{2.2}$$

where ν_l is a neutrino of arbitrary flavor (ν_μ, ν_e or ν_τ), N is the target nucleon, l is the corresponding lepton (μ^-, e^- or τ^-) and X is the hadronic product of the interaction leading, eventually, to a hadronic cascade. CC interactions are mediated by the exchange of $W^\pm$ boson, in opposition to NC interactions via Z^0 boson. These interactions are shown in Figure 2.1.

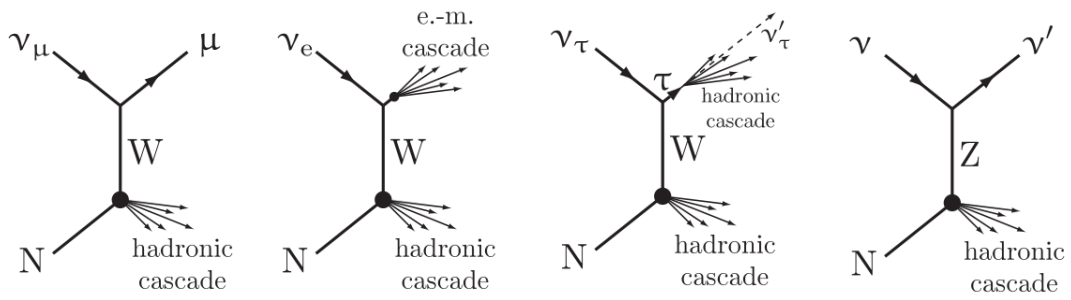

(a) CC $\mu^{\pm}$ (b) CC $e^{\pm}$ (c) CC $\tau^{\pm}$ (d) NC

Figure 2.1: Illustration of the neutrino interaction channels. Charged current interactions for muon, electron and tau are shown in (a), (b) and (c) respectively, whereas neutral current interaction is presented in (d). Figure taken from [66].

Neutrino telescopes can detect the secondary particle showers initiated by neutrinos of all flavors, as well as the leading secondary muon tracks initiated by ν_μ only. The probability to detect neutrinos raises as a function of the neutrino energy, since the cross-section of neutrino-nucleon interactions increases with energy, as shown in Figure 2.2. Depending on the channel, different signatures can be observed in the detector. In NC interactions, only the resulting hadronic cascade can be observed, as the outgoing neutrino does not have a visible signature. Furthermore, it is impossible to identify the flavor type of the neutrino in a NC reaction. So, we will focus on CC channels with which different event topologies can be seen depending on the neutrino flavor.

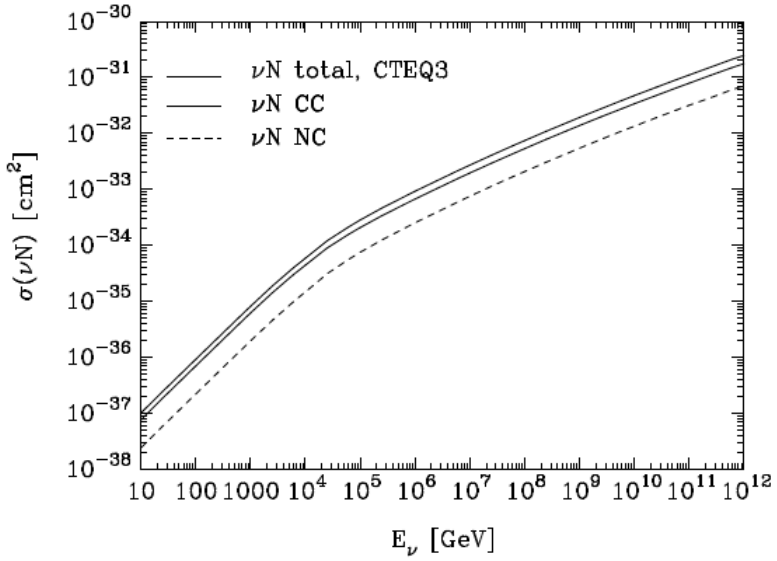

Figure 2.2: Neutrino-nucleon interaction cross-section as a function of the neutrino energy. Charged and neutral current contributions to the cross-section are shown with thin solid and dashed lines, respectively. The total cross-section is presented by a thick solid line. See [67] for details.

Muon neutrinos Secondary muons initiated by muon neutrinos have the longest tracks in the medium, due to their larger mass with respect to the electron and longer lifetime with respect to the tau. Muon tracks can be detected even if the interaction happens outside the instrumented volume of the detector. The average angle between the neutrino direction and the resulting muon can be approximated by:

$$< \theta_{\nu,\mu} >= \frac{0.64^\circ}{(E_\nu/\mathrm{TeV})^{0.56}} \tag{2.3}$$

At high energies ($E_\nu > 10$ TeV), the angular resolution of the telescope is fully dependent on the reconstruction quality, since the neutrino direction and the muon track are almost collinear. Hadronic products of the interaction form a hadronic shower, but its size rather small with respect to the muon track makes it difficult to detect.
Neutrino telescopes are primarily designed for the detection of muons, as it represents the most efficient and precise method.

Electron neutrinos The electron neutrino events produce an electron and a hadronic cascade. As the electron has a short free path length in matter, it will produce bremsstrahlung photons after a few centimeters. These photons can, in turn, interact via $\gamma \rightarrow e^+e^-$ pair production. This leads to an electromagnetic cascade which overlays the hadronic one. For a 10 TeV electron, the shower length is only about 10 m. These showers are unlikely to reach the detector and in case of detection, the direction can be reconstructed but with a poorer accuracy than what can be achieved with muon neutrinos.

Tau neutrinos The main signature of high energy tau neutrinos is the so-called *double-bang* structure, with a first shower coming from the interaction point of the incident neutrino and a second one due to the tau decay. These two showers are connected with a detectable tau track and should be separated by the tau decay length. Below a few PeV, the tau particle decays immediately and therefore the two showers cannot be distinguished. In the case that the interaction occurs outside the detector and the emerging tau decays inside the detector, a *lollipop* event signature with a track ending in a cascade will be produced. Detection of these intriguing events will probably be reserved for km^3-scale instruments, where the detection of showers will play an important role.

2.1.2 Cherenkov radiation

Cherenkov radiation is emitted when charged particles pass through a dielectric medium with a velocity greater than the speed of light in the medium. This phenomenon, first observed in the 1930s [68], is the result of the polarization of the

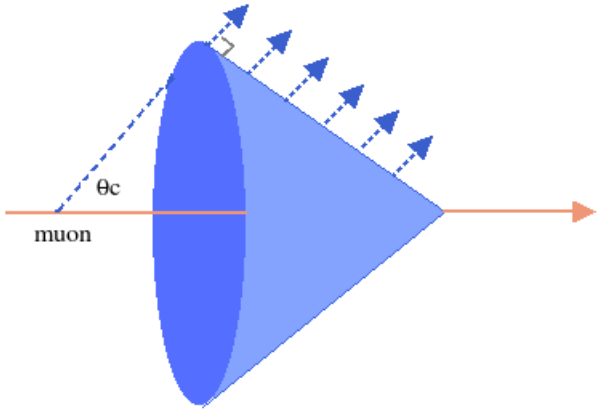

Figure 2.3: Illustration of Cherenkov radiation.

medium along the particle trajectory. If the charged particle moves slowly compared to the speed of light, electric dipoles are symmetrically oriented around the track and no radiation is produced. At higher particle velocities, this symmetry is broken and a Cherenkov light is emitted due to the dipole radiation. This light is emitted in a cone with a characteristic angle θ_c (Figure 2.3) which depends on the velocity β of the particle and the refractive index n of the medium:

$$cos\theta_c = \frac{1}{\beta n} \tag{2.4}$$

For relativistic particles ($\beta \simeq 1$) in sea water ($n \simeq 1.364$) the Cherenkov angle is $\theta_c \simeq 43°$.

The number of Cherenkov photons emitted per track length x and wavelength λ can be estimated using the following equation:

$$\frac{d^2N}{dxd\lambda} = \frac{2\pi\alpha Z^2}{\lambda^2}(1 - \frac{1}{\beta^2 n^2}) \tag{2.5}$$

where Z is the charge of the particle and α is the fine-structure constant. In the wavelength range relevant for water-based neutrino telescopes of about 300 nm to 600 nm, the number of Cherenkov photons emitted per meter is about 3.5×10^4.

The detection principle of neutrino telescopes is based on the Cherenkov radiation. By measuring the light produced by a charged particle in several places of the detector with a good timing resolution, it is possible to reconstruct the particle trajectory.

2.1.3 Muon propagation and energy losses

A muon propagating through matter loses energy due to ionization and radiative processes (bremsstrahlung, pair production and photo-nuclear interactions) [69]. An overview of the different contributions to the energy losses depending on the muon energy is shown in Figure 2.4. Below ∼1 TeV, the main contribution comes

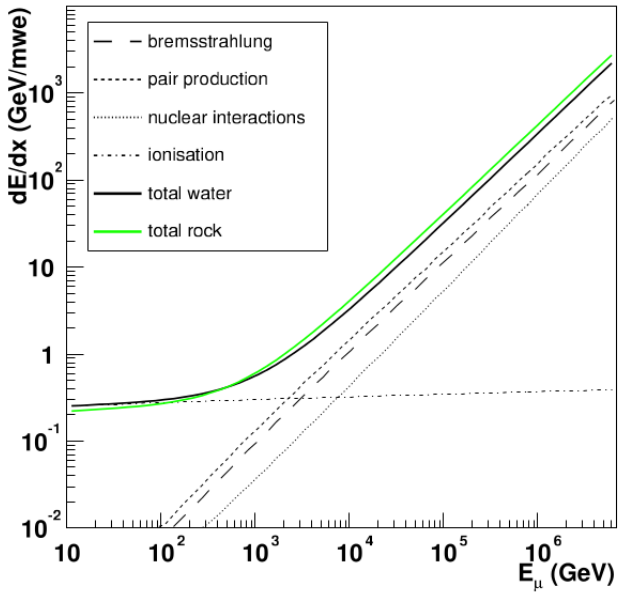

Figure 2.4: Average energy loss per meter of water equivalent for muons in rock and sea water as a function of the muon energy. For the energy loss in water, the contributions of the different processes are shown separately. Data taken from [70].

from ionization and is roughly constant at about 0.3 GeV per meter of water. At higher energies, radiative losses dominate. These losses are strongly energy dependent and stochastic. Therefore, only the average total energy loss can be calculated:

$$-\left\langle \frac{dE}{dx} \right\rangle = \alpha(E) + \beta(E).E \tag{2.6}$$

where α accounts for the ionization losses and β describes the energy loss by the three radiative processes. The first term is almost constant, while the second term grows linearly with the energy. The radiative processes produce hadronic and electromagnetic cascades along the muon track, which allow the reconstruction of the muon energy.

2.1.4 Physical background

Neutrino telescopes are not background free. Showers induced by interactions of cosmic rays with the Earth's atmosphere produce atmospheric muons and atmospheric neutrinos (Figure 2.5). Atmospheric muons can penetrate the atmosphere and go through several km of water or ice. To reduce this background, neutrino telescopes are installed at large depths. The matter above the detector acts as a shield against these muons. However, even at these depths the down-going atmospheric muon background is still higher than the expected signal. Therefore, the search for cosmic signal concentrates on up-going events, which corresponds to the neutrinos which have passed through the Earth and interacted within or close to the detector.

Decays of charged pions and kaons produced in hadronic air showers, also yield

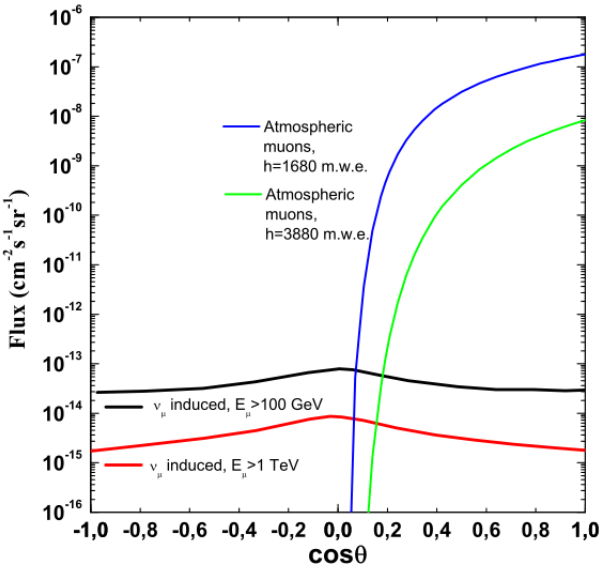

Figure 2.5: Muon flux due to atmospheric muons (computed according to [71]) at two different depths in meter water equivalent (m.w.e.) and to atmospheric neutrinos (from [72]) for two different muon energy thresholds, as a function of the cosine of the zenith angle.

a large flux of atmospheric neutrinos. These neutrinos may lead to up-going tracks in the detector and represent an irreducible background. The measurement of any cosmic neutrino signal would thus be inferred by observing a significant statistical excess over the background. At high energy, as the spectrum of atmospheric neutrinos is steeper than the expected source spectra, the signal-to-noise ratio can be improved.

2.2 Neutrino telescopes

The DUMAND experiment [73] based in Hawaii was the pioneer project to attempt the construction of a neutrino telescope in 1976. Although the project was canceled before the end of the construction due to a lack of funding, the DUMAND collaboration provided a valuable experience for subsequent projects.

Baikal The Baikal collaboration was the first to complete the construction of an underwater neutrino telescope [74]. Its first stage (NT36) has been deployed in 1993 in the Lake Baikal with the first three strings containing 36 photomultiplier tubes (PMTs), while the NT200 (made of 200 PMTs) has been in operation since 1998 and has been upgraded to the 10-Mton scale detector NT200+ in 2005. Compared to neutrino telescopes in the deep sea, the Baikal setup offers several advantages and drawbacks: the background contribution from ^{40}K decays is significantly reduced in fresh water but the relatively low depth ($\sim$1100 m) of the detector leads to a larger atmospheric muon background.

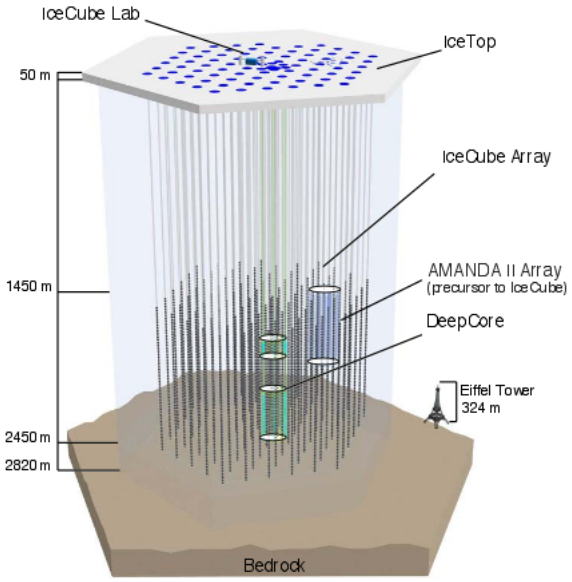

Figure 2.6: Schematic view of the IceCube neutrino telescope. Image from [75].

IceCube The IceCube detector [75] is currently the largest neutrino telescope in operation. Successor of the AMANDA project [76], the IceCube telescope was completed in 2011 and consists of 86 strings embedded in the South Pole ice. A total of 5160 optical modules (OMs) are distributed along these strings, covering a surface of about 1 km^2. A schematic view of the detector is shown in Figure 2.6. The observatory also includes a surface array (IceTop) composed of 160 tanks placed in pairs above each detector string. It is used for extensive air shower measurements and serves as a veto for atmospheric muons.

ANTARES Located in the Mediterranean Sea, the ANTARES (Astronomy with a Neutrino Telescope and Abyss environmental RESearch) detector [27] is the largest neutrino telescope operating in the Northern hemisphere. Detailed description of the ANTARES experiment will be given in the next section.

KM3NeT The KM3NeT project [77] represents the major effort to design and build a multi-km^3 scale neutrino telescope in the Mediterranean Sea. It will complement the IceCube detector in the Southern hemisphere and exceed it substantially in sensitivity. The detector will have a modular structure with six building blocks, each consisting of about one hundred detection units. Each detection unit will be equipped with 18 OMs containing 31 PMTs. The first phase of construction has started.

2.3 The ANTARES detector

The ANTARES detector, completed in 2008, is the largest underwater neutrino telescope in operation. It is located in the Mediterranean Sea at a depth of 2475 m, 40 km off Toulon in the South of France (Figure 2.7 (left)). The design of the ANTARES telescope was optimized to detect Cherenkov light produced by highly relativistic muons from charged current interactions of cosmic muon neutrinos with matter in or close by the detector. ANTARES is sensitive to neutrinos in the TeV-PeV energy range and thanks to its location, it can cover a large part of the Southern sky, including the Galactic Center region (Figure 2.7 (right)).

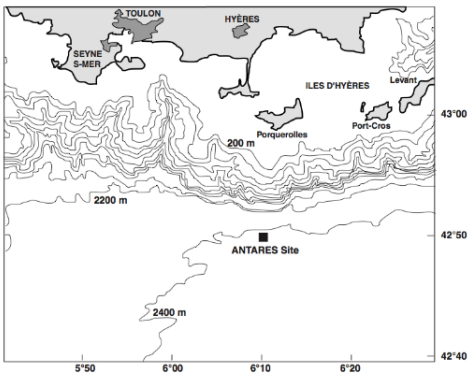

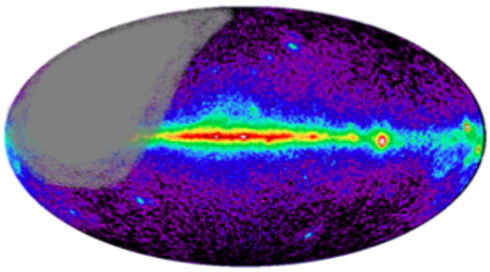

Figure 2.7: Left: depth contour plot near the ANTARES site. Each profile line corresponds to 200 m depth change. Right: observable sky by the ANTARES detector in galactic coordinates. The map represents all photons with energies greater than 100 MeV observed by EGRET on board CGRO. The gray-zone is not visible with ANTARES.

2.3.1 Detector layout

The ANTARES neutrino telescope consists of a three dimension array of 885 PMTs distributed over twelve 480 m high vertical lines. A schematic view of the detector is shown in Figure 2.8. The lines, spaced out by $60-70$ m, are anchored to the seabed and kept taut by a buoy at the top. Each line comprises up to 25 storeys hosting triplets of OMs (Figure 2.9) looking downward[1] to optimize the detection of up-going muons. Each of these OMs consists of a large area PMT and its associated electronics housed in a pressure resistant glass sphere. The triplets of OMs are connected to the line via the Local Control Module (LCM) which holds the electronics for the trigger, signal digitization, slow-control and data transmission (see Section 2.3.3). Each of the twelve lines is connected to the Junction Box (JB) which provides power and receives the data from the line. The JB is linked to the shore station through the Main Electro-Optical Cable (MEOC), a 40 km cable reaching the power hut in La Seyne-sur-Mer. An additional 13th line (instrumentation line IL13), also connected to the JB, is

[1] At 45° with respect to the vertical.

dedicated to the monitoring of the sea environment, as ANTARES provides an unprecedented infrastructure for oceanographic science.

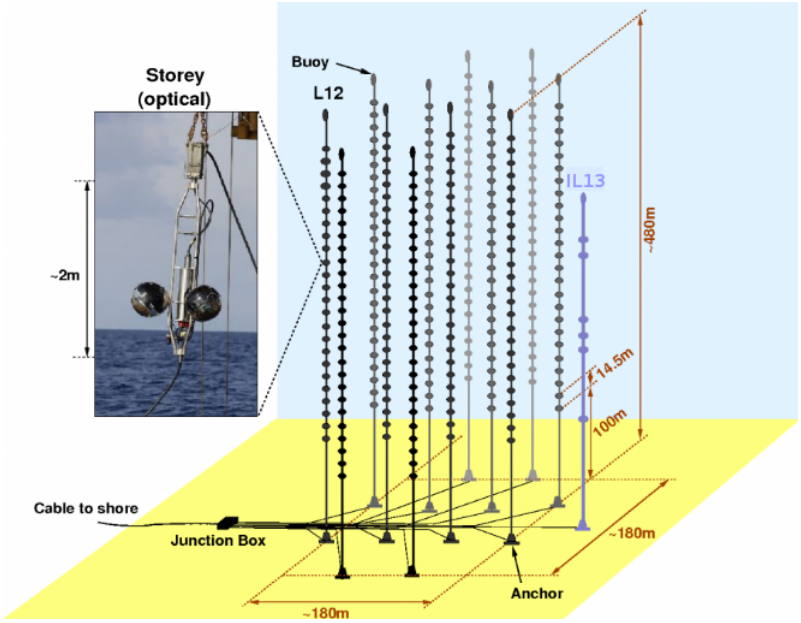

Figure 2.8: Schematic view of the ANTARES neutrino telescope.

2.3.2 Optical background

Due to its location in the deep sea, the ANTARES detector is subject to environmental background that has to be accounted for. The two main contributions come from the decay of radioactive elements in seawater and the bioluminescence. The ^{40}K is the dominant radioactive isotope in the natural seawater and decays through two channels:

$$\begin{aligned} {}^{40}K &\rightarrow {}^{40}Ca + e^- + \overline{\nu}_e \qquad (BR = 89.3\ \%) \\ {}^{40}K + e^- &\rightarrow {}^{40}Ar + \nu_e + \gamma \qquad (BR = 10.7\ \%) \end{aligned} \tag{2.7}$$

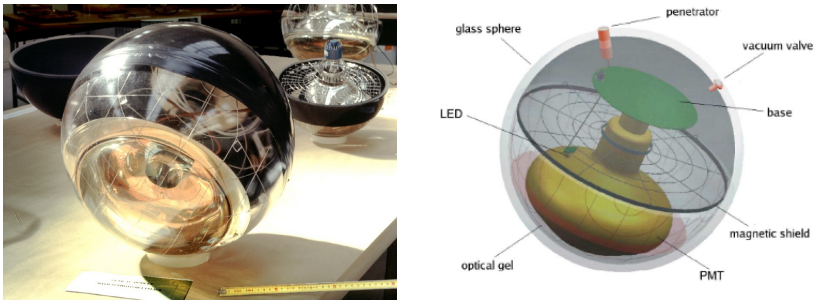

Figure 2.9: Illustration of an optical module of ANTARES containing a photomultiplier tube.

These reactions both contribute to the production of optical noise. A large fraction of electrons produced in the first decay is above the threshold for Cherenkov light production[2]. The photon produced in the second reaction has an energy of 1.46 MeV and can therefore lead (through Compton scattering) to electrons above the Cherenkov threshold. The optical background due to ^{40}K is almost constant at $\sim 30 - 40$ kHz.

The rate of bioluminescence light produced by micro-organisms varies in time, depending on environmental conditions like deep-sea current and weather conditions on the sea surface. Bioluminescence can give rise to optical background up to several orders of magnitude above the ^{40}K contribution.

Figure 2.10 shows the median rate recorded by two different OMs from 2006 to 2008. A baseline of ∼70 kHz is dominated by optical background due to ^{40}K decays and bioluminescence coming from bacteria, as well as bursts of a few seconds duration, probably produced by bioluminescent emission of marine animals.

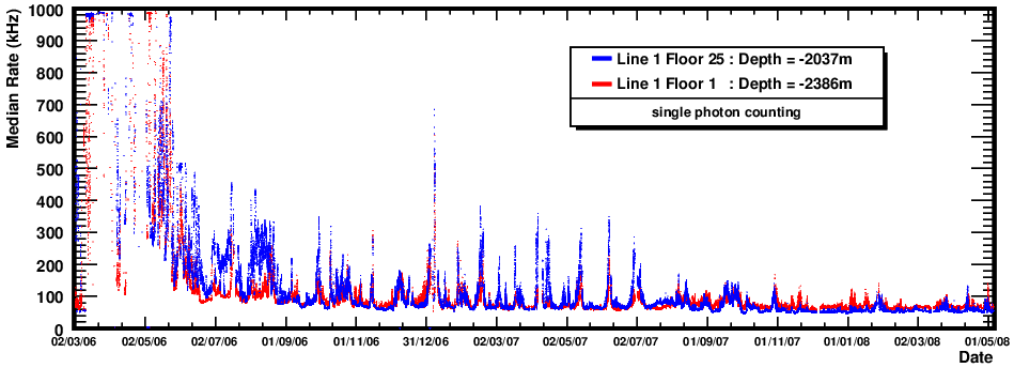

Figure 2.10: Median rate (in kHz) measured by two OMs at different depths between 2006 and 2008.

2.3.3 Data acquisition and triggers

The data acquisition system (DAQ) of ANTARES, described in [79], serves to digitize analog signals of PMTs, transfer the data to shore, filter it and store it on the disks. As the DAQ uses the *all-data-to-shore* concept, the underwater part of the detector only performs digitization of the signal, and all the filtering is done on-shore.

Signal digitization and data transmission

During data taking, the analog signals from the PMTs are digitized by the Analog Ring Sampler (ARS) chips, which reads the timing of each PMT signal and the total charge of the pulse. A voltage threshold of 0.3 photo-electron (pe) is set to trigger the digitization process. This threshold, denoted as the Level 0 (L0)

[2]The Cherenkov threshold at the ANTARES site is about 0.25 MeV [78].

condition, is set to eliminate small pulses due to the dark current inside the PMT. To reject the contribution due to electronic noise, a timing gate is tuned to integrate PMT signals in a window of 35 ns. A local clock, synchronized with a 20 MHz master clock on shore, is used by the ARS chips to timestamp each PMT signal above the threshold. The combined time and charge information of a digitized PMT signal is called *a hit*. After the integration time, the ARS chip has a dead time of about 200 ns, therefore each PMT is connected to two ARS chips. After the integration time of the first ARS chip, the second takes over. The readout system of the ARS chips is implemented in a Field Programmable Gate Array (FPGA) that arranges the hits produced by each ARS in a time window of 104.8 μs into separate data frames.

The *all-data-to-shore* scheme implies that all digitized signals exceeding the L0 level are sent to shore (700 Mb/s per line) and processed in real-time by a farm of PCs. The data transport is made by using the Dense Wavelength Division Multiplexing (DWDM) technique [80]. This is an optical technology that uses multiple wavelengths to transmit different streams of data.

Data filtering and storage

The enormous amount of data recorded by the optical modules[3], is mostly due to optical background and has to be filtered appropriately. Trigger algorithms are applied to separate signal from background by searching for space-time correlations between hits. Signal events are selected with the DataFilter program that looks for a set of correlated hits in the full detector in a time window of about 4 μs. This time window covers the passage of a muon through the detector. Once an event is selected, it can be stored with the DataWriter program.

The first level trigger, applied on L0 hits, allows the background to be reduced by a factor of at least 10^4. Such a reduction is achieved by searching for hits within 20 ns in different PMTs of the same storey or single hits with an amplitude higher than 3 pe. A time window of 20 ns is chosen to detect scattered hits, as the distance of two PMTs on the same storey is about 0.7 m. Hits satisfying these criteria are called Level 1 (L1) hits. This kind of selection is based on the assumption that background caused by bioluminescence or ^{40}K decay mostly leads to single, uncorrelated hits.

In addition to this first level selection, a second trigger level can be applied to search for clusters of L1 hits and to check the compatibility with different track directions. Clusters are formed by hits connected by the following causality relation:

$$|\Delta t| \leq \frac{n_g}{c} d \tag{2.8}$$

where Δt is the time difference between two hits, n_g/c is the group velocity of light in seawater and d is the distance between the two PMT hits. Different triggers can be used during data taking depending on the optical background conditions. They have different efficiency on neutrino detection and different event purity. Some of these triggers are:

[3]The data output rate is from 0.3 GB/s to 1 GB/s, depending on background and number of active lines.

- T3: Coincidence of two L1 in two adjacent floors within 80 ns or within 150 ns in two next-to-adjacent floors.
- 3N: At least 5 L1 in a time window corresponding to a muon track ($\sim$4 μs).
- GC: 1 L1 and 4 L0 in the direction of the Galactic Center. It is used to maximize the detection efficiency of neutrinos coming from the Galactic Center.
- K40: 2 L0 on 2 PMTs of the same storey. It is used for the in situ calibration.

The main strategy is to have a final detector event rate of $\sim$100 Hz which produces about 1 GB of physics events per $1-2$ hours of data taking.

2.3.4 Calibration

To ensure accurate reconstruction of muon trajectories, a precise knowledge of the position and arrival time of Cherenkov photons on PMTs is needed. The measurement of the deposited charge is also crucial to estimate the muon energy.

Time calibration

The time calibration of ANTARES, described in [81], is performed by using a master clock and an optical beacon system. The absolute timing of the recorded data is ensured by a 20 MHz master clock system generated on-shore that receives the Global Positioning System (GPS) time. Individual time offsets of each PMTs with respect to this reference time are determined by flashing light sources that can be activated externally. Each detection string is equipped with four LED optical beacons that have been previously synchronized in the lab with an accuracy better than 0.1 ns. These beacons are used to calibrate the PMTs between them. To calibrate the time offsets between the lines, two laser beacons are used. They are placed on the bottom of two lines and produce a light which is spread out by a diffuser to illuminate the adjacent lines. The timestamps of the detected light are compared with the estimated ones from the line positions and the calibrations in the lab. This time calibration system provides a timing resolution of $\sim$1 ns.

Charge calibration

The charge calibration enables to translate the signal amplitudes into number of photo-electrons, which is the relevant information for muon energy reconstruction. This calibration is also performed to monitor possible PMT ageing effects that could reduce the detector performances.

The relation between the signal amplitude and the number of photo-electrons is given by the transfer function of the Amplitude-to-Voltage Converter (AVC). For the calibration, the charge corresponding to one photon and the charge in absence of signal (pedestal) have to be measured. Regular in situ calibration runs are performed to determine these values. The pedestal value of the AVC, namely the AVC offset, $\mathrm{AVC_{0pe}}$, is obtained by integrating the charge at some random start time, whereas the 1 photo-electron charge ($\mathrm{AVC_{1pe}}$) is determined from ^{40}K

decays and bioluminescence which mainly lead to single photon hits. With these values, the charge Q in photo-electrons for any hit can be calculated:

$$Q = \frac{\mathrm{AVC} - \mathrm{AVC}_{0\mathrm{pe}}}{\mathrm{AVC}_{1\mathrm{pe}} - \mathrm{AVC}_{0\mathrm{pe}}} \tag{2.9}$$

where AVC is the measured charge in AVC channels.

Positioning system

The position of the lines anchored to the seabed are well known and stable in time. However, as the detector is composed of flexible lines, even relatively small sea currents of about 5 cm/s can result in displacements of the top storeys of a few meters, as shown in Figure 2.11. Therefore, an essential element of the calibration of the detector is the real-time positioning. This is achieved through two independent systems [82]: an acoustic positioning system and a set of compasses and tiltmeters.

Each line is equipped with 5 acoustic receivers (hydrophones) which measure high-frequency acoustic signals ($40 - 60$ kHz) emitted by transmitters installed at the line anchor. The distances, obtained by measuring the travel times of the acoustic waves, are used to triangulate the position of each receiver with respect to the emitters. The shape of each line is reconstructed by a global χ^2 fit using this position information and the data from compasses and tiltmeters that are installed on each storey.

With this positioning system, the relative position of each OM can be known with an accuracy better than 20 cm.

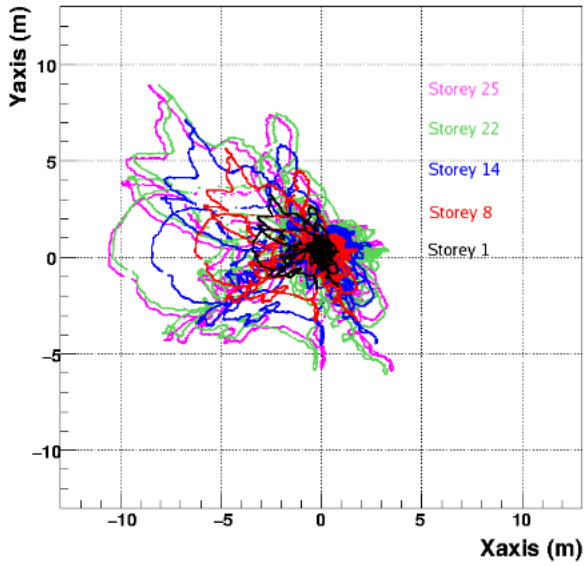

Figure 2.11: Horizontal displacements of the hydrophones of one of the lines with respect to the anchor for a period of 6 months [82].

CHAPTER 3

TAToO

To enhance the sensitivity to transient sources, such as GRBs or CCSNe, a multi-wavelength follow-up program, named TAToO, has been implemented within the ANTARES experiment in 2009 [83]. This system triggers a network of robotic optical telescopes and the *Swift*-XRT [84] quickly after the detection of a special neutrino event, which will point into the neutrino direction and start follow-up observations. These events are selected if they fulfill energy, direction or multiplet criteria, as described in the following sections.

Two basic requirements for the coincident observation of a neutrino and an optical or a X-ray counterpart from transient sources are that the pointing accuracy of the neutrino detector should be at least comparable to the field of view (FoV) of the telescopes and that the response time of the system should be as fast as the duration of the transient event. The TAToO system is able to send alerts within few seconds ($\sim 3 - 5$ s), and the wide FoV and the rapid response time of the telescopes are well-suited to this kind of searches.

Although the work of this thesis focuses on the search for GRB afterglows and CCSNe, with such an alert system, no hypothesis is made on the nature of the underlying source. By combining information provided by the ANTARES neutrino detector with information coming from other observatories, the probability of detecting a source is enhanced since the neutrino background is reduced in the time window of the transient event. Therefore, one neutrino associated with a transient counterpart would be a significant event.

The principle of the TAToO alert system is illustrated in Figure 3.1 and is fully described in the following sections, with first a description of the reconstruction algorithms used in ANTARES, as well as the trigger criteria applied to select interesting events. The alert sending, the telescope network and the observation strategy are then detailed. A current status of TAToO ends this chapter.

3.1 The alert system

As explained in Section 2.3.3, the *all-data-to-shore* concept is used in ANTARES. The data recorded by the detector are sent to the shore for filtering (DataFilter)

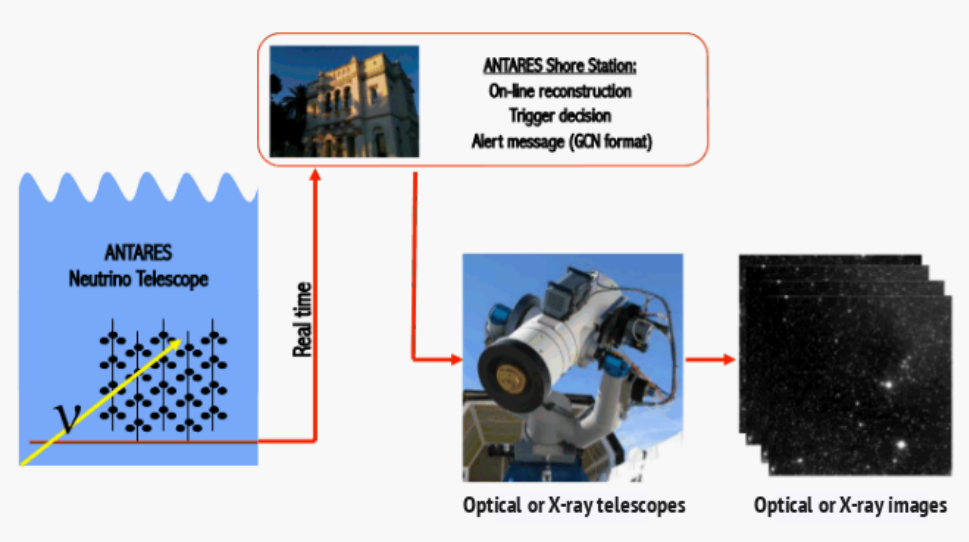

Figure 3.1: Illustration of the TAToO alert system implemented in the ANTARES experiment.

and writing (DataWriter). The alert system, TAToO, is implemented in parallel to the DataWriter (Figure 3.2). Two programs, `BBalert` and `AAalert`, are used to reconstruct the events online and offline, respectively. This reconstruction reduces the rate of events from a few Hz down to a few mHz by selecting neutrino candidates with an increased probability to be of cosmic origin. Trigger criteria are then applied to surviving events and an alert is generated if they fulfill energy, direction or multiplet conditions (see Section 3.1.3).

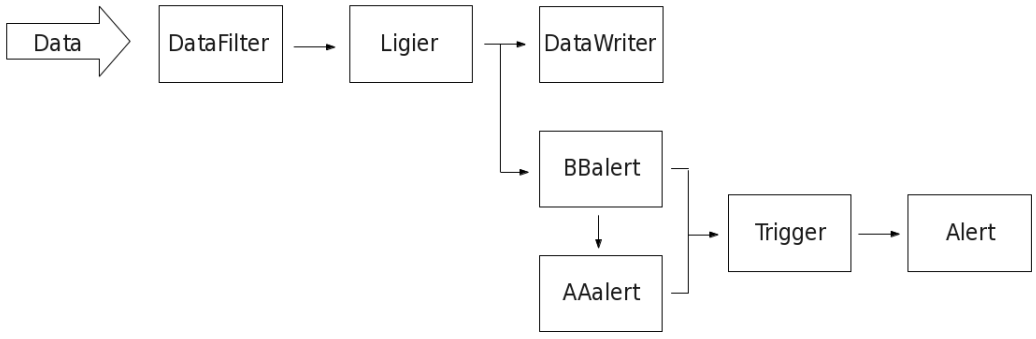

Figure 3.2: Scheme of the alert system implemented in parallel to the DataWriter of ANTARES. The data recorded by the detector are filtered on-shore and dispatched by the Ligier to the DataWriter and the alert system.

3.1.1 Event reconstruction

To select the events which might trigger an alert, a fast and robust algorithm (`BBfit`) is used to reconstruct the calibrated data. A detailed description of this

algorithm and its performance can be found in [85]. The principle is to minimize a χ^2 function which compares the times of selected hits with the expectation from a Cherenkov signal generated by a muon track. This algorithm, part of `BBalert`, uses an idealized detector geometry which does not rely on the dynamical positioning calibration: each detector line is considered as straight line and the detailed geometry of each storey is ignored. This algorithm is then coupled to a more precise reconstruction tool (`AAfit`) [28] which allows the neutrino nature of the event to be confirmed and the angular resolution to be improved.

Hit selection

As a first step of the track reconstruction, time and charge calibrations are applied to transform raw data into physical units (time in nanoseconds and charge in equivalent number of photo-electrons, see Section 2.3.4). Then, among the hits above the low-threshold amplitude of 0.3 pe (L0 condition, see Section 2.3.3), those satisfying L1 and T3 conditions are selected for the fitting procedure. For the L1 condition, it implies hits within 20 ns in two OMs of the same storey or single hits with an amplitude higher than 3 pe. As the fitting procedure allows only one hit per storey, all hits coming from the same storey are time-ordered, regardless from which OM they originate, and merged if they come within the predefined time window of 20 ns. Merging implies adding the hit amplitudes and keeping the time of the earliest hit. For the T3 condition, it implies two coincident L1 hits within 80 ns for two adjacent storeys or within 150 ns for two next-to-adjacent storeys. To avoid the attribution of isolated noise hits to a track, only detector lines having at least one T3 are considered. Using these T3 hits as "root hits", new hits are added to the list of selected hits. By calculating the expected hit times on adjacent floors of a T3 cluster, L0 hits at 1 pe level are searched for within a narrow time window around the T3 times. The final list of selected hits is exclusively based on timing information and serves for all subsequent fitting steps.

Before starting any fit, the list of selected hits is examined and only events with more than 5 hits are considered. Two fitting procedures are implemented on `BBfit`. A single-line fit procedure is performed if all selected hits are on a single detector line, otherwise a multi-line fit procedure is started.

Fitting particle tracks

A particle track is considered as a straight line and can be parameterized as:

$$\overrightarrow{p}(t) = \overrightarrow{q}(t_0) + c(t - t_0)\overrightarrow{u} \tag{3.1}$$

if the particle is assumed to move with the speed of light in vacuum. The particle passes through the point $\overrightarrow{q}$ at time t_0 and moves in the direction $\overrightarrow{u}$. The vector $\overrightarrow{q}$ can be shifted along the track by redefining t_0. The track of a particle is thus defined by a set of 5 parameters: three values to fix $\overrightarrow{q}$ for a given time and two angles to define $\overrightarrow{u}$:

$$\overrightarrow{u} = \{\cos\theta\,\cos\phi,\ \cos\theta\,\sin\phi,\ \sin\theta\} \tag{3.2}$$

where θ is the elevation (zenith) angle and ϕ the azimuth angle.

As illustrated in Figure 3.3, the detector lines are considered as vertical lines along the z-axis with a fixed position at (L_x, L_y). For each particle track, the point of closest approach between the detector line and the track can be defined along the z-axis as follows:

$$z_c = \frac{q_z - u_z(\vec{q}\,.\,\vec{u})}{1 - u_z^2} \tag{3.3}$$

The particle passes at a distance

$$d_c = \sqrt{p_x^2(t_c) + p_y^2(t_c) + (p_z(t_c) - z_c)^2} \tag{3.4}$$

from this point at a time

$$t_c = t_0 + \frac{q_z u_z - (\vec{q}\,.\,\vec{u})}{c(1 - u_z^2)} \tag{3.5}$$

For exactly vertical tracks (single-line fit), $t_c = t_0$ and $z_c = q_z$. As a single detector line is invariant against a rotation around the z-axis, a particle track can be reparameterized with the four parameters z_c, t_c, d_c and u_z (the latter being nothing other than the cosine of its zenith angle).

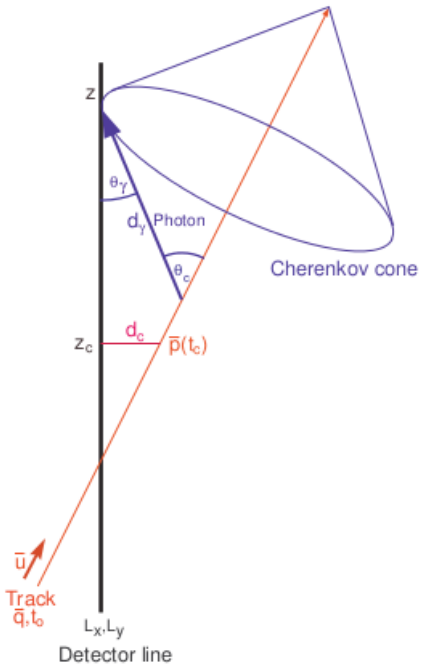

Figure 3.3: Illustration of the variables used to describe a track and its corresponding Cherenkov cone with respect to a vertical detector line.

To perform a track fit, it is necessary to know the arrival time t_γ of a Cherenkov photon at the detector line position (L_x, L_y, z), its corresponding travel path d_γ

and its inclination with respect to the detector line cos θ_γ. All these values can be derived from the four parameters defined above:

$$d_\gamma(z) = \frac{n}{\sqrt{n^2-1}}\sqrt{d_c^2 + (z-z_c)^2(1-u_z^2)} \tag{3.6}$$

$$t_\gamma(z) = (t_c - t_0) + \frac{1}{c}\left((z-z_c)u_z + \frac{n^2-1}{n}d_\gamma(z)\right) \tag{3.7}$$

$$\cos\,\theta_\gamma(z) = (1-u_z^2)\frac{z-z_c}{d_\gamma(z)} + \frac{u_z}{n} \tag{3.8}$$

These equations hold exactly for Cherenkov photons of a given wavelength. Dispersion and group velocity effects, as well as delays due to light scattering are ignored. A refractive index $n = 1.38$ is used in the `BBfit` algorithm.

Quality function and minimization procedure

The quality function relies on the time difference between the hit times t_i and the expected arrival time of photons from the track t_γ, as in a standard χ^2 fit. This function is extended with a term accounting for the measured hit amplitudes a_i and the calculated photon travel distances d_γ. The full quality function is:

$$Q = \sum_{i=1}^{N_{hit}}\left[\frac{(t_\gamma - t_i)^2}{\sigma_i^2} + \frac{a(a_i)d(d_\gamma)}{< a > d_0}\right] \tag{3.9}$$

where σ_i is the timing uncertainty set to 10 ns for $a_i > 2.5$ pe and to 20 ns otherwise[1]. The second term on the right hand side of the equation gives a penalty to the combination of high amplitude and large distance. An accumulation of storeys with high charges is expected on each detector line at its point of closest approach to the track. The product is divided by the average amplitude $< a >$ of all the selected hits of an event, to compensate for the fact that higher energy tracks or showers produce more light at the same distance. $d_0 = 50$ m is a normalization factor which balances the weight between the two terms. At this distance, 1 pe is expected from PMTs pointing straight into the Cherenkov light front.

The minimization of the quality function Q is performed by the MIGRAD function of the MINUIT package [86]. For the single-line fit, the particle track is parameterized through its point of closest approach, i.e., z_c, t_c, d_c and u_z, and Equations 3.6, 3.7 and 3.8 are used to obtain d_γ, t_γ and cos θ_γ. In the case of the multi-line track fit, the same set of equations is used but one additional parameter is needed to evaluate them as multi-line events do not have rotational symmetry. $\overrightarrow{q}$, u_z and ϕ are used. After minimization, the value of the quality function divided by the number of degrees of freedom is called fit quality $\tilde{Q}$ and is used for further selections. For example, badly reconstructed tracks can be

[1]These values, significantly higher than the PMT transit time spread of 1.3 ns, take into account the smearing due to the applied geometrical approximations and due to occasional late hits from small angle scattering.

discarded by applying cuts on the fit quality parameter.

With the online algorithm, `BBfit`, the direction of the reconstructed muon track is available within 10 ms and an angular resolution better than 0.5 degree can be achieved for the highest energy events. Figure 3.4 shows this angular resolution for events reconstructed with different number of lines. This resolution is defined as the median of the space angular difference between the incoming neutrino and the reconstructed neutrino induced muon track.

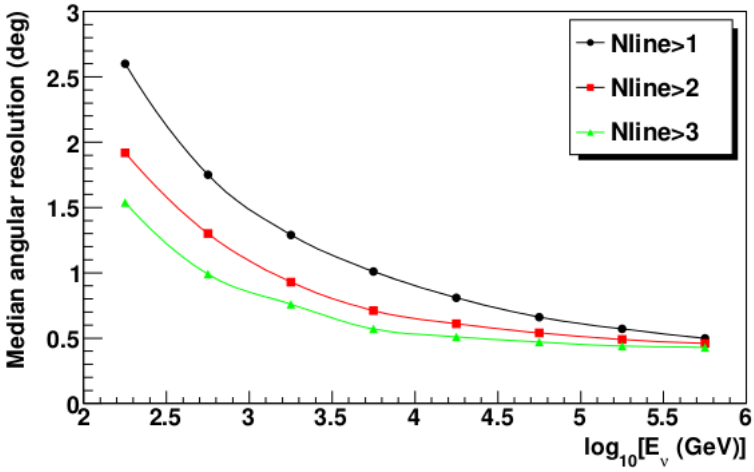

Figure 3.4: Angular resolution of the online algorithm for event tracks reconstructed with different number of lines, as a function of the neutrino energy.

Offline reconstruction

Although the angular resolution of the online reconstruction is suitable for the FoV of the telescopes used for the follow-up, the pointing accuracy can be improved with the `AAfit` algorithm [28]. This offline reconstruction takes into account the detailed geometry of the detector. As a consequence, the time used for the reconstruction is increased by comparison to the `BBfit` algorithm. Therefore, only the events passing through the `BBalert` cuts (see Section 3.1.2) are reconstructed with the `AAfit` algorithm.

The real-time positioning of the detector is performed by an acoustic system and a set of compasses and tiltmeters, as explained in Section 2.3.4. With such systems, the relative positioning of each OM is known with an accuracy better than 20 cm, equivalent to 1 ns timing precision. With the `AAfit` algorithm, the detailed geometry of the storey is not ignored, therefore the hits selected for the reconstruction are not grouped and assigned to the center of the storey.

The `AAfit` reconstruction algorithm is based in a multi-step fitting procedure to reconstruct muon tracks from timing and position information of the hits. The initial steps provide the hit selection and a starting point for the final fit. The final step consists of a maximum likelihood fit. The likelihood is defined as the probability density of the observed hit time residuals, r, given the track

parameters. The time residuals represent the differences between the expected and measured arrival times of the hits from Cherenkov photons emitted along the muon track.

As the likelihood function contains many local maxima, the maximization procedure needs to be started with track parameters close to the optimal values. The initial steps of the algorithm provide this near-optimal solution by using a linear χ^2 fit (the so-called M-Estimator) and a simplified version of the full likelihood fit. Each fit uses increasingly more inclusive hit selections based on the preceding stage. This sequence is started at nine different starting points to further increase the probability of finding the global optimum.

The final likelihood function uses parameterizations for the probability density function (PDF) of the signal hit time residual, derived from Monte Carlo (MC) simulations. The PDF also takes into account the Cherenkov photons that scatter in the water and the additional photons that are generated by secondary particles (e.g. electromagnetic showers created along the muon trajectory).

The quality of the reconstruction is estimated by:

$$\Lambda = \frac{log(L)}{N_{\text{hits}} - 5} + 0.1 \times (N_{\text{comp}} - 1) \tag{3.10}$$

where L is the maximum value for the likelihood, divided by the number of degrees of freedom of the fit, i.e., the number of hits N_{hits} used for the fit minus the number of fit parameters, and N_{comp} is the number of initial tracks converged to the same final track. In general, N_{comp}=1 for badly reconstructed events and goes till N_{comp}=9 for the well reconstructed events.

The angular uncertainty on the muon track direction, β, is also estimated. Neutrinos simulations with E^{-2} spectrum have been performed to estimate the angle between the direction of the reconstructed muon and that of the true neutrino [28].

Compared with the online algorithm, the angular resolution is improved with the `AAfit` reconstruction. This improvement is clearly visible at low energies, as shown in Figure 3.5. For high energy neutrinos, the angular resolution is better than 0.3° for the offline reconstruction against ∼0.45° for the online one.

3.1.2 Quality cuts

Down-going atmospheric muons, whose abundance at the ANTARES detector is roughly six orders of magnitude larger than the muons induced by atmospheric neutrinos, are the main background for alerts and have to be efficiently suppressed. Although an elevation cut is applied to reject down-going events, some badly reconstructed atmospheric muons classified as up-going may remain. Quality cuts on reconstructed events are applied to reduce this contamination to an acceptable level.

In order to select the best reconstructed events, quality cuts have been optimized using MC simulations. A subsample of data taken by ANTARES with the full detector configuration from September to December 2008, representing a live-time of 70.3 days, have been analyzed. During this period, around 350 up-going

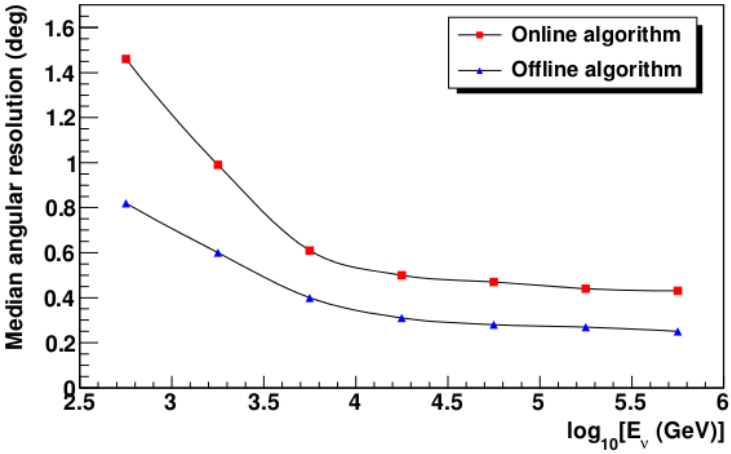

Figure 3.5: Angular resolution of the online and offline reconstructions as a function of the neutrino energy with at least 2 lines.

neutrino candidates were reconstructed and compared to a MC simulation of atmospheric muons and neutrinos using the same livetime. Down-going atmospheric muons were simulated with *Corsika* [87] and the *QGSJET* hadronic model [88] was used for the shower development. Up-going neutrinos were simulated with *genhen* [89], according to the parameterization from [90] for the atmospheric neutrino flux. Only charged current interactions were considered and the Cherenkov light produced in the vicinity of the ANTARES detector was propagated taking into account light absorption and scattering in sea water. The angular acceptance and characteristics of the OMs were taken from [91].

First quality cuts are applied at the end of the `BBfit` algorithm. These cuts rely on the number of lines used for the fit, the zenith angle θ and the track fit quality $\tilde{Q}$. It allows a subsample of good events, which will pass through the offline reconstruction algorithm `AAfit`, to be selected.

Two simple cuts are applied on the number of lines and on the zenith angle: a minimum of two lines is required to obtain the information about the track direction, and only the events reconstructed as up-going, i.e., with $\sin\theta < 0$, are selected. Figure 3.6 shows the zenith angle distribution for all events reconstructed on at least two lines for both data and simulated atmospheric neutrino and muon samples. With a cut on the elevation angle, atmospheric muons are efficiently rejected.

Figure 3.7 shows the distribution of the track fit quality $\tilde{Q}$ for all up-going events reconstructed with at least two lines. To reduce the number of atmospheric muons reconstructed as up-going, a dynamic cut on $\tilde{Q}$ is applied. Because the fit quality is correlated to the number of hits used to reconstruct the event, the cut is set to different values depending on N_{hits}: $\tilde{Q} \leq 1.3 + [0.04 \times (N_{\text{hits}} - 5)]^2$. $N_{\text{hits}} - 5$ represents the number of degrees of freedom and is used as a simple energy estimator. An additional cut $\tilde{Q} < 10$ is applied to avoid accounting for sparking OMs[2] which record high N_{hits} values.

[2]Due to ionized gas particles inside the PMT, an intense light flash can be recorded.

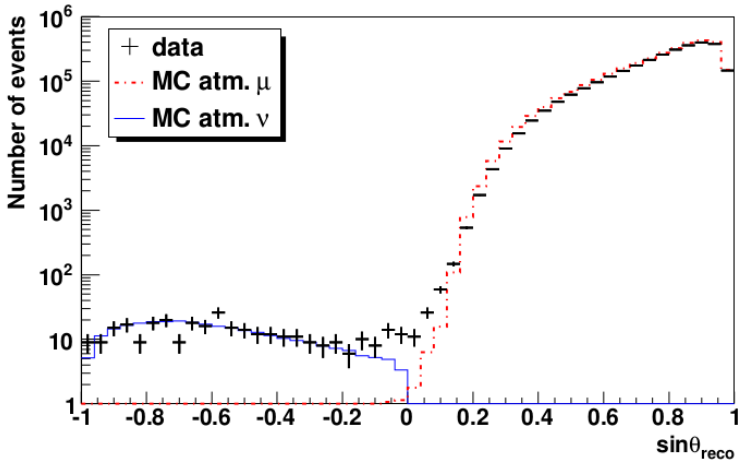

Figure 3.6: Elevation angle distribution after a selection cut on the fit quality for all events reconstructed on at least two lines, for both data and MC simulations.

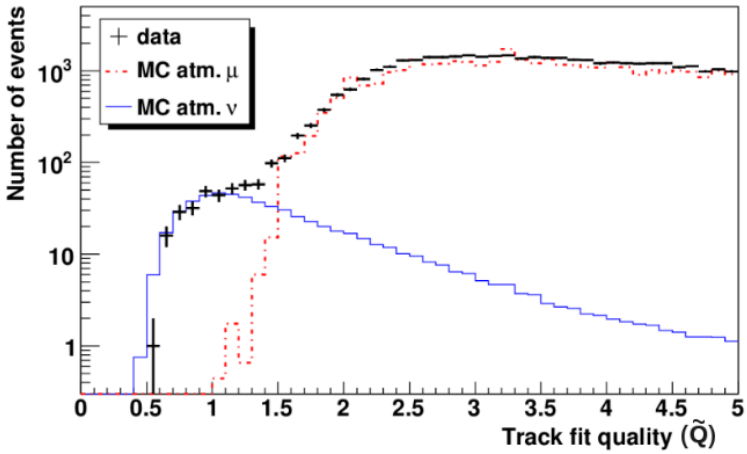

Figure 3.7: Track fit quality ($\tilde{Q}$) distribution for all up-going events reconstructed on at least two lines.

All the events passing through these quality cuts are then reconstructed with the `AAfit` algorithm and two additional cuts are applied on Λ and β. Λ is a track fit quality parameter and is used to further reject badly reconstructed events, such as atmospheric muons that are misreconstructed as up-going tracks. β is the angular uncertainty on the muon track direction and is required to be smaller than 1°. The distribution of the variable Λ is shown in Figure 3.8 for both data and MC events. Only tracks reconstructed with $\Lambda > -5.2$ and $\beta < 1°$ are kept for the next steps.

3.1.3 Triggers

Among the best reconstructed events, neutrino candidates with an increased probability to be of cosmic origin are selected with trigger criteria. Three online

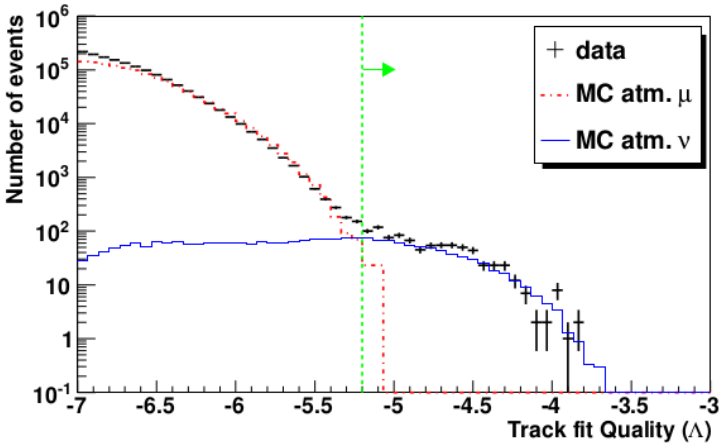

Figure 3.8: Track fit quality (Λ) distribution for up-going events in both data and atmospheric MC samples. A quality cut is applied at $\Lambda > -5.2$ to reject badly reconstructed tracks.

neutrino triggers are currently implemented in the TAToO alert system: high energy, directional and multiplet neutrinos. The main performances of these three triggers are described in Table 3.1. The selection is based on the features of the neutrino signal expected from astrophysical sources and was also tuned (via MC simulations) to comply with the alert rate to send to the telescope network. An agreement between ANTARES and the optical telescope collaborations allows sending ∼25 alerts per year to each optical telescope, while an agreement to send 6 alerts per year to the *Swift* satellite has been accepted. A dedicated trigger for the X-ray follow-up has thus been created by applying more restrictive requirements on the high energy trigger.

Table 3.1: Performances of the three alert criteria.

Trigger	Angular resolution (median)	PSF coverage[a]	Muon contamination	Mean energy[b]
High energy	$0.25 - 0.3°$	96 % (GRB) 68 % (SN)	< 0.1 %	~ 7 TeV
Directional	$0.3 - 0.4°$	90 % (GRB) 50 % (SN)	~ 2 %	~ 1 TeV
Doublet	$\leq 0.7°$		0 %	~ 100 GeV

[a] Percentage of the ANTARES PSF covered by a $2° \times 2°$ telescope field of view, assuming events produced in GRBs and SNe.
[b] Neutrino energy weighted assuming the atmospheric muon neutrino spectrum.

High energy trigger

Several models predict the production of neutrinos with energies greater than 1 TeV from transient sources, such as GRBs [92, 93, 94, 95] and CCSNe [64]. The detection of single high energy neutrinos is based on two simple energy estimators: the number of hits used in the track fit and the total amplitude of the hits in photo-electrons. Since the neutrino energy spectrum $\propto E^{-2}$ for signal events

is expected to be harder than for atmospheric neutrinos (Figure 3.9), a cut on these two parameters efficiently reduces the atmospheric neutrino background while most of the signal events are kept. The event selection for the high energy trigger has been tuned to obtain a rate of about 12 high energy alerts per year. The current cuts are (N_{hits}, amp) = (70, 150). For the highest energy events, the angular resolution gets down to less than 0.3° for this trigger. The bi-dimensional point spread function (PSF) for a typical neutrino event selected by the high energy trigger is shown in Figure 3.10.

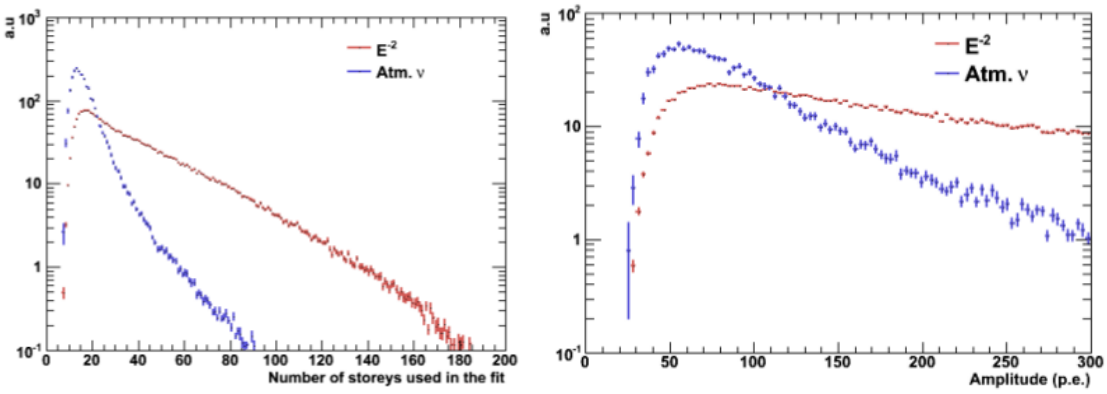

(a) Number of hits distribution. (b) Amplitude distribution.

Figure 3.9: Number of hits and amplitude distributions for atmospheric neutrinos and E^{-2} spectrum. Y-axes are in arbitrary units.

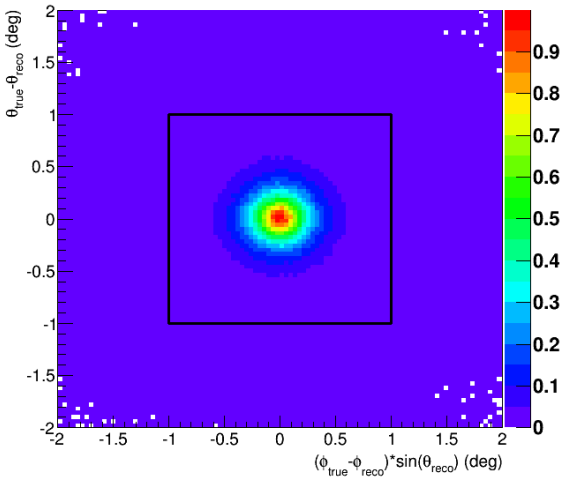

Figure 3.10: Bi-dimensional angular resolution for a typical high energy neutrino alert. The black square corresponds to the TAROT and ROTSE telescope FoV ($\sim 2° \times 2°$).

A subset of the high energy trigger with more restrictive requirements, namely more than 80 hits and a total amplitude greater than 300 pe, provides a dedicated trigger for the XRT on board the *Swift* satellite. This very high energy trigger

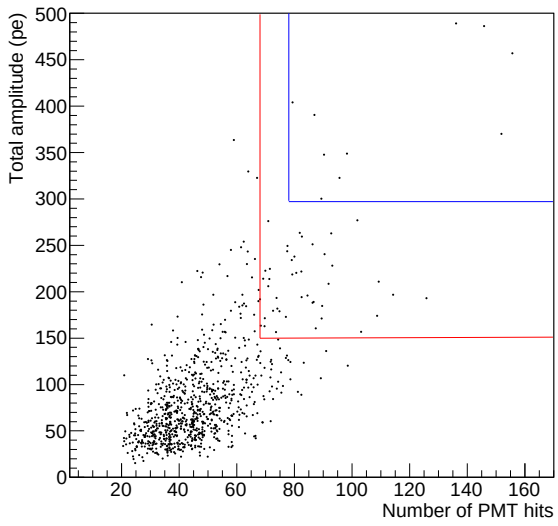

Figure 3.11: Scatter plot of the number of PMT hits vs. the total amplitude for neutrino candidates. The high energy trigger criterion is fulfilled by events inside the red box. Events inside the blue box correspond to the very high energy trigger for the *Swift*-XRT.

has been implemented in 2013 and has been tuned to respect the agreement of 6 alerts per year. The selection of high energy and very high energy triggers is illustrated in Figure 3.11 for neutrino candidates recorded from January 2012 to March 2015.

Directional trigger

As the high energy trigger is well-suited to detect the most energetic transient sources, such as GRBs, an additional trigger has been implemented in TAToO in November 2011 to enhance the detection prospects of softer emission, from CCSNe for example [64]. This trigger, denoted as directional, relies on the detection of a single neutrino event for which the direction points toward a local galaxy (< 20 Mpc). Transient sources such as CCSNe are more likely to be located in galaxies. The cuts on the number of hits and the amplitude are relaxed ($N_{\text{hits}} > 20$, amp > 10 pe) and a condition on the angle between the neutrino direction and the galaxy is set at $\Delta\theta < 0.4°$. Galaxies are selected among the Gravitational Wave Galaxy Catalog (GWGC) [96] and a cut at 20 Mpc is set to obtain a rate of about 12 directional alerts per year. Figure 3.12 shows the distribution of local galaxies from the GWGC catalog along with the ANTARES visibility in gray scale. With the directional trigger, a median angular resolution of better than $0.4°$ is achieved.

Multiplet trigger

The typical signature of a neutrino emission from transient sources is a neutrino burst, i.e., two or more coincident neutrinos originating from a source within a short time window. A multiplet trigger is implemented in TAToO to detect

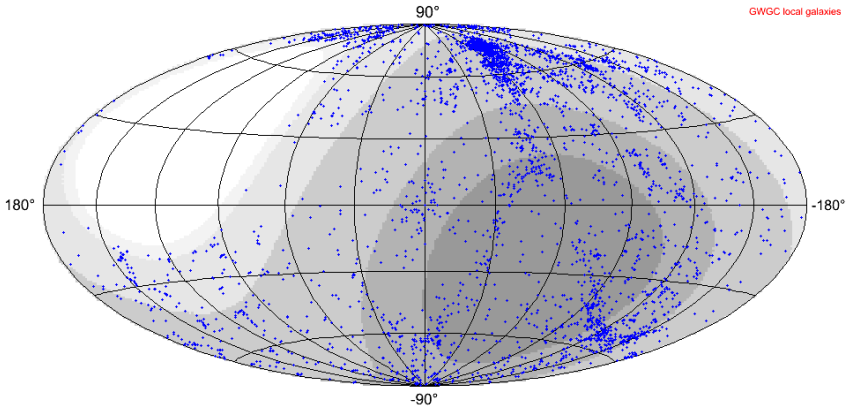

Figure 3.12: Distribution of local galaxies (< 20 Mpc) from the GWGC catalog in galactic coordinates. The gray scale represents the visibility of the ANTARES detector where the white zone is not visible and the darkest zone is 100 % observable.

these events. It requires the detection of at least two events coming from similar directions ($< 3°$) within a time window of 15 minutes. The angular window has been chosen to match the convolution of the track reconstruction angular resolution and the FoV of robotic optical telescopes ($\approx 2° \times 2°$) used for the follow-up of these events. The time window of 15 minutes has been optimized to comply with the expected neutrino emission from various transient sources (for example, it represents the maximum T_{90} GRB duration from the BATSE catalog [97]). No cuts are applied on the number of hits and the amplitude, therefore events with a mean energy of 100 GeV can be detected with an angular resolution better than 0.7°. Until now, no multiplet events have been recorded in TAToO. The serendipitous coincidence rate due to background events, i.e., from two uncorrelated up-going atmospheric neutrinos is estimated to be 7×10^{-3} per year. Therefore, the detection of one doublet or triplet event would have a significance of about 3 σ or 5 σ, respectively.

3.1.4 Alert sending and TAToO Run Control

The filtering described above suppresses the background and selects the most interesting neutrino candidates providing accurate directional information. Once an event is selected, an alert containing the celestial coordinates needs to be transferred to the telescopes. The TAToO Run Control is the main interface between the alert system and the telescope network, it insures the communication between both. This is a stand-alone application which channels the triggers generated by the alert system to the telescope network.

An important parameter for the TAToO alert system, is the time between the detection of a high energy muon crossing the detector and the time at which the alert is sent to the telescope network. This time includes the data dispatching from the off-shore PMTs to the on-shore computing farm ($\sim$ 1.5 s), the raw data filtering (< 5 s), the reconstruction of the events and the selection with the trigger criteria (a few ms). Therefore, alerts are sent with a delay of few seconds after

the neutrino detection.

The alert sending is automatically performed by an ANTARES server using a socket protocol, similar to the GCN system. Each alert message contains the direction and time information of the event, a unique identifier, the number of hits, the total amplitude and the quality of the reconstruction. Once an alert is sent to the telescopes, the TAToO team members are alerted by e-mail and SMS messages, allowing them to check if the alert has correctly been received by the telescopes and if the follow-up of the neutrino alert is possible. In order to avoid alert pileup in the telescope schedule, a blocking time of 1 hour prevents the sending of an alert immediately after the previous one.

The TAToO Run Control is also used to monitor the entire alert system. Figure 3.13 shows a screen snapshot of the Run Control window. On the left side of the panel, the online trigger rates as well as the status of the online and offline reconstruction are displayed. The right side shows the connection status to the telescope network and the list of the recent and pending alerts. The bottom part of the panel displays the status of the alert sending to the *Swift*-XRT as well as the blocking time, the rate threshold and the current trigger rate.

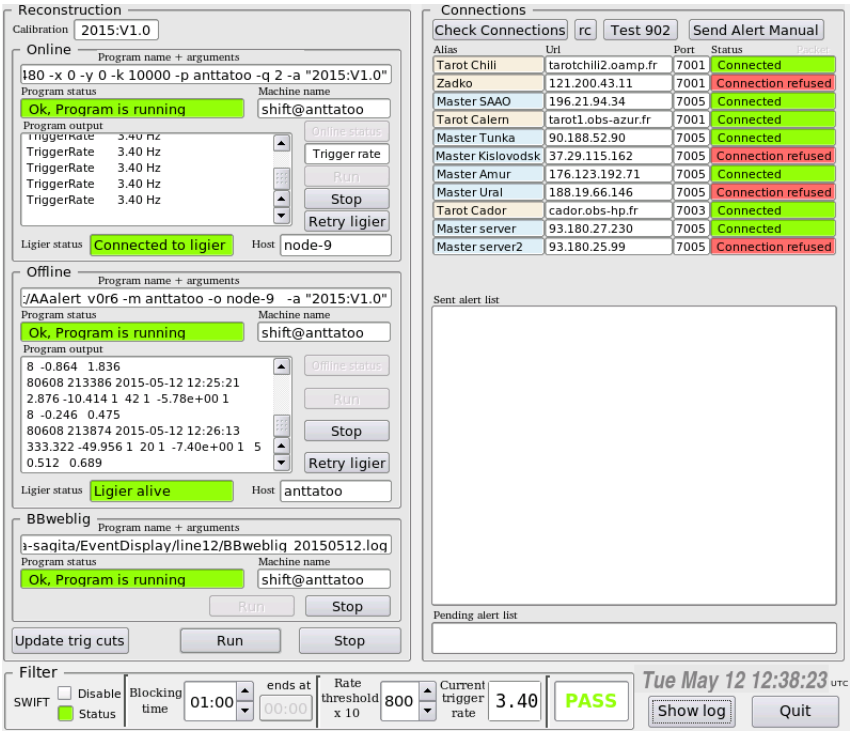

Figure 3.13: Illustration of the TAToO Run Control.

3.2 Follow-up

3.2.1 Telescope network

The follow-up of ANTARES neutrino alerts is performed with ground-based optical telescopes and with the XRT on board the *Swift* satellite. As the angular

resolution of the different triggers varies from 0.3° to 0.7°, wide field telescopes are needed. Furthermore, a fast response is required to catch rapidly decaying signals, such as GRB afterglows, and to provide early data points of slowly variable light curves.

TAROT

The TAROT (*Télescopes à Action Rapide pour les Objets Transitoires*) telescopes [98], designed to observe the early optical counterparts of GRBs, are two identical 0.25 m robotic observatories located in France and Chile (see Table 3.2.1). These telescopes have a FoV of 1.86°×1.86° and a rapid response as the mount can move as fast as 50° s^{-1}. The TAROT telescopes are equipped with Andor CCD cameras (Marconi 4240 back-illuminated) providing a spatial sampling of 3.26 arcsec/pixels and images with 2048 × 2048 pixels. Although six filters are available (B, V, R, I, a clear filter C and a 2.7 density coupled to V), only observations with the clear filter are performed in the context of the TAToO program. This allows a limiting magnitude of ∼18.5 for an exposure time of 180 s and a signal-to-noise ratio of 5 to be reached. The TAROT Chile telescope is shown in Figure 3.14.

Table 3.2: Locations of the two TAROT telescopes.

Telescope	Location	Longitude	Latitude	Altitude [m]
TAROT-Ca	Calern, France	6° 55′ 26″ E	43° 45′ 8″ N	1270
TAROT-Ch	La Silla, Chile	70° 43′ 56″ W	29° 15′ 39″ S	2347

Figure 3.14: Photograph of the TAROT telescope in Chile.

ROTSE

The Robotic Optical Transient Search Experiment (ROTSE) [99] consisted of four identical 0.45 m telescopes located in Australia (3a), USA (3b), Namibia (3c) and Turkey (3d). Table 3.2.1 shows the coordinates of each telescope. The activity of

these four telescopes has been stopped progressively in 07/2011, 09/2014, 12/2010 and 12/2012, respectively. The instruments were fully automatic and had a rapid response time of typically 4 s to point to any desired position from the stand-by mode (pointed at zenith). The wide FoV of 1.85°× 1.85° was imaged with a Marconi back-illuminated thinned CCD with 2048 × 2048 pixels. The ROTSE telescopes were capable of attaining ∼18.5 magnitude with a 60 s exposure and a clear filter. ROTSE 3b is shown in Figure 3.15.

Table 3.3: Locations of the four ROTSE telescopes.

Telescope	Location	Longitude	Latitude	Altitude [m]
3a	Coonabaraban, Australia	149° 03′ 40″ E	31° 16′ 24″ S	1149
3b	Fort Davis, Texas, USA	104° 01′ 20″ W	30° 40′ 17″ N	2075
3c	Mt. Gamsberg, Namibia	16° 30′ 00 ″ E	23° 16′ 18″ S	1800
3d	Bakirlitepe, Turkey	30° 20′ 00″ E	36° 49′ 30″ N	2550

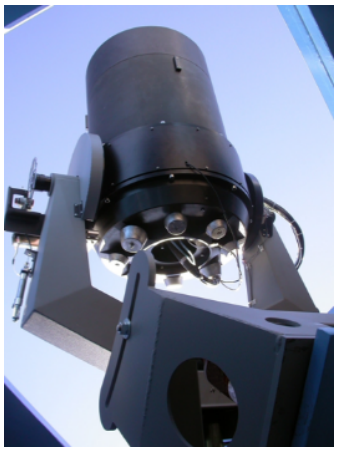

Figure 3.15: ROTSE 3b telescope located in Texas.

Zadko

Since 2013, the Zadko telescope [100] has been included in the telescope network (Figure 3.16). This is a one-meter fully robotic telescope located at the Gingin observatory in Western Australia (Table 3.2.1), covering a FoV of 23.6 arcmin × 23.6 arcmin. The Zadko telescope is equipped with an Andor CCD camera (iKon-L DW436-BV) with 2048 × 2048 13.5 μm square pixels. The mount is able to move with a maximum slew speed of 3.0° s^{-1}. With the clear filter and an exposure of 60 s, a magnitude of ∼20 can be reached. Due to the quite small FoV of the telescope, tiling has been set up in 2015 to cover the error box of an ANTARES alert. Figure 3.17 shows this tiling which consists of 7 images of 60 s exposure each, and covers ∼1°×1°.

Table 3.4: Location of the Zadko telescope.

Telescope	Location	Longitude	Latitude	Altitude [m]
Zadko	Western Australia	115° 42′ 49″ E	31° 21′ 24″ S	47

Figure 3.16: Photograph of the Zadko telescope in Australia.

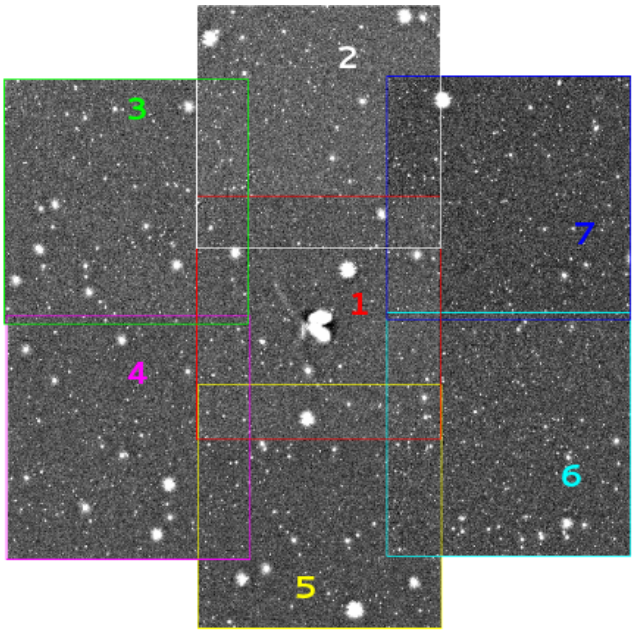

Figure 3.17: Tiled observation of a TAToO alert performed by the Zadko telescope. Images are taken from 1 to 7 with a 60 s exposure and cover a total area of $\sim 1^\circ \times 1^\circ$.

MASTER

Five MASTER (Mobile Astronomical System of TElescope Robots) wide-field optical telescopes [101], located in Russia and in South Africa (Table 3.2.1) have joined the TAToO program in 2015. Each of them consists of two 40 cm tele-

scopes, illustrated in Figure 3.18, covering a maximum FoV of 8 square degrees ($2\times(2^\circ\times2^\circ)$). This configuration allows the telescope tubes to be aligned or misaligned and makes possible synchronous photometry measurements of rapidly varying objects in standard broad-band filters (B, V, R, I). Each of the two tubes is equipped with an Apogee AltaU16 CCD camera providing 4k × 4k pixels images. The maximum positioning speed of the mount is 30° s^{-1}. A limiting magnitude of 19 can be reached with a 60 s exposure.

Table 3.5: Locations of the five MASTER telescopes used for TAToO.

Telescope	Location	Longitude	Latitude	Altitude [m]
Kislovodsk	Kislovodsk, Russia	42° 31′ 25″ E	43° 44′ 46″ N	2067
Ural	Kourovka, Russia	59° 32′ 30″ E	57° 02′ 11″ N	260
Tunka	Irkutsk, Tunka Valley, Russia	103° 04′ 02 ″ E	51° 48′ 36″ N	680
Amur	Blagoveschensk, Russia	127° 28′ 55″ E	50° 19′ 07″ N	260
SAAO	Sutherland, South Africa	20° 48′ 40″ E	32° 22′ 49″ S	1760

Figure 3.18: The MASTER Kislovodsk telescope in Russia, which consists of two wide FoV telescopes.

Swift-XRT

In June 2013, the follow-up of neutrino alerts has been extended to the X-ray domain with the arrival of the XRT telescope in the TAToO network (Figure 3.19). The XRT instrument [84], on board the *Swift* satellite, covers an energy band from 0.3 keV to 10 keV and reaches a detection sensitivity of 5×10^{-13} erg cm^{-2} s^{-1} in a 1 ks exposure. Due to the small FoV of the XRT (23.6 arcmin × 23.6 arcmin) and the typical error radius of an ANTARES alert ($\sim 0.3 - 0.4^\circ$), each observation is composed of 4 tiles up to 2 ks exposure each. This mapping covers about 72 % of the ANTARES PSF for a very high energy neutrino, as shown in Figure 3.20. Due to its low Earth orbit (96 minutes), *Swift* cannot observe an object continuously for more than 2.7 ks, thus for each neutrino trigger, the 4 observations are spread over multiple spacecraft orbits.

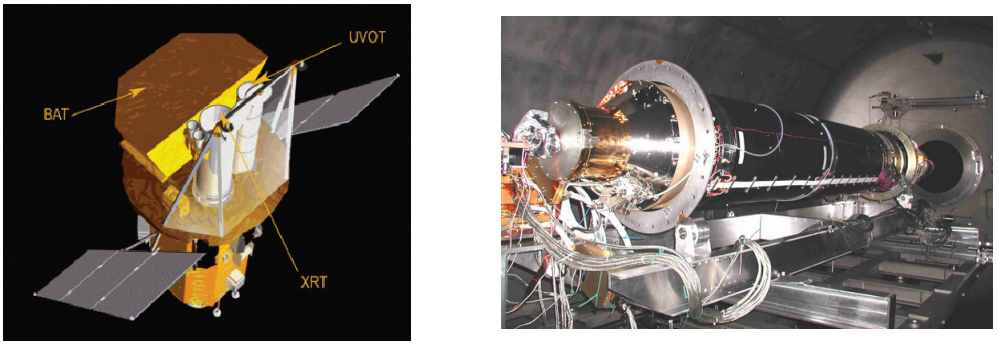

Figure 3.19: Left: picture of the *Swift* satellite with its three instruments. Right: photograph of the X-ray telescope.

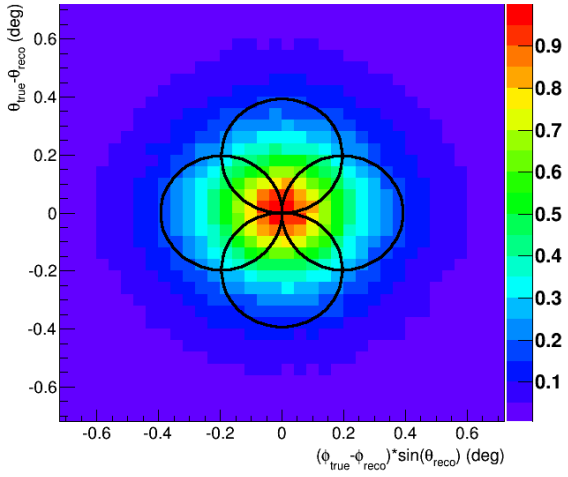

Figure 3.20: Each *Swift*-XRT observation of an ANTARES trigger consists of 4 tiles (black circles), which cover an area of radius of $\sim 0.4°$. With such a mapping, 72 % of the bi-directional uncertainty of a TAToO alert is covered.

Telescope availability

A global view of the TAToO telescope network over the last years is shown in Figure 3.21. Currently, the *Swift*-XRT, the two TAROT, the Zadko and five MASTER telescopes are composing the network. The analyses presented in the next chapters focused on images taken up to the beginning of 2015 and are thus based on TAROT and ROTSE images.

3.2.2 Observation strategy

The optical follow-up strategy is based on early and long term observations to search for rapidly and slowly varying transient sources, respectively. Once the alert is sent at time T0, optical images are collected as soon as possible by the available telescopes. The strategy of TAROT consists in taking 6 images of 180 seconds exposure at T0 and T0 + 1 hour, while for ROTSE, up to 30 images of 20 to 60 seconds exposure are taken (depending on the presence of the Moon in

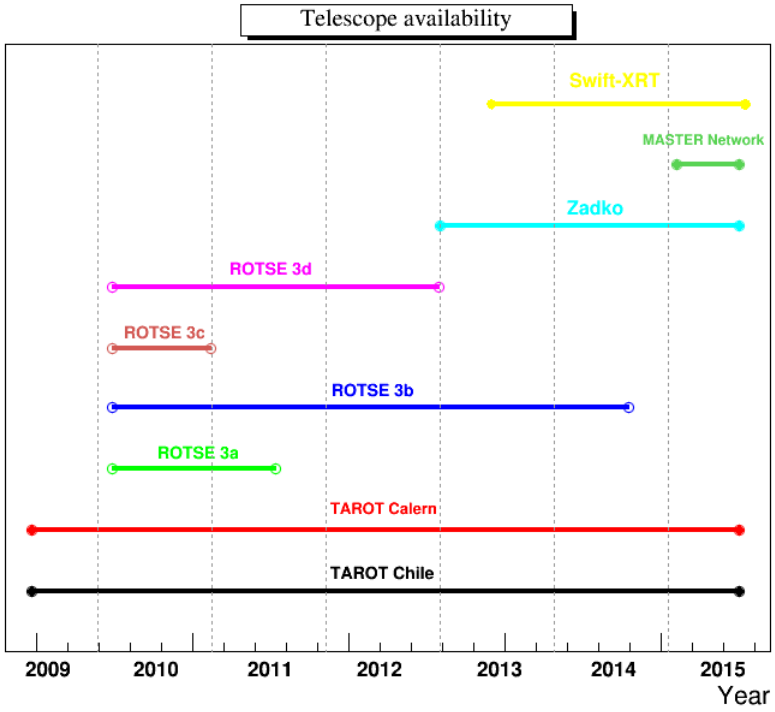

Figure 3.21: Connection of the different telescopes to the TAToO network up to 2015. Short disconnections due to technical issues are not shown.

the observed sky). For the Zadko telescope, 4 images composed of 7 tiles of 60 seconds exposure each are taken at T0 and T0 + 1 hour following the scheme depicted in Figure 3.17. After these prompt observations, the optical telescopes point into the neutrino direction up to 2 months after the alert. Long term follow-up images are taken each night during the first week and then at T0 + 9 days, T0 + 15 days, T0 + 16 days, T0 + 27 days , T0 + 28 days, T0 + 45 days, T0 + 60 days. For these delayed observations, the strategy of TAROT and Zadko remains unchanged (i.e., 6 images of 180 seconds for TAROT and 4 images of 7×60 seconds for Zadko) while for ROTSE, 8 images of 60 seconds exposure are scheduled for each night. Of course, these long term observations are performed even if the early follow-up was not possible.

Concerning X-ray follow-up by the *Swift*-XRT, observations start as soon as possible after the neutrino alert. *Swift* automatically divides the visibility window of the ANTARES trigger location in each spacecraft orbit between the 4 tiles. This is repeated on each orbit until the requested exposure time of 2 ks has been gathered for each tile. An automatic analysis of the data, described in Section 4.8, is performed soon after and in the case where an interesting candidate to be the counterpart is found, further observations are scheduled.

3.3 Status of TAToO

Online

The ANTARES telescope has detection conditions that are ever changing due to its environment. Of course, a monitoring in real time allows these conditions to be known, but an alert system such as TAToO must be adapted.

Since ANTARES is operating, more than 10 000 cosmic muon neutrino candidates have been detected. The rate of muons observed by ANTARES and reconstructed by algorithms is shown in Figure 3.22. An efficiency loss of OMs is responsible for this rate decreasing over the years. Among these events, those satisfying quality cuts described in Section 3.1.2, are kept. This corresponds to a rate of about 3 up-going neutrinos detected by ANTARES per day (Figure 3.23).

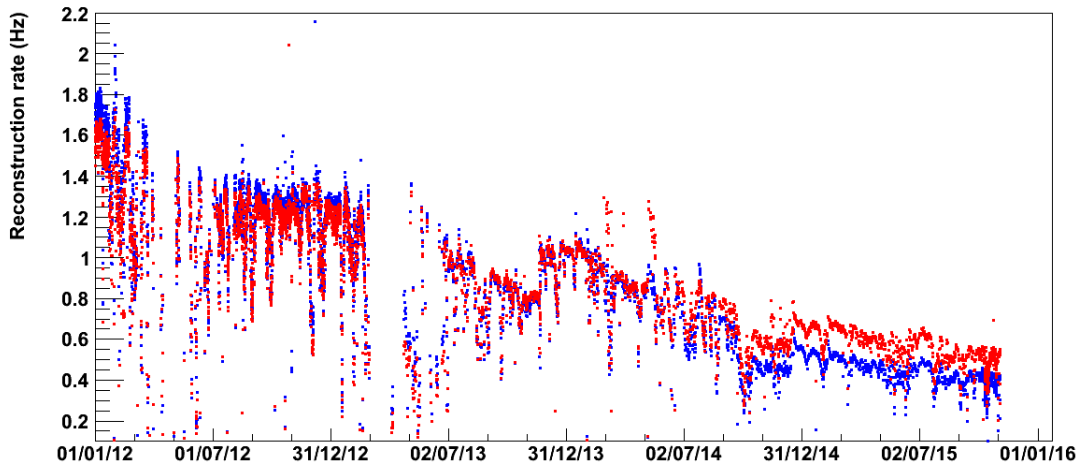

Figure 3.22: Muon rate detected by the ANTARES telescope. Blue and red points represent reconstructions of events with single and multi-lines, respectively.

Among these events, trigger criteria presented in Section 3.1.3 allows the selection of interesting candidates for which an alert is sent to the telescope network. However, due to the changing conditions of the detector, some cuts have been slightly modified during the last years to comply with the rate of alerts to send to telescopes, as illustrated in Figure 3.24.

Alert system

Since 2009, the beginning of the TAToO program, more than 160 neutrino alerts[3] have been sent to the telescope network, with about two thirds due to the high energy trigger criterion (Table 3.6). The directional trigger has been implemented in November 2011, while the very high energy trigger for *Swift* has been created in mid 2013. Among these alerts, 42 have early optical images (i.e., images taken after a delay < 24 h) and 10 alerts have been followed-up by the *Swift*-XRT.

[3] 157 alerts between October 2009 and September 2015.

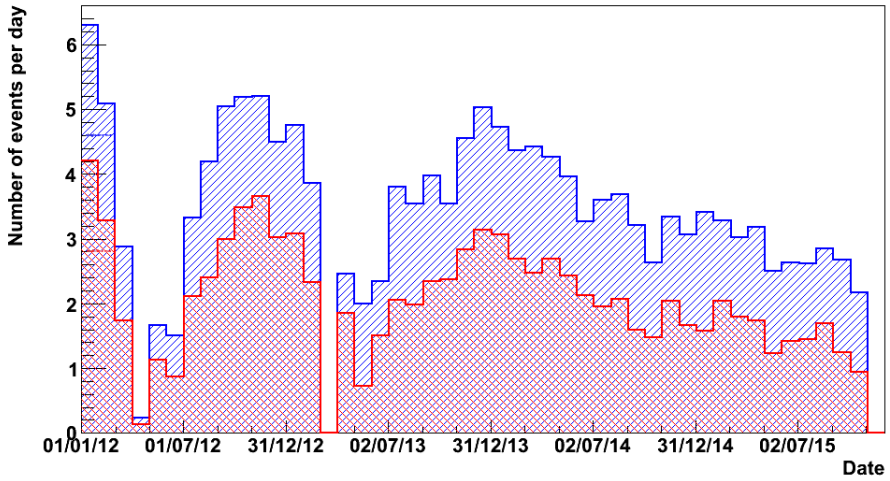

Figure 3.23: Number of up-going neutrino events detected by ANTARES per day. Events reconstructed with single and multi-lines, and multi-lines only are represented in blue and red, respectively.

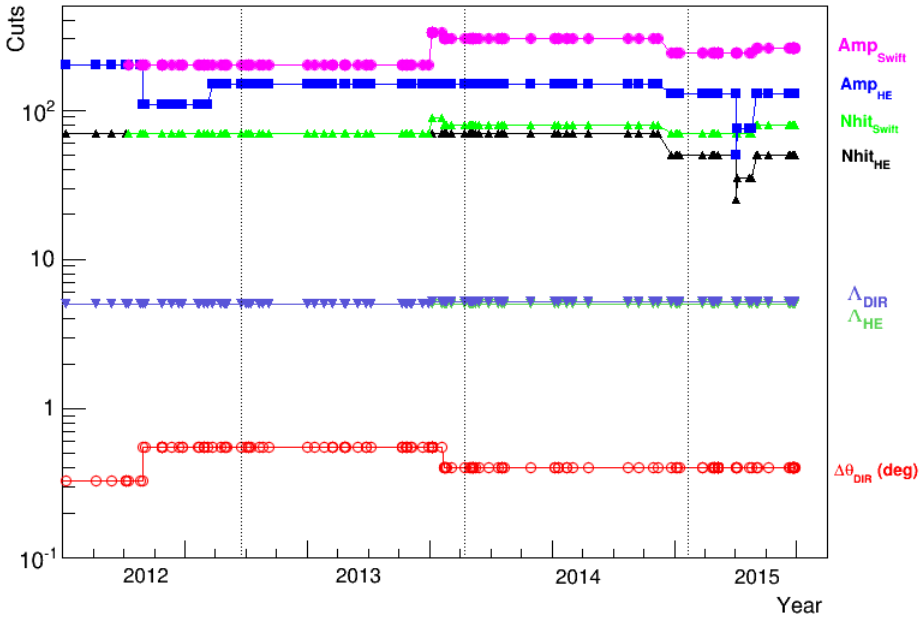

Figure 3.24: Evolution of cuts in TAToO over time. Trigger cuts not represented are constant.

For each alert, the reconstruction of the neutrino event has been performed by both the online (`BBfit`) and offline (`AAfit`) algorithms. The angular difference between the `BBfit` and `AAfit` reconstruction of the neutrino event direction is shown in Figure 3.25 for each alert. About two thirds of the neutrino events that triggered an alert have been reconstructed by the online and offline algorithms with a consistency of less than 1°.

Table 3.6: Details of the 157 alerts sent from October 2009 to September 2015. About two thirds of the alerts were due to the high energy trigger, among which 10 alerts were very energetic and sent to the *Swift*-XRT. Early and long follow-up refer to the number of alerts with good quality images, i.e., analyzable, for the two types of observation.

Year	Alerts	HE (VHE)	Dir.	Early follow-up	Long follow-up
2009	4	4	0	0	3
2010	13	13	0	4	9
2011	29	24	5	11	22
2012	22	13	9	10	17
2013	24	16 (3)	8	6	22
2014	35	19 (3)	16	10	25
2015	30	18 (4)	12	1	11
Total	**157**	**107 (10)**	**50**	**42**	**109**

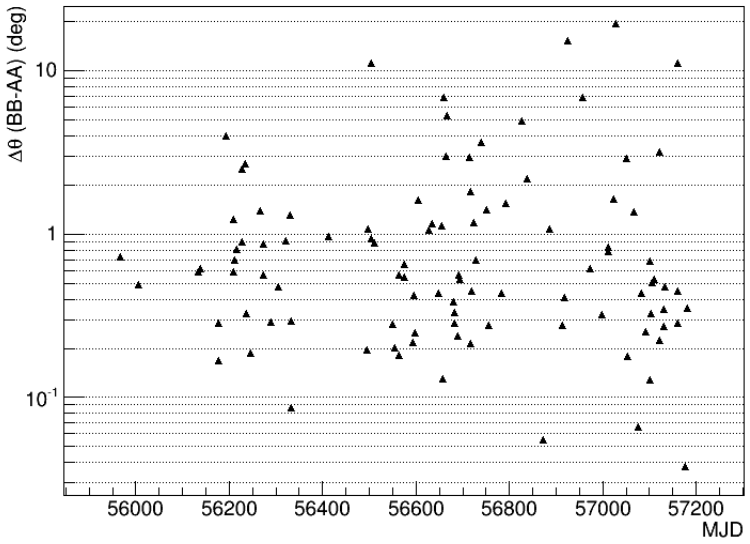

Figure 3.25: Angular difference between the `BBfit` and `AAfit` reconstruction of the neutrino event direction for each alert.

Neutrino alerts have been sent to the network of telescopes following the `AAfit` direction, and the skymap in galactic coordinates of these neutrino alerts is displayed, along with the ANTARES visibility, in Figure 3.26.

Figure 3.27 shows the latency of each neutrino trigger sent by the alert system. In 2012, a major DAQ system improvement has led TAToO to send alerts in a few seconds ($\sim 3-5$ seconds) after the detection of neutrinos.

Optical follow-up

With the rapid response of telescopes, optical images can be taken with a delay less than 20 seconds after the detection, which is well-suited for the search for rapidly decaying sources, such as GRB afterglows. The delay of the first image is displayed in Figure 3.28 for TAROT Chile, TAROT Calern and Zadko. One can

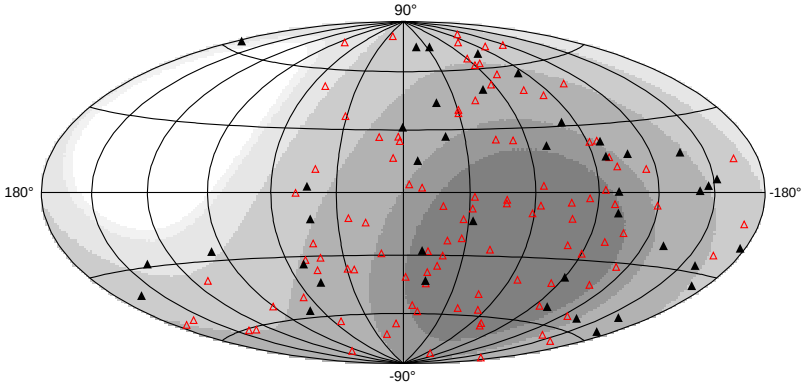

Figure 3.26: Skymap in galactic coordinates of the neutrino events that triggered the alert system. Black triangles refer to the triggers which had an early follow-up, while red triangles show the triggers with no early observation. The visibility of the ANTARES detector is represented in gray scale, with a visibility of 100 % for the darkest zone and a white region with no visibility.

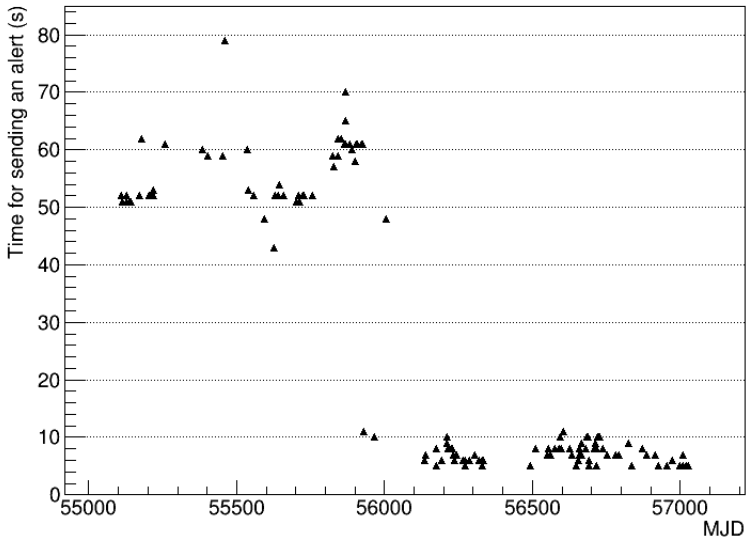

Figure 3.27: Latency of each neutrino trigger sent by the TAToO alert system between the end of 2009 and the beginning of 2015. The gap from 50 to 5 seconds corresponds to an upgrade of the ANTARES DAQ system in 2012.

notice that for most of the alerts, the first image was taken with a delay higher than 24 hours with a big gap between a few minutes to a few hours. This gap was due to an issue with the scheduler of the TAROT and Zadko telescopes and has been corrected in 2015 (see Section 3.3.1) allowing the early follow-up efficiency to be improved.

For early observations, the efficiency of an optical ground telescope depends on the object visibility (night and field elevation) and the local conditions (weather and technical problems). For example, Figure 3.29 shows that only 20 % of the

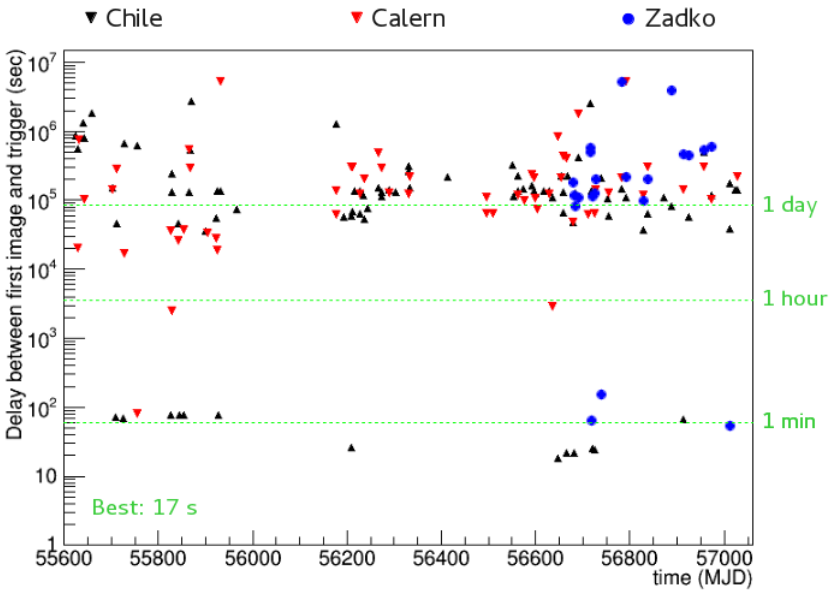

Figure 3.28: Delay of the first image taken by the TAROT and Zadko telescopes. The best response time is currently 17 seconds between the neutrino detection and the first image.

ANTARES triggers (i.e., 30 among 150) are promptly accessible from TAROT Chile. However, only 11 triggers were really observed in $\lesssim$ 1 minute by TAROT Chile (see Table 5.1), leading to an efficiency of about 30 %. The combination of visibility, weather and reliability of TAROT Chile allows the prompt observation of one trigger every 15. This proves the necessity of using a telescope network to cover an early follow-up of the ANTARES triggers, and to optimize the prompt observation strategy.

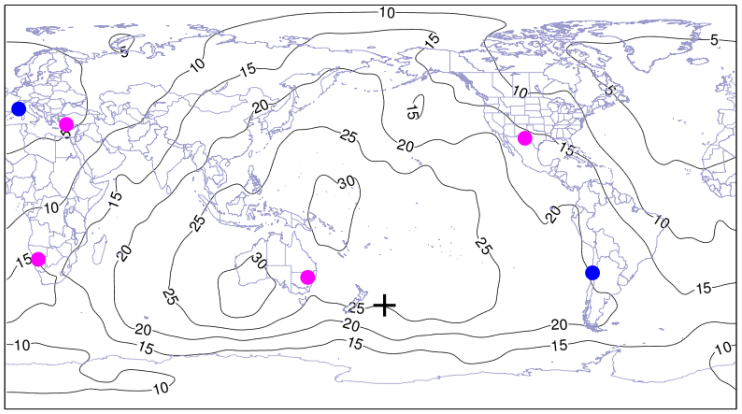

Figure 3.29: The contours of the world map indicate the percentage of neutrino triggers visible immediately (based on 140 ANTARES alerts). Blue and magenta points are the locations of the TAROT and ROTSE telescopes, respectively. The black cross indicates the antipodal point of the ANTARES experiment.

Concerning long term follow-up, the strategy chosen for the optical telescopes

provides up to 14 nights of follow-up observations, depending mainly on the efficiency of the telescopes and on the weather during observations. The response of the TAROT, Zadko and ROTSE telescopes to this strategy is shown in Figures 3.30 and 3.31 for each alert between the end of 2009 to the end of 2014.

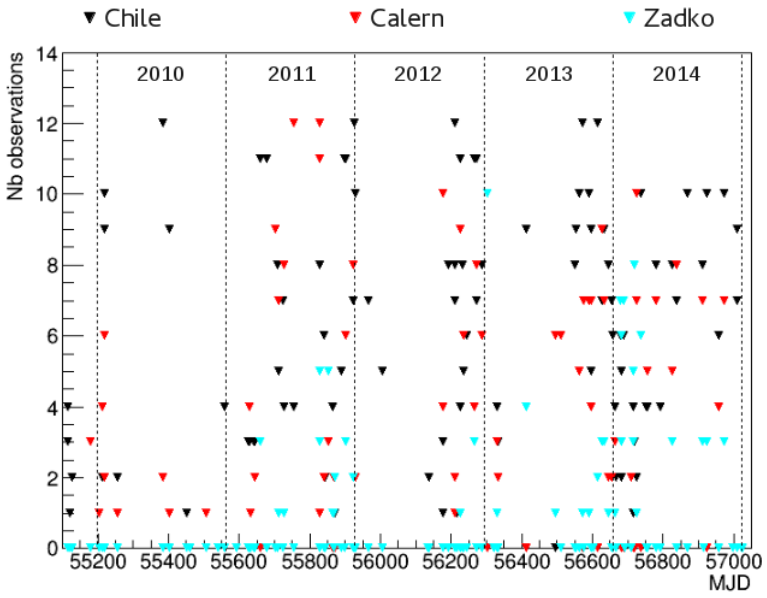

Figure 3.30: Response of TAROT Chile, TAROT Calern and Zadko up to the end of 2014. The number of observations performed for each alert between the end of 2009 to the end of 2014 is represented.

X-ray follow-up

The 10 neutrino alerts sent to the *Swift*-XRT between July 2013 and September 2015 have been observed after a mean delay of 6.3 hours after the trigger, with a best response as low as 1.1 hours for one of the alerts (Figure 3.32). For each trigger, the number of tiles as well as the exposure of each tile are represented in Figure 3.33. The request of 4 tiles with 2 ks exposure is more or less fulfilled depending on the alert. For the 10 triggers, 4 tiles with exposure varying from 0.8 ks to 1.9 ks have been observed, except for the fifth alert (ANT140311A) for which only 3 tiles have been observed probably due to the receipt of a GCN message by the satellite.

3.3.1 New early observation strategy for TAROT and Zadko

The efficiency of an early follow-up program depends mainly on the ability of telescopes to take images as soon as possible after the reception of an alert. In the case of the TAROT and Zadko telescopes, the early observation strategy was not optimized before 2015. For instance, if an alert was received during the day by the telescopes, i.e., if the field was not immediately observable, the observation at T0 was canceled by the scheduler of the telescopes and reported at T0 + 1

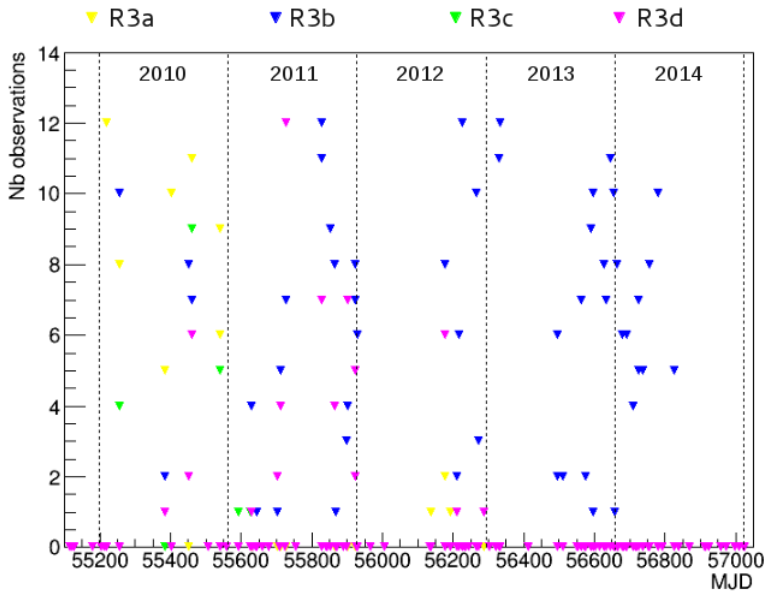

Figure 3.31: Response of the four ROTSE telescopes to the observation strategy. Y axis indicates the number of observations made according to the 14 foreseen by the strategy. ROTSE 3b in Texas was the last telescope active and connected to the TAToO network up to 2014.

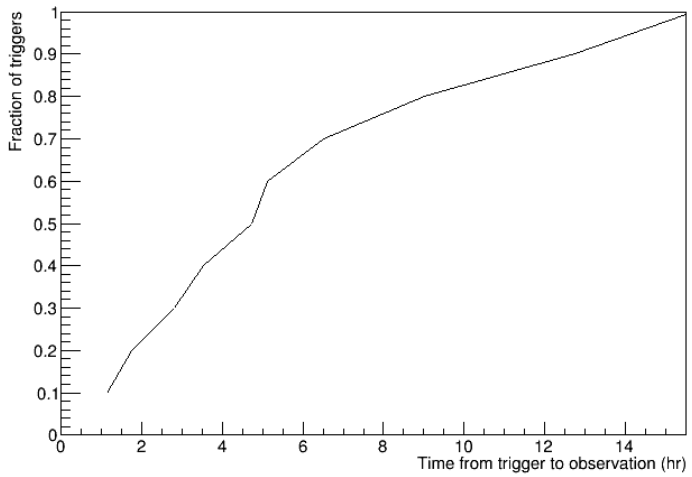

Figure 3.32: Delay of the first observation by the *Swift*-XRT for the 10 neutrino triggers.

day, even if the field would have been observable in a few minutes or hours. Since beginning of 2015, this issue, not convenient for an early follow-up program, has been corrected. When a field is not immediately visible, the time at which it will be observable is computed, knowing its elevation over time and the sky level[4]. An observation is then scheduled at this time. Figure 3.34 shows an example of

[4]The sky level is a measurement of the background light of the sky. A high sky level indicates a dark night.

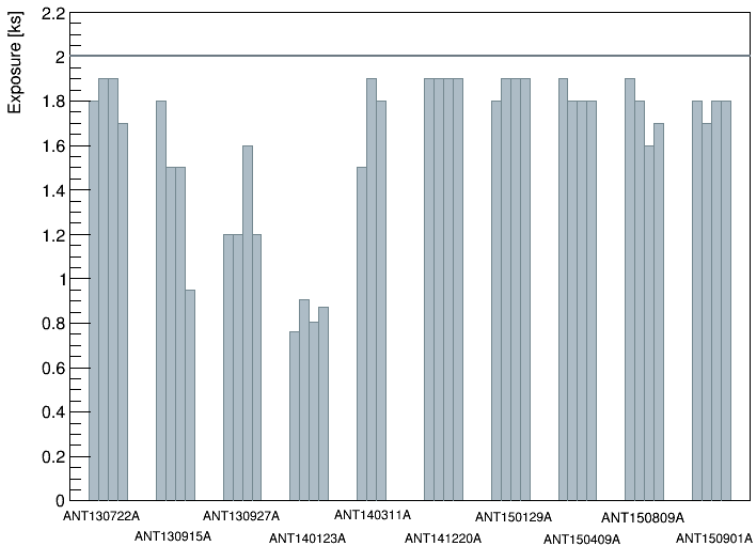

Figure 3.33: Exposure of each tile for the 10 triggers observed by the *Swift*-XRT. The horizontal line corresponds to the expected exposure of 2 ks.

the new T0 strategy for a neutrino trigger sent to the Zadko telescope.

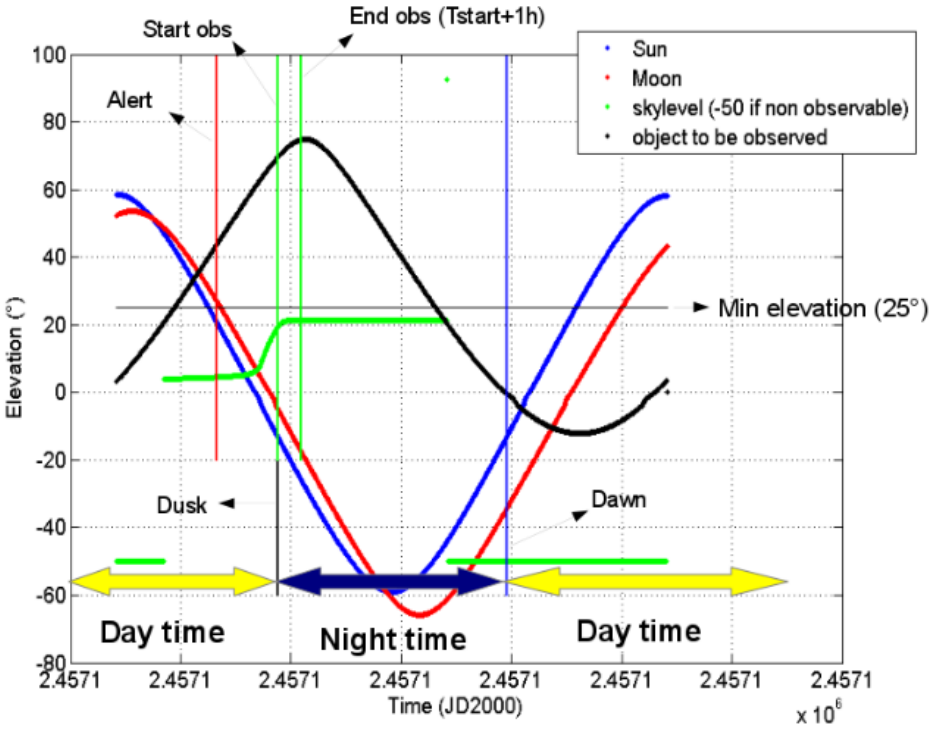

Figure 3.34: Illustration of the new T0 observation strategy for Zadko. Blue, red and black curves represent the elevation of the Sun, the Moon and the field to observe, respectively, as a function of time. The black vertical line indicates the beginning of the night (dusk), while the blue vertical line shows the end of the night (dawn). The horizontal black line indicates the minimum elevation ($\delta_{\min} = 25°$) of an object to be observed by Zadko. In this example, an alert is received by Zadko at 8:45 am (red vertical line) and is not immediately observable. With this new strategy, the observation starts as soon as the field is observable (vertical green lines) and is not anymore scheduled at T0 + 1 day.

CHAPTER 4

Image analysis

To search for optical or X-ray counterparts, images provided by follow-up observations of neutrino alerts must be processed and analyzed. Concerning the optical domain, a new automatic program based on public tools has been developed during this thesis. This program relies on an image subtraction method, which is a widely used technique in astronomy. Several optical image analysis pipelines based on this method already exist (SNLS [102], ROTSE [103]...). However, the search for transient sources with an alert system such as TAToO implies that the quality of images taken by the different telescopes can be highly variable, as illustrated in Figure 4.1. Indeed, two basic requirements for the coincident observation of a neutrino and a transient counterpart are that the telescope's FoV should be comparable to the pointing accuracy of the neutrino detector and that the telescopes should be fast pointing. The large FoV of TAROT and ROTSE telescopes ($\sim 1.9° \times 1.9°$) implies non-uniformities across the images taken by these telescopes, as shown for example in Figure 4.1 (b). Furthermore, with the TAToO alert system, the conditions of observation cannot be chosen and are thus rarely optimal. When an alert is received by the telescopes, they take images if the field is observable and if they are capable of observing (i.e., during the night without rain or high wind).

Optical image analysis pipelines developed for the processing of high quality images, such as the SNLS pipeline for images taken by the CFHT in Hawaii, are not suited for the processing of images with lower quality, highly variable depending on the observations. In addition, existing pipelines have generally been developed to process images taken by a single telescope or by similar telescopes from a network. The use of such pipelines to analyze images from other telescopes is not always efficient.

The development of a new pipeline dedicated to the analysis of images taken by the telescopes part of the TAToO network was needed[1]. The idea was to create an automatic image analysis program efficient and robust, which allows

[1]This pipeline is only used for TAROT, ROTSE and Zadko images, since the MASTER collaboration uses its own image analysis program. In addition, images provided by different telescopes are always analyzed separately.

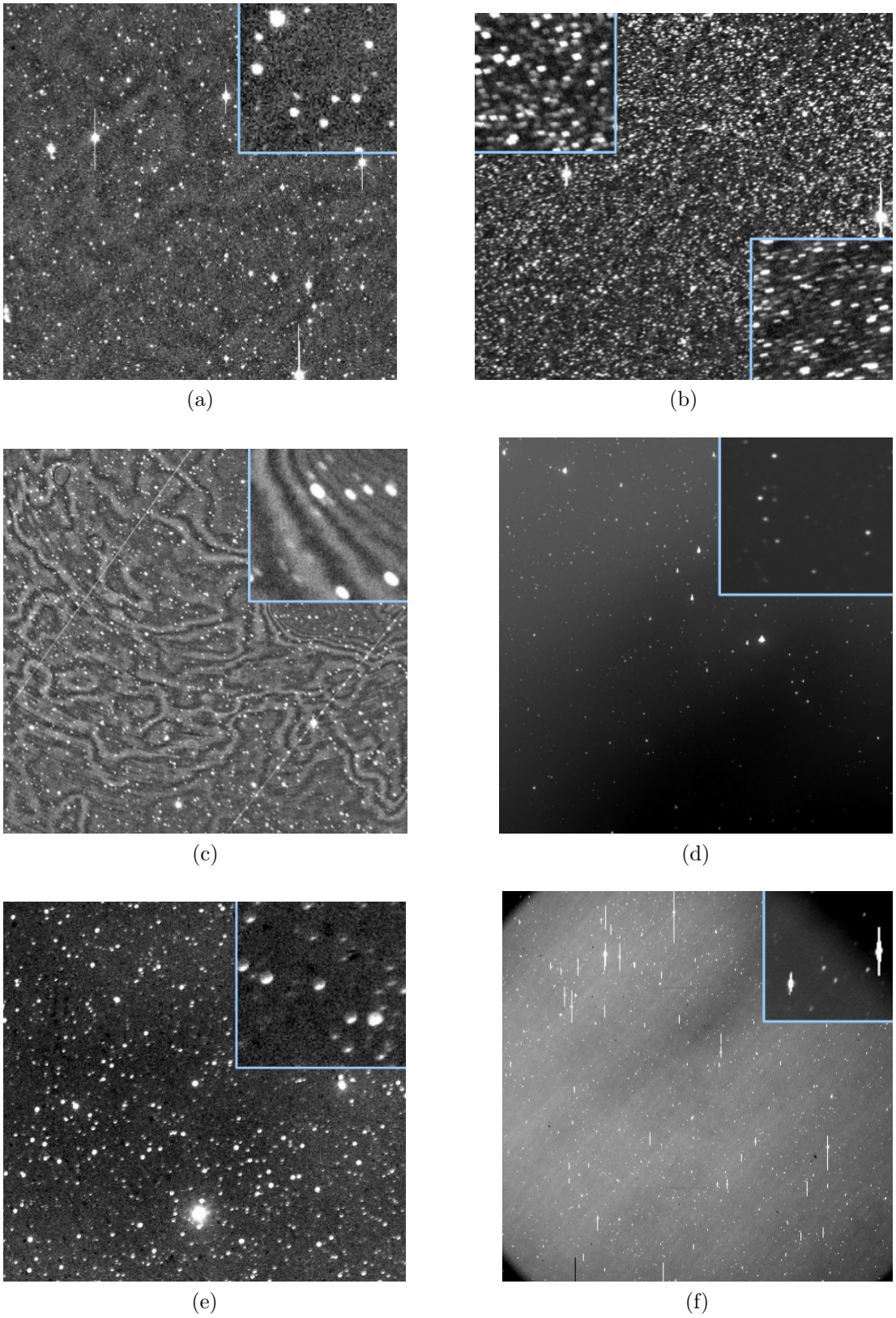

(a) (b) (c) (d) (e) (f)

Figure 4.1: Sample of TAROT (a, b, c) and ROTSE (d, e, f) images. A zoom is shown in the blue box for each image.

the processing of a large number of images with different qualities, and to obtain consistent results. The program is based on public tools, such as SExtractor [104], SCAMP [105] and SWarp [106], and a lot of effort was made in this thesis on the optimization of their parameters to obtain a successful program.

The main steps of the pipeline are shown in Figure 4.2. As the images are taken with Charged Coupled Devices (CCDs), a preprocessing is directly made on the site of telescopes. Images are then downloaded in FITS format (Flexible Image Transport System) and pass through the different calibration and analysis steps of the pipeline. Human scanning of selected candidates is then required for transient identification.

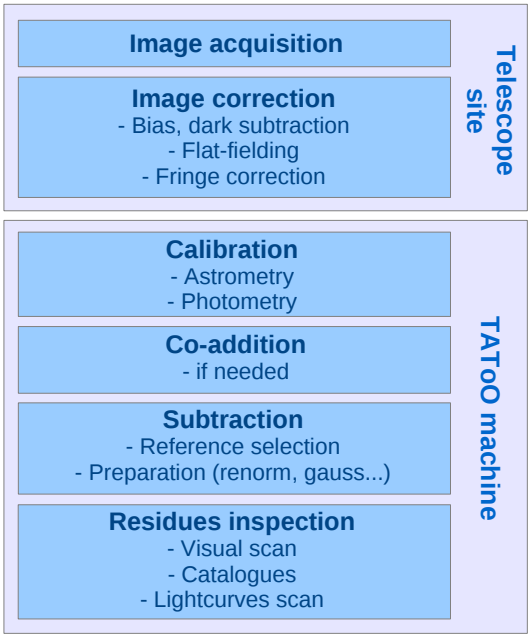

Figure 4.2: Structure of the image analysis pipeline developed for transient source search.

Concerning follow-up observations performed by *Swift*, X-ray data are automatically analyzed at the UK Swift Science Data Centre. Source detection algorithms are applied to each 4-tile observation, and different tests are carried out on each uncataloged X-ray source to determine if it could be the counterpart to the ANTARES trigger.

In this chapter, the various steps of the optical image analysis program that has been developed during this thesis, as well as the selection and identification of transient candidates, are presented. The last part of this chapter describes the analysis of X-ray data automatically performed with dedicated pipelines.

4.1 Preprocessing of CCD images

The first step of CCD image processing is to remove any effects that are due to the nature of the detector: the "instrumental signature". Raw images must be

corrected for a number of artifacts. Each image is dark and flat field corrected, and can also be subtracted by a fringe map as described below. After these corrections, pixel values are directly related to the number of photons detected in each CCD pixel.

Dark field

A dark field is a measure of the dark current in the CCD at a specific temperature for a specific exposure time. It is obtained by taking an image with the same exposure length than the raw image, in total darkness (i.e., with the shutter closed). Dark images are subtracted pixel by pixel from image frames to remove the bias level, the dark level, and to subtract hot pixels. The bias level is an electronic offset which ensures that the Analogue-to-Digital Converter (ADC) always receives a positive signal. The ADC is responsible for converting the signal representing the amount of charge accumulated in a CCD pixel to a digital value. The dark level is an electron count that accumulates in each pixel due to thermal noise. Usually, one dark run per night is performed. An example of dark field taken by TAROT Chile is shown in Figure 4.3.

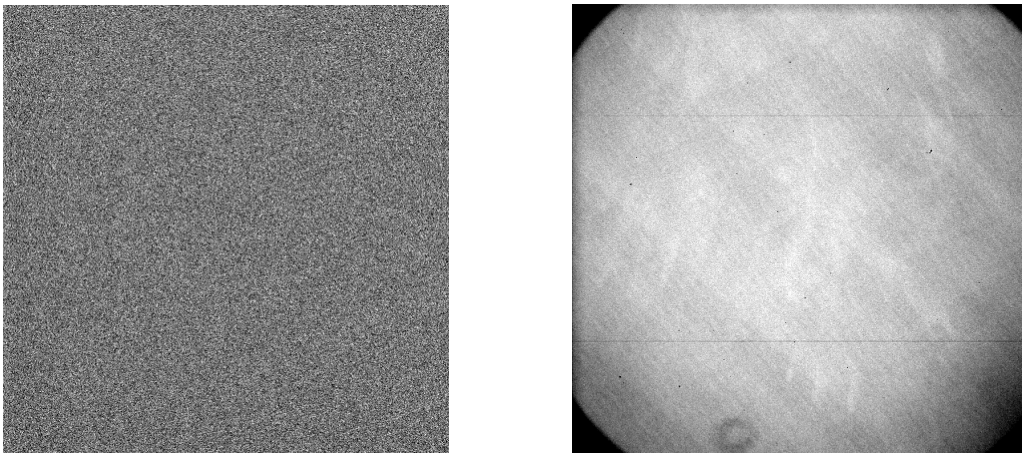

Figure 4.3: Dark (left) and flat (right) fields taken by TAROT Chile.

Flat field

The sensitivity of CCDs varies from point to point: the recorded signal per unit of incident photons is not uniform across the CCD. The goal of the flat field correction is to remove the effect of the pixel-to-pixel sensitivity variations, as well as the effect of dust or scratches on the CCD window. A flat field is obtained by uniformly illuminating the CCD (typically, during twilight). Images, previously corrected for bias and dark levels, are divided by the flat. A twilight flat field taken by TAROT Chile is displayed in Figure 4.3.

Fringe map

In addition to a standard preprocessing (bias, dark current and flat field), ROTSE images are corrected for fringing[2]. Interference fringes appear when light of a certain wavelength is reflected on thin CCD layers and interferes with itself. The fringe pattern is consistent from image to image, although the amplitude varies. The fringe correction consists of scaling and removing the fringe pattern from images. A fringe map is obtained by subtracting a twilight flat from a sky flat. Most of the night sky brightness is contained in emission lines, which can create strong fringe pattern. In contrast, a twilight flat does not display a fringe pattern because of the broadband light from the Sun. Once the fringe pattern is scaled, it is subtracted from the images. A fringe map used to correct ROTSE 3b images is shown in Figure 4.4.

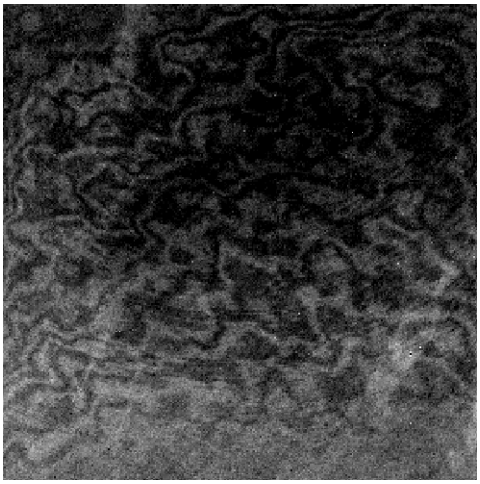

Figure 4.4: Fringe map used to correct ROTSE 3b images.

Once these corrections are performed on the telescope sites, images are downloaded locally, and the analysis can start with the dedicated pipeline.

4.2 Image subtraction method

A source can be identified as transient if its flux varies during the observation period. The principle of the image subtraction method is to observe this flux variation by subtracting images taken at different times, as illustrated in Figure 4.5. The subtraction of a reference image (REF), in which no or less signal is expected, from an image (IM) that could contain the optical transient counterpart to the neutrino trigger, would reveal this source in the subtracted image (SUB). Further analyses, such as the inspection of the source light curve and the cross-match with catalogs, would allow its identification. However, several steps are required

[2]TAROT images are not corrected for fringing, as a perfect subtraction of this effect is difficult and as the pattern will not significantly affect the rest of the calibration.

to perform good subtractions, and to obtain correct information about transient candidates.

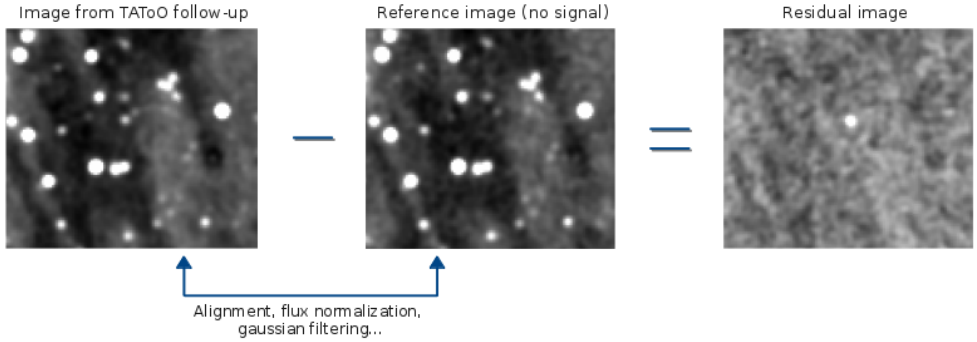

Figure 4.5: Image analysis based on the subtraction method.

4.3 Source extraction with SExtractor

The extraction of meaningful information from images is one of the key point of image analysis, and is performed with SExtractor (Source Extractor) [104]. This is a program that extracts sources from an astronomical image and builds a catalog. Its main features are:

- Background estimation and subtraction
- Extraction: thresholding and deblending
- Photometry
- Weighting

To be run properly, SExtractor needs two files: a configuration file which allows the user to choose the extraction conditions by setting configuration parameters, and a parameter file to obtain a flexible output catalog of desired parameters only.

4.3.1 Background estimation and subtraction

In images, the value measured at each pixel is a function of the sum of a background and a signal light coming from the objects of interest. To measure accurately the flux of these objects, one needs to have a good estimation of the background level in any place of the image. For this, SExtractor builds a background map by computing an estimate of the background in each mesh of a grid that covers the whole frame.

A mesh size can be set in the configuration file of SExtractor via the `BACK_SIZE` parameter. Obviously, the choice of the mesh size is very important, too small and the background estimate will be dominated by the object flux, too large and

small scale variations cannot be taken into account. As TAROT and ROTSE images consist of 2048 × 2048 pixels, a `BACK_SIZE` of 256 pixels has been chosen, corresponding to a grid of 8 × 8 meshes.

In each mesh, the mean and the standard deviation σ of the distribution of pixel values are computed. The most deviant values are discarded and, mean and σ are computed again. The background histogram is clipped, in this way, until convergence at $\pm$ 3 σ around its median. If σ changed by less than 20 % per iteration, the field is considered as not crowded[3] and the mean of the clipped histogram is simply taken as a value for the background. Otherwise, this value is estimated with: $2.5 \times \text{median} - 1.5 \times \text{mean}$. With the background values obtained for each mesh of the whole frame, a background map is built, and automatically subtracted from the image.

4.3.2 Extraction: thresholding and deblending

Thresholding is applied to a background-subtracted image to isolate groups of adjacent pixels. SExtractor considers each pixel above a certain threshold to be part of an object. The thresholding is mostly controlled by two parameters in the configuration file: `DETECT_THRESH` and `DETECT_MINAREA`.

- `DETECT_THRESH` sets the threshold value in units of the background's standard deviation. Depending on the sources (bright or faint) we want to extract, different threshold values are chosen throughout the pipeline. For instance, to extract all the sources of an image, a threshold of 2 σ is applied, while to extract bright stars a threshold value up to a few tens of σ is chosen.

- `DETECT_MINAREA` sets the minimum number of adjacent pixels above the threshold to trigger a detection. This value is set at 5 pixels for both TAROT and ROTSE images. It allows faulty pixels and cosmic ray hits to be discarded.

With only these two parameters, a single detection may include more than one celestial object. So, each time an object detection is completed, the group of pixels passes through a sort of filter that tries to split it into eventual overlapping component. This operation is called deblending and is useful in case of crowded fields. A simplified example of the deblending process is illustrated in Figure 4.6. To determine if a detected cluster of pixels corresponds to one or several objects, the threshold is lowered from the maximal pixel value in 32 exponential steps, and each time the cluster identification is repeated. If more than one cluster is found with a number of counts greater than a fraction δ_c of the total counts of the initial cluster ($\delta_c = 0.005$ for TAROT and ROTSE), they are considered as two objects.

[3]Typically, a TAROT or ROTSE field is considered as crowded if more than a few tens of thousands of stars are extracted. This is the case for images taken towards the galactic plane.

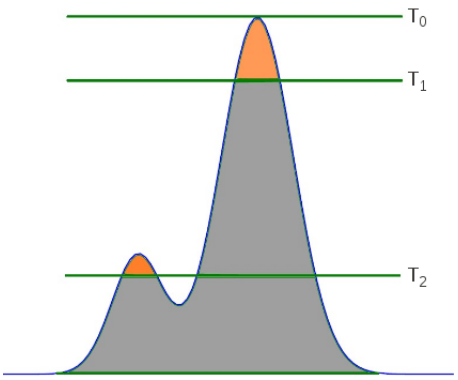

Figure 4.6: Deblending: The detection threshold is lowered from the maximum pixel value T_0 of a cluster in exponential steps. Two steps are illustrated here. In the first step, the threshold is lowered from T_0 to T_1. One cluster of pixels is found. If the orange area is larger than a certain fraction δ_c of the total area, it is considered as an object. The threshold is then lowered further to T_2. An additional cluster is found, and again is considered as a separate object if the orange area is larger than δ_c.

4.3.3 Photometry with SExtractor

Measuring the total flux of light collected from a source is of fundamental importance for CCD image processing in astronomy. Such measurements are made by counting the number of electrons released by the incident photons. A pixel value (in units of "counts" or "ADU" for Analog to Digital Units) is equal to the number of electrons detected in that pixel, divided by the gain G of the CCD, where G is in units of electrons/ADU. For TAROT and ROTSE CCDs, $G = 2.8$ electrons/ADU.

To complete the extraction, SExtractor performs photometry and has currently the possibility to compute different types of magnitude. We chose to work with automatic aperture magnitudes (`MAG_AUTO`) which are intended to give the most precise estimate.

Aperture photometry, illustrated in Figure 4.7, consists in measuring the flux of an object without including possible contributions from the background or from nearby sources. For this, the flux of each pixel inside an aperture centered on the object is added to give the total flux from the object, and the flux from the background sky is subtracted. However, the precision of the global background computed earlier by SExtractor (Section 4.3.1) may not be sufficient for a photometry measurement. Hence, SExtractor recomputes the background locally in a "rectangular annulus" centered on each object.

The size of the aperture is very important for photometry measurements: too small involves a loss of flux from the object, while too large involves a large error estimate. With the automatic aperture photometry of SExtractor, inspired by Kron's "first moment" algorithm [107], a flexible elliptical aperture is used. First, an elliptical aperture, with eccentricity ϵ, is defined by second order moments of the object's light distribution. Then, the "first moment" is computed within this

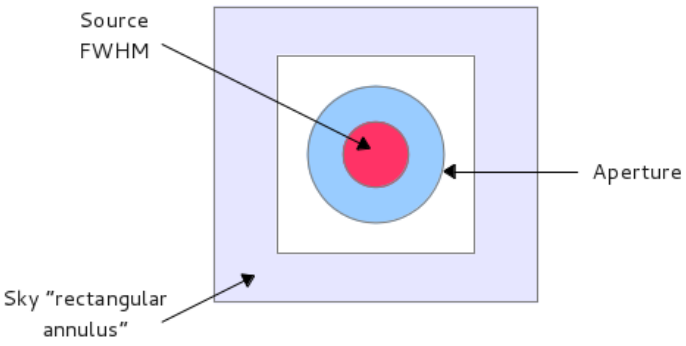

Figure 4.7: Principle of the aperture photometry. For each detected object, the flux inside an aperture centered on the object and slightly larger than the full width at half maximum (FWHM) of the object, is measured. A similar measurement is made in a "rectangular annulus" outside this aperture to estimate the flux from the background sky.

aperture:

$$R_k = \frac{\sum RI(R)}{\sum I(R)} \tag{4.1}$$

where R_k is the Kron radius and $I(R)$ the total flux in a radius R. For TAROT and ROTSE images, the typical Kron radius varies from 2 to 7 pixels. More than 90 % of the object flux should be contained in an elliptical aperture with $\epsilon k R_k$ and kR_k/ϵ as principal axes, where k is the Kron factor set by default at 2.5, which corresponds to the number of Kron radii the aperture is set at.

The flux of each source is then converted to the so-called instrumental magnitude using the formula:

$$m_{\text{inst}} = -2.5 \log_{10}(f) + m_0 \tag{4.2}$$

where $f = N_{\text{counts}}/t_{\text{exp}}$ is the flux in ADU/s, with N_{counts} the total number of counts from the source and t_{exp} the exposure time of the image in seconds. m_0 is an arbitrary constant defined as the zero point magnitude. Any value can be chosen as long as it is used consistently for calculating all the instrumental magnitudes. For TAROT images, $m_0 = 26$, while for ROTSE images $m_0 = 24$. A zero point offset will then be applied to the m_0 constant to convert instrumental magnitudes to calibrated magnitudes (see Section 4.4.2).

Errors on magnitude

An estimate of the magnitude error is provided for each extracted source and is computed through:

$$\Delta m = 1.0857 \frac{\sqrt{A\sigma^2 + \frac{F}{G}}}{F} \tag{4.3}$$

where A is the area (in pixels) over which the total flux F (in ADU) is summed, σ is the standard deviation of noise (in ADU) estimated from the background, and G is the detector gain (in e^-/ADU).

4.3.4 Weighting

During the extraction, relative importance can be given to individual pixels by using a weight for each of them. In this way, bad pixels can be discarded. Bad pixels are defined as pixels which do not behave in the same manner as the average of CCD pixels. They are not representative of the flux of the object and have to be ignored. SExtractor accepts in input weight maps listing all the bad pixels of a CCD.

A flat field image is generally a good approximation of a perfect bad pixel map, as it is created to measure the pixel-to-pixel sensitivity variations. From a flat field, a weight can be attributed to each pixel of an image: 1 for a good pixel and 0 for a bad one. Only pixels with a weight of 1 are then considered by SExtractor. Of course, each CCD has its own bad pixels. A specific bad pixel map is thus used for each image coming from the different telescopes[4]. Figure 4.8 shows the bad pixel maps used for TAROT Chile and ROTSE 3b images. While only a few bad pixels and a dead column appear on the weight map of TAROT Chile, a lot of ROTSE 3b pixels are faulty.

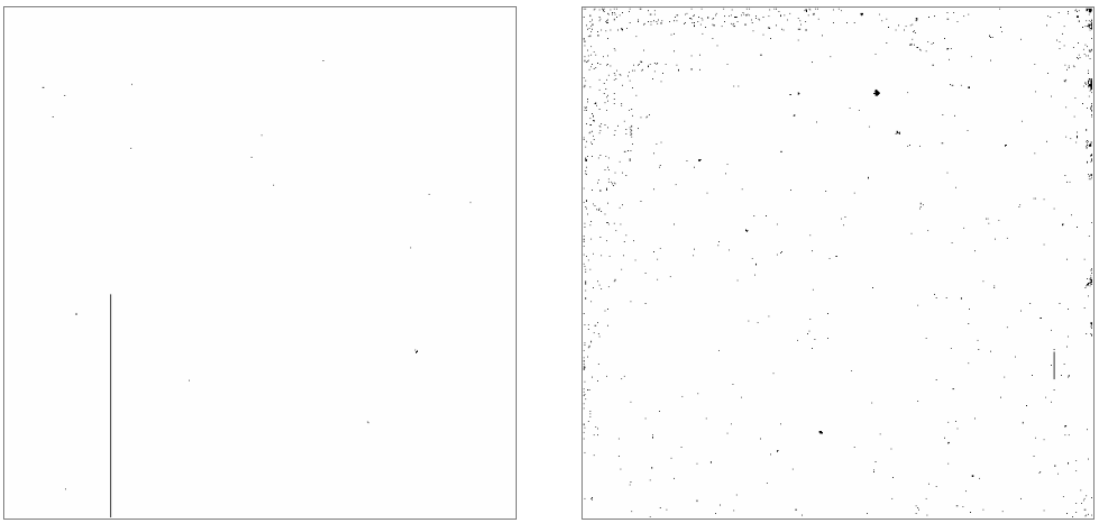

Figure 4.8: Bad pixel maps for TAROT Chile (left) and ROTSE 3b (right) obtained from flat field images.

[4]No bad pixel map is used for TAROT Calern images, since only few pixels are bad.

4.4 Calibration

4.4.1 Astrometry

One of the key of the image subtraction method is to calibrate and align all the images taken for an alert on a same grid. The astrometric calibration, which consists in converting the pixel positions (x,y) in (RA,dec) coordinates according to the World Coordinate System (WCS) standard[5], and the alignment of images are performed by SCAMP (Software for Calibrating AstroMetry and Photometry) [105]. To avoid a misalignment, we choose to perform a relative astrometric calibration. It means that all the images taken for a neutrino alert (up to 14 observation nights) are aligned on the first image of the first observation, which serves as astrometric reference. If the quality of this image is not sufficient to provide an accurate calibration, the second image is used, and so on.

SCAMP is a tool specially created to read SExtractor output catalogs and compute astrometric solutions. The catalog generated by SExtractor after the source extraction of an image must contain a copy of the original FITS image header. This header provides fundamental information such as frame dimensions, WCS data and many other FITS keywords that SCAMP will use to derive a full astrometric calibration. A non-exhaustive list of these image header keywords with arbitrary values is shown in Table 4.4.1. In addition to this header, the output catalog of SExtractor must contain several parameter values for each extracted source in the image, like the centroid coordinates `XWIN_IMAGE` and `YWIN_IMAGE` in pixel units and the centroid errors `ERRAWIN_IMAGE`, `ERRBWIN_IMAGE` and `ERRTHETAWIN_IMAGE`.

SExtractor is first applied on the first image. A copy of the header of this image, as well as the coordinates in pixels of each extracted source constitute the reference catalog. This tool is then used for each image taken during the follow-up of a neutrino trigger. By using a fast cross-matching between these output catalogs and the reference catalog, SCAMP automatically determines the pixel scale, the position angle, the flipping and the coordinate shift of each image compared to the first one. The tolerance radius for the matching is set at 4". New FITS header keywords containing updated astrometric information for each image are finally generated. These keywords are written into external header files, with the .head filename extension.

Additional astrometric corrections

In the case of TAROT Chile images, an additional astrometric correction may be necessary. It appears that some images taken by this telescope are shifted in coordinates due to encoder issues, as shown in Figure 4.9. These shifts are from a few arcseconds to several arcminutes and can vary from one night to another one. SCAMP cannot deal with such defaults and a correction must be applied before to use it.

[5]The FITS WCS standard defines keywords and usage that provides for the description of astronomical coordinate systems in a FITS image header.

Table 4.1: Non-exhaustive list of FITS image header keywords with arbitrary values.

SIMPLE	T	/ File does conform to FITS standard
BITPIX	16	/ Number of bits per data pixel
NAXIS	2	/ Number of data axes
NAXIS1	2048	/ Length of data axis 1
NAXIS2	2048	/ Length of data axis 2
EQUINOX	2000.	/ System of equatorial coordinates
RADECSYS	FK5	/ Mean Place IAU 1984 system
CTYPE1	RA-TAN	/ Gnomonic projection
CUNIT1	deg	/ Angles are degrees always
CRVAL1	105.95500718	/ [degree] Reference coordinate for naxis1
CRPIX1	1024.	/ [pixel] Reference pixel for naxis1
CD1_1	-0.00091090	/ [deg/pixel] Coord. transf. matrix
CD1_2	0.	/ [deg/pixel] Coord. transf. matrix
CTYPE2	DEC-TAN	/ Gnomonic projection
CUNIT2	deg	/ Angles are degrees always
CRVAL2	-4.73037172	/ [degree] Reference coordinate for naxis2
CRPIX2	1024.	/ [pixel] Reference pixel for naxis2
CD2_1	0.	/ [deg/pixel] Coord. transf. matrix
CD2_2	0.00091090	/ [deg/pixel] Coord. transf. matrix

The astrometric pipeline *astrometry.net* [108] is a reliable and robust system that takes as input an astronomical image and computes an astrometric calibration using the information in the image pixels alone. In this way, the pipeline can solve the "lost in space" problem in which nothing (even the image scale) is known.
The method used is based on a pattern recognition procedure. After a robust source detection in the input image, groups of four or five stars (asterisms) are geometrically hashed and compared with pre-computed index files of known asterisms. These index files are built from reference catalogs of stars such as USNO-B1 [109] or 2MASS [110].

Once a field is solved, a FITS WCS header for the solution and a new FITS file containing the WCS header are created. As more than 35 % of TAROT Chile images are affected by these coordinate shifts and as images from TAROT Calern and TAROT Chile are calibrated together, all TAROT images automatically pass through the *astrometry.net* pipeline before any processing. Corrected images are then renamed with the suffix _corr.fits.

4.4.2 Photometry

The instrumental magnitude of each source computed by SExtractor (see Section 4.3.3) depends on the characteristics of the instrument used to obtain the data. The principle of photometric calibration is to convert the instrumental magnitude of an object, m_{inst}, to a magnitude m tied to a photometric system. This conversion is made by determining the zero point offset (m_{offset}) to apply to the

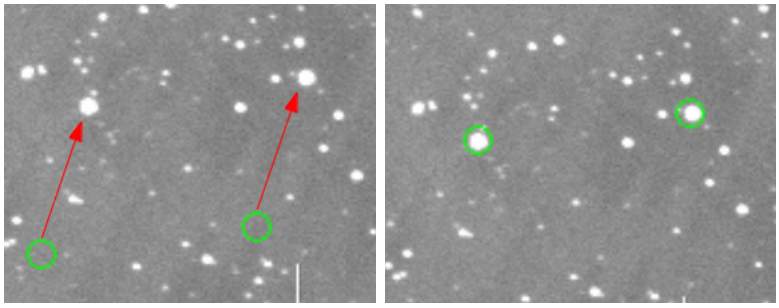

Figure 4.9: Coordinates of TAROT Chile images can be shifted (left) from few a arcseconds to several arcminutes according to reference catalogs, such as USNO-B1 (green circle). The pipeline *astrometry.net* is used to correct these shifts and to create a new FITS image containing the WCS header for the solution (right).

arbitrary zero point magnitude m_0 first used in SExtractor for each image. The zero point magnitude, $m_{\mathrm{ZP}} = m_0 + m_{\mathrm{offset}}$, is defined as the magnitude of an object that produces one count per second. The connection between m_{inst} and m is done as follows:

$$m = m_{\mathrm{inst}} + m_{\mathrm{offset}} \tag{4.4}$$

with m_0 already included in m_{inst} as shown in Equation 4.2.

A way to determine the zero point offset value is to compare instrumental magnitudes with existing catalog values. The differences give the correction to apply to instrumental magnitudes. However, each star has a different magnitude depending on the band in which we observe. As all of our images are taken with the clear filter (C), the measured magnitudes do not correspond to a specific band, such as expressed by catalogs. A photometric calibration in the CCD response band must therefore be carried out.

LePHARE [111] is a set of programs used to compute theoretical magnitudes in different bands. By knowing the CCD and different filter response curves, LePHARE creates a magnitude template for this set of bands from a list of spectral energy distribution (SED) files. A χ^2 fitting analysis is then performed between the template and the observed magnitudes, allowing m_{offset} to be derived.

A preliminary phase to select the SED models, the set of filters and to compute the template magnitudes is done with three programs:

- ***sedtolib***: the program *sedtolib* is used to build a stellar library from a list of SED files. The goal of this program is to generate from different SEDs a unique binary file that can be easily read in the next steps. A list containing 131 stellar SEDs from Pickles [112] is provided with the program and written in ASCII with the following format (λ(Å), flux (erg/s/Å/cm^2)).

- ***filter***: the program *filter* puts together a list of filter response curves defining in which bands the theoretical magnitudes will be computed. A predefined set of filters is available with the program among which we choose the B, V, R, J, H and K filters[6]. To this list, we add the CCD response curves

[6]B and R filters are from Bessel (1990) [113], V is from Azusienis & Straizys (1969) [114] and J, H and K are from 2MASS [110].

of the TAROT and ROTSE telescopes, which show a maximum efficiency centered on 600 nm (between V and R bands). The response curve of the CCD of TAROT is illustrated in Figure 4.10.

- ***mag_star***: the program *mag_star* is used to derive magnitudes for the star sample. It reads the filter information and the stellar library, and compute theoretical magnitudes.

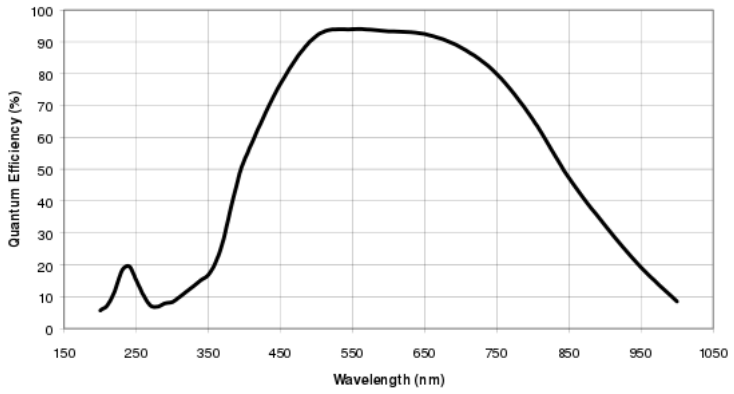

Figure 4.10: Response curve of the CCD (Andor DW436) of TAROT. The maximum efficiency is between 500 to 680 nm.

The program *zphota* from LePHARE is then used to perform a χ^2 fitting between this template and the observed magnitudes. The most important input of this program is the catalog containing the observed magnitudes (photometric catalog). It is obtained by extracting bright sources from an image with the corresponding arbitrary zero point value (i.e., $m_0 = 26$ for TAROT images and $m_0 = 24$ for ROTSE images). A detection threshold set at 60 σ is applied in SExtractor to extract a minimum of 30 bright stars. If this condition is not fulfilled, the initial threshold is progressively lowered to 7.5 σ. An example of bright stars extracted with a threshold of 60 σ from a TAROT Calern image is illustrated in Figure 4.11. The output catalog of SExtractor containing instrumental magnitudes is then cross-matched with the NOMAD catalog [115] to obtain the magnitude of each associated source in the B, V, R, J, H and K bands.

To create the photometric catalog, we only select objects with a known magnitude in each of the 6 bands, and we add in another column the instrumental magnitudes computed by SExtractor, which represent the CCD band. The list of these bands must be in the same order than in the input list of the *filter* program. In addition to these magnitudes, the input catalog of *zphota* must contain the associated uncertainties. For magnitudes from NOMAD, we set the errors at 0.1 magnitude, as the catalog does not provide this information, and for magnitudes in the CCD band, we take the errors computed by SExtractor.

Finally, to complete the photometric catalog, we add in a last column the context, which is an integer value specifying the filter combination to be used for the χ^2 fitting. It is defined as the sum of powers of 2: $\sum_{i=1}^{i=N} 2^{i-1}$, where i is the filter number as ordered in the photometric catalog and N is the total number

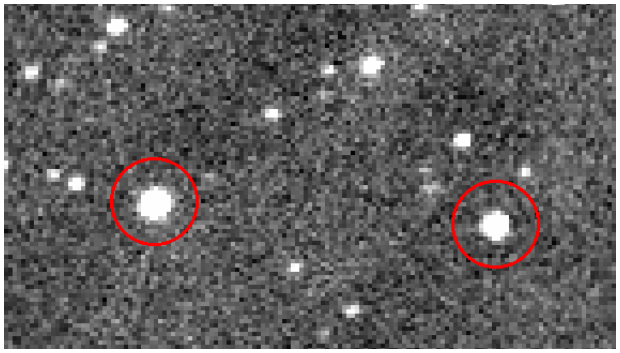

Figure 4.11: Example of two bright stars (circled in red) extracted from a TAROT Calern image with a detection threshold at 60 σ. Other stars are not extracted with such a threshold.

of filters. As we do not want to bias the fitting by the arbitrary magnitudes of SExtractor, the context is set at a value of 63 to only take into account the 6 first filters.

The χ^2 fitting procedure of *zphota* between the observed fluxes[7] ($F_{\rm obs}$) and their corresponding uncertainties (σ) from the photometric catalog, and the flux from the templates ($F_{\rm temp}$) is defined as follows:

$$\chi^2 = \sum_i [\frac{F_{{\rm obs},i} - sF_{{\rm temp},i}}{\sigma_i}]^2 \tag{4.5}$$

where i refers to the band used for the analysis and s is the scaling factor chosen to minimize the χ^2 values:

$$s = \sum_j [\frac{F_{{\rm obs},j} F_{{\rm temp},j}}{\sigma_j^2}] / \sum_j [\frac{F_{{\rm temp},j}^2}{\sigma_j^2}] \tag{4.6}$$

where j refers to the band used for the scaling (j can be different from i). The result of the fitting is reported in an output catalog and can be illustrated by a spectrum as shown in Figure 4.12.

For magnitudes in the CCD band of the telescope, the mean difference between the theoretical magnitudes and the observed ones gives the zero point offset $m_{\rm offset}$ (Figure 4.13). The sigma of the Gaussian used to fit the distribution is taken as the zero point error. By using the new zero point value ($m_{\rm ZP} = m_0 + m_{\rm offset}$) in SExtractor, all the extracted sources will have calibrated magnitudes.

4.4.3 Quality of images

The quality of an image mainly depends on the observing conditions and can be represented by its limiting magnitude. The limiting magnitude $m_{\rm lim}$ of an image is defined as the mean magnitude of the faintest detectable objects in the image over a certain threshold. To determine the limiting magnitude of an image, SExtractor is first used to extract all the visible sources (`DETECT_THRESH`=2 σ).

[7] As magnitudes are used in input, they are first converted to fluxes in the code.

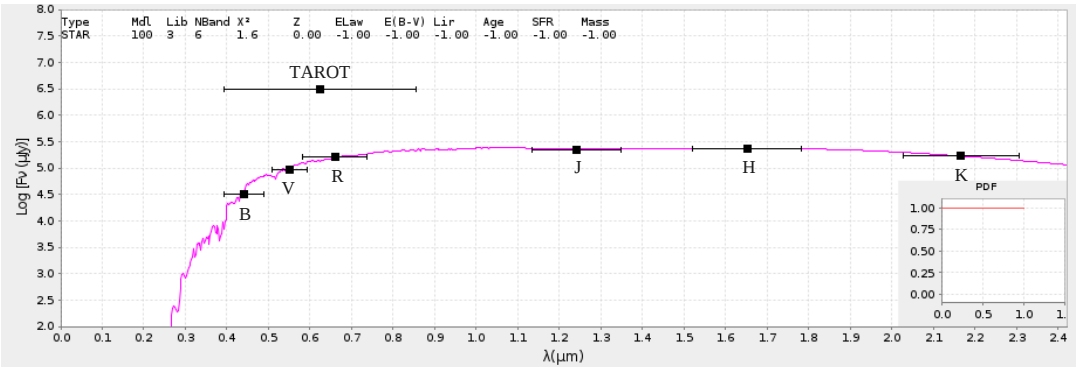

Figure 4.12: Output spectrum of LePHARE showing the result of the χ^2 fitting between the observed flux (black squares) and the flux from the template (pink line) for B, V, R, J, H and K bands. The CCD band of the telescope (in this case, TAROT) is not considered for the fitting to not bias it.

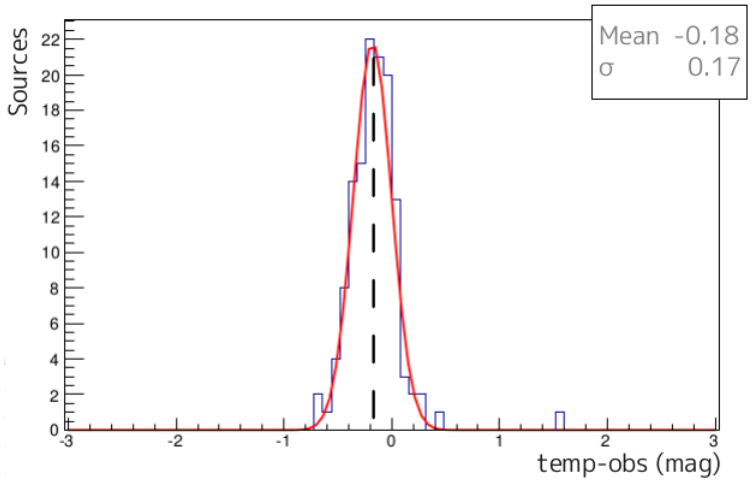

Figure 4.13: Gaussian fit of the magnitude differences between the template and the observations for a TAROT image from which 130 bright sources have been extracted. The mean value of the fit gives the correction to apply to the arbitrary zero point value initially set at $m_0 = 26$.

Then, the estimated magnitude error of each source is plotted against its magnitude (Figure 4.14(a)). As the 5 σ detection limit corresponds to a magnitude error of 0.198, all the sources with a magnitude error between 0.19 and 0.21 are considered to derive the limiting magnitude at the 5 σ level. The mean of the Gaussian fit of the magnitudes distribution included in this error range gives the limiting magnitude of the image, as shown in Figure 4.14(b). TAROT and ROTSE images with $m_{\rm lim} > 17$ are high quality images, while images with $m_{\rm lim} < 15$ are considered as low quality images. Figure 4.15 shows a good quality and a bad quality image.

The error on the limiting magnitude depends on the zero point error ($\Delta m_{\rm ZP}$)

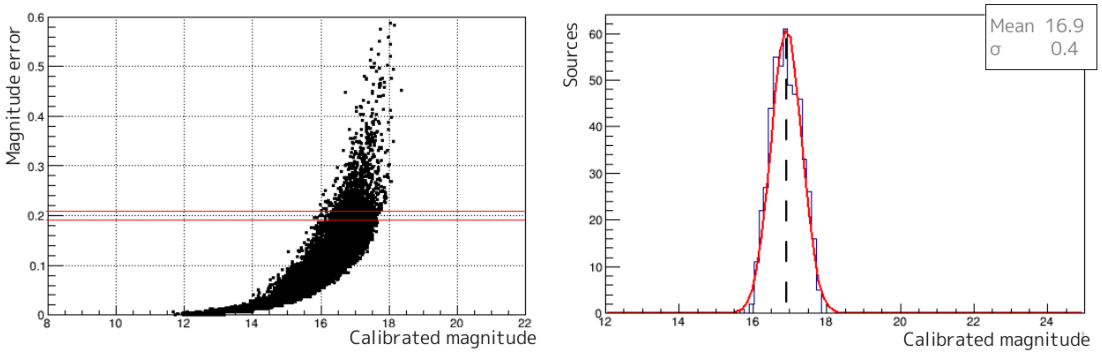

(a) Distribution of extracted sources as a function of the magnitude. The red vertical lines indicate a magnitude error between 0.19 and 0.21.

(b) Gaussian fit of the distribution of magnitudes with errors included in the interval (0.19,0.21). The mean of the fit gives the limiting magnitude of the image.

Figure 4.14: Determination of the limiting magnitude of images in two steps.

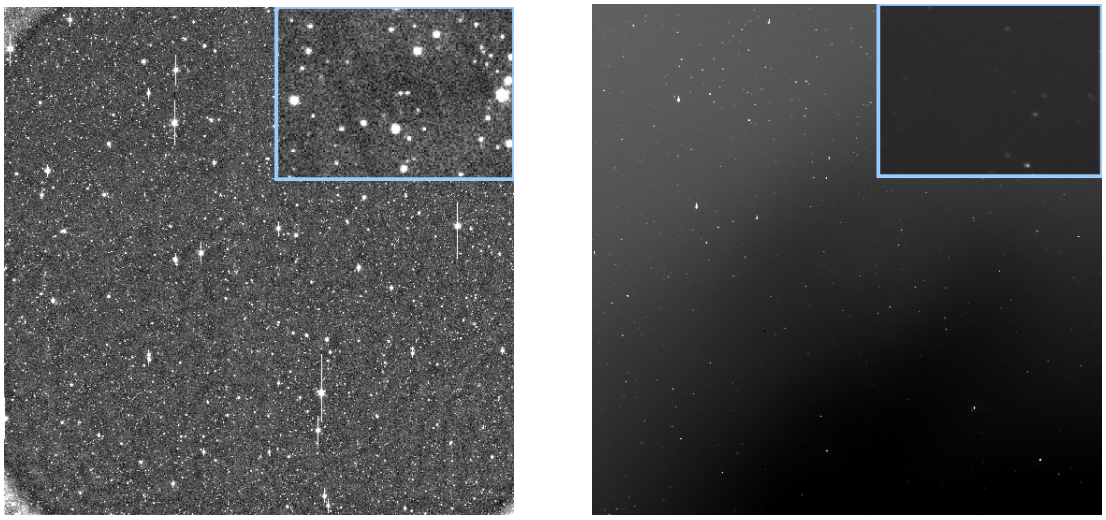

Figure 4.15: Illustration of a very good quality image (left) and a bad quality image (right). The image on the left is from TAROT Chile and has a 5 σ limiting magnitude of 18.1, while the image on the right is from ROTSE 3c and has a 5 σ limiting magnitude of 13.4. Zooms of these images appear in the upper right rectangles.

and on the sigma of the Gaussian fit (σ), and is calculated as follows:

$$\Delta m_{\mathrm{lim}} = \sqrt{{\Delta m_{\mathrm{ZP}}}^2 + \sigma^2} \tag{4.7}$$

At the end of the calibration step and having determined the limiting magnitude of each image, the analysis pipeline automatically sorts out images according to their quality. Images are tagged as *good* if two criteria are filled. First, the number of sources used to determine the zero point and the limiting magnitudes must be greater than 30. This is justified by the fact that if the number of extracted sources is not large enough, it means that the quality of the image is too poor to be correctly calibrated. The second criterion is that the error on the

zero point value and on the limiting magnitude must be lower than 1.0. All the images not satisfying these conditions are automatically put in directory called "bad" and are not further used.

An additional quality criterion based on the FWHM of sources is considered. The FWHM is a good approximation of the seeing, which represents the effect of atmospheric blurring on the angular resolution power. It is a simple number that can be used to compare the quality of images obtained under different observing conditions. Assuming objects with a Gaussian profile, the FWHM is defined as the width across the profile when it drops to half of its peak value. The FWHM is measured by SExtractor for each extracted sources in the image and the mean value is taken as the image FWHM. If the mean FWHM reaches 7 or 8 pixels, images can be rejected. Typically, good quality images have a mean FWHM of $\sim 2-3$ pixels.

4.5 Operations on images

4.5.1 Resampling and co-addition

Image co-addition is a widely used technique in astronomy. It increases, by about one magnitude, the limiting magnitude of images, allowing fainter objects to be detected. As the signal-to-noise ratio increases as the square root of the image exposure time[8], it is possible to enhance it by co-adding images together. The increase in limiting magnitude as a function of the number of co-added images is illustrated in Figure 4.16. Of course, to perform co-additions, images must be perfectly aligned on the same grid and the flux of each pixel has to be correctly distributed in the stacked image. Therefore, in addition to the relative astrometric calibration step (see Section 4.4.1), images are resampled by using SWarp [106].

SWarp is a program dedicated to FITS images resampling and combination. The resampling is the action of projecting a grid of pixels on another one. To this purpose, SWarp uses the "inverse mapping" method which consists of scanning the output frame pixel by pixel and using inverse projection to associate each output pixel center to a position in the input frame, at which the image will be interpolated. Then, SWarp combine data values coming from all the resampled images to obtain one single frame.

In addition to FITS images, SWarp considers input weight maps and external header files to resample and co-add images. Weight maps are the bad pixel maps of the telescopes described in Section 4.3.4, and external header files are the output .head files produced by SCAMP at the end of the astrometric calibration step. For every input FITS image, SWarp looks for the corresponding .head file and extracts several parameters necessary for inverse projection: CRVAL1, CRVAL2, CRPIX1, CRPIX2, CD1, CD2, CTYPE1 and CTYPE2 parameters. The output projection used is the traditional gnomonic tangential projection, as it is advised for images such as TAROT and ROTSE images (i.e., $\sim 2^\circ \times 2^\circ$). Because SWarp uses reverse-mapping, interpolation is made on the input images

[8]Considering Poisson statistics, the noise N can be expressed as $N = \sqrt{S}$, where S is $N_{\text{counts}}/t_{\text{exp}}$ according to Equation 4.2.

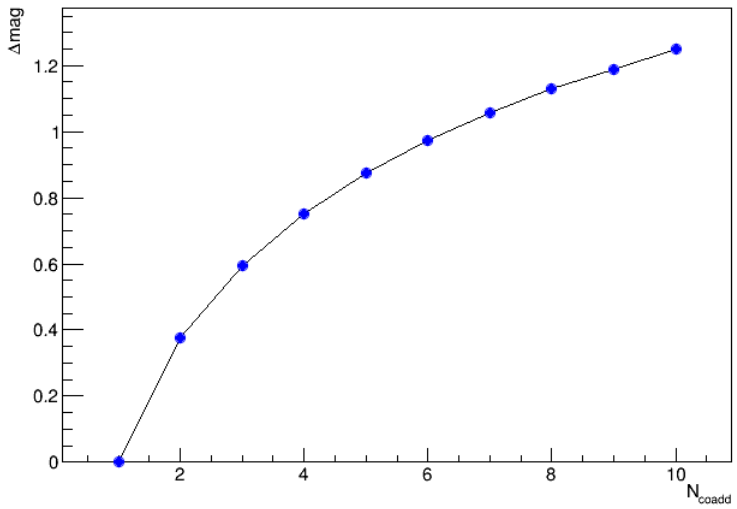

Figure 4.16: Increase in limiting magnitude as a function of the number of co-added images. Typically, images are co-added night by night (i.e., 6 images for TAROT, and 8 images for ROTSE), allowing a limiting magnitude improvement of about 1 magnitude.

by using Lanczos resampling. The resampling of weight maps follows that of input images except that for an input pixel weight of zero (bad pixels), the interpolated weight is also zero.

At the end of this step, resampled images and their corresponding weight maps are available and co-additions can be made. Among the various types of image combination that can be performed by SWarp, we choose the `MEDIAN` combination in which all scaled pixel values with non-zero weights are taken into account. Of course, co-addition is not a mandatory step, images can be processed individually by SWarp. This is the case for example to search for fast transient sources in early optical images. As a signal from such sources is expected to decay quickly in a few minutes, images taken by TAROT and ROTSE during the first night of observation are analyzed individually. The co-addition is also not useful for images with different qualities: the combination of a low quality image with a high quality one does not improve the limiting magnitude.

The quality of each new stacked image is then automatically determined by computing their zero point and limiting magnitudes as described in Sections 4.4.2 and 4.4.3.

4.5.2 Preparation and subtraction

In order to perform image subtraction, we have to select a reference (REF) which must be one of the best quality images and with a fainter signal than in the other images of the follow-up. It means that the REF should have been taken with a sufficient delay after the trigger, depending on the source that we are looking for. Typically, the REF image is the co-addition of the best images of a night.

Once the REF image is selected, a flux normalization between images to be

analyzed (IM) and the REF image has to be performed to avoid false positive residuals due to the bad subtraction of steady sources. It means that to detect a real flux variation of a transient source with a IM-REF subtraction, the flux of steady sources has to be equal in IM and in REF. As the majority of sources are standard stars which do not show variability, the normalization factor is determined by extracting sources in IM and in REF with SExtractor, cross-matching the two catalogs and dividing the flux of each source in REF by the flux of each associated source in IM. The mean of the obtained values is taken as the normalization factor, which will be applied to each IM pixel above a threshold value.

Although images are background-subtracted, the value of a background pixel can vary from tens to hundreds ADU around zero, and thus should not be multiplied by the factor. By plotting the pixel distribution of an image, as shown in Figure 4.17, the contribution of background pixels from the one of source pixels can be separated. The tail of the distribution, which consists of high ADU values, represents the pixels coming from sources. As this tail spans over thousands of ADU, we consider that below 1200 pixels per ADU value, pixels come exclusively from sources and therefore have to be multiplied by the normalization factor. This limit in number of pixels gives us the threshold in ADU above which the factor will be applied (Figure 4.17(b)). For each IM, the multiplication of each pixel above the threshold is performed by using the `imexpr` tool from the IRAF package [116].

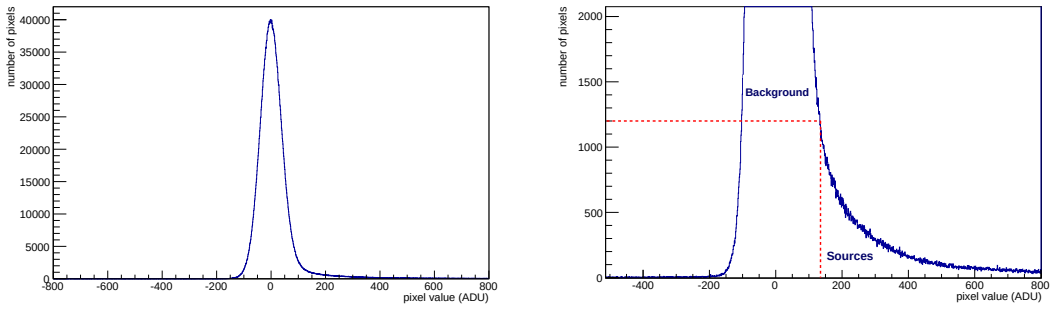

(a) Pixels with a value between -140 and 140 ADU are background pixels, while the tail of the distribution corresponds to source pixels.

(b) Zoom on the tail of the pixel distribution. Below 1200 pixels per positive ADU value, we consider that pixels come from sources and the red vertical dashed line shows the corresponding ADU threshold above which pixels will be multiplied by the normalization factor.

Figure 4.17: Example of a pixel distribution used to determine the normalization threshold.

Another thing to take into account to avoid bad subtractions is the "shape" of sources. If the FWHM of a source is different in IM and in REF or if the edges of the source are not identical in the two images, bright pixels can remain in the subtracted image. For instance, as the REF is a very good quality image,

its mean FWHM is generally smaller than the mean FWHM of IM. A Gaussian filter is thus applied to "blur" images and to remove detail and noise. The degree of smoothing is determined by the standard deviation of the Gaussian and has to be set carefully to not lose flux from faint sources. The Gaussian smoothing is performed with the tool `gauss` of the IRAF package. Each image is convolved with an elliptical Gaussian function with $\sigma = 1.5$ pixels. The effect of this smoothing is illustrated in Figure 4.18. After smoothing, we check that the difference between the FWHM of sources in IM and in REF is small, otherwise a correction is applied by changing the σ value of the Gaussian for IM or REF.

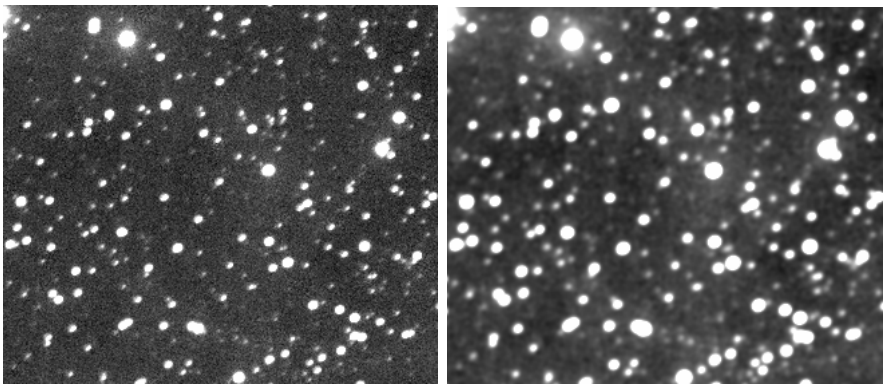

Figure 4.18: Illustration of a Gaussian smoothing. Left: before smoothing (mean FWHM = 2.6 pixels), right: after smoothing (mean FWHM = 3.7 pixels).

Finally, the subtraction is performed pixel by pixel with the `imarith` tool of the IRAF package. The REF image is subtracted to each IM (or to each stacked image) as follows: IM-REF=SUB, where SUB is the resulting image of the subtraction.

4.6 Analysis

4.6.1 Candidate selection

Any residual object in the SUB images is required to fulfill one of two criteria to be considered as a candidate transient. These criteria, illustrated in Figure 4.19, are:

- New source: the residual object must correspond to the detection of a source in IM but not in REF. If the source is not visible in the REF image, this could indicate the presence of a transient source and thus, an interesting candidate.

- Magnitude variation: the residual object must reveal a magnitude variation between a source in IM and in REF. A minimum variation of 0.5 magnitude is required to trigger the selection. As the pipeline can only detect positive residuals, a source brighter in REF than in IM would not be detected, hence the importance to select a REF image where a lower flux is expected.

To apply these criteria, a source extraction is performed on IM, REF and SUB with a detection threshold of 2.5 σ. The three catalogs are then cross-matched and a cut is applied to discard sources within 0.02 degrees (∼22 pixels) of the edges of the image, as they can have a truncated flux. All the residual objects satisfying the above conditions are automatically selected by the pipeline for a visual check by the user.

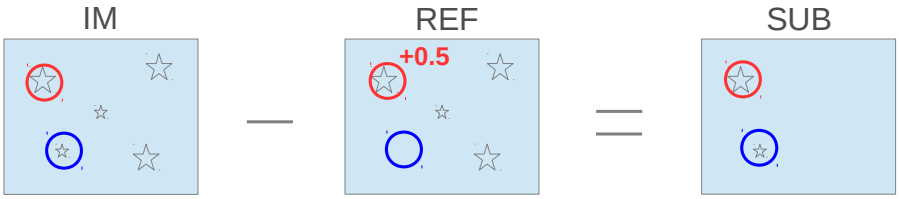

Figure 4.19: Selection criteria for transient candidates. Blue: a source detected in IM but not in REF gives a positive residual object in SUB and is thus considered to be transient. Red: a magnitude variation of at least 0.5 magnitude between a source in IM and in REF is required to select the corresponding residual object.

These criteria, and the parameters of the various programs used all along the pipeline have been optimized to our search for transient sources. Particularly, the "new source" and "magnitude variation" criteria have been set to select a hundred candidates per image. For this purpose, fake sources with various magnitudes have been injected in real images. The difficulty was to find to best compromise between the number of candidates selected and missed by the pipeline, and that criteria are sufficiently efficient regardless of image quality. Indeed, the candidates automatically selected must then be visually inspected by a human eye. Too many candidates to visualize would not be efficient and would take too much time (it takes approximately 2 seconds per candidate), and if the above cuts are too restricting, several candidates would be missed, such as faint or slightly varying sources.

The average number of candidates selected by the pipeline for each alert analyzed during this thesis is indicated in Tables 5.1 and C.1.

4.6.2 Visual check and light curves

Human scanning is required to distinguish candidates of astrophysical interest from those due to poor image subtraction or those due to minor planets, for example.

For each list of selected candidates, the pipeline generates an HTML page which can be opened in a web browser. A web page, illustrated in Figure 4.20, contains helpful information to identify the candidates. On the top, the IM (left), REF (middle) and SUB (right) images zoomed on the candidate are shown. The candidate is circled in blue if it has been selected with the "new source" criterion and in red if it corresponds to the "magnitude variation" criterion. In this latter case, the magnitude of the candidate in IM and in REF is written above the

red circles to indicate the variation. To be interesting, a candidate must clearly appear on the SUB image in order to discard any eventual bad subtraction.

Below the images, a table displays information on the candidate, including the coordinates, magnitude, signal-to-noise ratio and FWHM. The bottom left panel shows the light curve of the candidate generated by the pipeline. The light curve displays the behavior of the candidate over time. To be interesting, the light curve must show significant variability. Usually, candidates with a light curve containing only one point (i.e., candidates detected in only one image) are rejected, as no information on their transient behavior is provided.

In the bottom right panel, links to various catalogs, such as SIMBAD[9], NOMAD, 2MASS and SDSS [117], are displayed to help the identification of the candidate. By clicking on one of these links, a cross-check is automatically performed with catalogs around the candidate position. If a candidate showing variability is not already cataloged, it could be the counterpart to the neutrino trigger. A link to the Minor Planet Checker (MPChecker)[10] is also available. MPChecker is useful to reject asteroids even if a light curve with one single point can be sufficient to discard them.

With all this information, the user can finally decide if the candidate is interesting or not and classify it in one of the four following categories: *Junk*, *Asteroid*, *Variable star* or *Interesting*. An additional comment can be written and saved.

4.6.3 Sample of candidates

A sample of candidates selected by the pipeline during the analysis of TAToO alerts, but rejected after visual inspection is shown in Figures 4.21, 4.22, 4.23. The criteria described in Section 4.6.1 are defined to select variable or transient objects. It is thus common that variable stars unrelated to the neutrino trigger are detected. The candidate shown in Figure 4.21 is a variable star selected by the pipeline and cataloged as an emission line star in SIMBAD. About 5 % of the candidates automatically selected by the pipeline are cataloged as variable objects.

Other sources selected by the pipeline with the "new source" criterion are asteroids. Figure 4.22 shows the asteroid Lermontov detected during the analysis of an alert. Asteroids are quite easy to identify and to reject. They only appear in one image as they move rapidly, in consequence, light curves only contain one point and are thus easily discarded as no information about the behavior of the candidate is provided. Furthermore, bright asteroids (up to magnitudes $17 - 18$) are quite well cataloged. The Minor Planet Center catalog contains hundreds of thousands minor planets, asteroids and comets. Asteroids represent a few percent of candidates selected by the pipeline.

Finally, more than 90 % of the candidates are due to bad subtractions or bad estimates of selection criteria. For example in Figure 4.23, a sample of badly subtracted sources is shown. Generally, bad subtractions occur close to

[9] www.simbad.u-strasbg.fr

[10] http://www.minorplanetcenter.net/cgi-bin/checkmp.cgi

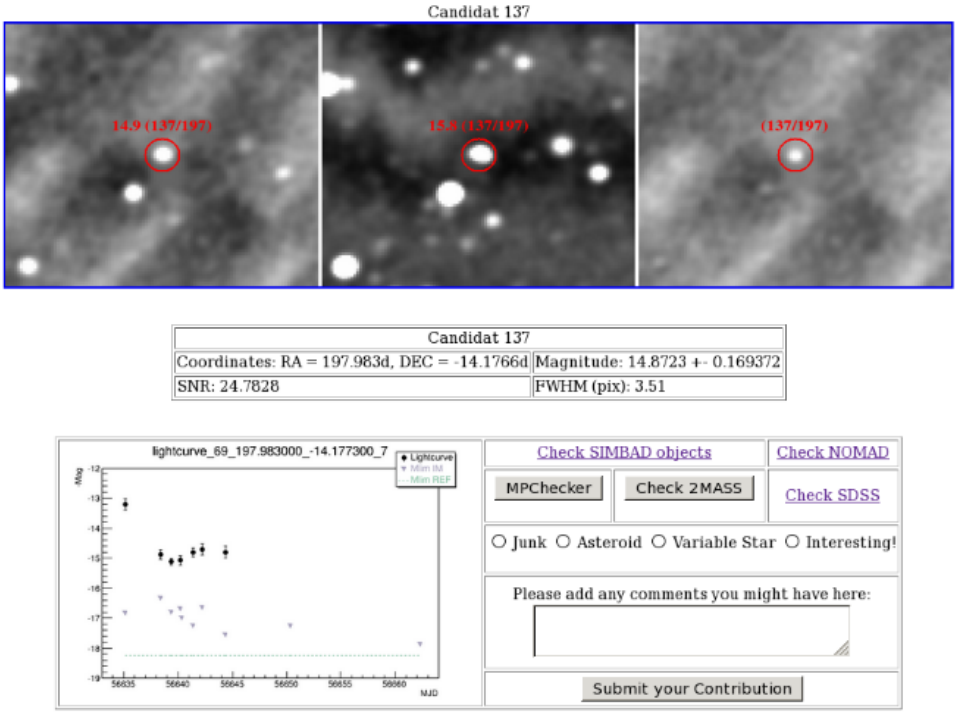

Figure 4.20: Example of web page created for a candidate. On the top, there are the IM (left), REF (middle) and SUB (right) images zoomed on the candidate. In the middle, a table shows information about the candidate. On the bottom panel, there are the light curve and several links to various catalogs.

saturated objects, in noisy regions, or for very faint objects where the magnitude and backgrounds are not well defined. In addition, positive residuals can appear in the subtracted image if a source in IM is at the same position than bad pixels masked in REF. The "new source" criterion is fulfilled as no source appear in the reference image. The rejection of all those bad candidates is quite easy after the visual inspection of the subtracted sources and the light curves, which generally contain no more than two points.

Among all these candidates, variable and transient sources which are not cataloged (or cataloged as possible high energy neutrino emitters) are interesting candidates to be the counterpart to the neutrino emission and are thus studied in more details. During the analysis of TAToO alerts presented in Chapters 5 and 6, only few variable or transient candidates potentially interesting have been detected.

4.7 Efficiency

The efficiency of the pipeline has been estimated for early and long term follow-up observations, dedicated to the search of fast and slowly varying transient sources, respectively. To quantify this efficiency, fake GRB afterglows and CCSNe have been inserted in different images.

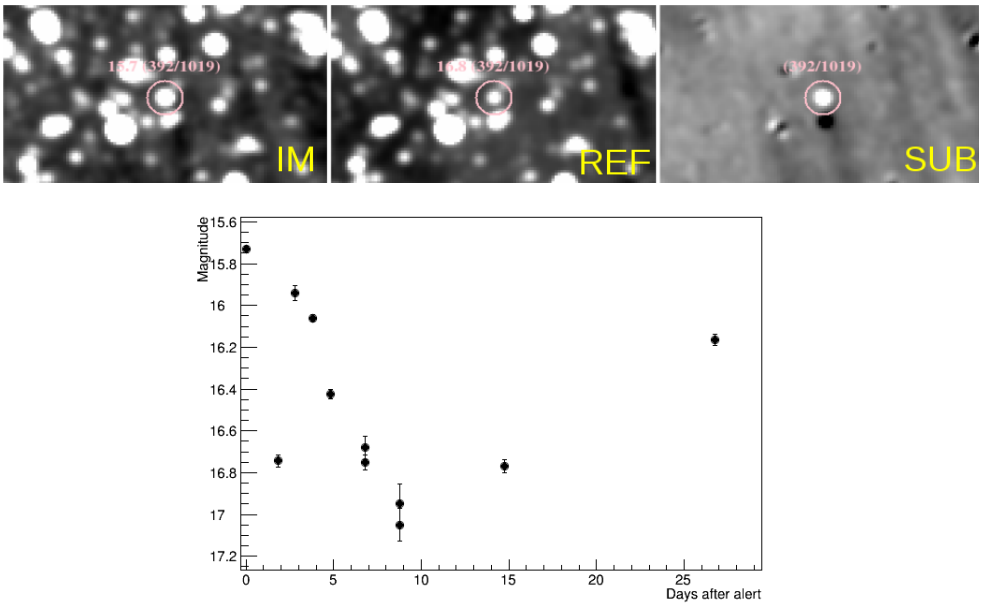

Figure 4.21: Example of a cataloged variable star and its light curve.

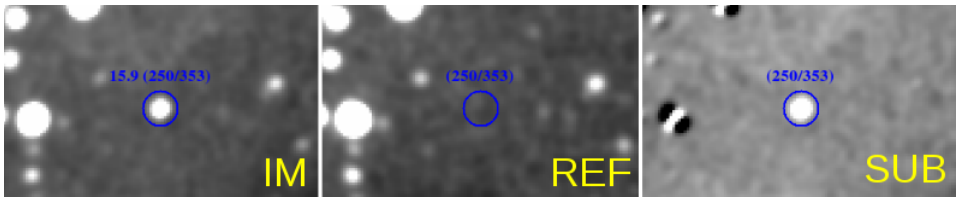

Figure 4.22: Example of an asteroid. It is cataloged in MPChecker as the Lermontov asteroid.

4.7.1 Gamma-ray burst afterglows

The GRB afterglow decay, which can start during the prompt event, is usually described by a power law of index α ($f(t) \propto t^{-\alpha}$, where $f(t)$ is the observed flux). According to [118], α lies between 0.5 and 1.7 with a median value of 1.0. To estimate the detection efficiency of the pipeline to such sources, fake GRB afterglows have been injected in 3 sets of images assuming a light curve decay $\propto t^{-1}$.

The detection efficiency depends on the performance of the pipeline but also on the quality of the images. Each set of images was composed of 6 images with 180 seconds exposure, and with a mean limiting magnitude of 16.5, 17.9 and 18.7, respectively. A total of 125 GRBs afterglows with apparent magnitudes between 12 and 19 have been injected in each of the 3 observations. Then, images have been analyzed and candidates have been checked by eye. An inserted GRB afterglow found during the visual analysis is shown as example in Figure 4.24.

The efficiency, presented in Figure 4.25, is given by the fraction of inserted GRB afterglows that has been detected by the processing and the candidate identification. The detection efficiency of the pipeline is better than 95 % for bright GRB afterglows (i.e., with a magnitude between 12 and 14) and reaches

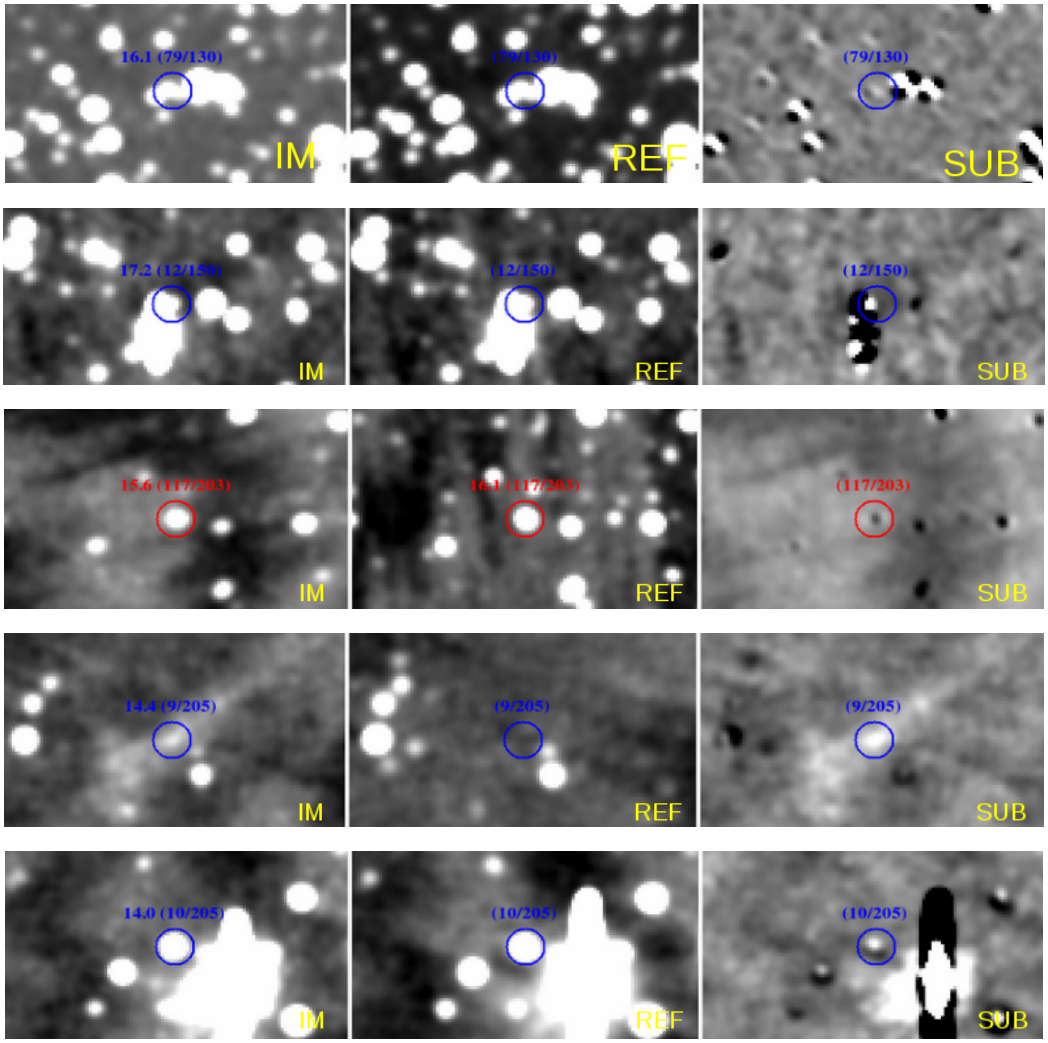

Figure 4.23: Examples of badly subtracted sources.

$\sim$ 50 % around 1 magnitude below the limiting magnitudes of images.

4.7.2 Core-collapse supernovae

The efficiency of the optical follow-up for detecting a CCSN has been estimated by injecting fake CCSN signals in images. This efficiency depends on the performance of the system, but also on the brightness of the source, and thus on the distance of the CCSN.

To compute this efficiency, fake sources have been injected in 3 sets of images. A SNIb/c template light curve based on SN1999ex [119], and represented in Figure 4.26, has been used to simulate a CCSN signal. Table 4.2 summarizes the characteristics of the 3 sets of images used for the injection. Two neutrino alerts with TAROT optical images and 1 alert with ROTSE images have been selected. Each alert is composed of 9 nights of observation with mean limiting magnitudes between 17.5 and 18.5. The first observation of each alert is assumed at T0 and represents the start time of the light curve. A total of 149, 140 and

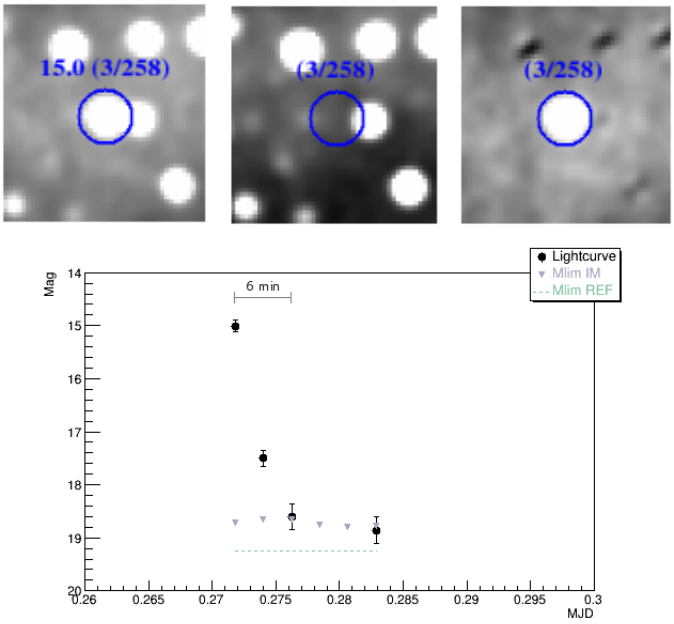

Figure 4.24: Injected GRB afterglow found during the visual inspection of candidates. Small pictures represent the bright GRB afterglow in IM, REF and SUB, respectively. The light curve, compatible with a decay expected from such a source, shows that it has been detected in 4 images.

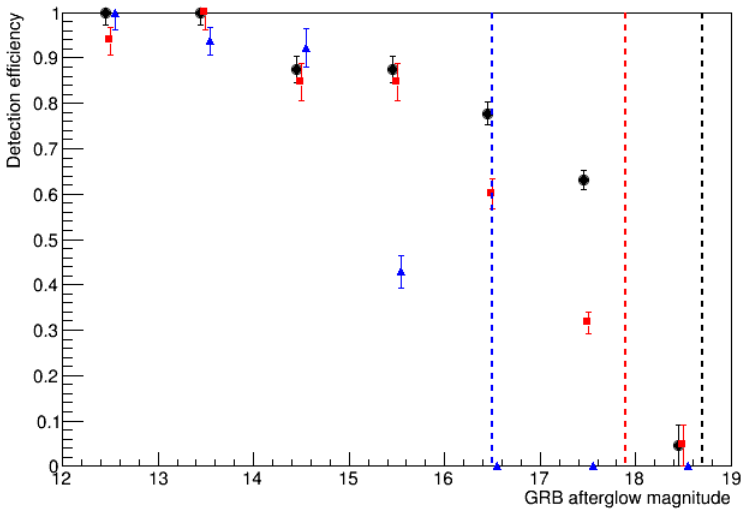

Figure 4.25: Detection efficiency of the optical image analysis pipeline estimated by inserting fake GRB afterglows in 3 sets of images with limiting magnitudes (vertical dashed lines) of 16.5 (blue), 17.9 (red) and 18.7 (black) and considering a light curve decay $\propto t^{-1}$.

168 fake CCSNe with peak magnitudes between 12 and 19 have been inserted in these observations. To reproduce the distribution of CCSNe in the Universe, injections have been made in the vicinity of extended objects, which represent

galaxies. To search for CCSN signals, images have been co-added night by night and analyzed with the dedicated pipeline. An example of CCSN found during visual inspection of candidates is displayed in Figure 4.27.

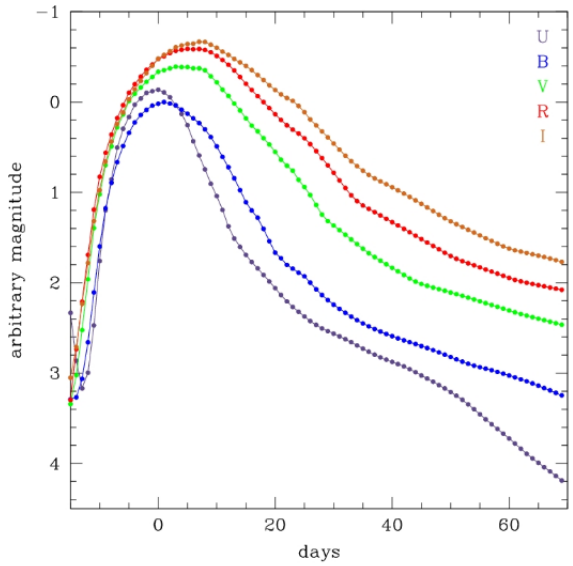

Figure 4.26: SNIb/c template light curves for different bands. TAROT and ROTSE have a maximum sensitivity between the V and R bands, thus the R-band light curve, shown in red, has been used to insert fake CCSNe.

Table 4.2: Details of the observations in which fake CCSN signals have been inserted.

Injection #	Telescope	Observations	Mean $m_{\rm lim}$	Injected sources
1	TAROT	T0, T0+3, 4, 5, 6, 8, 14, 26, 44 days	17.5 - 18.5	149
2	TAROT	T0, T0+4, 5, 6, 8, 9, 10, 12, 18 days	17.5 - 18.5	140
3	ROTSE	T0, T0+1, 2, 3, 5, 7, 17, 16, 27 days	17.5 - 18.5	168

The efficiency is given by the fraction of injected SNe that has been detected by the processing and candidate identification. Figure 4.28 shows this fraction as a function of the injected apparent peak magnitude. The efficiency of the pipeline is better than 95 % for CCSNe with magnitudes brighter than 14.5, and decreases progressively up to the limiting magnitudes of images, where the efficiency does not exceed a few percents.

This efficiency as a function of the apparent peak magnitude can be converted to the efficiency as a function of the SN distance. The relation between distance and magnitude is given by:

$$m = M + 5\left(log_{10}\frac{d}{1\text{pc}} - 1\right) \tag{4.8}$$

where m is the apparent magnitude, M the absolute magnitude, and d the SN distance. The efficiency as a function of the CCSN distance has been computed

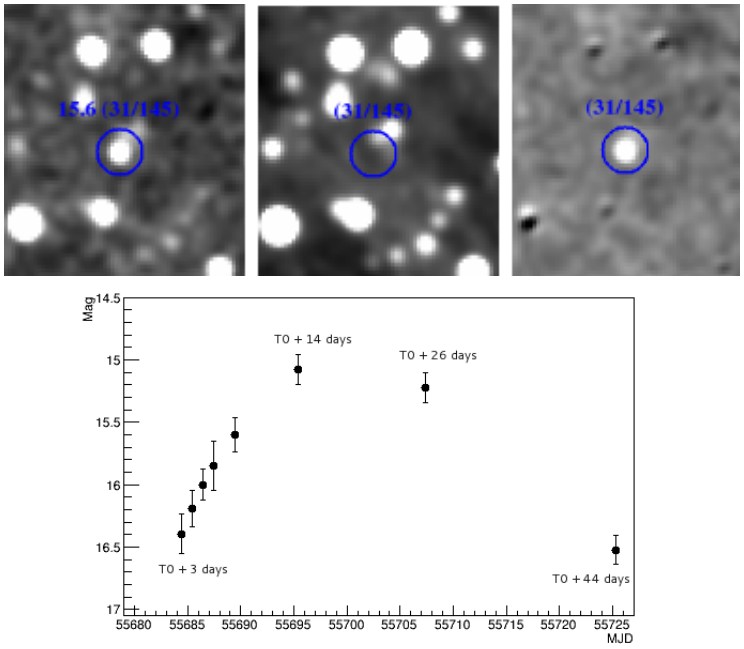

Figure 4.27: Injected CCSN found during the analysis of candidates. Small pictures correspond to IM, REF and SUB, respectively. The rising of the light curve, as well as the decay after $\sim$ T0 + 20 days are typical signatures of CCSNe of type Ib/c.

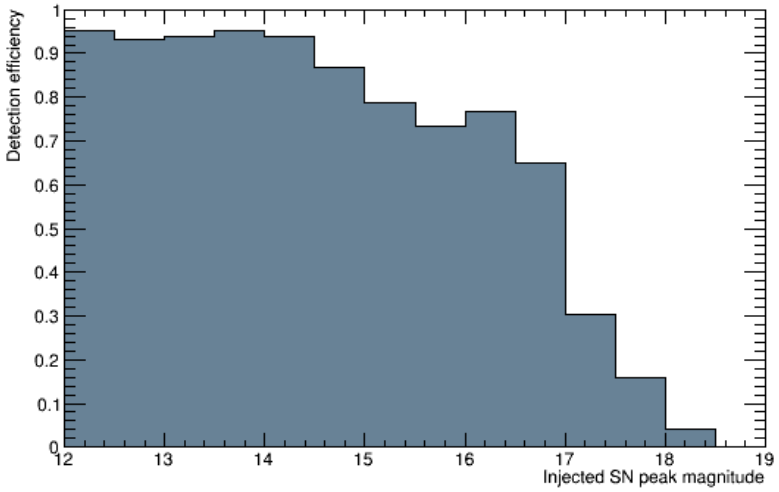

Figure 4.28: Efficiency to detect CCSNe as a function of the apparent peak magnitude.

assuming a Gaussian absolute R-band magnitude distribution of CCSNe with mean of -18 magnitude and standard deviation of 1 magnitude [120]. As the limiting magnitudes of images in which fake sources have been injected correspond approximately to the maximum sensitivity that can be reached with the TAROT and ROTSE telescopes, the efficiency as a function of the CCSN distance allows the horizon sensitivity of these telescopes to be derived. Figure 4.29 shows that CCSNe at a distance greater than 230 Mpc cannot be detected.

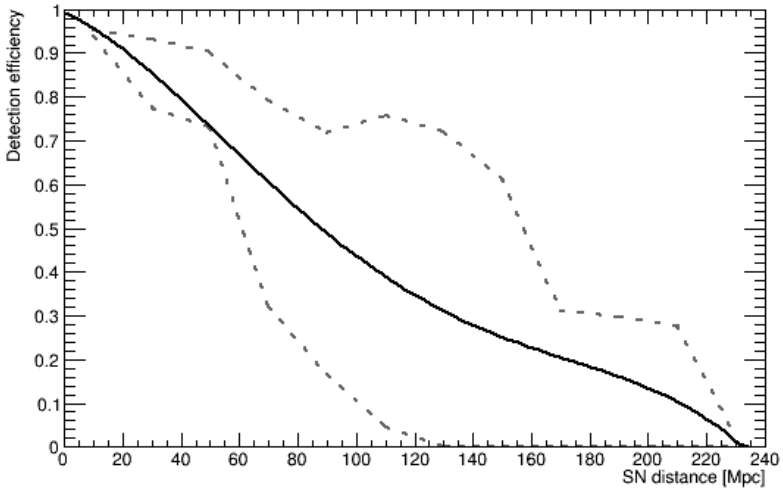

Figure 4.29: Efficiency to detect a CCSN as a function of its distance assuming an absolute magnitude distribution of -18 ± 1 (black curve). The gray dashed lines are the lower and upper bounds assuming an absolute magnitude of -17 and -19, respectively. The breaks in these lines are connected to the binning in Figure 4.28. The binning effect is washed out in the black curve due to the assumed uncertainty in the absolute magnitude distribution of ± 1.

4.8 X-ray data analysis

X-ray data obtained from follow-up observations by the *Swift*-XRT are automatically analyzed at the UK Swift Science Data Centre. The first step of the analysis is to combine the 4 tiles into a single image, as illustrated in Figure 4.30, and to apply the source detection algorithm which has been developed for the 1SXPS catalog [121]. It identifies sources, localizes them, and assigns each one a detection flag.

The source positions are determined using the on-board star trackers with an accuracy of 3.5 arcsec [122] 90 % of the time. However, it is sometimes possible to enhance the astrometry by using stars in the field of view of the UV/optical telescope [123, 124], or by matching the detected XRT sources with the 2MASS catalog. The position with the smallest error is reported.

A detection flag is assigned to each detected source to indicate the probability of the source being spurious. This flag can be either *Good* (0.3 % of sources flagged as *Good* are spurious), *Reasonable* (7 % of false positive) or *Poor* (35 % of false positive) [121].

For each detected source in the 4-tile images, light curves and spectra are built, and a cross-correlation with the X-ray master catalog, the 1SXPS catalog and SIMBAD is performed to check if the source is already cataloged or not. Two tests are then automatically carried out on each uncataloged X-ray source to determine if it could be the counterpart to the ANTARES neutrino trigger. The first test relies on brightness and variability measurements: if a source is so bright that

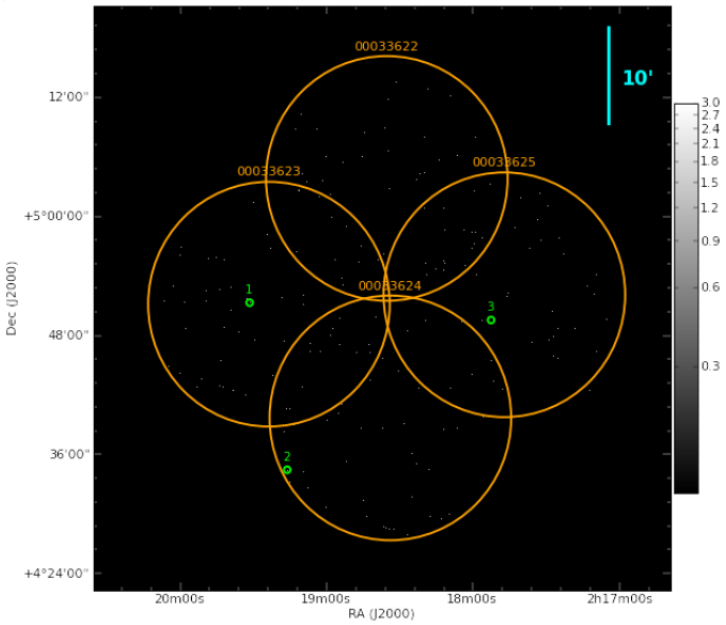

Figure 4.30: Image obtained after combination of the 4 tiles for one of the ANTARES neutrino trigger. In this image, 3 X-ray sources have been detected (green circles).

it should have been discovered previously[11], it means that the source is assumed to be new and therefore potentially the counterpart. The other possibility is if the source shows variability, and in particular significant signs of fading[12], it is considered as a potential counterpart. Such behavior is expected from explosive transients such as GRBs or CCSNe.

The second test is based on the probability that the uncataloged X-ray source is unrelated to the neutrino trigger. The number of expected serendipitous sources with a count-rate at least that of the detected source in each 4-tile observation is calculated by combining the minimum exposure necessary to detect the XRT source, the sky area observed with at least this exposure, the sky density of sources at least as bright as the XRT source, and the completeness of the detection system. Figure 4.31 shows the levels at which the XRT is 50 % and 90 % complete (black), and the expected number of serendipitous sources per XRT field of view (red) above these levels, as a function of the exposure time. The typical RASS limit is also indicated (green line). Note that the number of expected serendipitous sources cannot be read independently of the other information. In particular, the quality flag must be taken into account. For example, a "poor" detection, has a $\sim$ 35 % probability of being a spurious detection; if it is spurious, the fact that it is unlikely to be a serendipitous source is irrelevant.

Once the X-ray processing is complete for an ANTARES trigger, an email is sent to the ANTARES and *Swift* collaborations, and the results giving details of the newly discovered X-ray sources and any catalogs matches, are presented

[11]The mean XRT count-rate must be more than 1 σ above the Rosat All-Sky Survey (RASS) 3 σ upper limit [125] calculated at the location of the X-ray source. The Rosat upper limit is derived using RASS images, exposure and background maps.

[12]The last bin of the source light curve must be at least 3 σ below the first bin.

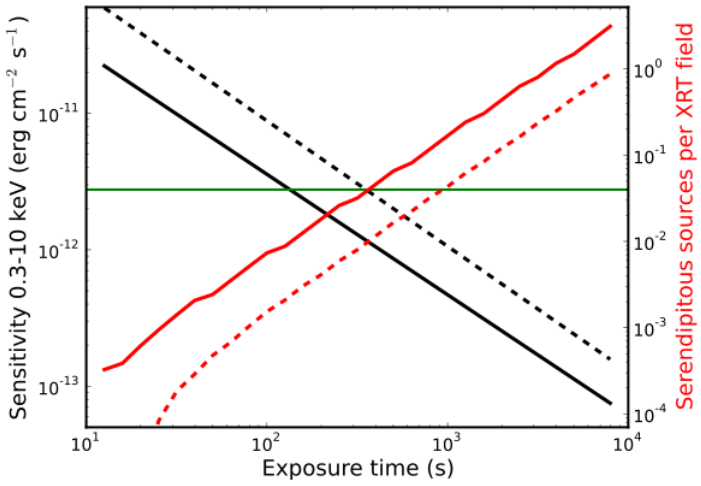

Figure 4.31: Sensitivity of the *Swift*-XRT (black lines), and number of serendipitous sources expected per XRT field above this limit (red lines), as a function of exposure time. The solid lines represent the 90 % completeness level of the XRT, while the dashed lines correspond to the 50 % completeness level. The green horizontal line shows the typical sensitivity limit of the RASS. Image taken from [126].

in a dedicated web page. Such a web page is illustrated in Figure 4.32. At the top of the page, details about the trigger are indicated, such as its location, the time trigger and the distance from the Sun/Moon at the time of the detection. Below this panel, a table lists all detected sources. The position and error, the detection flag, the distance from the ANTARES position and any notes (e.g. details of catalog matches) are indicated. More details are displayed when a link ("details") is clicked: the mean and peak XRT count-rate of the source (based on the light curve), the Rosat upper limit, the XRT mean and peak count-rate converted into Rosat PSPC[13] count rates (using the XRT spectrum), the mean and peak XRT flux (derived from the XRT spectrum and light curve), and links to the various products available for that source.

[13]Position Sensitive Proportional Counters are multiwire proportional counters developed for the Rosat satellite. Two wire grids are used to detect position and charge of an electron cloud produced by an incoming X-ray photon.

J0218.6+0452: Swift observation summary

Mission:	ANTARES	**Sun distance:**	84.91°
ANTARES RA:	34.656°	**Sun angle:**	5.54 [hr](East of Sun)
ANTARES Dec:	+4.863°	**Moon distance:**	32.38°
ANTARES Err:	21.0 arcmin	Visibility of this field.	
T0:	2015-01-29 10:19:58 UT		
Galactic:	159.58° -51.70°		
Galactic N_H:	3.68× 10^{20} cm^{-2}		
Galactic E(B-V):	0.04103699		

#	RA (J2000)	Dec (J2000)	Err_{90} [1]	Detection Flag [2]	Dist from ANTARES pos	Exposure	Notes	Vizier
1 [Hide details]	02h 19m 31.60s	+04° 51′ 18.5″	7.0″	Good	13.5′	1.9 ks		
	• Mean XRT rate: 5.4 (±2.5) ×10^{-3} ct s^{-1} • Peak XRT rate: 5.4 (±2.5) ×10^{-3} ct s^{-1} • RASS PSPC 3-σ upper limit: 0.07 ct s^{-1} (PSPC count-rate) • Mean XRT rate converted to PSPC: 0.011 (±0.005) ct s^{-1} • Peak XRT rate converted to PSPC: 0.011 (±0.005) ct s^{-1} • Mean XRT flux: 1.3 (±0.6) ×10^{-13} erg $cm^{-1}s^{-1}$ • Peak XRT flux: 1.3 (±0.6) ×10^{-13} erg $cm^{-1}s^{-1}$ • Products: Light curve | Spectrum | • Expected serendipitous sources: ~1.4 [What is this?]						
2 [details]	02h 19m 16.21s	+04° 34′ 27.7″	7.0″	Good	19.8′	1.4 ks		
3 [details]	02h 17m 52.65s	+04° 49′ 33.4″	5.9″	Good	11.4′	1.4 ks		

Figure 4.32: Example of a web page created after the analysis of X-ray data taken in response of an ANTARES neutrino trigger.

CHAPTER 5

Early follow-up analysis

To search for transient counterparts to neutrino alerts, images provided by the TAROT and ROTSE optical telescopes, and by the *Swift*-XRT have been analyzed. The early follow-up analysis is dedicated to the search for fast transient sources with variations on the minute or hour timescale. Therefore, only observations made during the first 24 hours after the neutrino trigger have been taken into account in this analysis.

In this chapter, the results of the early follow-up analysis are presented for both the optical and X-ray wavelengths. These results are then discussed in the case of GRBs.

5.1 Neutrino data set

A total of 59 neutrino alerts sent from October 2009 to the end of September 2015 have been early followed-up. Among them, 17 alerts have been discarded from this analysis due to the bad quality of their early images. Hence, the neutrino data set is composed of 42 alerts with an early optical follow-up and 10 alerts with a X-ray follow-up. Only one alert has been early followed-up by both the optical and X-ray telescopes. The trigger time, coordinates, type and energy of the alerts are reported in Appendix A. A total of 27, 14 and 10 neutrinos have been triggered as high energy, directional and very high energy alerts, respectively. Figure 5.1 shows the distribution of the total amplitude in photo-electrons as a function of the number of hits for each neutrino alerts with early follow-up observations.

5.2 Optical follow-up results

A total of 42 alerts have been processed with the image analysis pipeline. The telescopes that observed the region around the neutrino direction, the number of early images and candidates analyzed, their exposure, the delay and the limiting magnitude of the first early image, as well as the date of the reference image chosen for the subtraction are given for each neutrino alert in Table 5.1. For 11

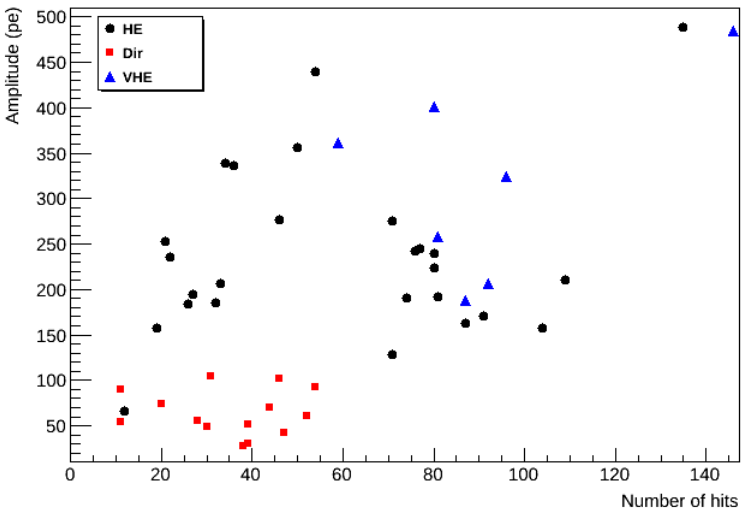

Figure 5.1: Amplitude distribution of neutrino alerts with early follow-up observations as a function of the number of hits, and for the three triggers.

alerts, the time between the neutrino detection and the start of the acquisition of the first image is less than 1.2 minutes and is lower than 27 seconds for 7 alerts. The combination of short observation delays with good quality images is required to detect fast transient sources. The mean quality of early images taken for the 42 neutrino alerts is displayed in Figure 5.2. It is interesting to notice that the best quality images, in terms of limiting magnitude and FWHM, have been taken by TAROT Chile. Among the 7 alerts with observations after a delay of about 25 seconds, 6 have also been taken by TAROT Chile.

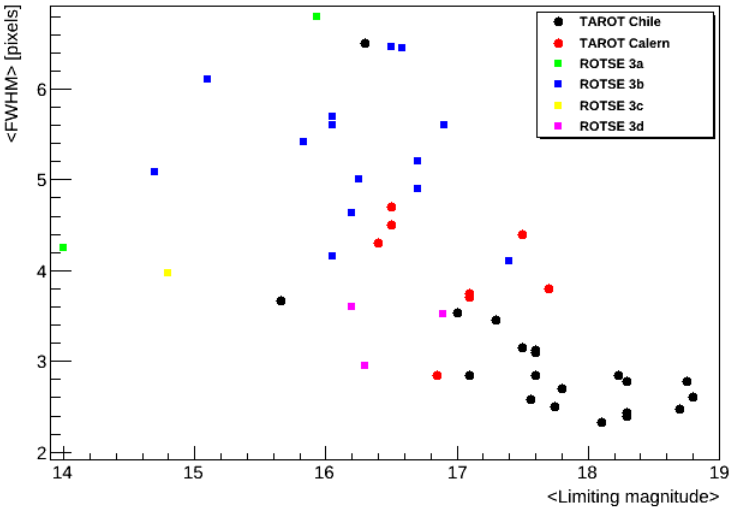

Figure 5.2: Scatter plot of the mean FWHM as a function of the mean limiting magnitude for early optical observations of 42 neutrino alerts. The best quality images have been taken by TAROT Chile.

After processing with the pipeline and visual inspection of candidates, no optical counterpart associated with one of the 42 neutrinos was found. This could indicate that the observations were made too late when the sources could have faded below the sensitivity of the optical telescopes, or that the sources occurred outside the field of view of the telescopes, or that the neutrinos that generated the triggers have another origin (i.e., an atmospheric origin).

Upper limits on the magnitude of possible transient sources which could have emitted the neutrino have been derived. As we are looking for rapidly-fading sources, the signal is supposed to be stronger in the first image of the observation, so the upper limits are the limiting magnitude of each first image computed at the 5 σ level and corrected for galactic extinction [127]. Indeed, the extinction caused by dust and gas in the galactic plane increases for decreasing distance to the Galactic plane, as shown in Figure 5.3. The results for each alert are presented in Table 5.1.

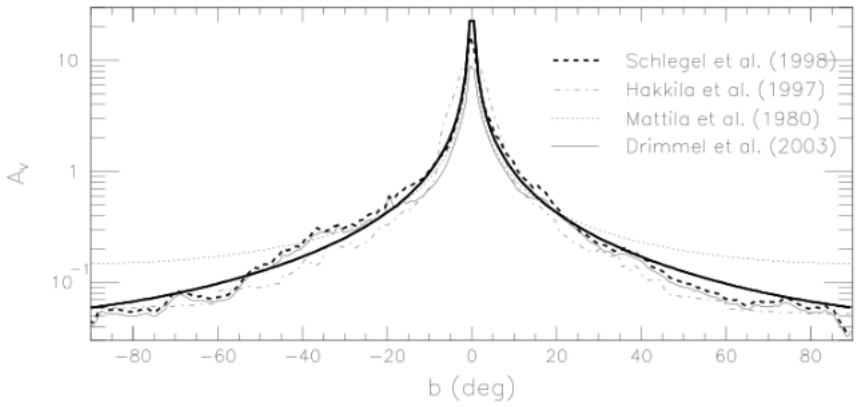

Figure 5.3: Extinction depending on the galactic latitude for different models. Towards the galactic plane, the extinction is highest. Image taken from [128].

5.2.1 Interesting candidates

Although no optical transient counterpart associated with one of neutrino triggers was identified during the analysis, two interesting candidates were detected during the visual inspection step. They are interesting because they are variable or transient and their behavior is not identified by catalogs. However, it is difficult to firmly conclude on these candidates due to the lack of information.

ANT110531A

The alert ANT110531A was triggered with the high energy criterion and followed-up by TAROT Chile after a delay of 12 hours and 34 minutes. During this early observation, 6 images of 180 seconds of exposure were taken with a mean limiting magnitude of $\sim$ 17.6. The optical counterpart search was performed on each image with the pipeline, with a reference image chosen at T0 + 27 days. During the visual inspection of residual objects, an interesting candidate was found. This

Table 5.1: Details of the 42 neutrino alerts for which early optical images have been taken.

Alert name ANTyymmddA/B	Telescope	Analyzed images	Candidates[a] visual insp.	Exposure[b] (sec)	Delay[c]	m_{lim}[d] (mag)	A_v[e] (mag)	Reference[f] (yymmdd)	$P_{reject}^{GRB,\nu}$[g]
ANT100123A	TAROT	6	138	180	17h47m	15.3	0.2	100211	0.00
ANT100725A	TAROT	6	144	180	1m17s	16.1	0.3	100727	0.50
	ROTSE	30	383	20	1m15s	13.1	0.3	100731	0.12
ANT100913A	TAROT	6	160	180	11h24m	17.6	0.0	100914	0.06
ANT100922A	ROTSE	26	92	20	1h08m	13.6	0.5	101202	0.00
ANT110305A	ROTSE	29	68	60	4h19m	15.7	0.1	110315	0.06
ANT110409A	TAROT	6	> 1000	180	1m08s	12.6	5.6	110423	0.04
ANT110531A	TAROT	6	402	180	12h34m	17.6	0.1	110628	0.06
ANT110923A	TAROT	7	302	180	9h58m	12.8	3.9	111001	0.00
ANT110925B	TAROT	6	232	180	2h01m	15.2	1.8	111125	0.10
	ROTSE	30	62	60	50m58s	13.9	1.8	110927	0.00
ANT111008A	TAROT	5	200	180	12h53m	14.3	2.5	111009	0.00
ANT111019A	ROTSE	8	110	60	18h22m	16.7	0.1	111029	0.02
ANT111019B	ROTSE	8	105	60	19h09m	16.9	0.1	111024	0.02
ANT111101A	ROTSE	8	117	60	13h33m	17.2	0.1	111130	0.02
ANT111205A	TAROT	6	341	180	10h05m	18.2	0.4	111207	0.16
ANT111228A	TAROT	6	111	180	7h44m	17.0	0.1	120124	0.04
	ROTSE	8	86	60	7h53m	16.6	0.1	111231	0.04
ANT120102A	TAROT	4	103	180	1m17s	17.0	0.1	120129	0.60
ANT120105A	ROTSE	8	128	60	17h39m	16.0	0.4	120112	0.02
ANT120730A	TAROT	26	89	180	20s	16.9	0.4	120807	0.88
ANT120907A	TAROT	14	142	180	9m53s	15.9	0.2	120909	0.31
ANT120907B	TAROT	11	102	180	18h15m	17.2	0.2	121106	0.02
	ROTSE	27	151	60	8h28m	15.9	0.2	121004	0.02
ANT120923A	TAROT	6	113	180	15h43m	18.0	0.1	121020	0.03
ANT121010A	TAROT	24	214	180	25s	18.6	0.0	121209	0.90
ANT121012A	TAROT	6	220	180	19h06m	16.5	0.7	121016	0.02
ANT121027A	ROTSE	8	195	20	14h56m	13.4	2.6	121124	0.00
ANT121206A	ROTSE	27	110	60	27s	15.6	1.1	121210	0.62
ANT130210A	ROTSE	8	164	60	14h46m	16.5	0.1	130216	0.02
ANT130724A	TAROT	3	209	180	18h04m	15.9	0.1	130729	0.02
ANT130928A	ROTSE	8	131	60	13h49m	15.9	0.1	131006	0.02
ANT131027A	ROTSE	8	207	20	18h14m	15.0	0.7	131112	0.00
ANT131209A	TAROT	6	102	180	1h14m	16.3	0.1	131215	0.14
ANT131221A	TAROT	2	345	180	18s	16.8	0.5	131222	0.83
ANT140123A	TAROT	23	194	180	13h21m	16.2	1.3	140126	0.02
ANT140125A	TAROT	6	156	180	1h14m	18.1	0.0	140128	0.43
ANT140203A	ROTSE	8	74	60	19h43m	14.9	0.1	140205	0.00
ANT140223A	TAROT	3	218	180	17h08m	15.9	0.1	140224	0.02
	ROTSE	3	186	60	31m29s	14.2	0.1	140227	0.02
ANT140304A	TAROT	18	400	180	25s	17.5	0.6	140304	0.92
ANT140309A	TAROT	16	120	180	24s	17.1	0.1	140309	0.88
ANT140323A	ROTSE	8	205	60	14h47m	16.2	0.2	140325	0.02
ANT140408A	TAROT	6	548	180	16h11m	16.7	0.1	140410	0.02
	ROTSE	8	85	60	19h07m	16.0	0.1	140410	0.02
ANT140505A	ROTSE	2	31	60	17h11m	14.7	0.1	140510	0.00
ANT140914A	TAROT	13	181	180	1m05s	16.9	0.5	140915	0.62
ANT150122A	TAROT	8	213	180	17s	18.6	0.1	150122	0.90

[a] Average number of candidates per image automatically selected by the pipeline, and which have been visually inspected. For the alert ANT110409A, more than 1000 candidates have been selected because of a neutrino direction towards the galactic plane.
[b] Exposure of each image.
[c] Delay in hours, minutes and/or seconds between the neutrino trigger and the first image.
[d] Limiting magnitude of the first image computed at the 5 σ level and corrected for the galactic extinction.
[e] Galactic extinction from [127].
[f] Date of the reference image used for the subtraction.
[g] Probability to reject the GRB origin hypothesis for this neutrino trigger (see Section 5.4.2).

candidate (RA = 327.648°; dec = -8.331° / l = 47.988°; b = -43.349°), presented in Figure 5.4, was selected with the "new source" criterion (i.e., a source detected in IM but not in REF) and is located at $\sim$ 50 arcmin from the neutrino position (Figure 5.5). The light curve of this candidate is shown in Figure 5.6.

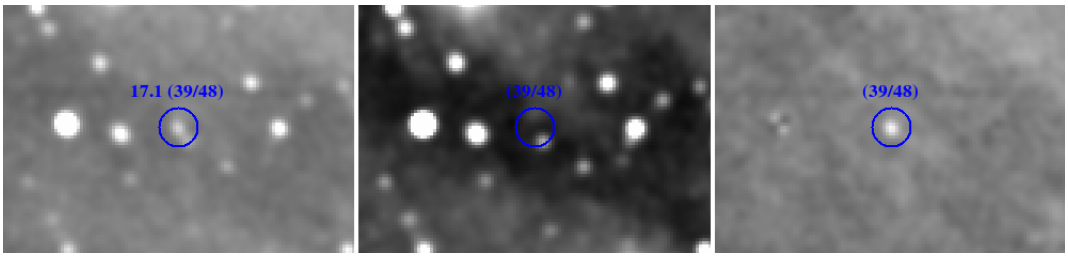

Figure 5.4: Candidate found in ANT110531A during visual inspection, i.e. after processing of the image. From left to right: IM (first image at T0), REF at T0 + 27 days and SUB.

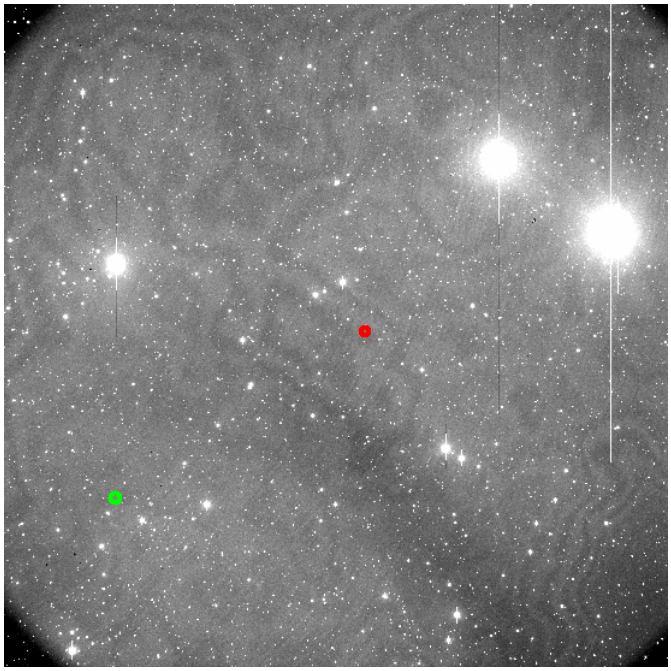

Figure 5.5: First raw image (1.86° × 1.86°) taken for the alert ANT110531A. The neutrino position is indicated with a red circle while the candidate position in shown in green. They are separated by about 50 arcmin. The error on the neutrino position is estimated at 18 arcmin.

This object is interesting because its magnitude varies from 17.1 to 17.7 in 18 minutes, it is not cataloged in optical (SIMBAD, NOMAD, SDSS), infrared (2MASS, AllWISE) and UV (GALEX) catalogs, and only detected at T0, as expected in the case of a fast transient source. Figure 5.7 shows the field around the candidate position in the optical band. Images taken with TAROT at T0 + 1, 2, 3, 7, 9, 15, 27 and 29 days for this alert do not reveal the presence of this source, as shown in Figure 5.8, although the limiting magnitudes of these

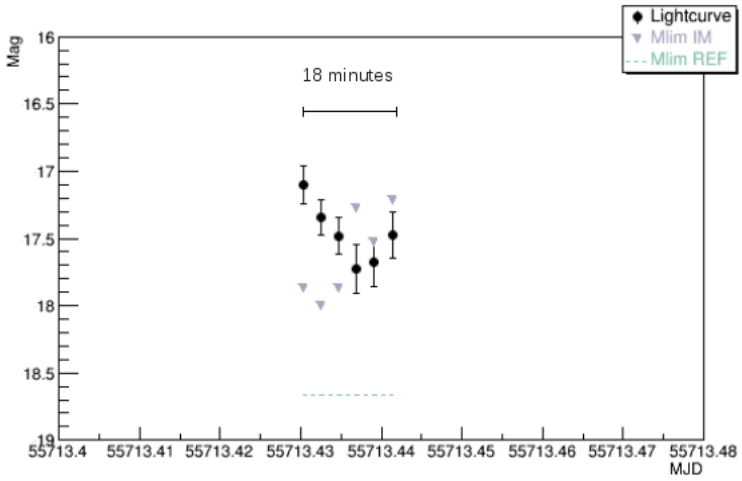

Figure 5.6: Light curve of the candidate found in ANT110531A. The candidate was only detected at T0. The green dashed line indicates the limiting magnitude of the REF image at $\sim$ 18.6, while blue triangles show the limiting magnitude of each IM at T0.

observations reach $\gtrsim$ 18. ROTSE images were also taken at T0 + 4, 5, 9, 15, 16 and 27 days after the trigger and the candidate does not appear. One observation with Zadko was performed at T0 + 5 days, but the mapping with Zadko was not implemented at this date and the candidate position is outside its field of view. In addition, a check with MPChecker was also performed to identify a possible minor planet, but no known object was found in the region of the candidate.

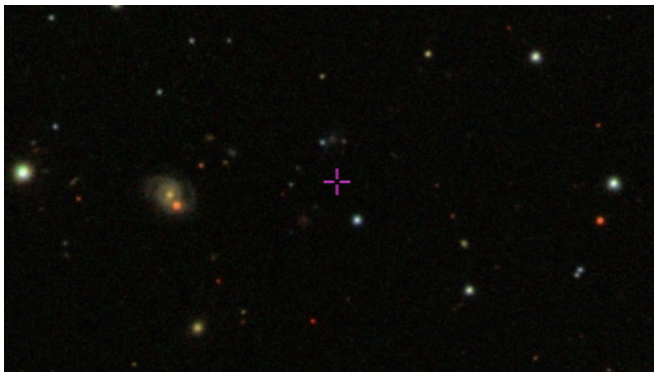

Figure 5.7: Optical field ($\sim$ 4 arcmin) from SDSS9 around the candidate position indicated with a pink cross.

To try to identify this source, a comparison between the candidate light curve and 301 GRB afterglow light curves detected from 1997 to 2014 was made, as shown in Figure 5.9. The candidate and GRB afterglow light curves are indicated in green and gray, respectively (the blue curve is for the other candidate detected in this analysis and for which a comparison with GRB afterglow light curves was also made). One can notice that less than 2 % of the detected GRB afterglows have a brighter magnitude than the candidate more than 12 hours after the burst.

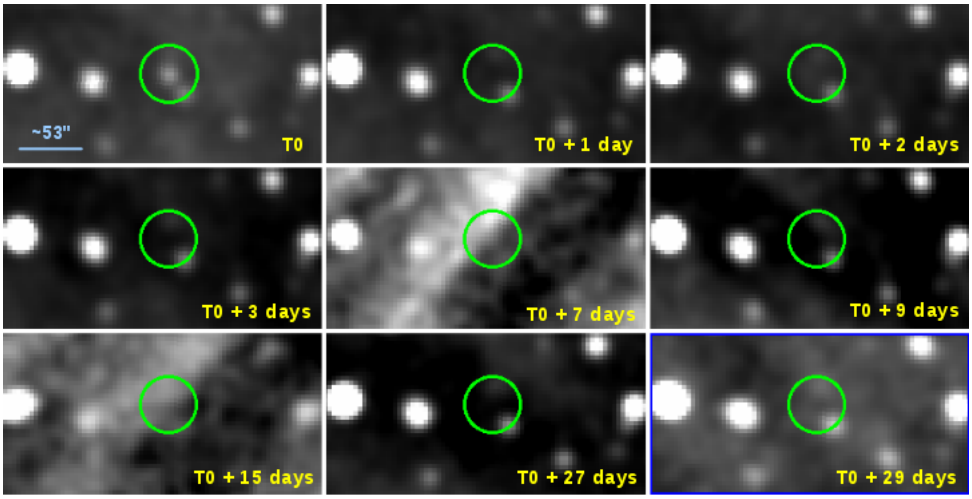

Figure 5.8: Observations at T0, T0 + 1, 2, 3, 7, 9, 15, 27 and 29 days after the neutrino alert ANT110531A. Images were co-added night by night . The candidate, circled in green, was only detected at T0.

This could indicate that the candidate is not the signature of a GRB afterglow, as the probability that such a bright GRB would have been missed by ground- and space-based observatories is low. Indeed, GCN notices have been checked and no GRB has been detected during this day. However, this information is not sufficient to firmly discard this candidate as possible counterpart to the neutrino trigger. The candidate light curve could also be compatible with an AGN flare, but those sources are quite well cataloged and the candidate is bright enough to have been observed previously. Therefore, this hypothesis is rejected with a high probability. To conclude, additional images taken between T0 and T0 + 1 day would have been necessary to obtain information about the behavior of the candidate, and to firmly conclude on his identification.

ANT111228A

This alert was sent to the optical telescope network after the detection of a neutrino in coincidence with the direction of the galaxy UGC 1281 (Figure 5.10 (a)). The first observation was made by TAROT Calern after a delay of 7 hours and 44 minutes. A total of 6 images of 180 seconds exposure with a mean limiting magnitude of $\sim$ 17.6 were taken. After processing, an interesting candidate was detected in four images (IM 2, 3, 4 and 5). In the first and last images (IM 1 and IM 6) of the night, the source was not bright enough to be selected by the pipeline. This candidate (RA=27.893°; dec=32.521° / l=137.365°; b = -28.660°) is shown in Figure 5.11.

The candidate is not cataloged in SIMBAD, NOMAD, USNO and 2MASS but a source appears in SDSS9 and AllWISE at 4.65 arcsec ($\sim$ 1.4 pixels) from the candidate position. This source (J015133.91+323113.2) is classified as a star with a R magnitude of 21.4 (Figure 5.10 (b)). However, the candidate was only detected at T0 although TAROT images were taken up to 60 days after the alert, as shown in Figure 5.12. ROTSE images were also taken at T0, T0 + 1, 3,

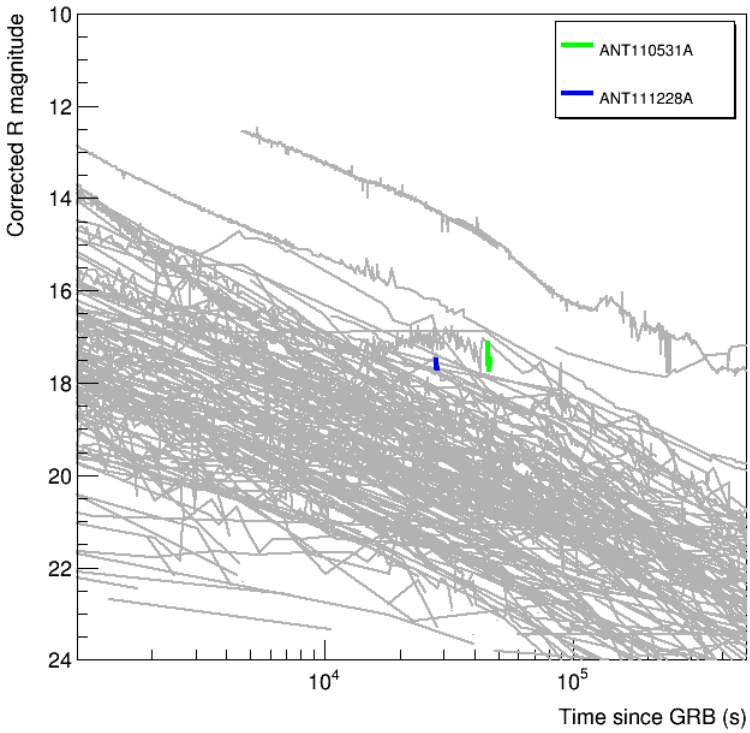

Figure 5.9: Comparison between the light curves of 2 candidates and 301 afterglow light curves for GRB detected with optical telescopes from 1997 to 2014.

(a) The neutrino alert was triggered with the directional criterion. The neutrino direction is indicated with a green circle, the candidate position is indicated in blue, and the galaxy UGC 1281 located at 0.39° from the neutrino direction and 0.43° from the candidate position is circled in red.

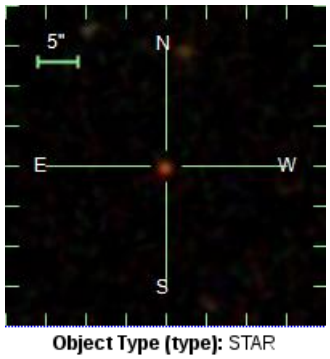

(b) Source cataloged at the position of the candidate.

Figure 5.10: Candidate position and source cataloged at this position.

4, 5, 6, 7, 8, 10 and 17 days after the trigger and the candidate is not present except at T0 but the source is partially masked because of bad pixels in this region. The candidate clearly shows a transient or variable behavior. Its light curve, illustrated in Figure 5.13, shows a decay of 0.2 magnitude between the first

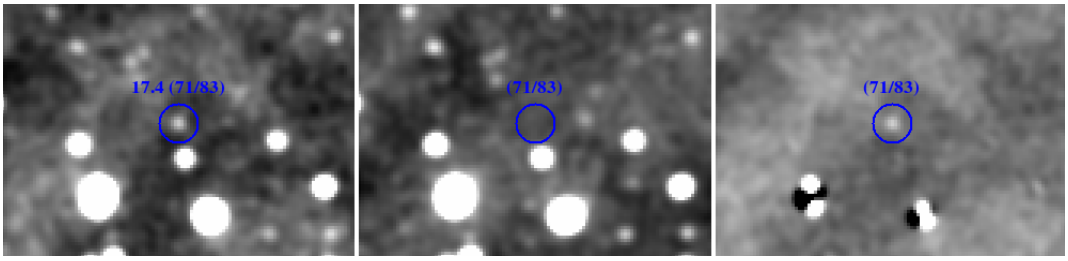

Figure 5.11: Candidate found in ANT111228A during visual inspection. From left to right: IM (second image at T0), REF at T0 + 27 days and SUB. The two bright objects at the bottom in the SUB image are bad subtractions of bright sources.

two points, and then a stable magnitude at 17.7, i.e., a few magnitudes brighter than the cataloged star. It may indicate the high variability of this cataloged source or the presence of another brighter source at the location of the cataloged star. The red color of the cataloged star may suggest the presence of a red dwarf. Those dwarfs are small and relatively cool stars (< 4000 K) on the main sequence and can be highly variable. They can emit flares on the minute timescale which increase their brightness by a few orders of magnitude. If the candidate found during the analysis correspond to this star, images were taken during a flare period as TAROT or ROTSE could not have detected such a source at the cataloged magnitude. However, this red dwarf cannot be identified as the counterpart to the neutrino trigger as no high energy production is expected from such a source. The second possibility, although less likely, is that a transient source possibly producing high energy neutrinos and brighter than the cataloged star appears at the same location of the red dwarf. In this case, a comparison between the candidate light curve and GRB afterglows was made as previously to test the GRB hypothesis (see the blue curve on Figure 5.9). More than 7 hours after the burst, less than 3 % of detected GRB afterglows are brighter than the candidate. This information is not sufficient to exclude the GRB hypothesis but tends to favor the first scenario. In any case, the candidate cannot be identified as the optical counterpart to the neutrino trigger.

5.3 X-ray results

The *Swift*-XRT has responded to 10 neutrino triggers from the ANTARES detector between mid 2013 and September 2015 (Table 5.2). These 10 alerts have been observed after a mean delay of 6.3 hours in 4 tiles with exposure varying from 0.8 to 1.9 ks. With such exposure times, a sensitivity from 6.0 to 2.6×10^{-13} erg cm^{-2} s^{-1} has been reached, respectively.

The tiled analysis found 35 X-ray sources, among which 6 sources were already known (see Appendix B, Table B.1). Although 29 new X-ray sources have been detected, none of them can be clearly associated with the neutrino trigger. However, for the alert ANT150901A, a variable X-ray signal has been observed in coincidence with the neutrino emission. This alert is discussed in the following section. The remaining 28 uncataloged sources were not bright enough to exceed

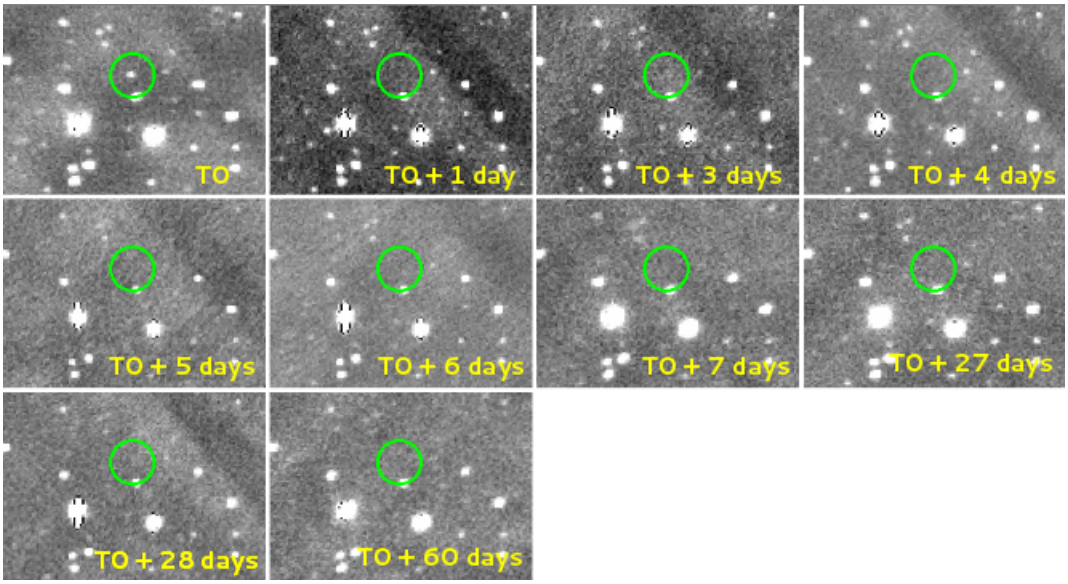

Figure 5.12: Observations at T0, T0 + 1, 3, 4, 5, 6, 7, 27, 28 and 60 days after the neutrino alert ANT111228A. Each image is the co-addition of all the images of a night. The candidate, circled in green, was only detected at T0.

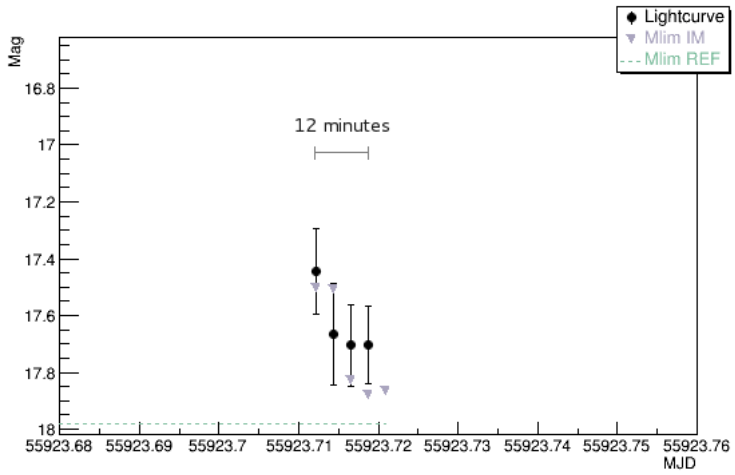

Figure 5.13: Light curve of the candidate found in ANT111228A. The candidate was detected at T0, in four images (IM 2, 3, 4 and 5), which represent a total time of 12 minutes. A variation of 0.2 magnitude is detected between IM 2 and IM 3. The green dashed line indicates the limiting magnitude of the REF image at $\sim$ 18, while blue triangles show the limiting magnitude of each IM at T0.

the 3 σ RASS upper limit (see Section 4.8). As the XRT failed to observe an X-ray counterpart to a neutrino trigger, this could indicate that the observation was made too late when the source could have faded below the limit of the existing catalogs, or that the source was outside the field of view of the XRT, or that the neutrino trigger was not originated by an X-ray source. Upper limits on the flux density from a potential X-ray counterpart has been derived. These limits correspond to the sensitivity reached for each 4-tile observation, and are

presented in Table 5.2.

5.3.1 ANT150901A

This alert was sent after 10 seconds to the optical telescope network and to the *Swift*-XRT after the detection of a very high energy neutrino ($N_{\rm hits}$=127, amp=356). The neutrino direction (RA = 246.306°; dec = -27.468° / l = 350.504°; b = 15.068°), with an uncertainty of 18 arcmin (radius, 50 % containment), was followed-up by MASTER SAAO and *Swift*-XRT after a delay of 9 hours 45 minutes, and 9 hours respectively. The alert was not followed-up by other optical telescopes because they were not connected (TAROT Chile, Zadko) or the field was not observable from the telescope position (TAROT Calern).

During the X-ray follow-up, *Swift* detected a bright object at this position: RA = 246.509°; dec = -27.304°, 6.8 arcmin away from the neutrino alert direction (Figure 5.14). The peak XRT count rate of this source was 0.087 (± 0.027) PSPC count/s, that is above the RASS upper limit at this location: 0.04 count/s (PSPC). This count rate corresponds to a peak 0.3-10 keV X-ray flux of $1.5(\pm0.5) \times 10^{-12}$ erg cm^{-2} s^{-1}, which is comparable to the deepest 0.2-12 keV flux limit from XMM-Newton (1.8×10^{-12} erg cm^{-2} s^{-1}). This source potentially interesting was not cataloged in X-rays, and was likely either a variable X-ray object or a transient possibly related to the ANTARES trigger. The probability that the X-ray source is simply part of the background population has been estimated: $\sim$ 0.1 serendipitous sources are expected at the observed brightness in this exposure.

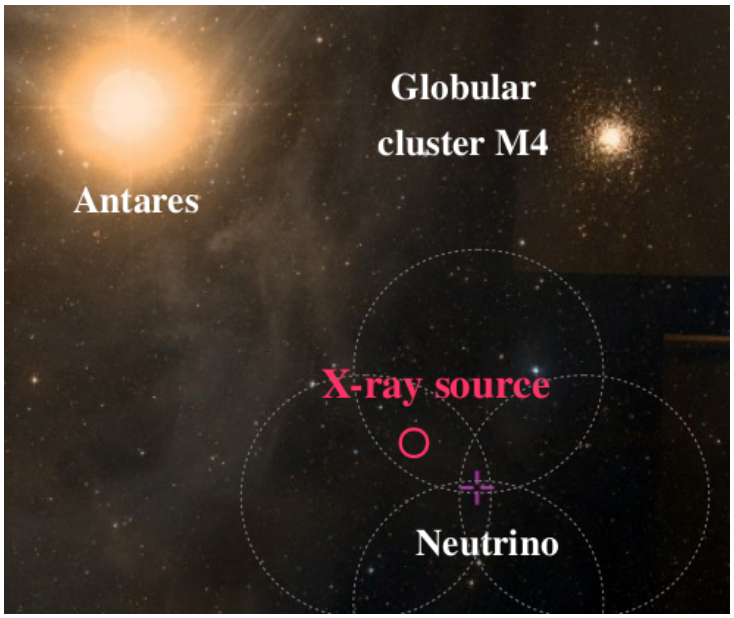

Figure 5.14: Direction of the neutrino that generated the alert ANT150901A (purple cross). The globular cluster M4 and the Antares star are located at 0.8° and 1.4° from the neutrino direction, respectively. A variable X-ray source was found at 6.8 arcmin from the neutrino direction and is indicated in pink. The four fields observed by the *Swift*-XRT are shown by gray dashed lines.

Table 5.2: Details of the 10 ANTARES triggers observed by the *Swift*-XRT since 2013.

Trigger name (ANTyymmddA)	Error radius (°)	Delay[a] (hours)	Mean exposure (ks)	Sensitivity ($\times 10^{-13}$ erg cm^{-2} s^{-1})	New sources (total)[b]	Counterpart candidates	$P_{\text{reject}}^{\text{GRB},\nu_c}$
ANT130722A	0.4	1.1	1.8	2.74	4 (5)	0	0.71
ANT130915A	0.3	6.5	1.4	3.48	2 (2)	0	0.60
ANT130927A	0.4	5.1	1.3	3.84	3 (4)	0	0.60
ANT140123A	0.35	4.7	0.8	5.99	1 (1)	0	0.55
ANT140311A	0.35	2.8	1.7	2.88	3 (3)	0	0.68
ANT141220A	0.4	3.5	1.9	2.63	2 (2)	0	0.67
ANT150129A	0.35	1.7	1.9	2.67	3 (3)	0	0.69
ANT150409A	0.33	12.7	1.8	2.74	5 (5)	0	0.56
ANT150809A	0.3	15.4	1.8	2.86	2 (2)	0	0.53
ANT150901A	0.3	9.0	1.8	2.82	4 (8)	1	0.61

[a] Delay between the neutrino trigger and the first observation by the *Swift*-XRT.
[b] Number of uncataloged sources among the total number of detected sources in each 4-tile observation. Details can be found in Appendix B.
[c] Probability to reject the hypothesis that the neutrino comes from a detectable GRB (see Section 5.4.3).

At the position of the X-ray source, a bright (R_{mag}=12.6) cataloged star (USNO-B1.0 0626-0501169) has been found, as shown in Figure 5.15. The question was to know if the neutrino emission was related to the X-ray source and/or the star. Follow-up observations by *Swift* have thus been made during the following days of the alert. A variable behavior has been observed, with a notable increase of the brightness several hours after the first observation with the XRT. However, no magnitude variation has been observed in optical wavelengths. The X-ray light curve obtained with observations up to 7 days after the neutrino detection is shown in Figure 5.16.

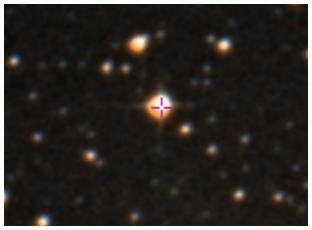

Figure 5.15: Bright star cataloged (USNO-B1: 0626-0501169) at the position of the X-ray source (purple cross) detected during the X-ray follow-up of ANT150901A. (DSS2 image).

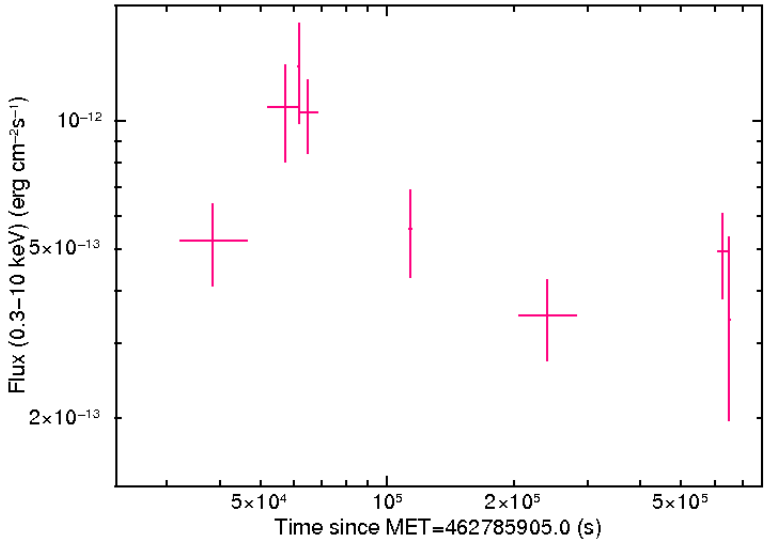

Figure 5.16: Light curve of the X-ray source detected during the follow-up of ANT150901A.

The first GCN and ATel (Astronomer's telegram) notices[1] of the ANTARES Collaboration have been sent 2 days after the neutrino detection to get more observations and try to identify the X-ray source. A large response from the astronomical community has been received, generating a total of 6 GCN notices and 14 ATels[2]. Among them, imaging of the X-ray source position with Pan-STARRS revealed that there are no galaxies within about 5 arcsec of the *Swift* X-ray position, to approximately i $\sim$ 23 (ATel #7992). In addition, there is no history of variable objects in the Pan-STARRS1 multi-epoch data or the Pan-STARRS Survey for Transients within the vicinity of the X-ray source. This indicates that the X-ray source is not obviously associated with an extragalactic

[1]GCN #18231 and ATel #987.

[2]GCN #18236, #18239, #18240, #18241, #18242, #18352, ATel #7992, #7993, #7994, #7995, #7996, #7998, #7999, #8000, #8002, #8003, #8006, #8027, #8097, #8124.

source, and it appeared that a physical association of the X-ray source, the bright star and the neutrino is unlikely.

The first explanation on the X-ray emission came from optical/near-infrared spectroscopy performed with the 2.5 m NOT telescope at La Palma (GCN #18236, ATel #7994). Spectra obtained with the FIES high resolution spectrograph in the visible and NOTCam in the near-infrared K-band revealed multiple absorption features as well as hydrogen Balmer lines in emission. This pointed to the star USNO-B1.0 0626-0501169 being a young accreting G-K star undergoing a flaring episode that produced the X-ray emission. Furthermore, this star is close to the nearby Rho Ophiuchi star forming region, being probably associated with it.

The multi-wavelength data set obtained from follow-up observations of the X-ray source position strengthens this hypothesis according to which the X-ray emission would be associated to the star, but not to the neutrino detection. Therefore, this X-ray flare cannot be identified as the counterpart to the ANTARES neutrino detection.

5.4 Limit on a GRB association

GRBs are the major candidate sources of high energy neutrinos among the population of fast transients. In the standard fireball model of GRBs [129], internal shocks between faster and slower shells of plasma expulsed in a highly relativistic jet would be responsible for the observed prompt gamma-ray emission, resulting in photohadronic interactions. Hadronic models of GRBs [130, 131] suggest that there could be a significant proton loading in GRB's jets. If these protons are sufficiently accelerated they can interact with the ambient gamma photon field via pγ mechanisms [132, 133]. The photohadronic interactions would produce charged pions, subsequently decaying into high energy neutrinos. Details of the physical processes taking place in the GRB prompt emission are still under debate and the neutrino expectations are highly dependent on the GRB prompt model used.

According to the standard framework of internal shocks, the expected number of detectable neutrinos from two luminous bursts GRB110918A, GRB130427A and one typical burst GRB081008 can be estimated. The predicted neutrino spectra from the NeuCosmA model [132, 134] that simulates the complete pγ mechanism (Δ-resonance, kaon production, multiple pions decay) in the internal shock GRB model are used. Standard values for the unknown physical parameters are assumed, such as the Lorentz factor $\Gamma = 316$, the baryonic loading $f_p = 10$ and the fraction of internal energy given to the magnetic field and electrons $\epsilon_B = \epsilon_e = 0.1$. The expected number of prompt neutrinos for each individual GRB is $\mu_s = 3.4 \times 10^{-2}$, $\mu_s = 6.6 \times 10^{-3}$ and $\mu_s = 2.3 \times 10^{-5}$ for GRB110918A, GRB130427A and GRB081008, respectively. So far, no neutrino signal has been observed in coincidence with a GRB. Nevertheless, the probability to observe n neutrinos with a given signal μ_s can be estimated with a Poissonian distribution. The probabilities to detect at least one neutrino from the mentioned GRBs are $P(X \geq 1|3.4 \times 10^{-2}) \sim 3.4$ %, $P(X \geq 1|6.6 \times 10^{-3}) \sim 0.7$ % and $P(X \geq 1|2.3 \times$

10^{-5}) ~ 0.002 %, respectively. Albeit these discovery probabilities are weak, one should not forget that they are affected by strong theoretical uncertainties. The TAToO program offers an opportunity to test the GRB origin for each detected neutrino with the advantage of not depending on an underlying GRB model.

5.4.1 Background expectation

As no GRB afterglow has been identified in early follow-up images, it is important to assess the compatibility of this measurement with the background expectation.

The probability, P_s, to detect a serendipitous GRB afterglow lying in the follow-up region for each neutrino alert is given by:

$$P_s(\mathrm{GRB}, \nu) = R_{\mathrm{GRB}} \times p(\mathrm{ag}|\mathrm{GRB}) \times \frac{\Omega}{4\pi} \times T_{\mathrm{obs}} \tag{5.1}$$

where R_{GRB} is the average GRB discovery rate (1000/yr) in the entire sky [135] and $p(\mathrm{ag}|\mathrm{GRB})$ is the probability of detecting the afterglow counterpart of a detected GRB. This probability is 0.4 and 0.5 for TAROT and ROTSE respectively [136, 137], and 0.95 for *Swift* [135]. The solid angle, Ω, viewed by the telescopes is given by $\Omega = 2\pi(1 - cos\ \theta)$ with $\theta \sim 1^\circ$ for TAROT and ROTSE, and $\theta \sim 0.2^\circ$ for the *Swift*-XRT. T_{obs} is the exposure time of the early observation of each neutrino alert. The optical follow-up lasts about 20 minutes, while the X-ray follow-up lasts 2 ks for each tile. Thus, $P_s(\mathrm{GRB}, \nu) = 1.2 \times 10^{-6}$ and 1.5×10^{-6} for each alert with an early optical follow-up with TAROT and ROTSE respectively, and $P_s(\mathrm{GRB}, \nu) = 1.8 \times 10^{-7}$ for each alert with X-ray images, and for each tile. Consequently, a discovery of a GRB afterglow would be unambiguously associated with the neutrino alert.

5.4.2 Optical GRB association

Because in this study no optical counterpart has been observed in coincidence with the 42 neutrino alerts, the probability to reject a GRB associated with each neutrino alert can be directly estimated. To do so, a comparison is made between the optical upper limits obtained for each neutrino alert with optical afterglow light curves of GRBs detected from 1997 to 2014, as shown in Figure 5.17.

The cumulative distribution functions (CDFs) of afterglow magnitudes (corrected by the galactic extinction) are computed at times coincident with the first early follow-up observation of the neutrino alerts. Figure 5.18 shows these CDFs at typical times t = 30 seconds, 5 minutes, 1 hour and 1 day after the GRB in the observer frame. The probability, $P_{\mathrm{reject}}^{\mathrm{GRB},\nu}$, to reject a GRB origin hypothesis for each detected neutrino can be directly extracted from the CDFs, accounting for the field of view of telescopes[3]. The $P_{\mathrm{reject}}^{\mathrm{GRB},\nu}$ are listed in Table 5.1 for each alert.

According to Figure 5.17, stringent upper limits on the early afterglow magnitude a few minutes after the neutrino trigger can be set. For the two neutrino

[3]The probabilities extracted from the CDFs are multiplied by the percentage of the ANTARES PSF covered by the telescopes: $\sim$ 90 % for a directional neutrino trigger and $\sim$ 96 % for a high energy trigger (see Table 3.1).

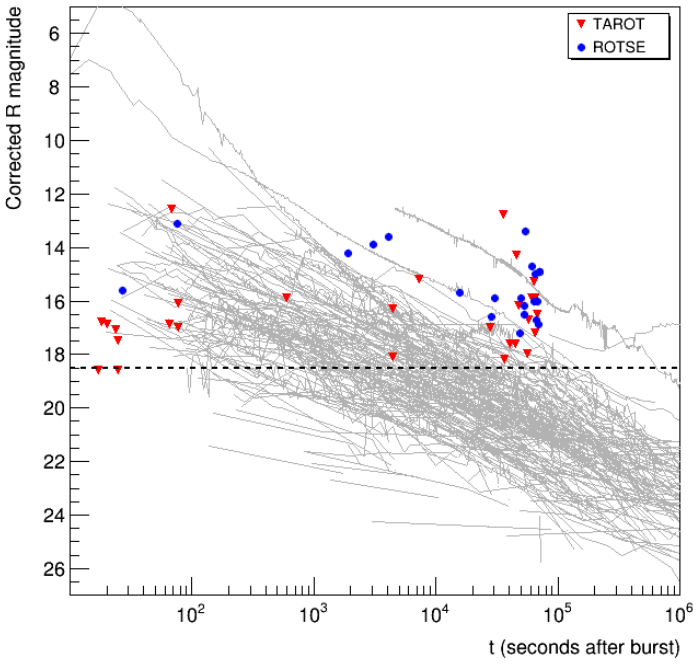

Figure 5.17: Gray lines: corrected R magnitude as a function of time for 301 GRB afterglows observed from 1997 to 2014 by optical telescopes. Red & blue dots: upper limits on GRB magnitudes for neutrino alerts observed by TAROT and ROTSE, respectively. Each point represents the first image of the observation, corresponding to an exposure of 180 seconds for TAROT images, and 20 or 60 seconds for ROTSE images. The horizontal dashed line corresponds to the maximum sensitivity of the telescopes.

alerts ANT121010A and ANT150122A, a GRB origin is strongly rejected since no early afterglow at a time t $<$ 30 seconds after the burst has ever been observed at weaker magnitude than $\sim$ 18. Except for the alert ANT121206A (low limiting magnitude), a GRB association is rejected at a better than 80 % confidence level within 1 minute after the neutrino trigger. On the contrary, when the optical follow-up starts more than a few minutes after the trigger, due to the sensitivity of the telescopes, the derived upper limits do not constraint a GRB origin for the detected neutrinos.

5.4.3 X-ray GRB association

As no X-ray counterpart has been identified in coincidence with the 10 neutrino alerts, an analysis similar to that in the optical domain is performed with 689 X-ray afterglow light curves detected by the *Swift*-XRT from 2007 to 2015 (Figure 5.19). A comparison is made between these light curves and the X-ray upper limits obtained for the 10 neutrino alerts.

The CDFs of the X-ray afterglow fluxes are also computed at times coincident with the first XRT observation of neutrino alerts. Figure 5.20 shows these CDFs at t = 1, 2, 4 and 8 hours after the GRB in the observer frame. The probabilities

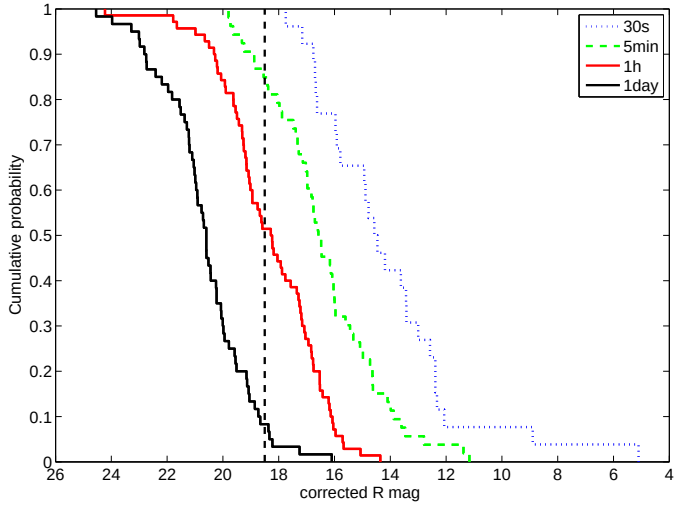

Figure 5.18: Cumulative distribution of afterglow magnitudes for 301 detected GRBs (Figure 5.17). Each line corresponds to different times after burst. The vertical dashed line represents the limiting magnitude of the optical telescopes.

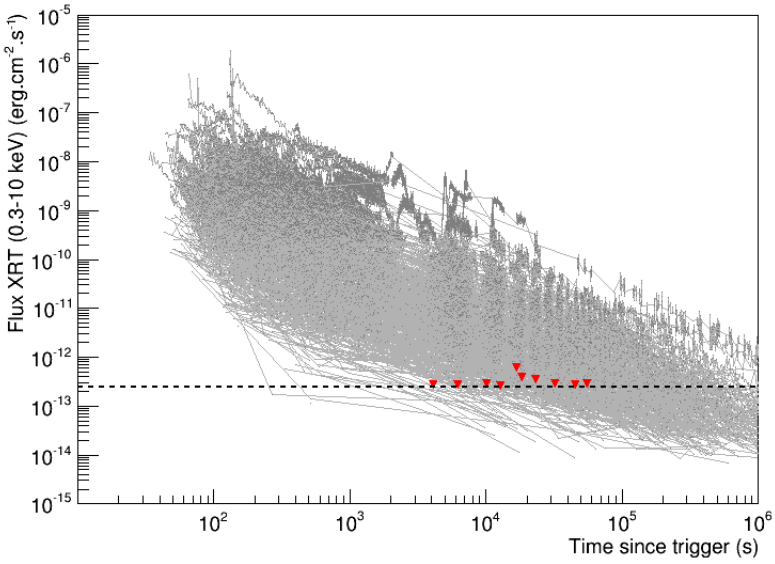

Figure 5.19: Gray lines: 689 X-ray afterglow fluxes in the energy band from 0.3 to 10 keV detected by the *Swift*-XRT from 2007 to 2015 as a function of time. The upper limits on GRB fluxes for 10 neutrino alerts are represented by red triangles. The horizontal dashed line corresponds to the sensitivity reached with a 2 ks exposure.

to reject a GRB origin of the neutrino events are calculated as previously[4] and are listed in Table 5.2. According to Figure 5.19, if each detected neutrino comes from a GRB, strong upper limits on the GRB afterglow X-ray flux can be set, $F_X \lesssim 2.5 \times 10^{-13}$ erg cm^{-2} s^{-1}. For the alert ANT130722A, the probability to

[4]For the X-ray follow-up, about 72 % of the ANTARES PSF is covered.

reject a GRB origin is as high as 71 % with an upper limit on the X-ray flux of $\sim 2.74 \times 10^{-13}$ erg cm^{-2} s^{-1} only 1.1 hours after the neutrino trigger. Clearly, a GRB origin is very unlikely for these neutrino events, since few GRBs are known to have weaker X-ray afterglows than these upper limits.

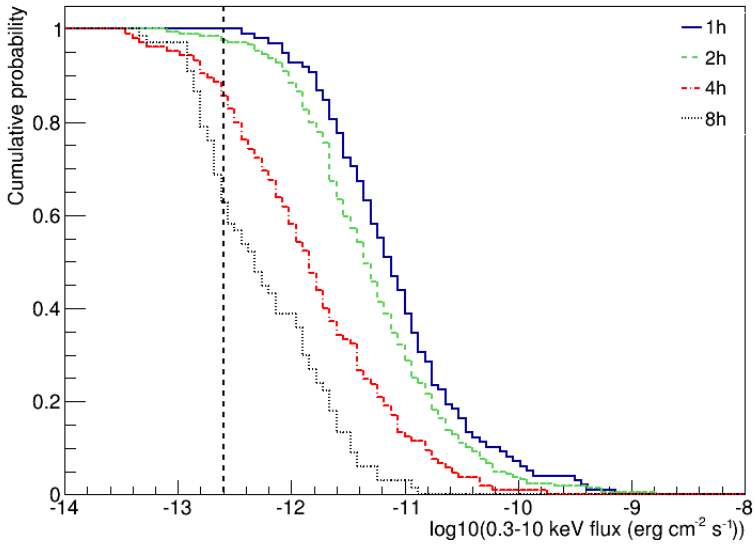

Figure 5.20: Cumulative distribution of X-ray afterglow magnitudes for 689 GRBs detected by the *Swift*-XRT since 2007. Each line represents different times after bursts. The vertical dashed line represents the sensitivity reached with a 2 ks exposure.

5.4.4 Consistency with the triggered search

Within the ANTARES collaboration, different multi-messenger analyses have been performed to search for neutrinos from GRBs. Besides the TAToO program, a triggered search method has been implemented. This method is based on the search for neutrino candidates in conjunction with an accurate timing and positional information provided by an external trigger, such as gamma-ray or X-ray satellites.

A search for neutrinos in coincidence with GRBs using ANTARES data from 2007 to 2011 has been performed [138], using a selected sample of 296 long GRBs representing a total equivalent live time of 6.6 hours. The time information has been provided by the *Swift* and *Fermi* satellites via the GCN system. The expected neutrino fluxes have been calculated for each burst individually with the NeuCosmA model.

No neutrino event was found in coincidence with the selected GRBs and within 10° around each. In total, 0.06 signal events were predicted from the NeuCosmA model against a background of 0.05 events. The 90 % confidence level upper limit has been placed on the cumulative flux of the whole sample according to the NeuCosmA model, as well as to the commonly used analytic Guetta model [49], as shown in Figure 5.21.

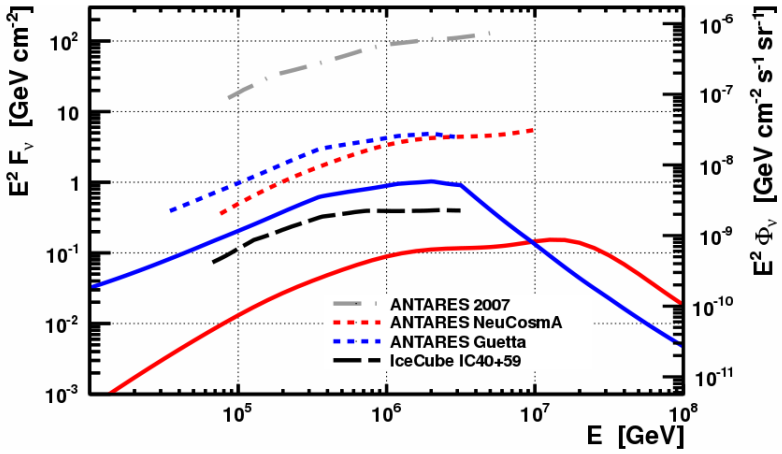

Figure 5.21: Sum of the 296 individual GRB neutrino spectra used in this analysis, for the NeuCosmA model in red and for the analytic Guetta model in blue. Short-dashed lines represent the limits set by this analysis. The experimental limits on the total flux for ANTARES [139] (gray) and IceCube IC40+59 [140] (black) are also shown.

This result is consistent with the non observation of GRBs associated with TAToO neutrino alerts.

5.5 Improvements for early follow-up

The optical and X-ray upper limits derived from the follow-up of 48 neutrino alerts have proved that the TAToO system is able to quickly check the GRB origin of the high energy neutrinos detected by ANTARES. Further improvements, such as starting the follow-up as soon as possible after the trigger, would enable more definite conclusions on the origin of these high energy neutrinos.

Optical domain

While small robotic telescopes, such as TAROT and ROTSE, are well-suited to quickly respond to ANTARES alerts, their diameters do not permit magnitudes deeper than ~ 18.5 to be reached. This limits the ability of the TAToO program to investigate a GRB origin of the detected neutrinos to within only a few minutes after the ANTARES trigger. A one-meter-class robotic telescope is crucial to efficiently extend the optical follow-up of ANTARES alerts with stronger constraints on the neutrino/GRB association up to a few hours after the neutrino trigger.

Since 2013, the Zadko telescope has been included in the optical telescope network (see Section 3.2.1). This one meter fully robotic telescope is very interesting for the TAToO program as it is located in the area where most of the ANTARES neutrino alerts are immediately visible (Figure 3.29). Thanks to its larger aperture, about 3 times larger than the TAROT and ROTSE telescopes, the limiting magnitude of the Zadko telescope with only 60 seconds of exposure

is 1.4 magnitudes deeper compared to the TAROT telescopes, with 180 seconds of exposure (Figure 5.22). This represents a gain of about a factor of 4 on the optical sensitivity. The best response of Zadko to an ANTARES alert achieved so far is about 70 seconds after the neutrino trigger. The combination of its reasonable response, its larger aperture and its good location will help to better constrain the origin of high energy neutrinos.

In addition, five telescopes from the MASTER network have also joined the TAToO program since March 2015 (see Section 3.2.1). The first alert sendings with MASTER demonstrate the rapid response time to the TAToO alert of about 24 seconds after the neutrino trigger (Figure 5.22), which is roughly the same performance as TAROT. Thanks to this new partnership with MASTER, the very early optical follow-up (less than a minute) of ANTARES alerts will be considerably more efficient at constraining the origin of each neutrino.

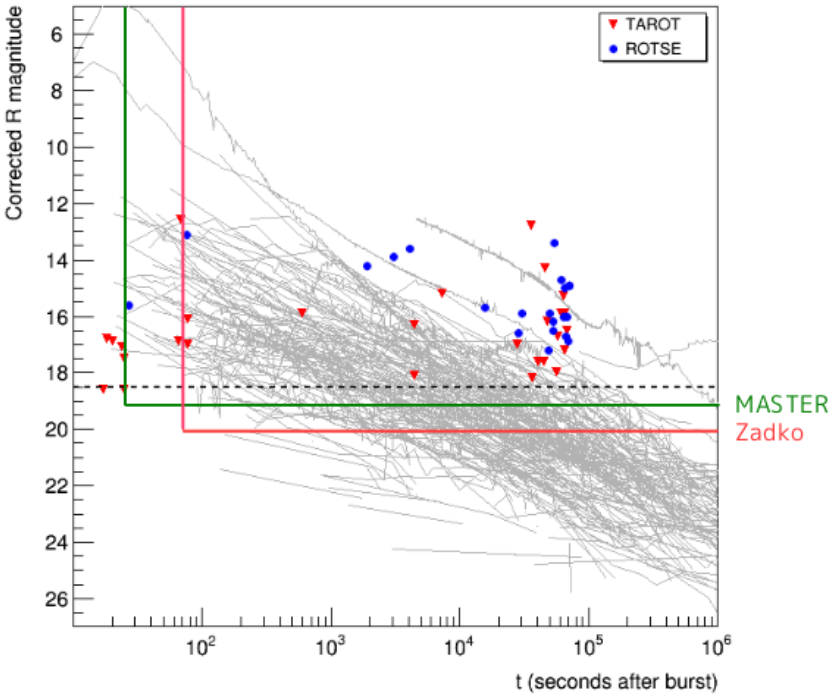

Figure 5.22: Sensitivity obtained with the MASTER (green) and Zadko (pink) telescopes compared to optical afterglow light curves.

Finally, the addition of an infrared follow-up to TAToO alerts would be very helpful, since this part of the electromagnetic spectrum is less subject to dust absorption. In the case of GRBs, this new wavelength domain will allow a larger population of GRBs (e.g., extinguished GRB afterglows) to be explored, with a correspondingly higher neutrino detection potential.

X-ray domain

In the X-ray domain, the fastest response to the 10 neutrino alerts was about 1 hour. While strong constraints on the GRB origin of the high energy neutrinos

detected are set, a faster response or a better X-ray sensitivity would almost undoubtedly allow for the rejection (or confirmation) of the GRB origin hypothesis.

With the next generation of neutrino telescopes, such as KM3NeT (see below), the X-ray follow-up will be possible with the arrival of new high energy missions. In the case of the SVOM mission ($\sim$ 2021) [141], Target-of-Opportunity alerts will be accepted, and X-ray follow-up of neutrino alerts by the MXT instrument [142] is under discussion. The sensitivity of the SVOM-MXT (3×10^{-12} erg cm^{-2} s^{-1} with 1 ks exposure) would allow roughly the same constraints as for the *Swift*-XRT to be reached. Moreover, with the field of view of the MXT ($\sim 1^\circ \times 1^\circ$), only one tile will be needed, allowing time to be saved for other neutrino alert follow-ups.

The future neutrino detector KM3NeT

KM3NeT[5] is the next-generation of neutrino telescope based on the same detection techniques as ANTARES in deep seawater. The size of the KM3NeT detector, at several cubic kilometers, will increase the sensitivity to neutrino fluxes by about a factor 50 compared to ANTARES. By convolving the expected KM3NeT response function with the neutrino flux expected from the NeuCosmA model, the number of high energy neutrinos, μ_s, expected from GRB110918A and GRB130427A can be estimated. For these two GRBs, $\mu_s = 1$ and $\mu_s = 0.4$, respectively. This expectation is clearly encouraging, and the detection of high energy neutrinos in coincidence with GRBs will be achievable with the future KM3NeT detector. Including the faster response of the future X-ray telescopes and a better optical/X-ray sensitivity of the TAToO telescope network, a factor of ~ 100 in sensitivity would be gained for probing a GRB origin for high energy neutrinos.

[5] www.km3net.org

CHAPTER 6

Long term follow-up analysis

In this chapter, the results from the analysis of long term follow-up observations to search for slowly varying transient sources are presented. This analysis relies on neutrino alerts sent from October 2009 to January 2015, for which optical observations have been made up to 2 months after the neutrino detection. The first part of the chapter describes the data set, as well as the results of the optical counterpart search. In the second part, the results are interpreted in the case of CCSNe, and the limit calculation on the Ando & Beacom model (AB05) [64] parameters for CCSNe with mildly relativistic jets is presented.

6.1 Data set

From October 10 2009 to January 29 2015, 132 alerts have been forwarded to the optical telescope network. Among them, 6 alerts were not followed-up due to a position too close to the Sun. For 25 neutrino alerts, follow-up images are of bad quality (i.e., they have been tagged as bad and discarded from the analysis by the pipeline) or have been taken for only one or two nights[1]. Furthermore, 7 alerts have been discarded from the analysis due to crowded fields or calibration issues. Finally, reference images are not available for 23 alerts. Indeed, as we are looking for slowly varying transients, such as CCSNe, reference images have to be taken typically at T0, T0 + 1, 2 or 60 days after the neutrino trigger, where the signal is supposed to be lower than in the other images. The search for optical counterparts has thus been performed for a total of 71 neutrino alerts.

The alert time and coordinates, the type of the trigger, and the energy in terms of number of hits and amplitude are presented in Appendix A for each of the 71 alerts with long term follow-up images. Figure 6.1 shows the amplitude distribution as a function of the number of hits for these alerts, among which 51 have been triggered with the high energy criterion, and 20 with the directional criterion.

[1]To detect a magnitude variation, the analysis of two IM is required. If only two observations have been performed for a neutrino alert, an additional REF image has to be taken by the telescopes.

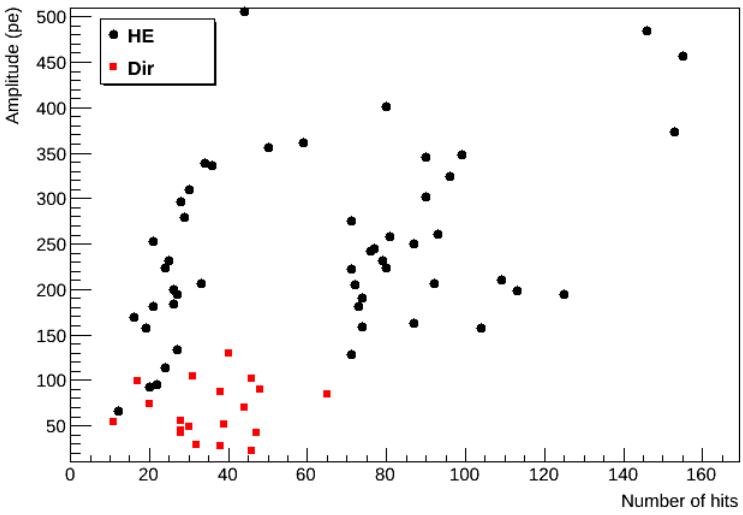

Figure 6.1: Amplitude distribution of 71 alerts for which long follow-up observations have been analyzed as a function of the number of hits. Red squares indicate the neutrinos selected with the directional criterion, while blue points show the high energy neutrino events.

6.2 Optical counterpart search

The optical counterpart search has been performed for 71 alerts, as described in Chapter 4. As we are looking for transient sources with variations at the day/week timescale such as for SNe, images have been co-added night by night to enhance the detection sensitivity. The details of follow-up observations are described in Appendix C for each alert. For most of the alerts, images have been taken by the TAROT telescopes (especially, by TAROT Chile). In the case where TAROT and ROTSE observations have been made on the same dates, the best quality images have been analyzed. Up to 12 nights have been processed for each alerts, with limiting magnitudes ranging from 14.0 to 19.4. The combination of a good follow-up and high limiting magnitudes, as for example for ANT111205A, ANT121010A and ANT121206A, is required to detect and identify slow transients.

After image analysis and visual inspection of candidates, no optical transient source was identified as the counterpart associated with one of the 71 detected neutrinos. However, many variable objects not compatible with what is expected from CCSNe (i.e., a rising signal starting at T0) were found during the image analysis. Two examples are discussed in the following section.

6.2.1 Examples of variable sources

ANT110428A

This alert, triggered by a high energy neutrino event, was followed-up by TAROT Chile during 10 observation nights, as shown in Table 6.1. A total of 46 good quality images, i.e., images tagged as good by the calibration step of the image

analysis pipeline, were analyzed as described in Chapter 4. Images were co-added night by night, and the observation at T0 + 61 days was used as reference for the subtraction step. During the visual inspection of residual objects, one variable candidate was found (Figures 6.2 and 6.3). This candidate (RA = 314.894°; dec = -42.942° / l = 358.259°; b = -41.012°) was detected in 4 nights, and the corresponding light curve is presented in Figure 6.4. The object was not detected in the other nights because its magnitude was too faint (see Figure 6.5).

Table 6.1: Details of the 10 follow-up observations for the ANT110428A alert performed from 2 to 61 days after the neutrino trigger. The number of good quality images is indicated in the second column. Images were co-added night by night and the limiting magnitude of the resulting stack is indicated in the last column. The observation at T0 + 61 days served as reference for the subtraction.

Night	Images	$m_{lim,stack}$
T0 + 2 days	6	18.1
T0 + 5 days	1	17.2
T0 + 6 days	3	17.5
T0 + 7 days	4	18.1
T0 + 8 days	2	16.1
T0 + 10 days	6	16.9
T0 + 16 days	6	18.9
T0 + 28 days	6	18.4
T0 + 46 days	6	17.8
T0 + 61 days	6	18.9

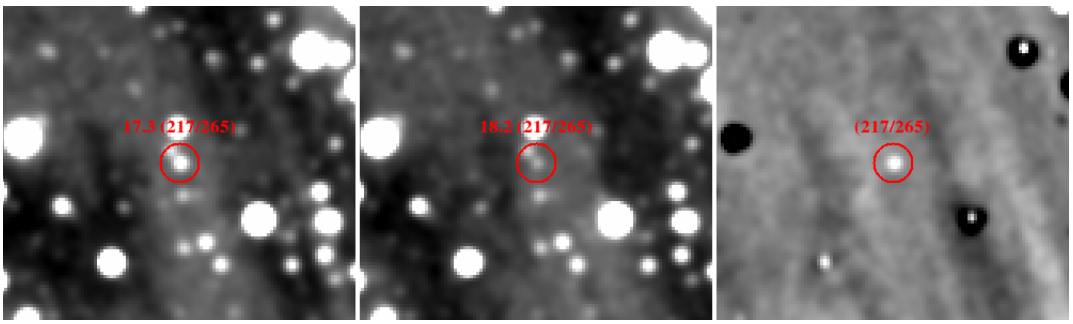

Figure 6.2: Candidate found during the visual inspection of ANT110428A. From left to right: IM at T0 + 16 days, REF at T0 + 61 days and SUB.

The candidate is cataloged in USNO-A2 (0450-39376511) with a R magnitude of 17.7 and appears on DSS2 images but not in 2MASS, as shown in Figure 6.6. No indication of the variability of this source is reported in catalogs. Hence, to know if it could be the optical counterpart to the neutrino trigger, its light curve was compared to a template of SNe Ib/c (see Chapter 4, Figure 4.26). Between T0 + 7 and T0 + 16 days, the candidate light curve decreases by about 1.3 magnitudes. Such a decrease for SNe Ib/c typically takes about 20 days after the peak magnitude. The candidate magnitude decreases too fast to be compatible

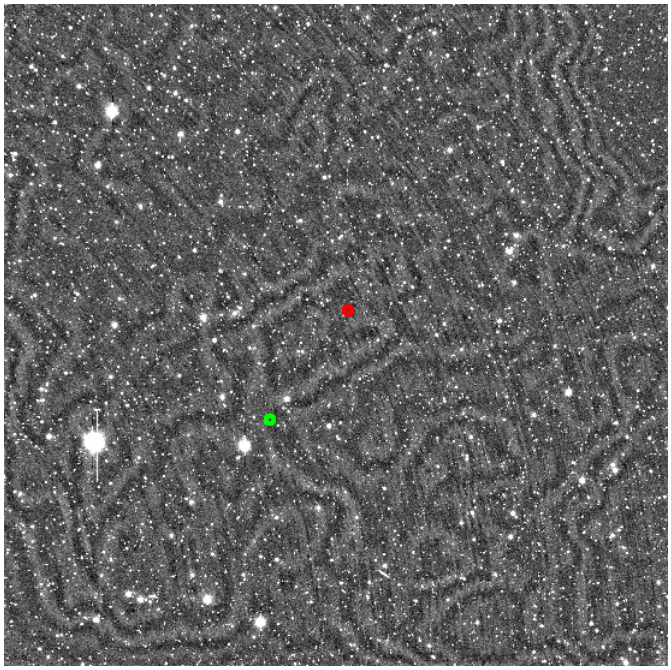

Figure 6.3: The candidate found in ANT110428A (green) is located at $\sim 0.4°$ from the neutrino direction (red).

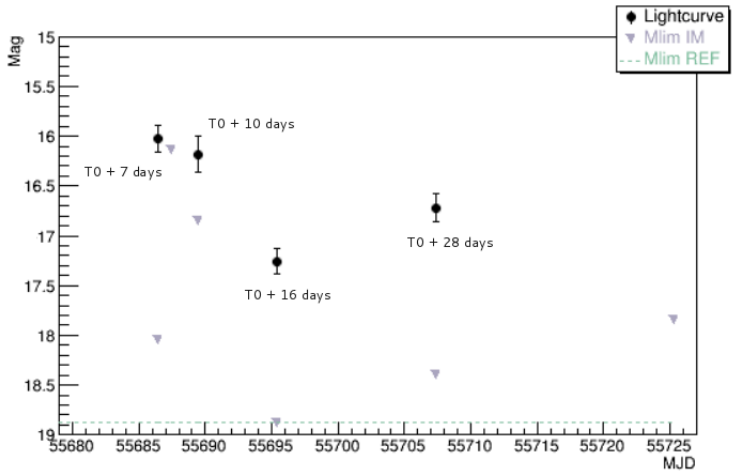

Figure 6.4: Light curve of the candidate found in ANT110428A. This candidate was detected at T0 + 7, 10, 16 and 28 days. The green dashed line indicates the limiting magnitude of the REF image at ~ 18.9, while blue triangles show the limiting magnitude of each IM.

with a standard SN Ib/c. Furthermore, if the decrease starts 7 days after the neutrino alert, it may indicate a SN explosion, and thus a possible high energy neutrino production, about 2 weeks before the neutrino alert ANT110428A as a SN light curve typically rises during 20 days after the explosion before decreasing.

Finally, the re-brightening of the candidate between T0 + 16 and T0 + 28 days confirm the non-detection of a SN and rather suggests the presence of a

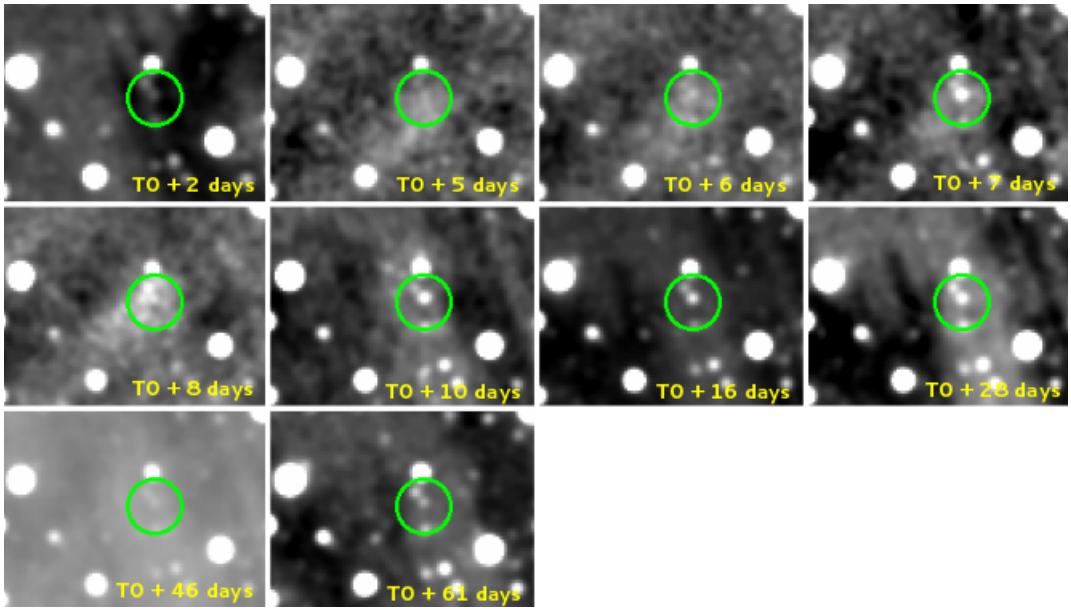

Figure 6.5: The candidate found during the image analysis of ANT110428A was detected at T0 + 7, 10, 16, 28 and 61 days after the alert. In the other nights, the object was too faint to be detected.

variable star. The candidate cannot be identified as the optical counterpart to the neutrino trigger as no high energy neutrino production is expected from such sources.

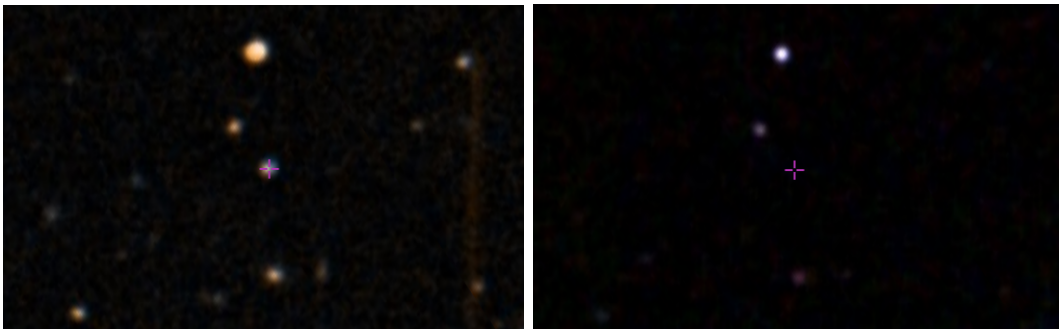

Figure 6.6: The candidate (pink cross) detected in ANT110428A appears on DSS2 images (left) but not in 2MASS (right). Field $\sim$ 2.7 arcmin.

ANT131009A

For the alert ANT131009A, 12 observations were made by TAROT Chile after the detection of a high energy neutrino event. Images from 2 to 61 days after the neutrino trigger were taken and analyzed with the dedicated pipeline. Co-addition was made for images of the same night to obtain deeper stack images (Table 6.2), and the reference image was chosen at T0 + 61 days. One variable candidate, presented in Figure 6.7, was found during visual inspection at coordinates RA = 104.793°; dec = -43.548° / l = 253.689°; b = -17.001°, about 0.3°

Table 6.2: Details of the 12 observations made by TAROT Chile up to 61 days after the alert ANT131009A. The number of good quality images is indicated in the second column. Images were co-added night by night and the limiting magnitude of the resulting stack is indicated in the last column. The observation at T0 + 61 days served as reference for the subtraction.

Night	Images	$m_{\mathrm{lim,stack}}$
T0 + 2 days	1	16.8
T0 + 3 days	2	17.3
T0 + 4 days	2	17.5
T0 + 5 days	3	17.9
T0 + 6 days	4	16.8
T0 + 7 days	5	18.2
T0 + 8 days	6	18.5
T0 + 10 days	6	18.3
T0 + 16 days	6	18.8
T0 + 28 days	6	18.9
T0 + 46 days	6	17.5
T0 + 61 days	6	18.9

from the neutrino direction (Figure 6.8). This candidate was selected with the "magnitude variation" criterion and only detected at T0 + 8, 10 and 16 days, and in the reference image at T0 + 61 days, as shown in Figure 6.9. In the other nights, the object did not seem to appear or was too faint to be detected by the pipeline. The candidate is not cataloged in NOMAD, SDSS and 2MASS. A DSS2 field of $\sim$ 2.3 arcmin is shown in Figure 6.10.

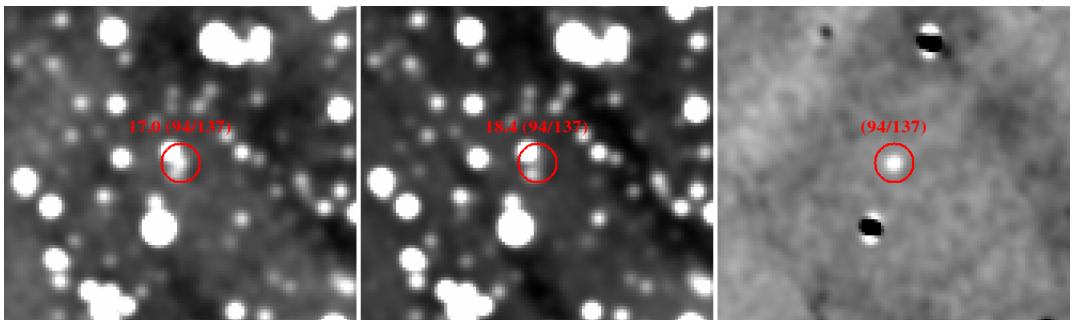

Figure 6.7: Candidate found in ANT131009A. From left to right: IM (T0 + 8 days), REF (T0 + 61 days), SUB.

The light curve of this candidate shows a decrease of 0.6 magnitude in 8 days (Figure 6.11), and was compared to a SN Ib/c template to identify a possible SN signature. This decrease is compatible with a typical SN Ib/c light curve if the peak magnitude was reached a few days before the start of such a decrease. In this case, the candidate would have been detected in images taken at T0 + 2, 3, 4, 5, 6 and 7 days because of a brighter magnitude, and the explosion of the SN would have occurred more than 10 days before the neutrino detection.

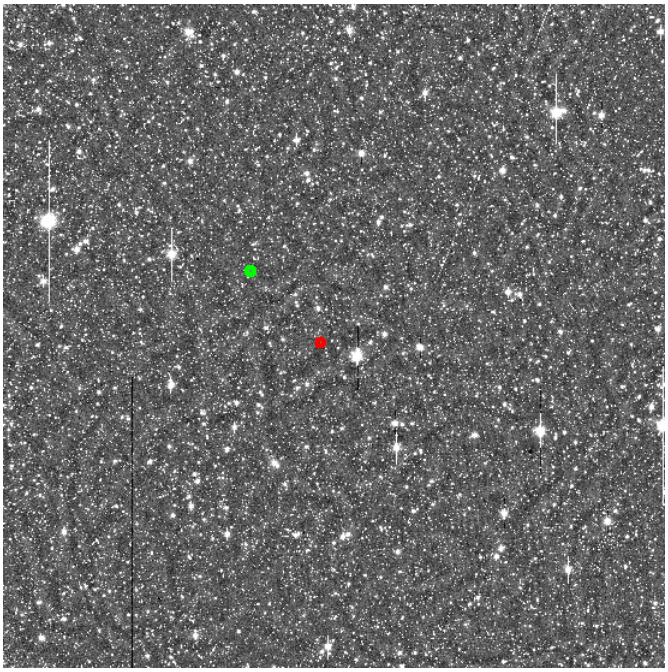

Figure 6.8: The candidate found during the image analysis of ANT131009A (green) is located at $\sim 0.3°$ from the neutrino direction (red).

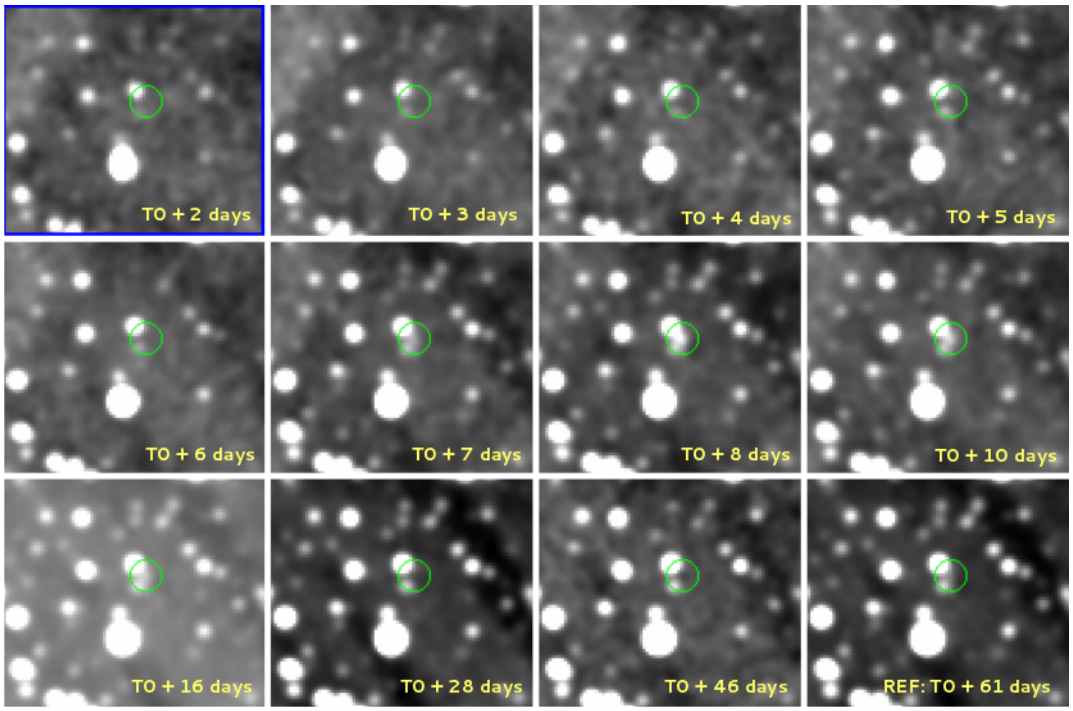

Figure 6.9: Stacked images for each night of observation of the alert ANT131009A. The candidate found during visual inspection is circled in green, and was only detected by the pipeline at T0 + 8, 10, 16 and 61 days. At T0 + 7 days, the signal was too faint to be detected.

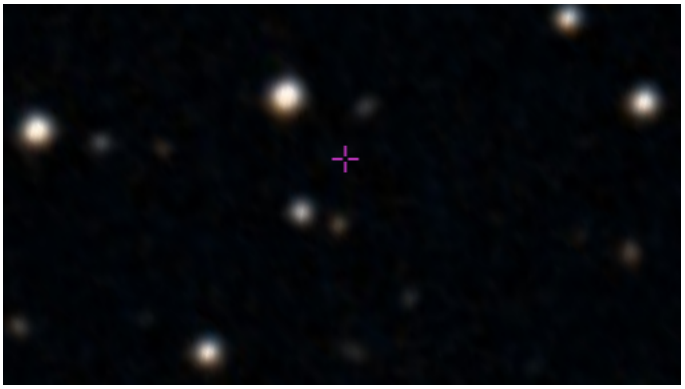

Figure 6.10: DSS2 field ($\sim$ 2.3 arcmin) where the pink cross indicates the position of the candidate found during the analysis of ANT131009A.

Therefore, the candidate is not compatible with a SN explosion correlated to the neutrino emission and cannot be identified as the optical counterpart to the neutrino trigger. Such a signal could be the signature of a variable star.

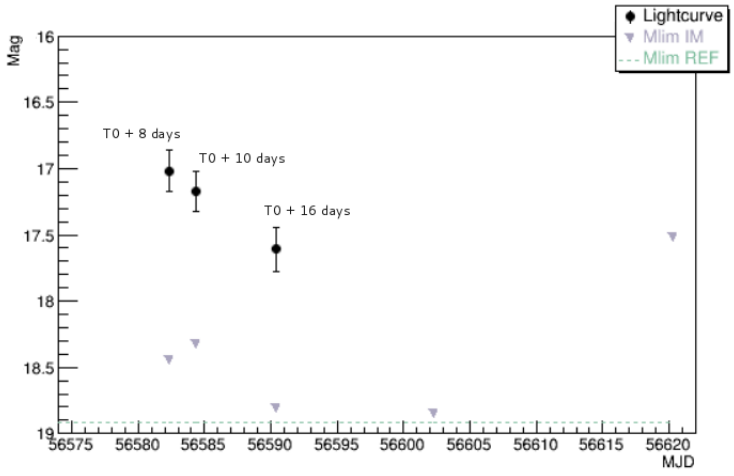

Figure 6.11: Light curve of the candidate found in ANT131009A. It was detected at T0 + 8, 10 and 16 days after the trigger. The green dashed line indicates the limiting magnitude of the REF image at $\sim$ 18.9, while blue triangles show the limiting magnitude of each IM.

6.3 Limit calculation in the case of CCSNe

CCSNe are promising candidates to emit high energy neutrinos (see Section 1.3.2). As no transient optical counterpart has been found in long term follow-up images, it is important to assess the compatibility of this result with the background expectations. Furthermore, this non-detection allows constraints on CCSN model parameters to be placed.

6.3.1 Background expectation

The number of expected accidental SN detections, i.e., a SN detection in coincidence with a background neutrino event, can be estimated with:

$$N_{\mathrm{SN,exp}} = \Delta T_{\mathrm{SN}} \times N_{\mathrm{alerts}} \times \frac{\Omega_{\mathrm{TEL}}}{\Omega_{\mathrm{sky}}} \times R^{\mathrm{TEL}}_{\mathrm{CCSN}} \tag{6.1}$$

where $N_{\mathrm{alerts}} = 71$ is the number of neutrino alerts followed-up by the optical telescopes, Ω_{TEL} is the solid angle covered by the optical telescopes ($1.85° \times 1.85°$ for ROTSE, and $1.86° \times 1.86°$ for TAROT), $\Omega_{\mathrm{sky}} = 41253(°)^2$ is the all-sky solid angle, and $R^{\mathrm{TEL}}_{\mathrm{CCSN}}$ is the rate of CCSNe that could be detected by the optical telescopes if they would continuously survey the full sky. This rate is calculated from the efficiency estimated in Section 4.7, assuming a CCSN rate of 1 per year within a sphere of radius 10 Mpc [143], i.e., 2.4×10^{-4} y^{-1} Mpc^{-3}. For this, the CCSN rate is integrated over the accessible volume weighted with the efficiency displayed in Figure 4.29. This gives $R^{\mathrm{TEL}}_{\mathrm{CCSN}} = 2518$ y^{-1}, as shown in Figure 6.12. ΔT_{SN} is the time window in which a coincidence between the neutrino event and the optical signal is accepted. It has to be larger than the uncertainty of the SN explosion time, therefore $\Delta T_{\mathrm{SN}} = 5$ days is chosen. The expected number of randomly coincident SN detections is thus $N_{\mathrm{SN,exp}} = 0.2$ for 71 alerts. The non-detection of optical SNe in our images is consistent with this small expectation value.

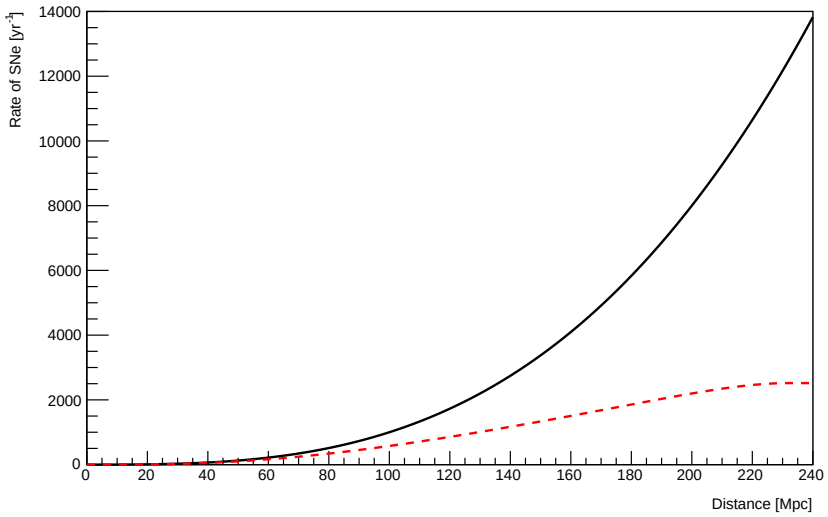

Figure 6.12: The CCSN rate of 2.4×10^{-4} y^{-1} Mpc^{-3} as a function of the distance is represented by the black curve, while the red dashed curve shows the rate of detectable CCSNe considering the TAROT and ROTSE optical telescopes, and the detection efficiency of the image analysis pipeline. If these optical telescopes would survey the full sky continuously, a rate of 2518 CCSNe per year could be detected.

6.3.2 Constraints on the AB05 model

The Ando & Beacom model (AB05) [64] predicts the production of high energy neutrinos in CCSN mildly relativistic jets, with a flux depending on the jet energy $E_{\rm jet}$ and the Lorentz boost factor of the jet Γ. The expected number of such neutrinos in ANTARES, $N_\nu^{\rm exp}(\Gamma, E_{\rm jet})$, can be estimated as follows:

$$N_\nu^{\rm exp}(\Gamma, E_{\rm jet}) = \int_{E_{\nu,\rm min}}^{E_{\nu,\rm max}} \left(\frac{dN}{dE_\nu}\right)_{\rm AB05} \times A_{\rm eff}(E_\nu) dE_\nu \tag{6.2}$$

where $\left(\frac{dN}{dE_\nu}\right)_{\rm AB05}$ is the expected number of neutrinos from a CCSN according to the AB05 model, and $A_{\rm eff}$ is the effective area of the ANTARES detector. As shown in Figure 6.13, the effective area depends on the cuts used for the selection of neutrinos which can trigger an alert. Hence, two different effective areas are taken into account for the calculation, one for the high energy trigger criterion and one for the directional trigger.

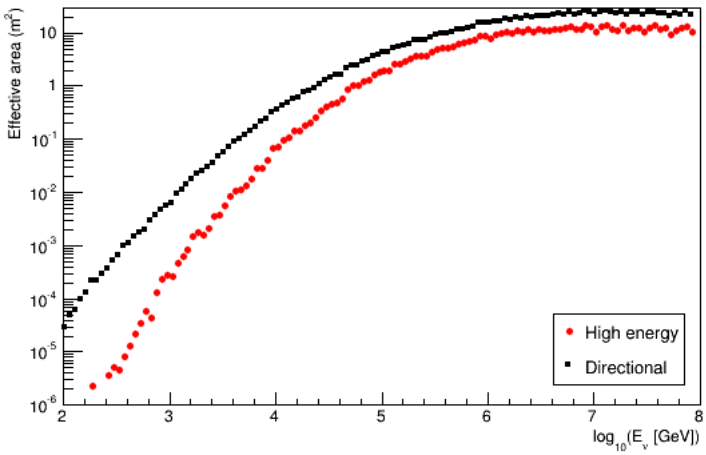

Figure 6.13: Neutrino effective area of ANTARES for both the high energy and directional trigger selections.

Figure 6.13 shows the number of expected neutrinos in ANTARES for a CCSN with a jet pointing towards Earth at a distance of 10 Mpc, 3 Mpc, 460 kpc and 50 kpc. Within 10 Mpc, the rate of CCSNe is ~ 1 yr^{-1}, with a large contribution from galaxies around $3-4$ Mpc, as shown in Figure 6.14. The distance $d = 50$ kpc corresponds to the distance of SN1987A. The number of neutrinos is calculated for the jet Lorentz boost factor Γ from 1 to 10, and for jet energies in the range $3 \times 10^{49}{\rm erg} \leq E_{\rm jet} \leq 3 \times 10^{53}{\rm erg}$. Standard values for a CCSN with mildly relativistic jets are $\Gamma = 3$ and $E_{\rm jet} = 3 \times 10^{51}$ erg.

As within 10 Mpc the detection efficiency of our system is better than 95 %, as illustrated in Figure 4.29, a CCSN within this distance associated with a neutrino trigger would have been detected. Therefore, as no optical CCSN has been found for the 71 alerts, combinations of model parameters producing a detectable signal in ANTARES can be excluded. A red line on each plot indicates the limit above which parameter combinations are excluded at 90 % confidence level.

At a distance $d = 10$ Mpc, a CCSN with $\Gamma \geq 8$ and $E_{\rm jet} \gtrsim 2 \times 10^{52}$ erg is excluded at 90 % confidence level, while for a closer CCSN at $d = 3$ Mpc, combinations with $\Gamma \geq 6$ and $E_{\rm jet} \gtrsim 2 \times 10^{51}$ erg are rejected. If we consider standard parameter values for soft jets ($\Gamma = 3$ and $E_{\rm jet} = 3 \times 10^{51}$ erg), a CCSN can be excluded up to 460 kpc, as shown in Figure 6.13 (c).

For a nearby CCSN, as it was the case for SN1987A at $d = 50$ kpc, all combinations with $\Gamma \geq 2$ are discarded at 90 % confidence level. As a CCSN with a jet energy lower than 3×10^{49} erg are unlikely, this limit allows a CCSN at this distance to be excluded. Conversely, a CCSN with $\Gamma = 10$ and $E_{\rm jet} = 3 \times 10^{53}$ erg is excluded up to ~ 52 Mpc. After this distance, no constraints can be placed as the neutrino flux, varying proportionally with d^{-2}, is too low to be detected by the ANTARES telescope.

The key remaining issue is the number of CCSNe with such mildly relativistic jets, which is perhaps ~ 1 %, significantly larger than the fraction of SNe with highly relativistic jets, i.e., GRBs. An additional limit can be placed on the rate of CCSNe with jets ρ, depending on Γ and $E_{\rm jet}$, as no optical SN counterpart has been found in this analysis. The limit is calculated for the jet Lorentz boost factors $\Gamma = 6, 8, 10$, for jet energies in the range $3 \times 10^{49}{\rm erg} \leq E_{\rm jet} \leq 3 \times 10^{53}{\rm erg}$, and for CCSN rates in the range 1.3×10^{-6} Mpc^{-3} y$^{-1} \leq \rho \leq 3.2 \times 10^{-4}$ Mpc^{-3} y^{-1}. Figure 6.15 shows the excluded regions at 90 % confidence level in the $E_{\rm jet} - \rho$ plane for different values of Γ. The most stringent limit can be set for high Lorentz factors Γ, which produce high neutrino fluxes. At 90 % confidence level, a sub-population of SNe with Γ=10 and $E_{\rm jet} = 3 \times 10^{51}$ erg does not exceed 11 %.

A similar analysis has been performed within the IceCube Collaboration, which has also a follow-up program of high energy neutrinos operating since 2008. Due to the larger effective area of IceCube compared to ANTARES, more stringent limits have been placed: a sub-population with Γ=10 and $E_{\rm jet} = 3 \times 10^{51}$ erg does not exceed 4.2 % [145].

6.4 Improvements to search for core-collapse supernovae

The results obtained from the follow-up of 71 neutrino alerts allowed stringent constraints on CCSN model parameters to be placed. However in a near future, further improvements will allow the detection sensitivity of CCSN neutrinos and optical counterparts to be enhanced.

In the case of CCSNe of type Ib/c, the peak brightness is expected ~ 20 days after the explosion, and is thus the time at which small robotic optical telescopes such as TAROT and ROTSE have the best chance to observe a counterpart associated with a neutrino signal. However, in case of detection, observations starting at early times and performed at regular intervals are necessary to estimate the SN explosion time and thus to establish the coincidence between the neutrino detection and the optical SN. The addition of more powerful telescopes, such as the one meter Zadko telescope or the five MASTER telescopes which joined the

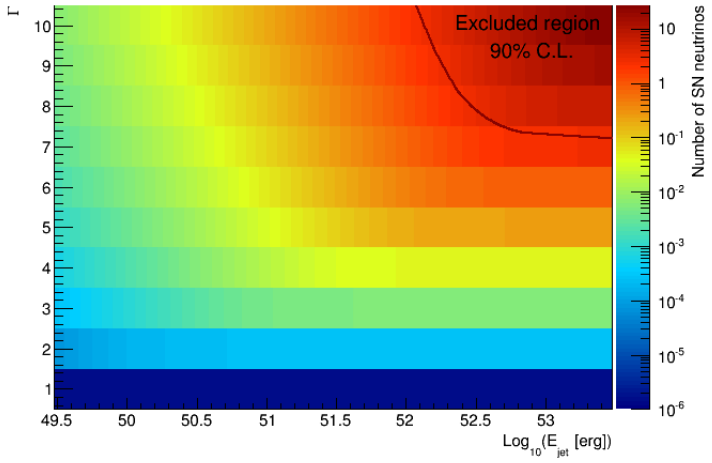

(a) $d = 10$ Mpc.

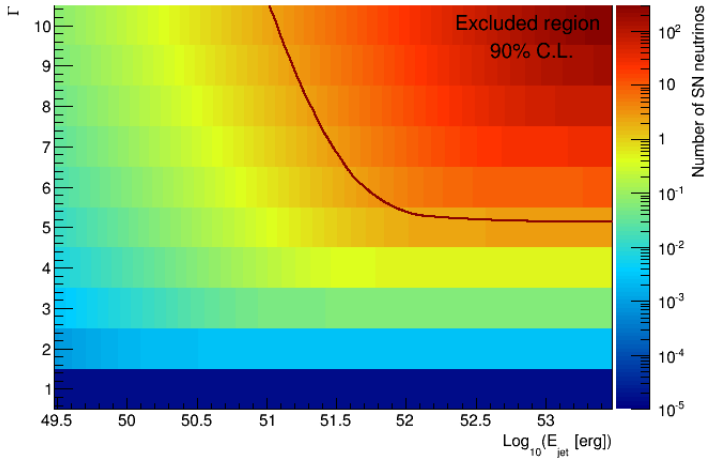

(b) $d = 3$ Mpc.

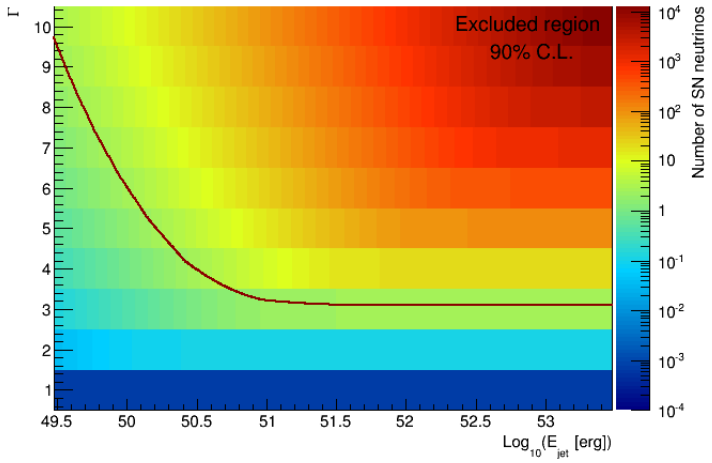

(c) $d = 460$ kpc.

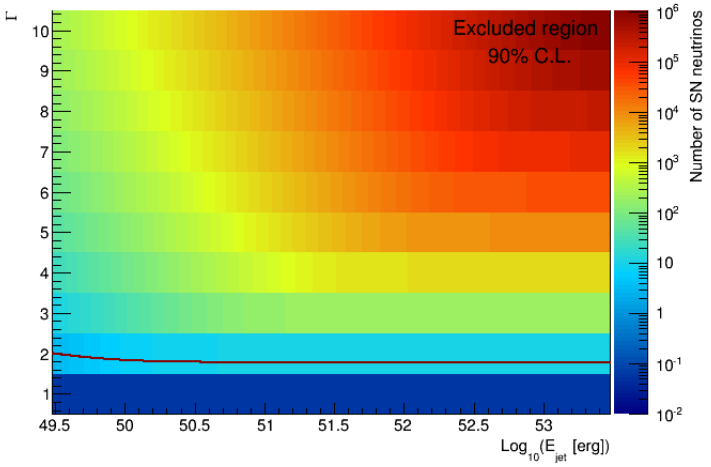

(d) $d = 50$ kpc.

Figure 6.13: Expected number of neutrinos in ANTARES from a CCSN at different distances for different model parameter combinations and considering the high energy and directional selections. The red line shows the limit above which combinations of $E_{\text{jet}} - \Gamma$ are excluded at 90 % confidence level as no CCSN neutrinos have been detected. Figure (c) shows that a CCSN with standard parameter values ($\Gamma = 3$ and $E_{\text{jet}} = 3 \times 10^{51}$ erg) is excluded up to 460 kpc.

TAToO network, would allow the detection of CCSN optical signals at early times with fainter peak magnitudes (i.e., more distant CCSNe).

Furthermore, by analyzing in near real-time optical images, the visual check of candidates could be performed day by day. Thus, in case of an interesting SN candidate, a spectroscopic follow-up with equipped telescopes could be triggered to help the identification.

Finally, as explained in Section 5.5 for early follow-up observations, the future KM3NeT detector will have a sensitivity to high energy neutrino fluxes increased by about a factor of 50 compared to the ANTARES telescope. With its higher effective area, the detection of CCSN neutrinos as predicted by the slow jet model will thus be much more likely. However, a non-detection will allow a larger fraction of the AB05 model parameter space to be excluded, as shown in Figures 6.16 and 6.17. For instance, a CCSN at $d = 10$ Mpc with $\Gamma \geq 4$ and $E_{\text{jet}} \gtrsim 3 \times 10^{50}$ erg would be excluded at 90 % confidence level. Furthermore, by considering the rate of CCSNe with jets, a sub-population with Γ=10 and $E_{\text{jet}} = 3 \times 10^{49}$ erg should not exceed 5.2 %. This limit could be lowered down to 3.3 % if an optical telescope such as Zadko is considered to perform the follow-up, as it is capable of detecting SNe up to a limiting magnitude of ~ 20.

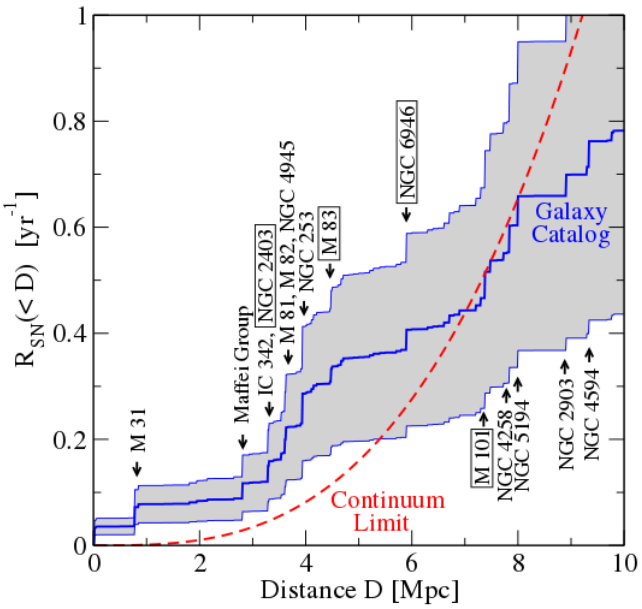

Figure 6.14: Cumulative CCSN rate as a function of distance in the local Universe. The dashed line is the continuum limit using the GALEX star formation rate [144]. The blue line is based on star formation rates for individual galaxies, with the uncertainty shown by the gray band. Some major galaxies are indicated, and those in boxes have especially high optical SN rates. Figure taken from [143].

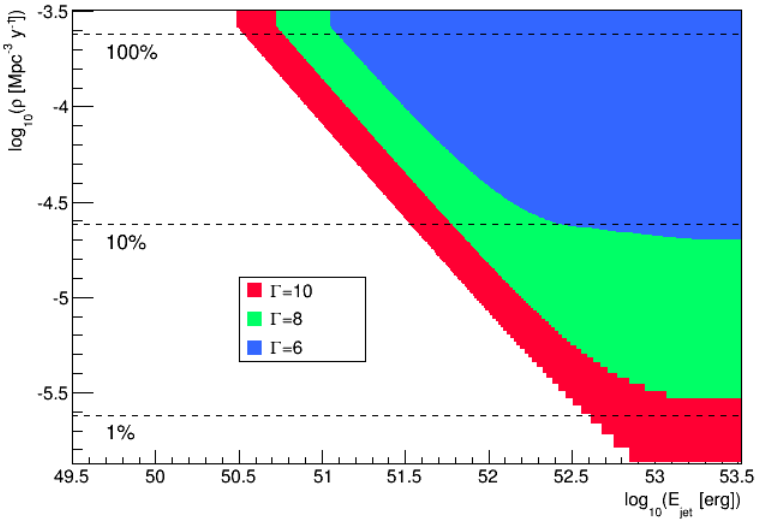

Figure 6.15: Limits on the AB05 model for different Lorentz boost factors Γ as a function of the rate of SNe with jets ρ and the jet energy $E_{\rm jet}$. The colored regions are excluded at 90 % confidence level. Horizontal dashed lines indicate the fraction of CCSNe with jets relative to an assumed CCSN rate of 2.4×10^{-4} y^{-1} Mpc^{-3}.

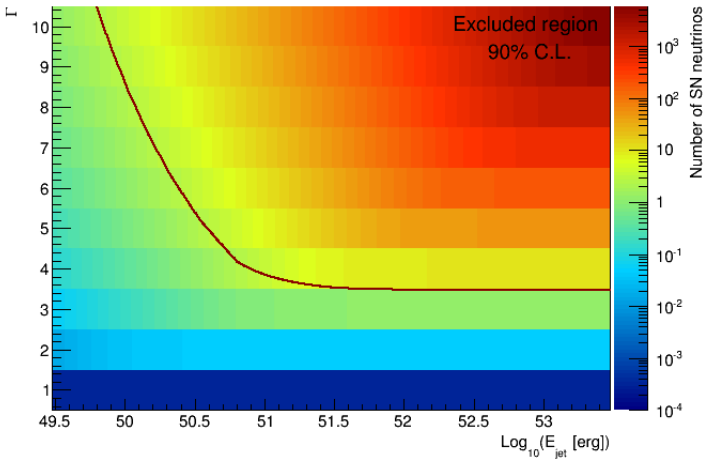

Figure 6.16: Expected number of SN neutrinos detectable with KM3NeT from a SN at distance 10 Mpc for different AB05 model parameter combinations. Parameter combinations above the red line are excluded at 90 % confidence level.

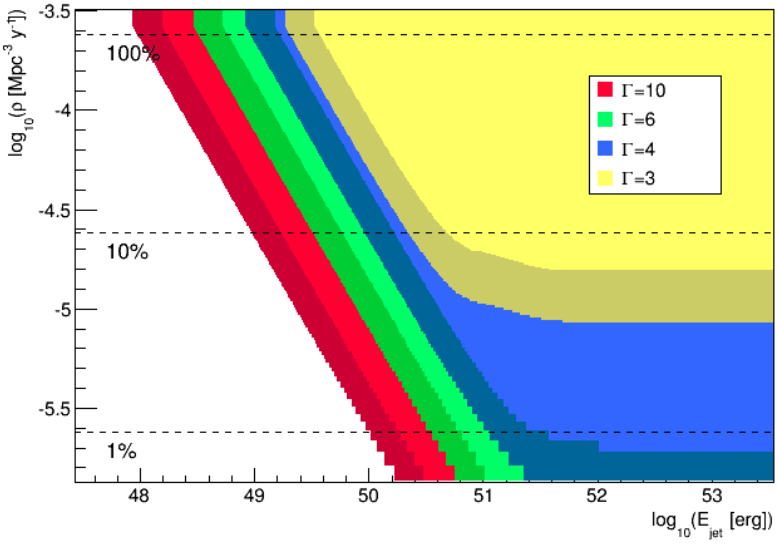

Figure 6.17: Estimated 90 % confidence level limits on the AB05 model parameters Γ and E_{jet}, and on the rate of CCSNe with jets ρ for KM3NeT combined with a more powerful optical telescope (darker colors), such as Zadko which is capable of detecting SNe up to a limiting magnitude of ~ 20.

Summary and outlook

Multi-messenger astronomy is a young and promising field of research, and follow-up observations of neutrino alerts at various energies is an unique approach to identify the sources of high energy neutrinos. During this thesis, the search for transient sources in coincidence with high energy neutrinos has been performed. Data provided by optical and X-ray telescopes following the detection of interesting neutrinos with the ANTARES telescope have been used. An image analysis pipeline has been specially developed in this work for the processing of optical images taken by the TAROT and ROTSE telescopes. With this program, 42 and 71 alerts have been analyzed to search for fast and slowly varying transient sources, respectively. In addition, 10 alerts sent to the *Swift*-XRT have been automatically analyzed with dedicated pipelines. For both the optical and X-ray wavelengths, no transient counterpart has been identified in coincidence with a neutrino emission. For the first time, a follow-up program of neutrino alerts allows stringent constraints on the GRB origin of individual high energy neutrinos to be placed. Based on the comparison between the obtained flux upper limits and historical GRB afterglow light curves, a GRB origin for these neutrinos has been rejected at a better than 80 % confidence level, depending on the observation delay. Furthermore, constraints on the AB05 model parameters $E_{\rm jet}$ and Γ for the production of high energy neutrinos in CCSN mildly relativistic jets, and on the rate of CCSNe with such jets have been set. At 90 % confidence level, a sub-population with Γ=10 and $E_{\rm jet} = 3 \times 10^{51}$ erg does not exceed 11 %.

The work performed during this thesis proves the feasibility and efficiency of an alert system accompanied with a robust image analysis pipeline that will have to be developed for future experiments involved in transient source searches. In neutrino astronomy, the future KM3NeT detector, which is being built in the Mediterranean Sea, will be distributed on two sites: a very dense array ($>$ Mtons) in France (KM3NeT-ORCA) dedicated to the study of the neutrino mass hierarchy, and a very large volume ($> 1\,{\rm km}^3$) in Italy (KM3NeT-ARCA) for high energy neutrino astronomy. With more than a hundred of detection units, KM3NeT-ARCA will be about a factor of 50 more sensitive to high energy neutrino fluxes than the ANTARES telescope, and will thus provide a unique opportunity to observe cosmic neutrinos from the Southern sky. Multi-messenger activities and

particularly the development of a real-time alert system, such as TAToO, are planned. However, such a system will have to be adapted to the higher neutrino fluxes. Currently, the alert system of ANTARES triggers the network of telescopes based on 3 criteria (high energy (or very high energy), directional and multiplet) allowing a rate of about 25 alerts per year to be issued. To keep this rate and reduce the number of triggers due to the atmospheric neutrino background, the increased size of KM3NeT will require more restrictive criteria. For instance, within the IceCube collaboration, which operates a follow-up program since 2008, an alert is only sent if two or more neutrinos are detected within a time window $\Delta t < 100$ s and an angular separation $\Delta\theta < 3.5°$.

The search for high energy transient phenomena and identification of counterpart candidates in real time is going to be increasingly important with future experiments. For instance, in the case of the SVOM mission, to be launched in 2021, many instruments in space and on ground will be coordinated to observe variable and transient objects at various wavelengths and also with different messengers. Target-Of-Opportunity alerts will be accepted from neutrino and gravitational wave detectors.

To identify the electromagnetic counterpart of a non-electromagnetic trigger, or to search for the counterpart of a transient event in different wavelengths, the coordination of instruments is crucial. The alert ANT150901A, described in this thesis, is a good example of a successful collaboration between various instruments. The detection by the *Swift*-XRT of a potential counterpart to the ANTARES neutrino trigger initiated several observations involving radio, optical, X-ray and gamma-ray telescopes, allowing the identification of the X-ray source. In the case of ANT110531A and ANT111228A, for which transient candidates have been detected in optical images, further multi-wavelength observations would have been necessary to identify these objects. Indeed, rapid follow-up and near real-time analyses of images are required, in order to trigger other observatories in case of interesting candidates.

The optical image analysis pipeline developed during this thesis is based on a subtraction method which is a widely used technique in the astronomical community to search for transient or variable sources. The major difficulty was to adapt the program to large field images with extremely variable qualities, leading to more than a hundred of candidates to check by eye for each image. For future experiments involved in transient searches, similar pipelines will have to be developed but some improvements will be required to isolate interesting counterpart candidates in less than a few minutes after the trigger. One of the goals of the SVOM mission will be to quickly identify GRB optical counterparts. If the profile of the object that is looked for is known, it will be easier to select candidates, for example, by applying variability cuts on candidate light curves. On the contrary, the search for neutrino and gravitational wave counterparts will be more difficult, as presently nobody knows what optical counterparts of such sources look like. Furthermore, in the coming years optical telescopes will be more sensitive allowing fainter sources to be detected, below the limit of existing catalogs, and possibly providing more counterpart candidates. A large effort of the involved communities will have to be done to develop successful instruments

but also to provide image analysis tools rapid and efficient.

The increasing number of instruments involved in science with different cosmic messengers highlights the interest of the astrophysical community in contributing to the detection of a multi-messenger source. This opens a wide variety of possibilities and may provide a unique opportunity to probe the most violent phenomena of the Universe.

BIBLIOGRAPHY

[1] W. B. Atwood, et al. The Large Area Telescope on the Fermi Gamma-Ray Space Telescope Mission. *The Astrophysical Journal*, 697:1071–1102, June 2009.

[2] N. Gehrels, et al. The Swift Gamma-Ray Burst Mission. *The Astrophysical Journal*, 611:1005–1020, August 2004.

[3] F. W. Stecker, O. C. de Jager, and M. H. Salamon. TeV gamma rays from 3C 279 - A possible probe of origin and intergalactic infrared radiation fields. *The Astrophysical Journal, Letters*, 390:L49–L52, May 1992.

[4] M. Spurio. *Particles and Astrophysics - A Multi-Messenger Approach.* Springer International Publishing, 2015.

[5] M. W. E. Smith, et al. The Astrophysical Multimessenger Observatory Network (AMON). *Astroparticle Physics*, 45:56–70, May 2013.

[6] A. Rau, et al. Exploring the Optical Transient Sky with the Palomar Transient Factory. *Publications of the Astronomical Society of the Pacific*, 121:1334–1351, December 2009.

[7] N. Gehrels, S. Barthelmy, and J. Cannizzo. Time-domain astronomy with Swift, Fermi and Lobster. volume 7, pages 41–46, 2011.

[8] R. Davis, D. S. Harmer, and K. C. Hoffman. Search for neutrinos from the Sun. *Physical Review Letters*, 20:1205, May 1968.

[9] K. Hirata, T. Kajita, M. Koshiba, M. Nakahata, and Y. Oyama. Observation of a neutrino burst from the supernova SN1987A. *Physical Review Letters*, 58:1490–1493, April 1987.

[10] T. Haines, et al. Neutrinos from SN1987a in the IMB detector. *Nuclear Instruments and Methods in Physics Research A*, 264:28–31, February 1988.

[11] E. N. Alekseev, L. N. Alekseeva, I. V. Krivosheina, and V. I. Volchenko. Detection of the neutrino signal from SN 1987A using the INR Baksan

underground scintillation telescope. In H. V. Klapdor and B. Povh, editors, *Neutrino Physics*, pages 288–298, 1988.

[12] J. K. Becker. High-energy neutrinos in the context of multimessenger astrophysics. *Physics Reports*, 458:173–246, March 2008.

[13] R. M. Kulsrud, J. P. Ostriker, and J. E. Gunn. Acceleration of Cosmic Rays in Supernova Remnants. *Physical Review Letters*, 28:636–639, March 1972.

[14] A. M. Hillas. The Origin of Ultra-High-Energy Cosmic Rays. *Annual Review of Astronomy and Astrophysics*, 22:425–444, 1984.

[15] K. Greisen. End to the cosmic ray spectrum? *Physical Review Letters*, 16:748–750, 1966.

[16] G. Zatsepin and V. Kuzmin. Upper limit of the spectrum of cosmic rays. *Journal of Experimental and Theoretical Physics Letters*, 4:78–90, 1966.

[17] J. Abraham, et al. Measurement of the energy spectrum of cosmic rays above 10^{18} eV using the Pierre Auger Observatory. *Physics Letters B*, 685:239–246, March 2010.

[18] A. M. Hillas. Cosmic Rays: Recent Progress and some Current Questions. *ArXiv Astrophysics e-prints*, July 2006.

[19] L. A. Anchordoqui and T. Montaruli. In Search of Extraterrestrial High-Energy Neutrinos. *Annual Review of Nuclear and Particle Science*, 60:129–162, November 2010.

[20] T. Chiarusi and M. Spurio. High-energy astrophysics with neutrino telescopes. *European Physical Journal C*, 65:649–701, February 2010.

[21] P. Lipari. Perspectives of high-energy neutrino astronomy. *Nuclear Instruments and Methods in Physics Research A*, 567:405–417, November 2006.

[22] H. Athar, M. Jeżabek, and O. Yasuda. Effects of neutrino mixing on high-energy cosmic neutrino flux. *Phys. Rev. D*, 62(10):103007, November 2000.

[23] M. G. Aartsen, et al. Evidence for High-Energy Extraterrestrial Neutrinos at the IceCube Detector. *Science*, 342:1, November 2013.

[24] S. Schönert, T. K. Gaisser, E. Resconi, and O. Schulz. Vetoing atmospheric neutrinos in a high energy neutrino telescope. *Physical Review D*, 79(4):043009, February 2009.

[25] M. G. Aartsen, et al. Observation of High-Energy Astrophysical Neutrinos in Three Years of IceCube Data. *Physical Review Letters*, 113(10):101101, September 2014.

[26] M. Spurio. Constraints to a Galactic component of the Ice Cube cosmic neutrino flux from ANTARES. *Physical Review D*, 90(10):103004, November 2014.

[27] M. Ageron, et al. ANTARES: The first undersea neutrino telescope. *Nuclear Instruments and Methods in Physics Research A*, 656:11–38, November 2011.

[28] S. Adrián-Martínez, et al. Search for Cosmic Neutrino Point Sources with Four Years of Data from the ANTARES Telescope. *Astrophysical Journal*, 760:53, November 2012.

[29] J. A. Aguilar, et al. Search for a diffuse flux of high-energy ν with the ANTARES neutrino telescope. *Physics Letters B*, 696:16–22, January 2011.

[30] ANTARES Collaboration, et al. A Search for Neutrino Emission from the Fermi Bubbles with the ANTARES Telescope. *ArXiv e-prints*, August 2013.

[31] R. W. Klebesadel, I. B. Strong, and R. A. Olson. Observations of Gamma-Ray Bursts of Cosmic Origin. *The Astrophysical Journal, Letters*, 182:L85, June 1973.

[32] E. P. Mazets, S. V. Golenetskii, and V. N. Ilinskii. A cosmic gamma-ray flare observed with Kosmos 461. *JETP Lett.*, 19:77, 1974.

[33] C. A. Meegan, et al. Spatial distribution of gamma-ray bursts observed by BATSE. *Nature*, 355:143–145, January 1992.

[34] D. Band, et al. BATSE observations of gamma-ray burst spectra. I - Spectral diversity. *The Astrophysical Journal*, 413:281–292, August 1993.

[35] R. Abbasi, et al. Search for Muon Neutrinos from Gamma-ray Bursts with the IceCube Neutrino Telescope. *The Astrophysical Journal*, 710:346–359, February 2010.

[36] J. van Paradijs, et al. Transient optical emission from the error box of the γ-ray burst of 28 February 1997. *Nature*, 386:686–689, April 1997.

[37] D. A. Frail, S. R. Kulkarni, L. Nicastro, M. Feroci, and G. B. Taylor. The radio afterglow from the γ-ray burst of 8 May 1997. *Nature*, 389:261–263, September 1997.

[38] M. R. Metzger, et al. Spectral constraints on the redshift of the optical counterpart to the γ-ray burst of 8 May 1997. *Nature*, 387:878–880, June 1997.

[39] S. D. Barthelmy, et al. The GRB coordinates network (GCN): A status report. In C. A. Meegan, R. D. Preece, and T. M. Koshut, editors, *Gamma-Ray Bursts, 4th Hunstville Symposium*, volume 428 of *American Institute of Physics Conference Series*, pages 99–103, May 1998.

[40] W. S. Paciesas, et al. The Fourth BATSE Gamma-Ray Burst Catalog (Revised). *The Astrophysical Journal, Supplement*, 122:465–495, June 1999.

[41] S. E. Woosley and J. S. Bloom. The Supernova Gamma-Ray Burst Connection. *Annual Review of Astronomy and Astrophysics*, 44:507–556, September 2006.

[42] A. I. MacFadyen and S. E. Woosley. Collapsars: Gamma-Ray Bursts and Explosions in "Failed Supernovae". *The Astrophysical Journal*, 524:262–289, October 1999.

[43] B. Paczynski. Gamma-ray bursters at cosmological distances. *The Astrophysical Journal, Letters*, 308:L43–L46, September 1986.

[44] P. Meszaros and M. J. Rees. High-entropy fireballs and jets in gamma-ray burst sources. *Monthly Notices of the Royal Astronomical Society*, 257:29P–31P, July 1992.

[45] R. Narayan, B. Paczynski, and T. Piran. Gamma-ray bursts as the death throes of massive binary stars. *The Astrophysical Journal, Letters*, 395:L83–L86, August 1992.

[46] S. E. Woosley. Gamma-ray bursts from stellar mass accretion disks around black holes. *The Astrophysical Journal*, 405:273–277, March 1993.

[47] A. Franckowiak. *Searching for High-energy Neutrinos from Supernovae with IceCube and an Optical Follow-up Program*. PhD thesis, Rheinischen Friedrich-Wilhelms-Universität Bonn, 2011.

[48] E. Waxman and J. Bahcall. High Energy Neutrinos from Cosmological Gamma-Ray Burst Fireballs. *Physical Review Letters*, 78:2292–2295, March 1997.

[49] D. Guetta, D. Hooper, J. Alvarez-Muñiz, F. Halzen, and E. Reuveni. Neutrinos from individual gamma-ray bursts in the BATSE catalog. *Astroparticle Physics*, 20:429–455, January 2004.

[50] L.-X. Li and B. Paczyński. Improved correlation between the variability and peak luminosity of gamma-ray bursts. *Monthly Notices of the Royal Astronomical Society*, 366:219–226, February 2006.

[51] C. Giunti and C. W. Kim. *Fundamentals of Neutrino Physics and Astrophysics*. OUP Oxford, 2007.

[52] S. Woosley and T. Janka. The physics of core-collapse supernovae. *Nature Physics*, 1:147–154, December 2005.

[53] S. Razzaque, P. Mészáros, and E. Waxman. High Energy Neutrinos from a Slow Jet Model of Core Collapse Supernovae. *Modern Physics Letters A*, 20:2351–2367, 2005.

[54] S. Campana, et al. The association of GRB 060218 with a supernova and the evolution of the shock wave. *Nature*, 442:1008–1010, August 2006.

[55] R. McCray. Supernova 1987A revisited. *Annual Review of Astronomy and Astrophysics*, 31:175–216, 1993.

[56] S. A. Colgate. Prompt gamma rays and X-rays from supernovae. *Canadian Journal of Physics*, 46:476, 1968.

[57] T. J. Galama, et al. An unusual supernova in the error box of the γ-ray burst of 25 April 1998. *Nature*, 395:670–672, October 1998.

[58] D. W. Fox, et al. Discovery of Early Optical Emission from GRB 021211. *The Astrophysical Journal, Letters*, 586:L5–L8, March 2003.

[59] P. A. Mazzali, et al. The Type Ic Hypernova SN 2003dh/GRB 030329. *The Astrophysical Journal, Letters*, 599:L95–L98, December 2003.

[60] D. Malesani, et al. SN 2003lw and GRB 031203: A Bright Supernova for a Faint Gamma-Ray Burst. *The Astrophysical Journal, Letters*, 609:L5–L8, July 2004.

[61] A. A. Hakobyan, et al. Five supernova survey galaxies in the southern hemisphere. II. The supernova rates. *Astrophysics*, 54:301–314, September 2011.

[62] A. Gal-Yam, et al. Radio and Optical Follow-up Observations of a Uniform Radio Transient Search: Implications for Gamma-Ray Bursts and Supernovae. *The Astrophysical Journal*, 639:331–339, March 2006.

[63] E. Berger, S. R. Kulkarni, D. A. Frail, and A. M. Soderberg. A Radio Survey of Type Ib and Ic Supernovae: Searching for Engine-driven Supernovae. *The Astrophysical Journal*, 599:408–418, December 2003.

[64] S. Ando and J. F. Beacom. Revealing the Supernova Gamma-Ray Burst Connection with TeV Neutrinos. *Physical Review Letters*, 95(6):061103, August 2005.

[65] M. A. Markov. In *Proceedings Int. Conf. on High Energy Physics*, page 183, 1960.

[66] C. Kopper. *Performance Studies for the KM3NeT Neutrino Telescope*. PhD thesis, University of Erlangen-Nürnberg, 2010.

[67] R. Gandhi, C. Quigg, M. Hall Reno, and I. Sarcevic. Ultrahigh-energy neutrino interactions. *Astroparticle Physics*, 5:81–110, August 1996.

[68] P. A. Čerenkov. Visible Radiation Produced by Electrons Moving in a Medium with Velocities Exceeding that of Light. *Physical Review*, 52:378–379, August 1937.

[69] S. I. Klimushin, E. V. Bugaev, and I. A. Sokalski. Precise parametrizations of muon energy losses in water. *International Cosmic Ray Conference*, 3:1009, 2001.

[70] A. Heijboer. *Track Reconstruction and Point Source Searches with ANTARES*. PhD thesis, NIKHEF, Amsterdam, 2004.

[71] G. Carminati, M. Bazzotti, A. Margiotta, and M. Spurio. Atmospheric MUons from PArametric formulas: a fast GEnerator for neutrino telescopes (MUPAGE). *Computer Physics Communications*, 179:915–923, December 2008.

[72] G. D. Barr, T. K. Gaisser, P. Lipari, S. Robbins, and T. Stanev. Three-dimensional calculation of atmospheric neutrinos. *Phys. Rev. D*, 70(2):023006, July 2004.

[73] P. K. F. Grieder. DUMAND. A new window on the universe. *Europhys. News, Vol. 23, No. 9, p. 167 - 170*, 23:167–170, October 1992.

[74] V. Aynutdinov, et al. The BAIKAL neutrino experiment: Physics results and perspectives. *Nuclear Instruments and Methods in Physics Research A*, 602:14–20, April 2009.

[75] A. Karle for the IceCube Collaboration. IceCube - status and recent results. *ArXiv e-prints*, January 2014.

[76] E. Andres, et al. The AMANDA neutrino telescope: principle of operation and first results. *Astroparticle Physics*, 13:1–20, March 2000.

[77] A. Margiotta. The KM3NeT deep-sea neutrino telescope. *Nuclear Instruments and Methods in Physics Research A*, 766:83–87, December 2014.

[78] D. Zaborov. The ^{40}K calibration method. *ANTARES internal notes*, ANTARES-CALI/2011-001, 2011.

[79] J. A. Aguilar, et al. The data acquisition system for the ANTARES neutrino telescope. *Nuclear Instruments and Methods in Physics Research A*, 570:107–116, January 2007.

[80] J. M. Senior. *Optical Fiber Communications: Principles and Practice*. Prentice-Hall international series in optoelectronics. Prentice Hall, 1992.

[81] J. A. Aguilar, et al. Time calibration of the ANTARES neutrino telescope. *Astroparticle Physics*, 34:539–549, February 2011.

[82] A. M. Brown for the ANTARES collaboration. Positioning system of the ANTARES Neutrino Telescope. *ArXiv e-prints*, August 2009.

[83] M. Ageron, et al. The ANTARES telescope neutrino alert system. *Astroparticle Physics*, 35:530–536, March 2012.

[84] D. N. Burrows, et al. The Swift X-Ray Telescope. *Space Science Reviews*, 120:165–195, October 2005.

[85] J. A. Aguilar, et al. A fast algorithm for muon track reconstruction and its application to the ANTARES neutrino telescope. *Astroparticle Physics*, 34:652–662, April 2011.

[86] F. James and M. Roos. Minuit - a system for function minimization and analysis of the parameter errors and correlations. *Computer Physics Communications*, 10:343–367, December 1975.

[87] D. Heck, J. Knapp, J. N. Capdevielle, G. Schatz, and T. Thouw. *CORSIKA: a Monte Carlo code to simulate extensive air showers.* February 1998.

[88] N. N. Kalmykov and S. S. Ostapchenko. The Nucleus-nucleus interaction, nuclear fragmentation, and fluctuations of extensive air showers. *Yad. Fiz.*, 56:105, 1993.

[89] T. Montaruli. Tech. Rep., ANTARES-SOFT-2004-010, 2004.

[90] G. Barr, T. K. Gaisser, and T. Stanev. Flux of atmospheric neutrinos. *Phys. Rev. D*, 39:3532–3534, June 1989.

[91] P. Amram, et al. The ANTARES optical module. *Nuclear Instruments and Methods in Physics Research A*, 484:369–383, May 2002.

[92] E. Waxman and J. Bahcall. High Energy Neutrinos from Cosmological Gamma-Ray Burst Fireballs. *Physical Review Letters*, 78:2292–2295, March 1997.

[93] P. Mészáros and E. Waxman. TeV Neutrinos from Successful and Choked Gamma-Ray Bursts. *Physical Review Letters*, 87(17):171102, October 2001.

[94] C. D. Dermer and A. Atoyan. High-Energy Neutrinos from Gamma Ray Bursts. *Physical Review Letters*, 91(7):071102, August 2003.

[95] S. Razzaque, P. Mészáros, and E. Waxman. High Energy Neutrinos from Gamma-Ray Bursts with Precursor Supernovae. *Physical Review Letters*, 90(24):241103, June 2003.

[96] D. J. White, E. J. Daw, and V. S. Dhillon. A list of galaxies for gravitational wave searches. *Classical and Quantum Gravity*, 28(8):085016, April 2011.

[97] A. Goldstein, et al. The BATSE 5B Gamma-Ray Burst Spectral Catalog. *The Astrophysical Journal, Supplement*, 208:21, October 2013.

[98] A. Klotz, M. Boër, J. L. Atteia, and B. Gendre. Early Optical Observations of Gamma-Ray Bursts by the TAROT Telescopes: Period 2001-2008. *The Astronomical Journal*, 137:4100–4108, May 2009.

[99] C. W. Akerlof, et al. The ROTSE-III Robotic Telescope System. *Publications of the Astronomical Society of the Pacific*, 115:132–140, January 2003.

[100] D. M. Coward, et al. The Zadko Telescope: A Southern Hemisphere Telescope for Optical Transient Searches, Multi-Messenger Astronomy and Education. *Publications of the Astronomical Society of Australia*, 27:331–339, September 2010.

[101] V. Lipunov, et al. Master Robotic Net. *Advances in Astronomy*, 2010:30, 2010.

[102] K. Perrett, et al. SNLS: Realtime Pipeline and Current Status. In *American Astronomical Society Meeting Abstracts*, volume 37 of *Bulletin of the American Astronomical Society*, page 1177, December 2005.

[103] F. Yuan and C. W. Akerlof. Astronomical Image Subtraction by Cross-Convolution. *The Astrophysical Journal*, 677:808–812, April 2008.

[104] E. Bertin and S. Arnouts. SExtractor: Software for source extraction. *Astronomy and Astrophysics, Supplement*, 117:393–404, June 1996.

[105] E. Bertin. Automatic Astrometric and Photometric Calibration with SCAMP. In C. Gabriel, C. Arviset, D. Ponz, and S. Enrique, editors, *Astronomical Data Analysis Software and Systems XV*, volume 351 of *Astronomical Society of the Pacific Conference Series*, page 112, July 2006.

[106] E. Bertin, et al. The TERAPIX Pipeline. In D. A. Bohlender, D. Durand, and T. H. Handley, editors, *Astronomical Data Analysis Software and Systems XI*, volume 281 of *Astronomical Society of the Pacific Conference Series*, page 228, 2002.

[107] R. G. Kron. Photometry of a complete sample of faint galaxies. *The Astrophysical Journal Supplement Series*, 43:305–325, June 1980.

[108] D. Lang, D. W. Hogg, K. Mierle, M. Blanton, and S. Roweis. Astrometry.net: Blind astrometric calibration of arbitrary astronomical images. *Astronomical Journal*, 139(5):1782, 2010.

[109] D. G. Monet, et al. The USNO-B Catalog. *Astronomical Journal*, 125:984–993, February 2003.

[110] M. F. Skrutskie, et al. The Two Micron All Sky Survey (2MASS). *Astronomical Journal*, 131:1163–1183, February 2006.

[111] S. Arnouts and O. Ilbert. LePHARE: Photometric Analysis for Redshift Estimate. Astrophysics Source Code Library, August 2011.

[112] A. J. Pickles. A Stellar Spectral Flux Library: 1150-25000 Å. *Publications of the Astronomical Society of the Pacific*, 110:863–878, July 1998.

[113] M. S. Bessell. UBVRI passbands. *Publications of the Astronomical Society of the Pacific*, 102:1181–1199, October 1990.

[114] A. Ažusienis and V. Straižys. Improved Determination of the Response Curves and Parameters of the UBV System. Summary of Results. *Soviet Astronomy*, 13:316, October 1969.

[115] N. Zacharias, et al. VizieR Online Data Catalog: NOMAD Catalog (Zacharias+ 2005). *VizieR Online Data Catalog*, 1297:0, November 2005.

[116] D. Tody. The IRAF Data Reduction and Analysis System. In D. L. Crawford, editor, *Instrumentation in astronomy VI*, volume 627 of *SPIE Conference Series*, page 733, January 1986.

[117] K. N. Abazajian, et al. The Seventh Data Release of the Sloan Digital Sky Survey. *The Astrophysical Journal, Supplement*, 182:543–558, June 2009.

[118] A. Zeh, S. Klose, and D. A. Kann. Gamma-Ray Burst Afterglow Light Curves in the Pre-Swift Era: A Statistical Study. *The Astrophysical Journal*, 637:889–900, February 2006.

[119] M. Hamuy, et al. Optical and Infrared Spectroscopy of SN 1999ee and SN 1999ex. *The Astronomical Journal*, 124:417–429, July 2002.

[120] D. Richardson, D. Branch, and E. Baron. Absolute Magnitude Distributions and Light Curves of Stripped-Envelope Supernovae. *The Astronomical Journal*, 131:2233–2244, April 2006.

[121] P. A. Evans, et al. 1SXPS: A Deep Swift X-Ray Telescope Point Source Catalog with Light Curves and Spectra. *The Astrophysical Journal, Supplement*, 210:8, January 2014.

[122] A. Moretti, et al. The swift-XRT imaging performances and serendipitous survey. In *SPIE Conference Series*, volume 6688, page 0, September 2007.

[123] M. R. Goad, et al. Accurate early positions for Swift GRBs: enhancing X-ray positions with UVOT astrometry. *Astronomy and Astrophysics*, 476:1401–1409, December 2007.

[124] P. A. Evans, A. P. Beardmore, J. P. Osborne, and G. A. Wynn. The unusual 2006 dwarf nova outburst of GK Persei. *Monthly Notices of the Royal Astronomical Society*, 399:1167–1174, November 2009.

[125] W. Voges, et al. The ROSAT all-sky survey bright source catalogue. *Astronomy and Astrophysics*, 349:389–405, September 1999.

[126] P. A. Evans, et al. Swift follow-up of IceCube triggers, and implications for the Advanced-LIGO era. *ArXiv e-prints*, January 2015.

[127] D. J. Schlegel, D. P. Finkbeiner, and M. Davis. Maps of Dust Infrared Emission for Use in Estimation of Reddening and Cosmic Microwave Background Radiation Foregrounds. *The Astrophysical Journal*, 500:525–553, June 1998.

[128] A. L. Melchior, F. Combes, and A. Gould. The surface brightness of the Galaxy at the Solar neighbourhood. *ArXiv e-prints*, February 2008.

[129] P. Kumar and B. Zhang. The Physics of Gamma-Ray Bursts and Relativistic Jets. *ArXiv e-prints*, October 2014.

[130] E. Waxman and J. Bahcall. High Energy Neutrinos from Cosmological Gamma-Ray Burst Fireballs. *Physical Review Letters*, 78:2292–2295, March 1997.

[131] D. Guetta, M. Spada, and E. Waxman. On the Neutrino Flux from Gamma-Ray Bursts. *The Astrophysical Journal*, 559:101–109, September 2001.

[132] S. Hümmer, M. Rüger, F. Spanier, and W. Winter. Simplified Models for Photohadronic Interactions in Cosmic Accelerators. *The Astrophysical Journal*, 721:630–652, September 2010.

[133] P. Mészáros, K. Asano, and P. Veres. Gamma Ray Bursts: recent results and connections to very high energy Cosmic Rays and Neutrinos. *ArXiv e-prints*, September 2012.

[134] S. Hümmer, P. Baerwald, and W. Winter. Neutrino Emission from Gamma-Ray Burst Fireballs, Revised. *Physical Review Letters*, 108(23):231101, June 2012.

[135] N. Gehrels, E. Ramirez-Ruiz, and D. B. Fox. Gamma-Ray Bursts in the Swift Era. *Annual Review of Astronomy and Astrophysics*, 47:567–617, September 2009.

[136] A. Klotz. . *Paper in prep.*, 2015.

[137] E. S. Rykoff, et al. A Search for Untriggered GRB Afterglows with ROTSE-III. *The Astrophysical Journal*, 631:1032–1038, October 2005.

[138] S. Adrián-Martínez, et al. Search for muon neutrinos from gamma-ray bursts with the ANTARES neutrino telescope using 2008 to 2011 data. *Astronomy and Astrophysics*, 559:A9, November 2013.

[139] ANTARES Collaboration. First search for neutrinos in correlation with gamma-ray bursts with the ANTARES neutrino telescope. *Journal of Cosmology and Astroparticle Physics*, 3:6, March 2013.

[140] R. Abbasi, et al. An absence of neutrinos associated with cosmic-ray acceleration in γ-ray bursts. *Nature*, 484:351–354, April 2012.

[141] O. Godet, et al. The Chinese-French SVOM Mission: studying the brightest astronomical explosions. In *Society of Photo-Optical Instrumentation Engineers (SPIE) Conference Series*, volume 8443 of *Society of Photo-Optical Instrumentation Engineers (SPIE) Conference Series*, page 1, September 2012.

[142] D. Götz, et al. The microchannel x-ray telescope for the gamma-ray burst mission SVOM. In *Society of Photo-Optical Instrumentation Engineers (SPIE) Conference Series*, volume 9144 of *Society of Photo-Optical Instrumentation Engineers (SPIE) Conference Series*, page 23, July 2014.

[143] S. Ando, J. F. Beacom, and H. Yüksel. Detection of Neutrinos from Supernovae in Nearby Galaxies. *Physical Review Letters*, 95(17):171101, October 2005.

[144] D. Schiminovich, et al. The GALEX-VVDS Measurement of the Evolution of the Far-Ultraviolet Luminosity Density and the Cosmic Star Formation Rate. *The Astrophysical Journal, Letters*, 619:L47–L50, January 2005.

[145] R. Abbasi, et al. Searching for soft relativistic jets in core-collapse supernovae with the IceCube optical follow-up program. *Astronomy & Astrophysics*, 539:A60, March 2012.

APPENDIX A

Neutrino data sets

Table A.1: Details of the neutrino alerts analyzed in this work, for which early and/or long term follow-up images have been taken.

Alert name ANTyymmddA/B	Time (UT)	Ra (°)	Dec (°)	Type	N_{hits}	Amplitude (pe)	Follow-up[a]
ANT091010A	16:14:57	294.960	-50.433	HE	16	169	l
ANT091010B	20:25:30	296.979	-57.244	HE	22	95	l
ANT091214A	19:35:58	314.227	-6.520	HE	28	296	l
ANT100123A	07:16:45	73.070	-2.990	HE	34	339	e/l
ANT100302A	03:51:06	152.770	-28.170	HE	26	200	l
ANT100706A	17:22:30	81.481	15.280	HE	44	506	l
ANT100725A	01:16:40	257.224	-63.188	HE	12	66	e/l
ANT100913A	21:55:25	165.142	41.391	HE	46	277	e
ANT100922A	11:24:23	43.578	13.458	HE	19	158	e/l
ANT101211A	08:12:21	323.070	-45.110	HE	30	309	l
ANT110305A	12:57:20	295.517	-48.193	HE	27	194	e/l
ANT110322A	00:48:04	346.754	-15.336	HE	20	93	l
ANT110409A	04:47:50	129.365	-40.207	HE	21	253	e/l
ANT110428A	14:09:39	314.595	-42.636	HE	24	114	l
ANT110521A	04:56:15	180.124	-13.155	HE	27	134	l
ANT110531A	21:45:16	326.944	-8.795	HE	54	439	e
ANT110613A	06:22:40	179.638	659.052	HE	21	181	l
ANT110615A	15:54:46	290.247	-12.346	HE	24	224	l
ANT110923A	08:26:33	285.194	10.244	HE	22	236	e
ANT110925A	11:38:17	58.385	-52.894	HE	29	279	l
ANT110925B	20:27:38	70.998	15.507	HE	50	356	e/l
ANT111008A	10:45:40	248.170	-25.834	HE	36	336	e/l
ANT111010A	03:43:34	124.983	-45.125	HE	25	231	l
ANT111019A	08:56:15	321.165	-0.692	HE	32	185	e
ANT111019B	08:56:15	322.070	-0.637	HE	32	185	e
ANT111101A	12:30:52	345.917	-5.698	HE	33	207	e/l
ANT111124A	16:13:52	102.041	-51.796	Dir	17	99	l
ANT111205A	21:33:11	146.411	-32.829	Dir	20	74	e/l
ANT111228A	09:18:42	27.025	32.323	Dir	11	90	e
ANT120102A	01:24:21	72.129	-59.709	Dir	11	54	e/l
ANT120105A	18:02:53	228.824	-26.121	HE	26	184	e/l
ANT120210A	08:48:15	42.711	-28.220	HE	90	302	l
ANT120730A	00:14:33	178.088	-40.096	HE	135	489	e
ANT120907A	01:25:10	220.171	-11.595	HE	77	245	e/l
ANT120907B	10:12:41	344.750	30.933	HE	76	242	e/l
ANT120923A	10:00:16	318.596	-51.071	HE	71	128	e/l
ANT121010A	06:31:01	52.841	-29.216	Dir	38	28	e/l

Table A.2: *Continued.*

Alert name ANTyymmddA/B	Time (UT)	Ra (°)	Dec (°)	Type	N_{hits}	Amplitude (pe)	Follow-up[a]
ANT121010B	07:05:47	248.801	14.102	HE	93	261	l
ANT121012A	04:42:49	239.512	-10.226	Dir	47	42	e/l
ANT121027A	18:47:58	105.552	-4.011	Dir	39	51	e/l
ANT121102A	17:02:09	355.916	-67.103	HE	74	159	l
ANT121105A	09:32:24	315.027	-18.31	HE	72	205	l
ANT121206A	10:02:42	62.001	2.434	HE	104	158	e/l
ANT121212A	01:13:10	206.703	-36.688	Dir	65	85	l
ANT121228A	18:18:11	191.467	3.019	Dir	40	130	l
ANT130112A	18:31:00	139.323	-33.102	HE	99	348	l
ANT130210A	14:00:10	185.433	5.897	Dir	52	61	e
ANT130430A	21:20:11	283.429	-57.196	HE	155	456	l
ANT130722A	20:38:24	74.570	3.411	VHE	87	188	e
ANT130724A	02:07:20	199.295	11.938	HE	91	171	e
ANT130915A	06:24:58	311.314	-51.603	VHE	146	485	e/l
ANT130918A	22:21:41	21.622	-51.570	HE	113	199	l
ANT130927A	18:22:56	106.948	-68.578	VHE	81	258	e/l
ANT130928A	20:03:18	121.865	-3.156	Dir	31	104	e/l
ANT131009A	17:31:34	104.522	-43.748	HE	153	373	l
ANT131011A	01:37:39	183.902	19.012	HE	90	345	l
ANT131027A	12:13:35	105.124	6.422	HE	74	190	e/l
ANT131031A	20:02:10	192.134	-11.166	Dir	46	22	l
ANT131102A	15:57:27	8.607	-16.705	HE	125	194	l
ANT131121A	14:58:28	53.495	-35.105	Dir	38	87	l
ANT131209A	01:56:24	197.235	-13.345	HE	87	163	e/l
ANT131221A	08:43:36	138.015	-23.930	Dir	30	49	e/l
ANT140123A	11:53:45	105.440	0.811	VHE*	80	401	e/l
ANT140125A	03:27:08	53.002	-49.491	HE	80	224	e/l
ANT140202A	07:27:04	95.161	-60.830	HE	79	231	l
ANT140203A	06:48:06	89.731	-23.394	Dir	54	93	e
ANT140223A	01:01:20	43.712	-10.802	Dir	39	30	e
ANT140301A	18:59:18	216.868	-64.285	HE	73	181	l
ANT140304A	05:19:15	117.930	-44.944	HE	81	192	e
ANT140309A	00:40:10	52.511	-12.955	HE	71	275	e/l
ANT140311A	13:16:20	237.416	31.826	VHE	96	324	e/l
ANT140323A	15:31:01	150.919	-27.371	Dir	46	102	e/l
ANT140408A	11:10:09	177.461	-3.301	Dir	44	70	e/l
ANT140505A	11:54:47	203.359	14.450	HE	80	239	e
ANT140515A	04:35:16	39.471	-19.731	HE	71	222	l
ANT140619A	18:08:45	339.243	-2.926	Dir	28	42	l
ANT140630A	14:23:27	20.933	1.280	Dir	32	29	l
ANT140802A	20:07:12	277.631	-62.719	HE	87	250	l
ANT140914A	05:13:35	298.424	2.677	HE	109	210	e/l
ANT140925A	15:06:59	64.101	-62.731	Dir	48	90	l
ANT141027A	16:32:27	173.144	-14.048	Dir	28	45	l
ANT141112A	00:10:59	127.887	-22.911	Dir	32	29	l
ANT141220A	14:53:59	71.679	-45.968	VHE	59	361	e/l
ANT150122A	07:09:35	168.551	-26.119	Dir	28	55	e/l
ANT150129A	10:20:12	34.656	4.863	VHE	92	207	e/l
ANT150409A	23:02:58	306.069	-47.863	VHE	101	410	e
ANT150809A	00:26:50	162.845	-56.512	VHE	118	396	e
ANT150901A	07:38:25	246.426	-27.390	VHE	127	356	e

[a] Data have been analyzed for early (e) and/or long term (l) follow-up observations.
* For this neutrino alert, early optical and X-ray observations have been performed, while for the other alerts triggered with the VHE trigger, only X-ray observations have been made.

APPENDIX B

Detected X-ray sources

Table B.1: Sources detected in the XRT follow-up of the ANTARES triggers.

Alert name (ANTyymmddA)	Source #	Location (J2000)	Flag[a]	Exposure (ks)	Mean flux ($\times 10^{-13}$ erg cm^{-2} s^{-1})	N_{seren}[b]	Catalogued?
ANT130722A	1	$04^h\ 57^m\ 51^s9$ +03° 32′ 01″	G	3.0	6.9 (±1.4)	0.2	Yes: 1RXS J045752.5+033200
	2	$04^h\ 59^m\ 46^s4$ +03° 23′ 34″	G	1.5	6.2 (±1.6)	0.4	No
	3	$04^h\ 58^m\ 06^s4$ +03° 27′ 20″	G	2.6	2.2 (±0.6)	1.0	No
	4	$04^h\ 58^m\ 58^s6$ +03° 14′ 54″	G	2.8	2.2 (±0.6)	1.3	No
	5	$04^h\ 57^m\ 44^s5$ +03° 16′ 33″	G	2.7	0.7 (±0.4)	0.9	No
ANT130915A	1	$20^h\ 46^m\ 05^s3$ -51° 49′ 41″	R	1.2	1.9 (±0.7)	1.0	No
	2	$20^h\ 44^m\ 47^s6$ -51° 37′ 16″	G	1.7	1.7 (±0.7)	1.0	No
ANT130927A	1	$07^h\ 08^m\ 10^s8$ -68° 50′ 55″	G	1.5	2.7 (±0.8)	0.6	Yes: 1RXS J070810.2-685054
	2	$07^h\ 06^m\ 06^s3$ -68° 35′ 57″	G	1.6	1.6 (±0.6)	1.3	No
	3	$07^h\ 09^m\ 32^s8$ -68° 35′ 31″	G	1.9	1.1 (±0.5)	1.7	No
	4	$07^h\ 05^m\ 44^s5$ -68° 46′ 25″	R	2.0	1.2 (±0.6)	1.7	No
ANT140123A	1	$07^h\ 00^m\ 20^s4$ +00° 49′ 27″	G	1.4	3.3 (±1.1)	0.6	No
ANT140311A	1	$15^h\ 50^m\ 10^s9$ +31° 39′ 30″	G	3.0	2.6 (±1.2)	1.2	No
	2	$15^h\ 49^m\ 31^s2$ +31° 29′ 14″	G	1.5	1.7 (±0.8)	0.8	No
	3	$15^h\ 51^m\ 02^s4$ +31° 56′ 15″	G	1.4	2.9 (±1.2)	1.1	No
ANT141220A	1	$04^h\ 47^m\ 35^s2$ -46° 10′ 54″	G	1.5	1.5 (±0.7)	1.3	No
	2	$04^h\ 46^m\ 10^s9$ -45° 58′ 44″	G	1.7	1.4 (±0.7)	1.9	No
ANT150129A	1	$02^h\ 19^m\ 31^s6$ +04° 51′ 18″	G	1.9	1.3 (±0.6)	1.4	No
	2	$02^h\ 19^m\ 16^s2$ +04° 34′ 29″	G	1.4	0.3 (±0.2)	1.5	No
	3	$02^h\ 17^m\ 52^s6$ +04° 49′ 32″	G	1.4	1.4 (±0.6)	1.4	No
ANT150409A	1	$20^h\ 24^m\ 03^s9$ -47° 38′ 21″	G	1.8	2.9 (±1.0)	0.8	No
	2	$20^h\ 24^m\ 50^s0$ -48° 05′ 08″	G	1.7	1.4 (±0.5)	1.1	No
	3	$20^h\ 22^m\ 55^s3$ -47° 40′ 06″	G	1.2	1.2 (±0.6)	1.8	No
	4	$20^h\ 24^m\ 36^s4$ -47° 57′ 09″	G	3.0	1.7 (±0.8)	1.3	No
	5	$20^h\ 24^m\ 27^s7$ -47° 57′ 13″	P	2.8	1.1 (±0.5)	1.4	No
ANT150809A	1	$10^h\ 51^m\ 28^s2$ -56° 34′ 19″	P	2.3	1.2 (±0.7)	1.3	No
	2	$10^h\ 51^m\ 15^s3$ -56° 22′ 34″	G	1.8	1.9 (±0.9)	1.5	No
ANT150901A	1	$16^h\ 26^m\ 02^s1$ -27° 18′ 15″	G	2.7	7.2 (±0.7)	0.1	No, brighter than the RASS limit
	2	$16^h\ 26^m\ 23^s4$ -27° 39′ 03″	G	1.4	5.8 (±0.9)	0.07	Yes: XMMSL1 J162624.0-273854
	3	$16^h\ 24^m\ 41^s6$ -27° 21′ 49″	G	1.8	6.1 (±1.3)	0.3	Yes: 1SXPS J162441.2-272145
	4	$16^h\ 26^m\ 23^s0$ -27° 15′ 03″	G	2.8	1.6 (±0.3)	0.5	Yes: CD-26 11339
	5	$16^h\ 26^m\ 30^s2$ -27° 41′ 22″	G	0.3	0.2 (±0.1)	0.03	Yes: HD 148040/1RXS J162630.3-274116
	6	$16^h\ 25^m\ 55^s8$ -27° 21′ 26″	G	2.5	1.2 (±0.2)	1.2	No
	7	$16^h\ 25^m\ 28^s5$ -27° 35′ 39″	G	1.7	2.3 (±1.1)	1.5	Yes: 1SXPS J162529.0-273541
	8	$16^h\ 25^m\ 10^s9$ -27° 40′ 43″	G	1.4	3.4 (±1.8)	0.7	No

[a] Indicates how likely the source is to be real. G=Good, R=Reasonable, P=Poor.
[b] Number of expected serendipitous sources in the field, at least as bright as the detected object.

APPENDIX C

Optical data from long follow-up observations

Table C.1: Details of the 71 neutrino alerts for which long term follow-up images have been analyzed. All the images from the same observation night are co-added together.

Alert name ANTyymmddA/B	Telescope	IM[a] (days)	REF[b] (days or year)	$m_{\rm lim}$ IM[c] (mag)	$m_{\rm lim}$ REF[d] (mag)	Candidates[e]
ANT091010A	TAROT	T0 + 3, 15	2014	14.2 - 18.2	18.5	377
ANT091010B	TAROT	T0 + 6, 15	2014	18.7	19.4	224
ANT091214A	TAROT	T0 + 2, 3, 4, 5, 6, 8, 12	T0 + 1	16.6 - 18.3	18.4	314
ANT100123A	TAROT	T0 + 1, 5, 6, 7, 9, 10, 11, 13, 19	2015	17.7 - 19.2	19.4	203
ANT100302A	ROTSE	T0 + 3, 4, 5, 6, 8, 10, 16, 17, 28	T0 + 2	17.2 - 18.0	18.0	337
ANT100706A	TAROT	T0 + 6, 7, 8, 9, 10, 12, 13, 17, 19, 47	T0 + 70	15.9 - 16.9	18.0	167
ANT100725A	TAROT	T0 + 1, 2, 6	T0	15.7 - 16.4	17.2	453
	ROTSE	T0 + 26, 27	T0 + 2	15.2 - 15.6	16.6	377
ANT100922A	ROTSE	T0 + 2, 6, 7, 8, 9, 11, 14, 18	T0 + 70	14.7 - 18.0	18.5	296
ANT101211A	ROTSE	T0 + 3, 4, 5, 8, 10	T0 + 2	15.5 - 16.2	17.3	295
ANT110305A	TAROT	T0 + 10, 28, 46	T0 + 61	17.7 - 17.9	17.8	406
ANT110322A	TAROT	T0 + 15, 27	T0 + 45	16.4 - 17.3	16.9	73
ANT110409A	TAROT	T0 + 1, 2, 3, 4, 5, 6, 8, 14, 26, 44	T0	17.7 - 18.6	18.6	279
ANT110428A	TAROT	T0 + 2, 5, 6, 7, 8, 10, 16, 28, 46	T0 + 61	16.2 - 18.8	18.9	224
ANT110521A	TAROT	T0 + 1, 2, 3, 4, 5, 6, 7, 9, 15, 26, 27	2015	16.6 - 18.9	19.0	159
ANT110613A	TAROT	T0 + 3, 4, 44, 59	T0 + 1	17.2 - 17.6	17.6	228
ANT110615A	TAROT	T0 + 5, 6, 7, 8, 10, 16, 28, 45	T0 + 61	16.9 - 17.8	17.8	224
ANT110925A	TAROT	T0 + 4, 5, 6, 7, 8	2014	18.9 - 19.1	19.1	138
ANT110925B	TAROT	T0, T0 + 1, 2, 3, 4, 5, 6, 7, 8, 10, 16	T0 + 61	17.4 - 18.8	18.9	117
ANT111008A	TAROT	T0 + 1, 3, 4, 7, 9	T0	17.1 - 17.5	17.9	298
ANT111010A	TAROT	T0 + 6, 15	T0 + 60	16.8 - 18.0	18.1	358
ANT111101A	TAROT	T0 + 2, 8, 15, 46	T0 + 61	17.5 - 18.0	18.1	172
	ROTSE	T0 + 6, 7, 8, 10, 16, 27, 28, 29	T0 + 1	16.9 - 17.4	17.9	246
ANT111124A	TAROT	T0 + 5, 10, 16, 28	T0 + 60	18.4 - 19.2	19.4	301
ANT111205A	TAROT	T0 + 2, 3, 6, 7, 8, 9, 10, 12, 18, 30, 48, 63	T0 + 1	17.8 - 19.0	19.0	283
ANT120102A	TAROT	T0, T0 + 1, 2, 3, 4, 5, 6, 7, 9, 27	T0 + 45	17.8 - 19.2	19.4	122
ANT120105A	TAROT	T0 + 2, 5, 6, 7, 8, 10, 16, 28, 46	T0 + 60	16.7 - 18.7	18.5	167
ANT120210A	TAROT	T0 + 4, 5, 6, 7, 10, 16	T0 + 2	17.5 - 18.2	19.3	124
ANT120907A	TAROT	T0 + 2, 3, 4, 5, 6, 8	T0 + 1	16.7 - 16.9	16.8	115
ANT120907B	TAROT	T0 + 1, 2, 3, 4, 5, 6, 7, 9, 15, 27	T0 + 60	17.3 - 18.4	18.1	93
ANT120923A	TAROT	T0 + 2, 3, 4, 5, 6, 7, 27	T0 + 1	18.2 - 18.7	18.8	175
ANT121010A	TAROT	T0 + 1, 2, 3, 4, 5, 6, 7, 9, 15, 27, 45, 60	T0	18.9 - 19.4	19.1	86
ANT121010B	TAROT	T0 + 1, 2, 4, 5, 6	T0	16.8 - 17.1	17.2	197
ANT121012A	TAROT	T0 + 1, 2, 3, 4, 8	T0	17.7 - 18.1	17.9	199
ANT121027A	TAROT	T0 + 2, 3, 4, 6, 7, 8, 10, 16, 28, 46	2014	16.4 - 18.3	18.1	304
ANT121102A	TAROT	T0 + 3, 4, 5, 6, 10, 16, 28	T0 + 2	18.0 - 18.7	18.7	113
ANT121105A	TAROT	T0 + 2, 3, 6, 7, 9, 15	T0 + 1	17.2 - 18.2	18.1	147

Table C.2: *Continued.*

Alert name ANTyymmddA/B	Telescope	IM[a] (days)	REF[b] (days or year)	$m_{\rm lim}$ IM[c] (mag)	$m_{\rm lim}$ REF[d] (mag)	Candidates[e]
ANT121206A	TAROT	T0 + 3, 4, 5, 6, 7, 8, 10, 16, 27, 28, 60, 61	T0 + 2	18.1 - 19.2	18.8	88
ANT121212A	TAROT	T0 + 2, 3, 4, 9, 15, 27	T0 + 45	18.1 - 18.5	18.2	221
ANT121228A	TAROT	T0 + 2, 3, 4, 5, 6, 10, 16, 28	T0 + 46	17.3 - 18.6	18.9	158
ANT130112A	TAROT	T0 + 2, 3, 4, 5, 6, 7, 10, 16, 46	T0 + 61	18.4 - 19.4	19.4	173
ANT130430A	TAROT	T0 + 3, 4, 5, 6, 7, 8, 16	T0 + 46	18.1 - 18.8	18.6	285
ANT130915A	TAROT	T0 + 5, 6, 7, 9, 15, 27	2014	18.1 - 18.9	19.0	121
ANT130918A	TAROT	T0 + 2, 3, 5, 6, 8, 10, 16, 28, 46	T0 + 61	18.3 - 19.4	19.0	50
ANT130927A	TAROT	T0 + 3, 5, 6, 7, 8, 10, 16, 28, 46	T0 + 61	17.7 - 18.9	18.9	85
ANT130928A	TAROT	T0 + 2, 4, 5, 6, 7, 8, 10, 16, 28, 46	T0 + 61	17.2 - 18.7	18.6	213
ANT131009A	TAROT	T0 + 2, 3, 4, 5, 6, 7, 8, 10, 16, 28, 46	T0 + 61	16.8 - 18.8	18.9	206
ANT131011A	TAROT	T0 + 7, 15, 27, 45	T0 + 60	15.8 - 17.2	17.7	74
ANT131027A	TAROT	T0 + 3, 4, 5, 6, 7, 8, 10, 16, 28, 46	T0 + 61	15.0 - 18.3	18.5	223
ANT131031A	TAROT	T0 + 16, 28, 46	T0 + 60	16.3 - 17.5	17.2	144
ANT131102A	TAROT	T0 + 3, 4, 5, 6, 7, 9, 10, 16, 27, 28	T0 + 2	17.2 - 18.8	18.9	132
ANT131121A	TAROT	T0 + 3, 4, 5, 6, 7, 8, 10, 16, 28, 46, 61	T0 + 2	17.5 - 19.4	19.2	123
ANT131209A	TAROT	T0, T0 + 3, 4, 5, 6, 7, 9, 15, 27	T0 + 60	16.1 - 17.9	18.2	129
ANT131221A	TAROT	T0, T0 + 1, 2, 3, 4, 6, 10, 15, 16, 27, 60	2015	17.4 - 19.3	19.3	125
ANT140123A	TAROT	T0 + 2, 3, 4, 5, 15, 16, 45, 60	T0 + 1	17.1 - 18.8	18.5	567
ANT140125A	TAROT	T0 + 2, 3, 4, 15	T0 + 1	17.8 - 18.2	18.5	78
ANT140202A	TAROT	T0 + 5, 6, 7, 9, 15, 27	2015	18.5 - 18.9	18.7	138
ANT140301A	TAROT	T0 + 2, 28, 46	T0 + 61	17.0 - 17.2	17.2	298
ANT140309A	TAROT	T0 + 1, 3, 8	T0	15.8 - 16.3	17.9	124
	ROTSE	T0 + 3, 4, 9	T0 + 2	14.0 - 16.6	16.4	143
ANT140311A	TAROT	T0 + 3, 4, 5, 6, 7, 8, 28, 46, 61	T0 + 2	17.5 - 18.8	18.8	107
ANT140323A	TAROT	T0 + 4, 5, 6, 7, 8, 10, 16, 28, 45	T0 + 3	17.5 - 19.0	19.1	113
ANT140408A	TAROT	T0 + 9, 15, 27	T0 + 2	15.4 - 18.5	18.1	116
	ROTSE	T0 + 2, 3	T0 + 1	15.5 - 17.3	17.4	164
ANT140515A	TAROT	T0 + 6, 9, 15, 60, 61	2015	16.9 - 17.9	18.5	112
ANT140619A	TAROT	T0 + 3, 4, 5, 6, 7, 8, 10, 16, 28, 46	T0 + 2	17.6 - 18.6	18.8	104
ANT140630A	TAROT	T0 + 3, 5, 6, 7, 8, 16, 28	T0 + 60	16.6 - 18.3	18.2	157
ANT140802A	TAROT	T0 + 3, 4, 5, 6, 7, 8, 10, 16, 60	T0 + 2	17.8 - 18.7	18.8	201
ANT140914A	TAROT	T0 + 2, 5, 6, 8, 9, 14, 15, 26	T0 + 1	15.9 - 18.2	18.3	255
ANT140925A	TAROT	T0 + 4, 5, 6, 7, 8, 16, 28, 46	T0 + 3	18.3 - 19.1	19.0	84
ANT141027A	TAROT	T0 + 10, 12, 18, 30, 48	T0 + 62	16.2 - 17.6	17.2	166
ANT141112A	TAROT	T0 + 1, 2, 3, 4, 5, 6, 7, 15, 27, 45	T0 + 60	16.9 - 18.6	18.4	163
ANT141220A	TAROT	T0 + 3, 4, 5, 6, 7, 8, 10, 16, 28, 46	T0 + 2	17.7 - 19.0	18.9	110
ANT150122A	TAROT	T0 + 1, 2, 3, 4, 5, 6, 7, 60	T0	17.4 - 19.4	19.3	117
ANT150129A	TAROT	T0 + 2, 3, 6, 7	T0 + 1	16.7 - 17.1	16.8	93

[a] Date of the analyzed observations in days after the neutrino alert.
[b] Date (in days after the alert, or year of the observation) of the reference images chosen for the subtraction.
[c] Limiting magnitude ranges for IM.
[d] Limiting magnitude of the REF image.
[e] Average number of candidates per IM automatically selected by the pipeline and visually checked.

Abstract

Transient sources are often associated with the most violent phenomena in the Universe, where the acceleration of hadrons may occur. Such sources include gamma-ray bursts (GRBs), active galactic nuclei (AGN) or core-collapse supernovae (CCSNe), and are promising candidates for the production of high energy cosmic rays and neutrinos. The ANTARES telescope, located in the Mediterranean sea, aims at detecting these high energy neutrinos, which could reveal the presence of a cosmic ray accelerator. However, to enhance the sensitivity to transient sources, a method based on multi-wavelength follow-up of neutrino alerts has been developed within the ANTARES collaboration. This program, denoted as TAToO, triggers a network of robotic optical telescopes and the *Swift*-XRT with a delay of only a few seconds after a neutrino detection. The telescopes start an observation program of the corresponding region of the sky in order to detect a possible electromagnetic counterpart to the neutrino event. The work presented in this thesis covers the development and implementation of an optical image analysis pipeline, as well as the analysis of optical and X-ray data to search for fast transient sources, such as GRB afterglows, and slowly varying transient sources, such as CCSNe.

Résumé

Les sources transitoires sont souvent associées aux phénomènes les plus violents de l'Univers, où l'accélération de hadrons peut avoir lieu. Parmi ces sources, les sursauts gamma, les noyaux actifs de galaxie ou encore les supernovae à effondrement de coeur sont des candidats prometteurs pour la production de rayons cosmiques et de neutrinos de haute énergie. Le télescope ANTARES, situé au fond de la Méditerranée, a pour but de détecter ces neutrinos, qui pourraient révéler la présence d'une source de rayons cosmiques. Cependant, pour augmenter sa sensibilité aux sources transitoires, une méthode basée sur le suivi multi-longueur d'onde d'alertes neutrino a été développée au sein de la collaboration ANTARES. Ce programme, TAToO, permet de déclencher un réseau de télescopes optiques et l'instrument XRT du satellite *Swift* seulement quelques secondes après la détection d'un neutrino par ANTARES. Les télescopes commencent un programme d'observation de la région du ciel correspondante pour tenter de détecter une contrepartie optique ou X à l'événement neutrino. Les travaux présentés dans cette thèse portent sur le développement et la mise en place d'un programme d'analyse d'images optiques, ainsi que sur l'analyse de données optiques et X obtenues lors des observations par les différents télescopes, pour identifier des sources transitoires rapides, telles que les émissions rémanentes de sursauts gamma, ou lentes, telles que les supernovae à effondrement de coeur.